Universitat Autònoma de Barcelona

FLUORIDE AND METAL IONS REMOVAL FROM WATER BY ADSORPTION ON NANOSTRUCTURED MATERIALS

SARA ISABEL GRÀCIA LANAS

FLUORIDE AND METAL IONS REMOVAL FROM WATER BY ADSORPTION ON NANOSTRUCTURED MATERIALS

SARA ISABEL GRÀCIA LANAS

2017

UNIVERSITÀ DEGLI STUDI DI UDINE

UAB
Universitat Autònoma de Barcelona

UNIVERSITÀ DEGLI STUDI DI UDINE

UAB Universitat Autònoma de Barcelona

FLUORIDE AND METAL IONS REMOVAL FROM WATER BY ADSORPTION ON NANOSTRUCTURED MATERIALS

SARA ISABEL GRÀCIA LANAS

Doctoral Thesis in Chemistry in Environmental and Energy Engineering Science

XXVIII cycle

Università degli Studi di Udine

Dipartimento Politecnico di Ingegneria e Architettura

Doctoral dissertation under International Joint Supervision with the

Universitat Autònoma de Barcelona

Departament de Química

April 2017

Supervisor: Prof. Andrea Melchior

Supervisor: Prof. Manuel Valiente

Co-Supervisor: Prof. Marilena Tolazzi

UNIVERSITÀ DEGLI STUDI DI UDINE

UAB
Universitat Autònoma de Barcelona

Thesis submitted for the award of the degree of Doctor in Chemistry in Environmental and Energy Engineering Science by

SARA ISABEL GRÀCIA LANAS

Approvement, the supervisors

Dr. Manuel Valiente Malmagro **Dr. Andrea Melchior**

April 2017

UNIVERSITÀ DEGLI STUDI DI UDINE

UAB

Universitat Autònoma de Barcelona

This PhD Thesis has been developed under the projects:

- PRIN 2010-2011. Nanotecnologia molecolari per il rilascio controllato di farmaci – NANOMED/Nanomolecular technologies for Drug delivery - NANOMED
- CHEMSYNCRO. Ref: CTM2012-30970 - Spanish Ministry: Ministerio de Economía y Competitividad (MINECO)
- CHENEXUS. Ref. CTM2015-65414-C2-1-R - Spanish Ministry: Ministerio de Economía y Competitividad (MINECO)

SUMMARY

SUMMARY

Nowadays the environmental pollution is a great global enemy, being one of the problems that most affect the whole world. It arises as a result of the addition of any pollutant substance to the environment, with an amount that causes adverse effects on living beings. The present work focuses on the elimination of certain aqueous contaminants, such as fluoride or different metal ions. Exist a great variety of methodologies for the treatment of wastewater, however, the adsorption is recognized as one of the most effective methods for this purpose, since offers simplicity of the experimental design and low cost of the methodology.

Different nanostructured materials have been applied for the adsorption of the aforementioned water contaminants. These materials have been chosen because of the high surface area that they offer in a very small volume. Therefore, they present ideal characteristics as adsorbent materials for the treatment of wastewater.

The first chapter of the thesis focuses on the removal of fluoride from contaminated water. Hierarchical alumina microspheres (HAM) have been selected as the optimum material, due to their high surface area and porosity, as well as the stability of the material against large changes in pH and temperature. The microspheres have been synthesized using the methodology described in the literature with significant modifications, and have subsequently been characterized with techniques such as SEM, TEM, XRD, DLS or BET, providing detailed information on the morphology and the structural properties of the material. Two types of HAM, differing mostly for crystallinity, surface area and pore size have been obtained.

Potentiometric studies have been performed to determine the fluoride remaining in solution. The obtained results have been adjusted with the Langmuir and Freundlich model to describe the adsorption mechanism, obtaining a better correlation with the Langmuir isotherm. The adsorption constant obtained for type A is 1 order of magnitude higher than for type B, showing that the synthetic protocol has a remarkable effect on this parameter. The highest defluoridation capacity reaches 26 $mmol \cdot g^{-1}$ after 1 hour of equilibration for the amorphous HAM, which is higher than for other adsorbents reported in the literature.

Accurate data on the enthalpy associated to the adsorption process allow the design of the best conditions both for the uptake and for the eventual successive release of a given chemical species. In previous works, the enthalpy associated to fluoride adsorption (ΔH_{ads}) has been calculated by the van't Hoff equation (using the temperature dependence of the Langmuir adsorption constant). However, many studies considered the discrepancies between enthalpy values obtained directly (ITC) and from van't Hoff equation and evidenced the large uncertainties associated to the latter method. In this work, ITC is applied for the first time to obtain direct determination of ΔH_{ads} for fluoride ion adsorption by HAM to provide independent and more robust thermodynamic parameters. The ΔH_{ads} values obtained are clearly negative for the different samples investigated.

The second part of the thesis focuses on the removal of heavy metals and precious metals from contaminated water. In this case, magnetic nanoparticles (SPION, Super Paramagentic Iron Oxide Nanoparticles) have been chosen as adsorbent. Magnetic materials (such as SPION) may represent an interesting tool for the removal/recovery of metal ions from aqueous media, as they can be dispersed in the sample and easily recovered by using a magnetic field. However, for the adsorption of metal ions, the unmodified SPION has been demonstrated to have a small adsorption capacity. One of the advantages of this material is that its surface is easily modifiable by adding an organic ligand. Therefore, following the HSAB theory, ligands with functional groups such as -SH or -RSR- have been selected for SPION modification.

The aim of this study is to synthesize SPION and functionalize them with sulphur containing groups for the selective removal of heavy metals such as Cd^{2+}, Hg^{2+}, Pb^{2+} and Cr^{6+} and, on the other hand, for the recovery of precious metals such as Ag^{+} and Pt^{4+} from aqueous solution, characterizing also the adsorption processes in terms of loading capacity and thermodynamic parameters.

SPION have been synthesized and functionalized with 3-mercaptopropionic acid (3-MPA) following the procedure published in the literature and then characterized by standard methods (SEM, TEM, BET, FT-IR, XRD and TGA), while the metal adsorption process has been studied using a new methodology which combines Inductively Coupled Plasma-Optical Emission Spectrometer (ICP-OES) and Isothermal Titration Calorimetry (ITC). While

in previous works ΔH_{ads} (adsorption enthalpy) related to metal adsorption have been calculated by the van't Hoff equation, ITC is applied for the first time in this work for the direct determination of ΔH_{ads}. In the present method, data obtained by ICP-OES have been fitted with a Langmuir isotherm to obtain the value of the adsorption constant (K_{ads}). Then, the K_{ads} has been used to calculate the free metal concentration for each titrant addition in the calorimetric titrations in order to fit the experimental heat and ultimately obtain the ΔH_{ads} value for the metal adsorption. Moreover, ITC is also applied as a screening of the adsorbent material, in order to discriminate the optimal candidate for metal removal/recovery applications.

RIASSUNTO

Attualmente, l'inquinamento ambientale è un importante nemico globale, uno dei problemi che maggiormente influenzano il nostro mondo. Si pone come risultato dell'aggiunta di sostanze nell'ambiente, con un importo che che gli effetti negativi sugli esseri viventi quando supera i livelli determinati dalla legge. Questo documento si concentra sulla eliminazione di alcuni contaminanti acquosi, come il fluoruro o ioni metallici. Esistono una grande varietà di metodologie per il trattamento delle acque reflue, tuttavia, adsorbimento è riconosciuto come uno dei metodi più efficaci per questo scopo, a causa della sua semplicità nel disegno sperimentale e basso costo del metodo.

Diversi materiali nanostrutturati sono stati utilizzati per l'adsorbimento dei contaminanti dell'acqua previamente nominati. Questi materiali sono stati scelti per l'area superficiale che offrono in un volume molto piccolo, in modo che hanno caratteristiche ideali come adsorbenti per il trattamento delle acque reflue.

La prima parte della tesi si concentra sulla rimozione di fluoruro dell'acqua contaminata. Microsfere di allumina gerarchiche (HAM) sono state selezionate come i materiali ottimali, per la sua elevata area superficiale e porosità e per la stabilità che presentando contro grandi variazioni di pH e temperatura. Le microsfere sono state sintetizzate utilizzando il metodo descritto in letteratura con variazioni significative, e poi caratterizzate utilizzando tecniche come SEM, TEM, XRD, BET DLS per fornire informazioni dettagliate sulle proprietà morfologiche e strutturali del materiale. Due tipi di HAM, con differenze principalmente nella cristallinità, area superficiale e dimensione dei pori.

Studi potenziometrici per determinare il fluoro residuo in soluzione sono stati sviluppati. I datti ottenuti sono stati aggiustati per il modello di Langmuir e Freundlich, con l'obiettivo di descrivere il meccanismo di adsorbimento, ottenendo una migliore correlazione con l'isoterma di Langmuir. La costante di adsorbimento ottenuta per il tipo A è 1 ordine di grandezza superiore a quello per il tipo B, che mostra che il protocollo sintetico ha un effetto notevole su questo parametro. La più alta capacità di carico dei fluoruro raggiunge 26 mmol g^{-1} dopo 1 ora di equilibrio per il materiale più amorfo, questo valore è anche superiore rispetto ad altri adsorbenti riportati in letteratura.

Dati precisi sulla entalpia associata al processo di adsorbimento consentono la progettazione delle migliori condizioni sia per l'assorbimento e per l'eventuale successiva liberazione di una data specie chimica. In lavori precedenti, l'entalpia associata ad adsorbimento fluoro (ΔH_{ads}) è stata calcolata con l'equazione di van't Hoff (utilizzando la dipendenza dalla temperatura della costante adsorbimento Langmuir). Tuttavia, molti studi considerano le discrepanze tra i valori di entalpia ottenuti direttamente (ITC) e dall'equazione Van't Hoff e evidenziano le grandi incertezze associate a quest'ultimo metodo. In questo lavoro, ITC viene applicato per la prima volta ad ottenere la determinazione diretta di ΔH_{ads} per l'adsorbimento di fluoruro in HAM per fornire i parametri termodinamici indipendenti e più robusti. I valori ottenuti sono chiaramente ΔH_{ads} negative per i diversi campioni esaminati.

La seconda parte della tesi si concentra sulla rimozione dei metalli pesanti e metalli preziosi da acqua contaminata. In questa occasione, sono stato scelte nanoparticelle magnetiche (SPION; Super Paramagnetic Iron Oxide Nanoparticles) come materiale adsorbente. I materiale mangnetici (ad esempio SPION), possono rappresentare un interessante strumento per la rimozione/recupero di ioni metallici da mezzi acquosi perché possono essere dispersi nel campione e recuperati facilmente utilizzando un campo magnetico. Tuttavia, per l'assorbimento di ioni metallici, il SPION non modificato presenta una capacità di carico per questi metalli molto bassa. Uno dei vantaggi di questo materiale è che è facilmente modificabile aggiungendo un ligando organico alla superficie. Seguendo teoria HSAB, leganti con gruppi funzionali come -SH o -RSR- sono stati selezionati per modificare la superficie delle nanoparticelle.

Quindi, l'obiettivo di questo studio è quello di sintetizzare SPION e modificarlo con ligandi continenti S nel loro gruppo funzionale per l'assorbimento selettivo di metalli pesanti come Cd^{2+}, Hg^{2+}, Pb^{2+} e Cr^{6+}, e per ricuperare metalli preziosi come Ag^{+} e di Pt^{4+} del mezzo acquoso, caratterizzando anche processi di adsorbimento in termini di capacità di carico e parametri termodinamici.

SPION sono state sintetizzate e funzionalizzate con acido 3-mercapto propionico (3-MPA) e acido 3,3'-tiodipropionico seguendo la procedura pubblicata in letteratura, e posteriormente caratterizzate con dei metodi standard (SEM, TEM, BET, FT-IR, XRD e TGA), mentre il processo di adsorbimento metallo è stata studiato utilizzando una nuova

procedura che combina ICP e ITC. Mentre nel lavoro precedente sono state calcolate ΔH_{ads} (entalpia di adsorbimento) relative a l'assorbimento di metalli di mediante l'equazione di van't Hoff, l'ITC è applicato per la prima volta in questo lavoro per la determinazione diretta di ΔH_{ads}. Nel presente metodo, i dati ottenuti da ICP-OES sono stati aggiustati con la isoterma di Langmuir e così ottenere il valore della costante di adsorbimento (K_{ads}). Poi K_{ads} è stata utilizzata per calcolare la concentrazione di metallo libero per ogni aggiunta di titolante nella titolazione calorimetrica per aggiustare il calore sperimentale e infine ottenere il valore di ΔH_{ads} per l'adsorbimento del metallo. Inoltre, l'ITC viene anche applicato come screening del materiale adsorbente con il fine di discriminare il candidato ottimale per applicazioni di estrazione/recupero del metallo.

INDEX

GENERAL INDEX

Abbreviations

WHO	World health Organization
UNICEF	United Nations Children's Fund
F^-	Fluoride anion
HM	Heavy Metals
PM	Precious Metals
e-wastes	Electrical and electronic wastes
pH_{pzc}	point of zero charge
NSMs	Nanostructured materials
HSAB	hard soft acid-base theory
3-MPA	3-mercaptopropionic acid
3,3-TDPA	3,3′-thiodipropionic acid
Y	Misono softness parameter
HAM	Hierarchical alumina microspheres
SPION	Superparamagnetic Iron Oxide Nanoparticles
TMAOH	Tetramethylammonium hydroxide
LA	Lauric acid
SPION@LA	SPION coated with LA
SPION@3-MPA	SPION coated with 3-MPA
SPION@3,3-TDPA	SPION coated with 3,3-TDPA
SEM	Scanning Electron Microscope
EDS	Energy dispersive X-ray spectrosco
TEM	Transmission Electron Microscope
XRD	X-ray diffraction
JCPDS	Joint Committee on Powder Diffraction Standards database
BET	Brunauer–Emmett–Teller
BJH	Barrett–Joyner–Halenda
DLS	Dynamic Light Scattering
TGA	Thermogravimetry
FT-IR	Fourier Transformation - Infrared spectrum
ICP-OES	Inductively Coupled Plasma Optical Emission Spectrometry
ITC	Isothermal Titration Calorimetry
Q_{max}	Loading capacity

b	Langmuir constant
K_f	Freundlich constant
n	Adsorption intensity

1. INTRODUCTION

1. INTRODUCTION

1.1. WATER RESOURCES

Water is a renewable but limited and vulnerable resource, essential to sustain life, development and environment, and most of it is stored as salt water in the oceans.[1] Contrarily to saltwater, freshwater, because of its purity, is generally utilized for human activities, but it is estimated that only the 3% of the total water of the whole world is freshwater and only a third of that is available as surface water or ground water.[1] It is accessible to most of the people in the world; however, in a study by the World Health Organization (WHO) along with United Nations Children's Fund (UNICEF), it has been stated that in 2015, 663 million people still lack improved drinking water sources.[2]

Since water quality is not access to all areas of the world, and the amount available for humans is limited in time, there is the necessity to manage water uses in a sustainable manner, by controlling the presence of contaminants for availability, renovation and maintenance of it. Furthermore, population and human activity are increasing rapidly, and consequently water consumption has considerably increased, affecting the chemical composition of water resources. The intensity and diversity of water uses is part of the problem. The other is the threat facing the quality of water sources of human contamination, such as agriculture, industry, leaking sewers or septic tanks.
The presence in discharge waters of ions such as fluoride, arsenic, nitrate, iron, manganese, chloride, selenium, toxic metals and radioactive materials, coming from natural or anthropogenic sources, may endanger water quality leading health problems to living organisms.[3]

In the recent decades, wastewater has represented one of the major problems worldwide, because of the damages caused through its release in the environment, including pollution in the natural environment and drinking water, affecting thousands of people. Therefore, several mechanisms have been developed over time with the purpose to purify wastewater, removing the components from contaminated water that may result in damages to human health, water quality and ecosystem status, returning the water safely to natural sources and avoiding the risks to humans and the environment. Figure 1.1 summarizes the water cycle through which water is treated to maintain the good quality of water.

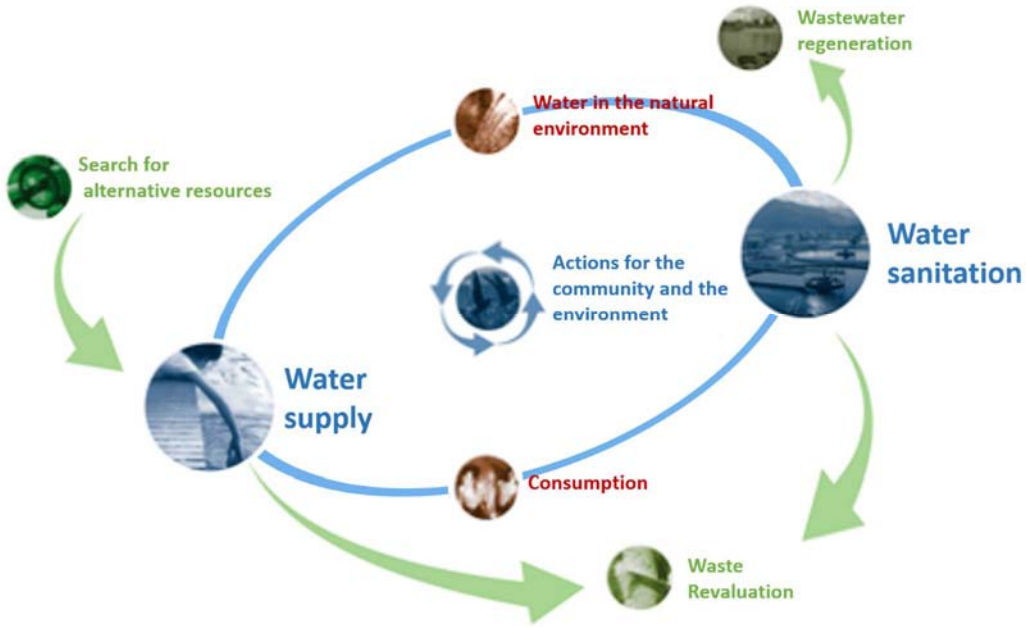

Figure 1.1. Integrated water cycle (figure adapted from [4]).

1.2. FLUORIDE

Fluorine is the lightest member of the halogen group and it is known as one of the most reactive element of the periodic table.[5,6] It is the most electronegative of all the elements[7], therefore, it has a strong tendency to acquire negative charge, and form fluoride anion (F^-) in solution, which is the only oxidation state found in the nature.[7]

Fluorine represents about 0.06–0.09 per cent of the earth's crust accounting about 0.3 g kg^{-1} of it,[5] and exists in the form of fluoride in more than 300 minerals,[6] of which fluorite (CaF_2), cryolite (Na_3AlF_6) and fluorapatite ($Ca_5(PO_4)_3F$) are the most common.[5]

Figure 1.2. Representative images of fluorite[8] (A), cryolite[9] (B) and fluorapatite[10] (C).

1.2.1. Natural sources

Waters with high fluoride concentrations occur in large and extensive geographical belts associated with several sources as sediments of marine origin in mountainous areas, volcanic rocks or ores, which are the main natural source of inorganic fluorides in soils, arriving to groundwater by the dissolution of them.[11]

1.2.2. Anthropogenic sources

Besides the natural geological sources for fluoride enrichment in groundwater, several human activities are also contributing to fluoride pollution. However, quantitative information about the release of fluoride into environment from anthropogenic sources is limited. Fluoride is discharged in the environment by exhaust gases, wastewaters and solid waste from several industrial processes,[11] such as glass, brick and ceramic production, semiconductor manufacturing, steel manufacture, aluminum, copper and nickel production, aluminum smelters or phosphate fertilizer production and use.[11,12] The effluents of those industries can elevate the fluoride concentration in water from tens to thousands of $mg \cdot L^{-1}$,[12] much higher that the concentration recommended by WHO (1.5 mg L^{-1}).[5,12] Therefore, it is necessary to develop techniques to remove F^- from wastewaters in order to maintain the concentration in water not upper 1.5mg L^{-1}. Figure 1.3. Schematic representation of fluoride reservoirs and flux on the Earth, with approximate volumes.[6]shows a schematic cycle of fluoride through the biogeosphere by natural and anthropogenic origins.

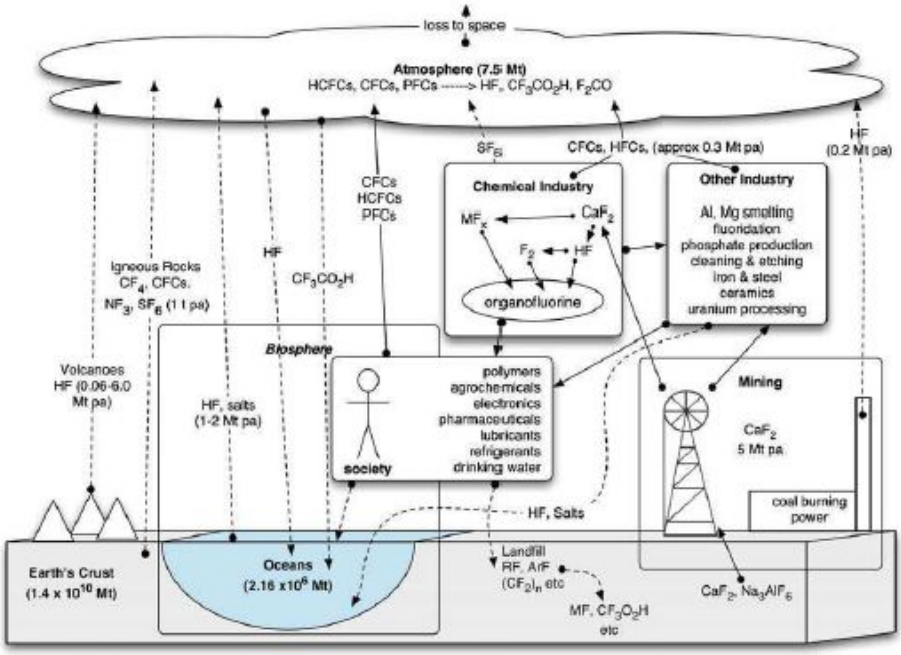

Figure 1.3. Schematic representation of fluoride reservoirs and flux on the Earth, with approximate volumes.[6]

1.2.3. Health effects

Fluoride is one of the very few chemicals that has been shown to cause significant effects in people through drinking water: depending on the amount of the ion intake it may cause beneficial or adverse effects.[5,12,13]

On the one hand, the exposure to low levels of fluoride in drinking-water (i.e., approximately 1 mg L^{-1}) has long been known to have a beneficial effect on the reduction of dental caries.[5] But on the contrary, the excessive exposure to fluoride from drinking-water or other sources, may cause a number of adverse harmful effects; from dental fluorosis, in mild cases, to osteoporosis, arthritis, cancer, infertility, brain damage, thyroid disorder or crippling skeletal fluorosis as the level and period of exposure increases.[5,12,13]

A high presence of fluoride in drinking water is affecting millions of people in several regions of the world such as south-east of Africa, United States, the Middle East of Asia, South America, and Asian countries. However, China and India are the worst affected countries[3] (* no recent data available. Figure 1.4).

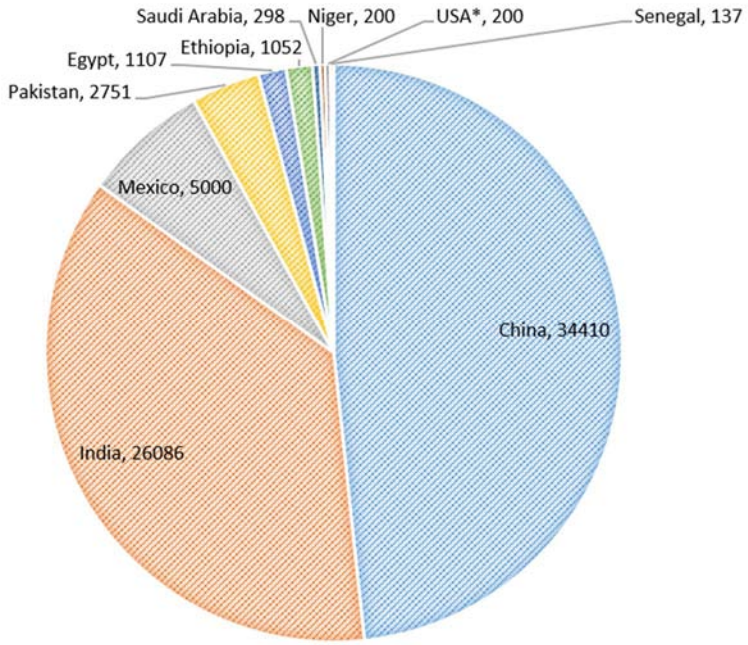

* no recent data available.

Figure 1.4. Estimated population exposed to fluoride contamination in selected countries ($x10^3$). (Figure adapted from reference[13]).

Keeping the view of toxic effects of fluoride on human health, there is an urgent need to find out an effective and robust technology for the removal of excess fluoride from drinking water.

1.3. HEAVY METALS

In the last decades, the term heavy metals (HM) has been widely used but there is not any authoritative definition in the literature.[14] A wide number of definitions exists, based to different characteristics of the metals and metalloids.

The oldest scientific definition of the term HM of the English literature,[15] may be found in Bjerrum's *Inorganic Chemistry*[16] published in 1936. Such definition is based on the density of the metals, and says that HM are those with a density greater than 7g cm^{-3}. The description of such metals has evolved over time, but there is no consistency on that. Several definitions exist in terms of density,[14,15,17,18] either greater than 4g cm^{-3}, higher than 5 or 6g cm^{-3} and even greater than 3.5g cm^{-3}. At some point in the history of the term, it has been realized that specific gravity is not of great significance in relation to the reactivity of the metal.[15] Therefore, several definitions have been formulated in terms of atomic weight. However, the standard of judgement still unclear, appearing scientists defining the HM as those metals with an atomic mass greater than 23 (Na),[19] higher than 40 (Sc). Even in some cases, HM have been defined in general way, described as such metals with high atomic weight,[20] the atomic number,[14,21] or the chemical properties; or the ones which give reaction with dithizone.[14] Not enough, another way to classify HM is to define them without clear basis other than toxicity as those elements commonly used in industry and generically toxic to animals.[14]

Even today, there is still no agreement about the specific gravity of HM. Attending this, there is not any conclusion to decide which metals should or not be included in the category of HM, being the term imprecise. In the present work, the term *heavy metals* is used to describe metals, characterized by their high density, which have been related with contamination and potential toxicity.[15]

Although few HM are essential for human health, an excess amount of these metals can have negative effects[18,22] such as zinc, which is essential for physiological of living tissue and regulation of several biochemical processes but in excess causes health problems such as stomach cramps, skin irritations, vomiting, nausea and anemia,[18] or copper, which is indispensable for animal metabolism, but an excessive ingestion of it leads vomiting, cramps, convulsions or even death.[18] Besides the HM which have essential functions to health, some others such as lead, cadmium and mercury have no relevance for living organisms and, even in traces, can cause severe damages to organisms.[23]

Because of their high solubility in aquatic environments, HM are absorbed by living organisms and contrary to organic contaminants, these metals are not biodegradable and tend to accumulate in them.[18] These toxic metals enter in the food chain, consequently large concentrations of these

pollutants may be accumulated in human body.[18,24] When the metals reach the concentration limited by law, they can cause several health problems.

Figure 1.5 below present cycle of the HM in the environment as well as the impact in humans.

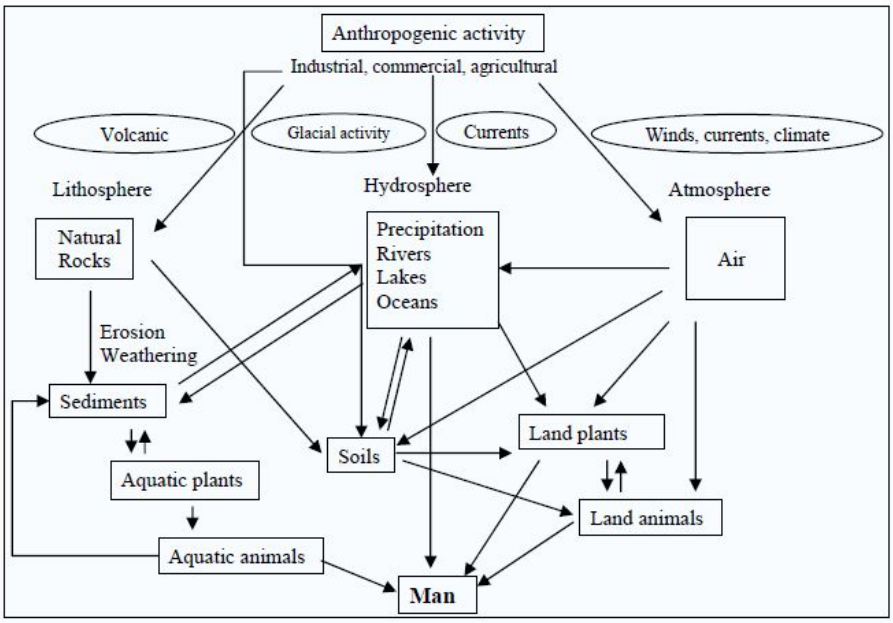

Figure 1.5. Cycle of HM within the environment.[25]

In the present work, some HM have been selected for the study of heavy metals removal including lead, chromium, mercury and cadmium. The main characteristics of such metals are described in Table 1.1.

METAL	Description	Sources	Health effects
Pb	The commonest of the HM[26] and it is a greyish-black soft solid, dense. It exists in two oxidation states (+4 and +2) but it is found in nature almost exclusively as lead sulfide (II) (galena).[27]	Volcanic activity or sea spray emissions contribute to lead pollution. However, most of the lead contamination is the result of human activity; smelting, refining and informal recycling of lead; use of gasoline; or production of lead-acid batteries.[28]	It is one of the most toxic elements of those we are exposed. At low concentrations, it causes anaemia and headache; but at high concentrations it causes serious problems such as kidney failure, convulsions, brain damage and even death.[27,28] The WHO has determined that the tolerable intake level in drinking water is 10 μg L^{-1}.[28]
Cr	It is a grey, hard metal widely distributed in Earth's crust and it can be found in oxidation states from +2 to +6,[29] being highest oxidation states those of highly interest due to its toxicity.[30] It has not been found in the pure form; its highest grade contains about 55% chromic oxide.[29]	The total natural chromium concentration in surface water depends on the region of the world. However, most of the chromium pollution is generated by the use of it and its salts in leather tanning or ceramic and glass industry, manufacture of catalysts, textile industries, fungicides or chromium metal production, chrome plating, and corrosion control. [30,31]	Cr(VI) is classified as human carcinogen, while and Cr(III) is not classifiable as to its carcinogenicity to humans.[32] The WHO have determined a limit concentration of total Cr of 0.05mg L^{-1}.[32] This value has been designated as provisional due to uncertainties in the toxicological database,[32] which is considered to be unlikely to cause health risks.
Hg	It is a liquid metal at room temperature. The elemental metal may be found combined with other elements to form inorganic compounds of its monovalent and divalent forms, existing a large number of them.[33]	It may be found naturally in the Earth's crust and can be transported throughout the environment by air and water.[33] Because of industrialization, human activities become a contribution to mercury release, due to mining operations, combustion of fossil fuels, cement production, plastic or electronic industry and incineration of wastes.[34,35]	Low exposures does not cause adverse health effects. However, if it exceeds the established levels may cause adverse effects on human health. Hg compounds act as poisoning causing hemorrhagic gastritis and colitis and then damages to kidneys.[27] The guideline value determined by WHO of maximum inorganic mercury concentration in water is 0.006 mg L^{-1}. [32]
Cd	It is a soft, ductile, silver-white metal with an oxidation state of +2. It is a relatively rare element; and it has not been found as native metal in the nature. [29,36] Cd has not been produced until the twentieth century. It is a by-product of zinc industry, thus, its production is determined by those of zinc.[29]	The major natural release into the environment comes from volcanic activity.[29,37] Although natural sources, the major part of Cd in the environment is due to industries such as smelting of non-ferrous metal ores, fossil fuel combustion and municipal waste incineration are the principle causes of cadmium discharge into the environment.[38]	The accumulation of that metal lead to tubular dysfunction, resulting in an increasing excretion of low molecular weight proteins in the urine.[38] Such effect on kidneys are generally irreversible. Then, the maximum concentration of cadmium in water suggested by WHO is 0.003mg L^{-1}.[37]

Table 1.1. Description of main characteristics of selected HM.

1.4. PRECIOUS METALS

Under the name of precious metals (PM) are grouped the called platinum group elements (PGM; Platinum Group of Metals); ruthenium, rhodium, palladium, platinum, osmium, iridium, along with gold and silver. The common property of these metals is the noble character of them due to their passivity through chemical reagents, makes them ideal for a wide range of applications.[39]

In recent decades, the development of electronic industry and the use throughout the world of electronic devices, mobile phones or PC's has increased rapidly and, consequently, the quantity of electrical and electronic wastes (e-wastes) generated is increasing dramatically.[40–42] The quantity of e-waste grow as the economies grow and new technologies are developed. According to the "Solving the E-Waste Problem Initiative",[42] about 49 million tons of e-waste have been generated in 2012 around the world, and it will be 65.4 million tons in 2017.[42] More than half of e-wastes consist of metals that include a significant proportion of valuable metals or their compounds, which indicates not only the loss of huge amount of resources but also the threat of environmental pollution.[25]

Therefore the recycling and reuse have become one of the promising options for e-waste treatment, which results in an important source of PM (much higher than those of any conventional natural ore[40]).

This thesis focused on the pre-concentration of two of the existing PM, silver and platinum. Silver has several applications in fields from electronics to catalisys or antibiotics.[43] Consequently, thousands of tons of such metal is then emitted to the environment.[43]

Platinum is also widely used in a variety of industries due to their unique physical and chemical properties. Their main uses are the automotive industry, the chemical industry process catalisys or the electrical industry.[25]

Considering the scarcity of natural sources, it is economically and ecologically important to recover that metal ions from industrial emissions. The principal characteristics of these metals are described in Table 1.2.

METAL	Description	Sources
Ag	Ag, along with Au and Cu, are known as coinage due to they are easily obtained in the metallic state; malleable; chemically unreactive; and, in the case of silver and gold, the low abundance of the metals involved that coins have intrinsic value of the metal itself.[27]	It is found in nature as free element or in minerals containing Ag. Significant amounts of Ag are also obtained during the extraction of Pb from their ores and electrolytic refining of Cu.[27,44] In almost all simple Ag compounds, the metal has an oxidation number of +1 and Ag(I) ion is the only stable ion in water.[27]
Pt	Is a silvery, shiny, lustrous, and poor reactive metal.[27,44] It is easily drawn and worked when pure. Its chemistry is largely that of the +2 and +4 oxidation states. However, there are a few, formally, +1 and +3 compounds.[44]	It is found in nature as the element along with small amounts of other metals of platinum group (ruthenium, rhodium, palladium, osmium, iridium, platinum) with a total annual production about 300 tons.[27,44]

Table 1.2. Main characteristics description of silver and platinum.

1.5. WASTEWATER TREATMENTS

The environment degradation, mostly caused by industrialization, has increased the public concern towards environment pollution and remediation. Therefore, in recent years several wastewater techniques have been developed to remove contaminants from aqueous medium; however they are still having some limitation especially that of high operation costs. The selection of a method for wastewater treatment should consider the conditions shown in Figure 1.6.

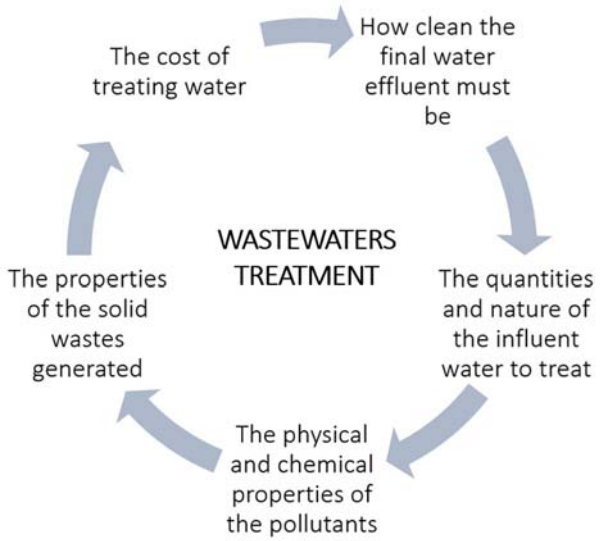

Figure 1.6. Conditions of wastewaters treatments (figure based on the reference [45]).

The main technologies for the removal of inorganic pollutants from wastewaters are summarized in Table 1.3.

Methodology	Description	Ref.
Precipitation	The soluble chemicals are removed from solution by the addition of a reagent with which they react to form a precipitate. Then it would be removed by standard flocculation, sedimentation, and/or filtration processes. The produced sludge have to be managed as hazardous waste due to the high concentrations of pollutants, increasing the cost of the method.[45]	46–55
Ion-exchange	A reversible chemical reaction wherein an ion from solution is exchanged with a similar ion attached to an immobile solid particle. Ion exchangers have a limited capacity; eventually become exhausted and must be regenerated by the appropriated solutions. Economic considerations of this methodology are the type and amounts of chemicals needed for regeneration.[45]	56–65
Membrane filtration	An interphase between two adjacent phases, which acts as a selective barrier controlling material transport between them. The main advantage relates to the transport selectivity of the membrane. This processes do not require additives but these are relatively expensive to install and operate and prone to fouling, scaling, or membrane degradation. Membrane techniques include reverse osmosis, nanofiltration, dialysis and electro-dialysis.[66]	67–79
Adsorption	It is defined as change in the concentration of a component in the surface layer in comparison with the bulk phase related to unit surface area. Adsorption involves interface accumulation of substances at a surface or interface. The process can occur at an interface between any two phases, in which the mass transfer becomes bound by physical and/or chemical interactions.[24,66]	80–90

Table 1.3. Description of inorganic contaminants removal methodologies.

Several research studies showed that treated wastewater is an important component of the water resources supply to cover the needs of a growing economy. However, the deficiency of the technologies for wastewater treatment are the high investment and maintenance of itself and the secondary pollution generated.[91] Hence, the greatest challenge in implementing a water treatment strategy is the adoption of low cost technologies.

1.6. ADSORPTION

As mentioned before, adsorption may be defined as an accumulation of compounds (adsorbate) on the surface provided by solid materials (adsorbent), and it is widely used to remove substances from fluid phases.[92,93] Figure 1.7 describes schematically the adsorption process as well as the components involved on such procedure. Changing the conditions of the system, as pH,

concentration or temperature, the species can be released to the liquid phase. This reverse process is called desorption.

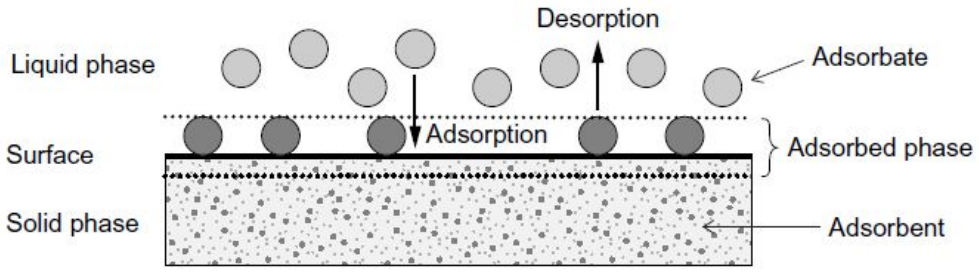

Figure 1.7. Basic terms of adsorption.[93]

1.6.1. Characteristics of adsorbents

Adsorbent materials are categorized depending on their characteristics along with the basis of their matrix composition, polarity, chemical and physical resistance as well as their particle size distribution, surface area, density, porosity and the pore radius distribution. Table 1.4 summarizes the previously mentioned features.

Material Features	Description
Density	It maybe defined depending on the volume used as reference. It may be broken down into *material density*; quotient of adsorbent mass and volume of the solid material without pores, *particle density*; the ratio of adsorbent mass and adsorbent volume including pores, and the *bulk density*; the amount of adsorbent needed to fill a vessel divided by the volume including the interparticle volume. [93]
Porosity	It specifies the fraction of void space on the total volume. Depending on the total volume considered, it can be distinguished between the particle porosity, and the bulk porosity. Both porosities can be derived from the densities. [92,93]
Surface area	The inner or specific surface area is a multiple of the outer surface of an adsorbent and is the site where adsorption occurs. Consequently, such parameter deserves special attention when choosing an adsorption material. The inner surface area is inversely proportional to the pore size; if the diameter is too small the adsorbate may not diffuse into the adsorbent. Therefore, the molecular size of the adsorbent constitutes a major limitation ot its application. [92,93]
Pore-size distribution	Due to the relevance of the pore system for both adsorption kinetics and adsorption equilibrium, it is interesting to get information about the frequency of occurrence of different pore

	sizes in the considered adsorbent. The adsorbents may have multitude of pores with different shapes and sizes. The pores allow the transport of the solute molecules, whereas inside the micropores adsorption and ion exchange occur.[92,93]
Surface chemistry	It is a very important aspect, since may affect the adsorbate/adsorbent interaction. The point of zero charge (pH_{pzc}) is the pH value at which the negative charges are equal to the positive ones, and the net charge of the surface is zero. Such parameter is important because helps in understanding the adsorption of charged species and the influence of pH on the adsorption process.[93]

Table 1.4. Adsorbent features definition.

1.6.2. Description of the adsorption process

Information about adsorption equilibrium data allows the evaluation of the efficiency of removal of water pollutants for the better design of the process.

Although single-solute adsorption is rather an exceptional case than a typical situation in water treatment practice, some general aspects of adsorption processes can be explained more clearly for the simple case where only one adsorbate should be considered. Furthermore, the mathematical models to describe the adsorption equilibrium are generally based on single-solute adsorption isotherms. Also, the comparison of the loading capacities of the adsorbents as well as the efficiency of these towards pollutants, are enough characterized by the description of single-solute adsorption.[93]

In order to describe the relation between the adsorbate and the adsorbent, adsorption isotherms are generally used. The detailed explanation of the different existing models are described in the Methodology chapter.

1.6.3. General thermodynamic considerations

The knowledge of thermodynamic parameters is of great importance in order to develop an effective and accurate design model for pollutants removal from water, since they provide information about energies associated with adsorption mechanism.

Negative Gibbs free energy (ΔG_{ads}) indicates the spontaneity of the adsorption mechanism and is related to enthalpy and entropy of adsorption as follows:[93]

$$\Delta G_{ads} = \Delta H_{ads} - T\Delta S_{ads} < 0 \qquad \text{Eq. 1.1}$$

The value of adsorption enthalpy (ΔH_{ads}) is used to identify the nature of adsorption. A positive value of ΔH_{ads} indicates an endothermic reaction; a negative one means that the adsorption process is exothermic. The adsorbate binding on the adsorbent material is controlled basically by the nature of the species. Depending on the value of the ΔH_{ads}, the adsorption process may be classified as physisorption or chemisorption. Physisorption commonly is reversible and rapid, mainly based on van der Waals forces, dipole forces, dipole-dipole forces, and dispersion forces as well as induction forces, which are usually below 50 kJ mol^{-1}. In contrast, chemisorption relates to a chemical bonding between the adsorbent active sites and adsorbate, the interaction forces are much higher and are reported to be > 50 kJ mol^{-1}.[92,93]

The variation of the adsorption entropy describes the change in the degree of disorder of the system.[93] Commonly, the particle immobilization on the surface of the adsorbate leads to an increase of the order of the system, therefore, the change of the adsorption entropy would be expected to be negative ($\Delta S_{ads} < 0$). However, it is not an established rule, existing situations where more species are desorbed than adsorbed (increasing the disorder of the system), thereby the entropy would be positive ($\Delta S_{ads} > 0$),[93,94] favouring the adsorption process.

1.6.4. Adsorption in water treatment

Adsorption processes do not add undesirable by-products when are applied for the pollutants removal, contrary to other methodologies such as precipitation, which generate a hazardous sludge. In addition, adsorption has been found to be better than other techniques for wastewater treatment in terms of simplicity of design and operation.[91]

The adsorption process of the pollutant agent on the adsorbent material takes place in three steps: [24,95]

(i) diffusion transport of the pollutant from the bulk solution to the adsorbent particle surface

(ii) adsorption on the particle surface

(iii) transport of the pollutant within the adsorbent particles, due to the exchange with the structural elements inside, depending on the chemistry of solids, or the transfusion to the internal surfaces for porous materials (intra particle diffusion)

The main aspects to consider when designing a suitable adsorption process to treat a contaminated effluent are: [91,96,97]

(i) nature and initial concentration of adsorbate

(ii) pH of the solution

(iii) temperature

(iv) interfering substances

(v) surface area of the adsorbent

(vi) nature and dose of adsorbent

(vii) cost-effectiveness of the method

To guarantee the efficient wastewater treatment, a wide number of adsorbents have been developed. Such materials are either of natural origin or the result of an industrial production and/or activation process. The main adsorbents as well as their features are summarized in Figure 1.8 below:

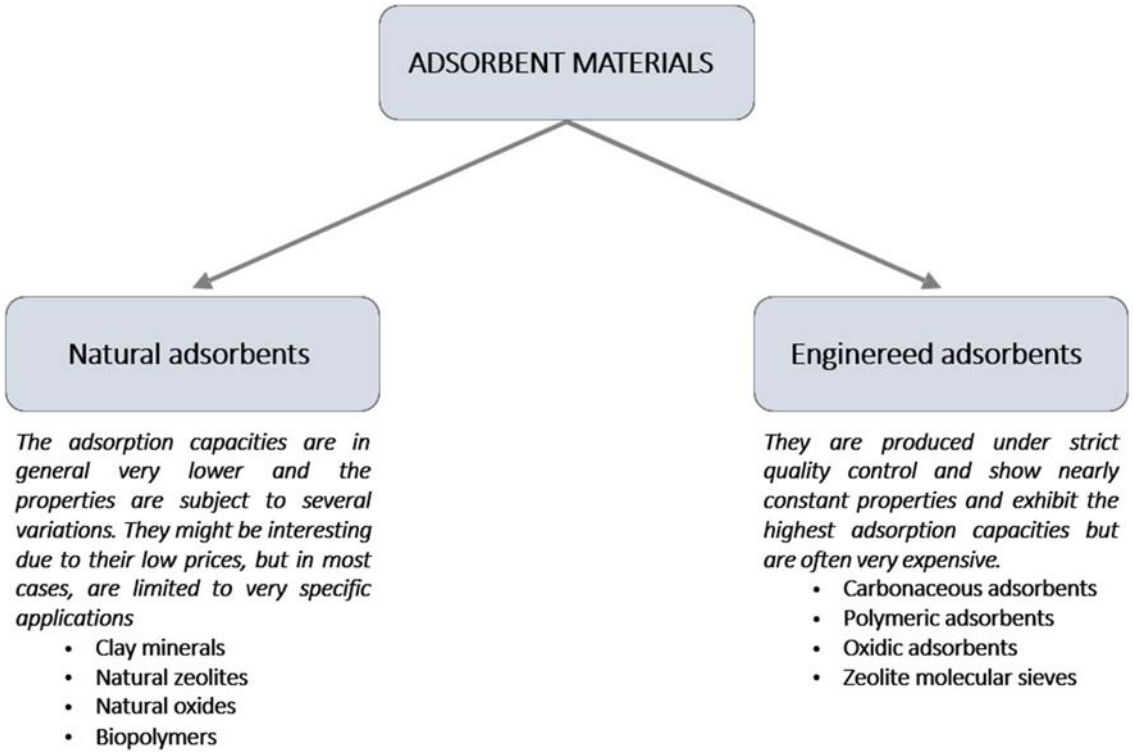

Figure 1.8. Adsorbent materials classified on the basis of their origin (figure based on the reference[93]).

Accordingly, engineered materials seem to be most suitable adsorbents for the treatment of contaminated effluents. At present time, the highlights of the development of the adsorption treatments are design, synthesis and application of nanoadsorbents.[97]

1.7. NANOSTRUCTURED ADSORBENT MATERIALS

1.7.1. A brief overview of Nanotechnology

Over the last decades, new terms have appeared such as nanoscience, nanotechnology, nanomaterials, nanostructures or nanoparticles, and it is because the world has experienced a

scientific "nano-revolution", in which one of the main areas in the current technological and scientific evolution is focused on Nanotechnology, involving the development of materials, structures and devices in a nanometer scale.

Up to now, there is not any provided definition from any international entity about the concept of nanoscale, which is proposed in some cases by sizes in the range of 1-1000nm[98,99], while in other descriptions the nanometer scale is within the range 1-100nm.[100] However, the size range that holds so much interest is typically below 100nm. Therefore, in this work the nanoscale will be considered the size within the range from one to few hundreds of nm.

Although nanotechnology is a recent discipline, the evidence of particular properties on nanometer scale is not new at all; it is well known that thousands of years ago, the Chinese used Au nanoparticles to red-colour their ceramic porcelains.[101] An interesting case is the *Lycurgus cup* (Figure 1.9); created in the time of Romans (4th century), such glass has the particularity that change its colour depending upon the light in which it is viewed; being green when the light is reflected and turns in red colour when the light comes from inside and is transmitted through the glass. This phenomenon is due to the presence of a small quantity of gold and silver nanoparticles with diameters about 70nm.[102]

Figure 1.9. Lycirgus cup with the light reflected (green) and transmitted (red) through the glass.[103]

Therefore, what is new is the understanding of atomic scale interactions. Nanoscience and Nanotechnology, theoretical and applied science respectively, are based on the study of phenomena occurring at the nanoscale and on the called nanomaterials, constituting a new scientific domain that has emerged for the design, development and application of nanosized materials, achieving the fundamental understanding of the relationship between the properties or physical and chemical phenomena and dimensions of materials.[98,99,104]

Nanoscience and Nanotechnology involves several disciplines, in particular, chemistry. Then, Nanochemistry is understood as the utilization of synthetic chemistry to make nanoscale building blocks of different size and shape, composition and surface structure, charge and functionality.

These building blocks may be useful in their own right, or form structures that perform an intelligent function and portend a particular use.[98]

1.7.2. Nanostructured materials

Nanostructured materials (NSMs) are low-dimensional materials comprising building units of a submicron or nanoscale size at least in one direction and exhibiting size effects.[105,106] In particular, such materials present relevant advances in surface effects. When particle size decrease leads to an increase in surface particle respect to the same volume of material, therefore the overall surface area increases significantly.[104]

In the past two decades, hundreds of NSMs have been synthesized; therefore, their classification is a necessity. One of the most successful proposals for nanomaterials classifications divides them based on their dimension or in that of their components.[106] Thereby, four categories have been established: 0D, 1D, 2D, and 3D (Figure 1.10).

All nanoparticles can be built from elementary units (blocks) having lower dimensionality 0D (clusters and particles), 1D (nanotubes and nanowires), and 2D (nanoplates and layers). Considering this definition of nanomaterial, materials called 3D should not be included in the category of nanostructures the, because their dimensions will be higher than 100 nm. However, 3D structures may be considered as nanomaterials if they involve the 0D, 1D, and 2D nanoparticles in their structure.[106]

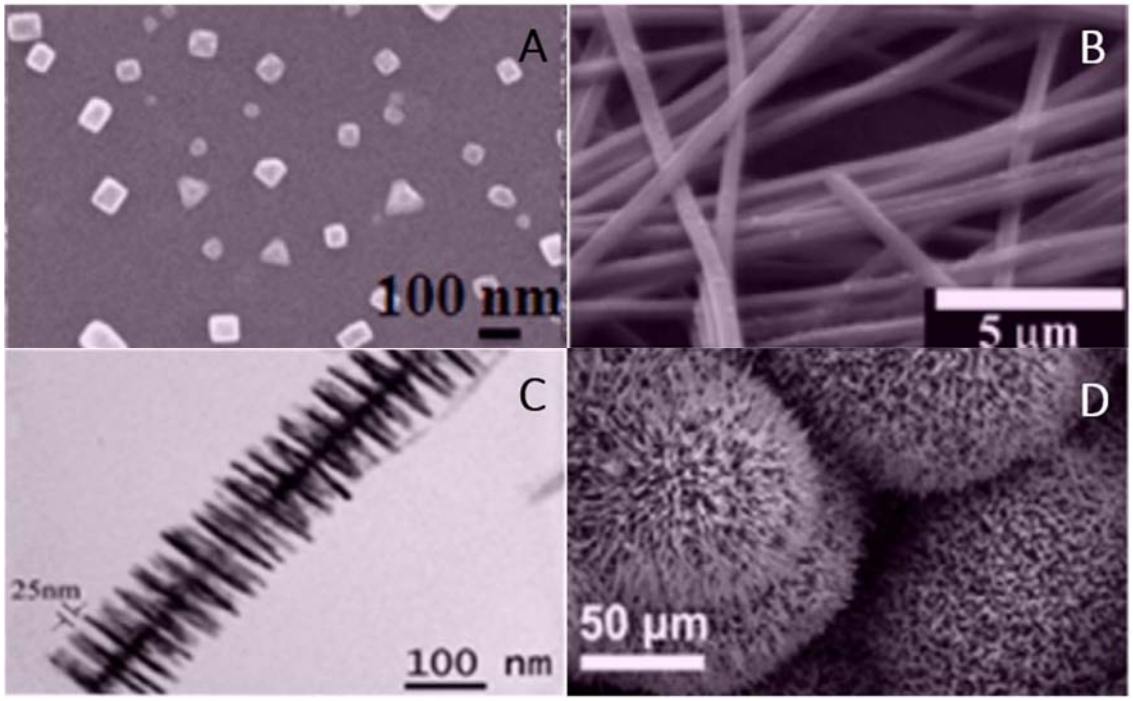

Figure 1.10. Representation of hierarchical materials; 0D-3D (Zero-dimensional (A), one-dimensional (B), two-dimensional (C) and three-dimensional (D) NSMs for advanced electrochemical energy devices). (0D: nanoparticles arrays, 1D: nanoribbons, 2D: branched structures, 3D: nanoflowers).[105]

1.7.3. Nanotechnology applied to wastewater treatment

The advances in nanotechnology may also be applied in wastewater treatments, offering large opportunities in the development of water supply systems. Nanotechnology offers an improvement of treatment efficiency as well as an increase in water supply through safe use of unconventional water sources.[100] The extraordinary properties of nanoscale materials, such as high surface area, photosensitivity, catalytic and antimicrobial activity, electrochemical, optical, and magnetic properties, and tunable pore size and surface chemistry, provide useful features for many applications.[107]

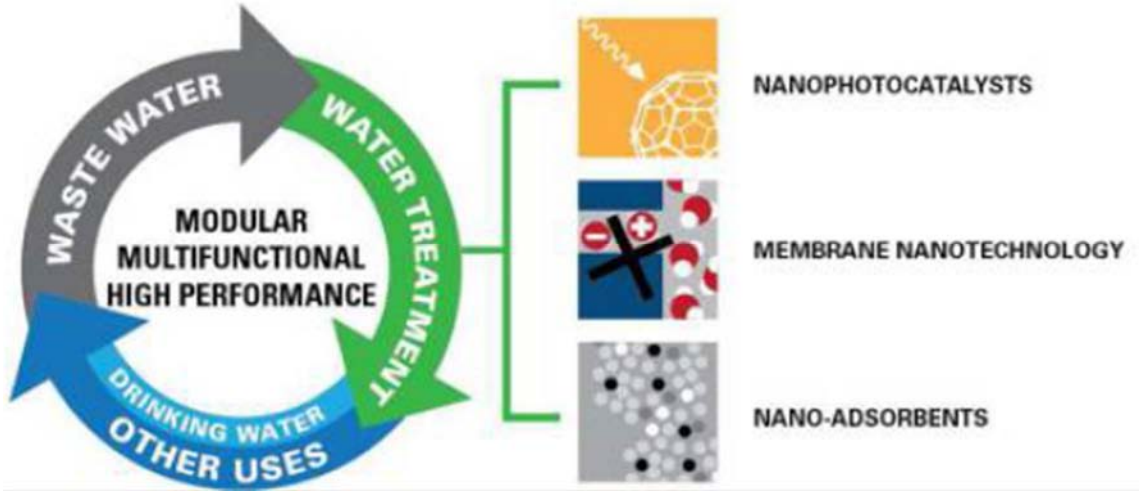

Figure 1.11. Nanotechnology applications for wastewater treatment.[107]

As mentioned above, adsorption is a widespread methodology used to remove pollutants from wastewaters. However, the efficiency of conventional materials are limited by the surface area or active sites, the lack of selectivity, and the adsorption kinetics.[100]

NSMs present significant improvements (Figure 1.11) confronted to conventional adsorbent materials with their extremely high specific surface area and associated sorption sites, short intraparticle diffusion distance, and adjustable pore size and surface chemistry.[100,107]

The high surface area that NSMs present is the mainly responsible of their high adsorption capacity. Furthermore, the high surface energy and size dependent surface structure at the nanoscale may create highly active adsorption sites, resulting in higher surface-area-normalized adsorption capacity. The surface of these materials can be functionalized to target specific contaminants achieving high selectivity.[107]

1.8. CASES OF STUDY

In this thesis, the research has been focused in the synthesis of NSMs and the study of their application for pollutants adsorption from aqueous media. In the first part, alumina-based material

has been used for fluoride removal, while the successive part is focused on the HM adsorption by functionalized magnetic nanoparticles.

1.8.1. Adsorbent materials for fluoride removal

The development of efficient adsorbent materials for fluoride removal from water is an aim of critical importance. Several adsorbent materials have been tasted for the purpose of an effective defluoridation, such as alumina (Al_2O_3)[82,108–111], biosorbents[83,112–114], clays[115,116] and composite materials.[117–120]

However, most of the fluoride adsorption methods are not able to reach the concentration requested by international regulations (1.5mg L^{-1}),[5] thus the optimization of materials for water defluoridation is still a challenge.

Among the wide range of materials used for fluoride adsorption, alumina is one of the most popular and widely used material. This adsorbent material, due to the high surface area and porosity, its stability in water without shrinking, swelling or softening,[121] and, for its low solubility in a wide range of pH,[122] is one of the most effective materials for fluoride adsorption from aqueous medium.

1.8.1.1. Mesoporous materials

According to the IUPAC classification,[123] the porous of the solids may be classified in three categories depending on the pore diameter: microporous (d < 2nm), mesoporous (2nm < d < 50nm) and macroporous (d > 50nm).

Mesoporous alumina-based materials have attracted especial attention due to their favourable physicochemical properties such as high surface area, large pore volume.[101,124]

Mesoporosity not only favours the dispersion but also increases the amount of accessible active site and enhances the diffusion of reactant and product molecules,[124] thus mesoporous alumina has been regarded as a promising adsorbent material for pollutants removal from wastewaters, including HM,[125,126] organic dyes,[127–129] inorganic anions,[130–132] or rare earth elements.[133]

1.8.1.2. Hierarchical materials

In the recent years, much interest has been devoted to hierarchical structured metal oxides. Such materials exhibit structure on more than one length scale,[98,134] where primary building blocks associate into more complex secondary structures that are integrated into the next size level in the hierarchy, as shown in Figure 1.12.[135]

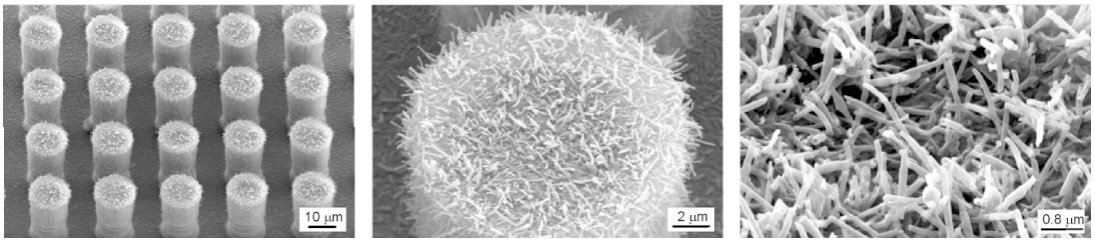

Figure 1.12. SEM micrographs of three different magnifications of a hierarchical material structure.

These hierarchical constructions may exhibit unique properties that are not found in the individual components and have been widely investigated in several fields from adsorption,[134,136]drug delivery[137] and catalysis[138] to sensors[139] and electronic conversion storage.[140]

Among the abundant hierarchical metal oxides developed for the applications abovementioned, alumina-based hierarchical structures have received a special attention because of its low cost, natural abundance and eco-friendly properties.[136]

1.8.2. Adsorbent materials for heavy metals removal from water

Nowadays, the high toxicity of HM and their accumulation in the organisms prompted the development and implementation of methodologies for the efficient removal of these undesirable metals from aqueous systems.

As mentioned above, adsorption is recognized as an effective and economic method to remove HM from effluents. Among the several adsorbent materials existing, nanosized metal oxides are classified as promising materials for HM removal from wastewaters,[141] being capable to bind with metal ions in solution. In particular, iron oxides have received special attention for their magnetic properties and low toxicity.[142,143] Nanosized ferric oxides may be used to the decontaminate water with negligible risks of secondary contamination, since elemental form of iron is environmentally friendly,[141,144]and easily removed by magnetic separation from aqueous media. In addition, iron is one of the widespread elements in the earth and easily accessible,[141] rendering the material a low-cost adsorbent which is a requisite for wastewaters treatment.

Several studies about the use of nanosized ferric oxides for HM removal from aqueous systems are reported in the literature. The widely studied forms are goethite (α-FeOOH), hematite (α-Fe_2O_3), amorphous hydrous Fe oxides, maghemite (ɣ-Fe_2O_3), magnetite (Fe_3O_4) and iron/iron oxide (Fe@Fe_xO_y).[141] At nanoscale, these iron oxides are potentially highly efficient for binding metal ions in comparison with the same oxides at macroscale.

The main iron oxides, which are of particular interest, include hematite (α-Fe_2O_3), amorphous hydrous iron oxides, maghemite (ɣ-Fe_2O_3) and magnetite (Fe_3O_4).

1.8.2.1. Special Features of Magnetic Nanoparticles

Magnetic materials have played an important role in the quotidian life since thousands of years. Nowadays, such materials are used in a variety of applications that range from microelectronic devices to motors and power distribution systems.[145] Magnetic materials are attractive adsorbents for water purification, as they combine adsorption process with magnetic separation.[146]

Materials can be classified into diamagnetic, paramagnetic, ferromagnetic, ferrimagnetic, and antiferromagnetic according to the arrangement of their magnetic dipoles in the absence and presence of an external magnetic field.[145] Figure 1.13 shows an schematic representation of the different types of magnetic dipoles, which are described in Table 1.5.

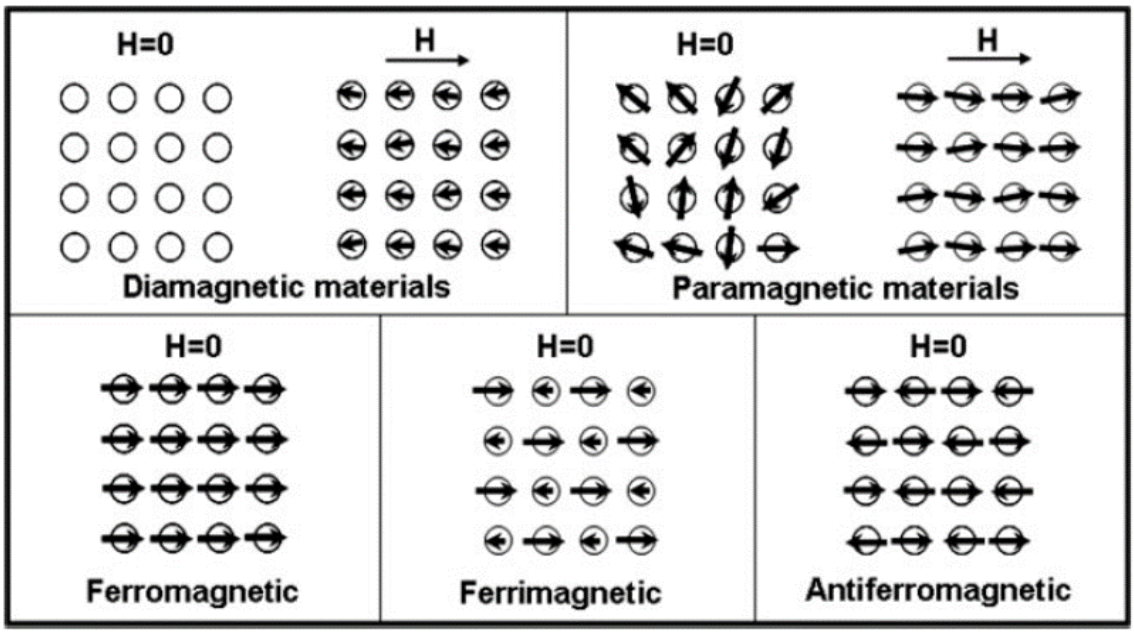

Figure 1.13. Schematic illustration of magnetic dipoles for five different types of materials in absence or presence of an external magnetic field (H).[145]

When the size of the magnetic particles is reduced to a few nanometers, they become superparamagnetic. Superparamagnetism is the phenomenon when thermal energy is enough to overcome the magnetic coupling forces, causing the atomic magnet moments to fluctuate randomly.[148] When an external magnetic field is applied, the particles acquire magnetization, but in the absence of that, the magnetization disappears being zero in average.[148]

Types of magnetism	Description
Diamagnetism	It is a property of such materials, which present weakly repulsive induced dipoles in the presence of an external magnetic field.[145,147]
Paramagnetism	The material has randomly oriented dipoles that can be (partial) aligned with an external field. Such substances present weakly attractive interaction toward a magnetic pole. Each atom, ion or molecule of a paramagnetic substance, can be visualized as a small magnet with its own inherent magnetic moment.[145,147]
Ferro-, Ferri- & Antimagnetism	For a **ferromagnetic** material, the magnetic dipoles always exist in the absence and presence of an external field and exhibit long-range order. Macroscopically, such a material displays a permanent magnetic moment. The difference in the source of the net magnetic moment can also be used to distinguish ferromagnetism from both ferrimagnetism and antiferromagnetism. In a **ferrimagnetic** material there are always weaker magnetic dipoles aligned antiparallel to the adjacent, stronger dipoles in the absence of an external magnetic field. For an **antiferromagnetic** material, the adjacent dipoles are antiparallel in the absence of an external field and cancel each other. In general, magnetic materials are refereed to those characterized by either ferro- or ferrimagnetic features.[145]

Table 1.5. Description of the different types of magnetism.

1.8.2.2. Super Paramagnetic Iron Oxide Nanoparticles (Fe_3O_4):

In the last decades, much effort has been devoted to the synthesis of magnetic nanoparticles. The most used methods include co-precipitation, thermal decomposition and/or reduction, micelle synthesis, hydrothermal synthesis and laser pyrolysis techniques. A few definition of the method, as well as the advantages and advantages of each methodology are described in the Table 1.6.

In this work, the chosen methodology for Fe_3O_4 nanoparticles synthesis was the co-precipitation method, due to its simplicity as well as the rapidity. The details of the synthesis are explained in the Methodology chapter.

The superparamagnetic nanoparticles are very attractive for a wide range of applications. However, the particles in this size present some problems, such as the intrinsic instability over long periods in which the nanosized particles tend to form agglomerates to reduce the energy associated with the high surface area respect the small volume. Furthermore, the naked particles are chemically high active, therefore are easily oxidized in air conditions resulting in the loss of magnetism and dispersibility.[143]

Co-precipitation[143]	
Addition of a base in a Fe^{3+}/Fe^{2+} salts solution under inert atmosphere at room temperature or at elevated temperature	
Advantages	*Disadvantages*
Facile and quick synthesis	Difficult to control of the particle size and thus achieve a narrow particle size distribution. In addition, presents problems of oxidation and aggregation.
Thermal decomposition[143,149]	
Thermal decomposition of organometallic precursors (iron acetylacetonate, iron cupferronates or carbonyls) in high boiling organic solvents containing stabilizing surfactants.	
Advantages	*Disadvantages*
High crystallinity, therefore high quality of magnetic nanoparticles.	Toxicity of the solvents, ligands and precursors and long reaction time.
Microemulsion[143,150]	
It is a thermodynamically stable dispersion of two relatively immiscible liquids stabilized by surfactant molecules. Iron precursors may precipitate as iron oxide in the water phase located in the centre of the micelles, the size of which depends on the molar ratio of water surfactant.	
Advantages	*Disadvantages*
Size and shape control. Easy to be scaled up to an industrial level	Particles less cristallyne and more polydispersed because of the slow nucleation rate. In addition, it requires large amounts of solvents.
Hydrothermal synthesis[143,150]	
Iron precursors in aqueous medium are heated at high temperature and autogenous pressure.	
Advantages	*Disadvantages*
Uniform size an easily to scaled up.	Long reaction time.

Table 1.6. Description of different SPION synthesis.

1.8.2.3. Functionalization of nanoparticles

It is very important to develop protection strategies to stabilize the magnetic nanoparticles against their degradation. To avoid that, the nanoparticles are coated with organic species or inorganic layers. Among all the existing routes for surface modification, such as ligand addition,[151] inorganic surface coating,[152,153] or ligand exchange[154], ligand addition and ligand exchange have been selected in this thesis for its simplicity and no need of a great quantity of reactants.

Moreover, the core-shell not only stabilizes the particles but, in many cases, is also used for functionalization of the adsorbent material for the desired application.[86,143] Therefore, if the surface

of magnetite is coated with an appropriate compound, the removal of hazardous compounds will be enhanced enabling the magnetic separation of the adsorbent from aqueous media.

According to Pearson's hard soft acid-base theory (HSAB),[155] soft bases such as –SH or –RSR– have excellent affinity towards several HM ions (considered soft acids), as a result of Lewis acid-base interactions. In this work, the adsorption capacity of iron oxide (Fe_3O_4) NP functionalized with –SH or –RSR– groups towards some HM including, Pb(II), Hg(II), Cd(II) and Cr(VI) has been investigated. Although Cr(VI) is considered as a hard acid and sulphur a soft base, the equilibrium constants for the formation of Cr(VI) thioesters is significantly high.[151] Hence, other sulphur containing groups could be effective ligands also for Cr(VI).

Moreover, based on the HSAB theory,[155] functional groups containing sulphur and nitrogen donor atoms are highly selective towards PM such as Ag and Pt. Therefore, magnetic NP functionalized with –SH or –RSR– prepared for HM adsorption may be also applied to recover Ag(I) and Pt(IV) in order to test an efficient separation and recovery of PM minimizing the production of secondary waste.

Several acid, silane, and diol head groups have been shown to have an interaction with the iron oxide surface. Among these, the carboxylate containing ligand seems to be the most useful anchor group, generating a wide range of magnetic sorbents containing a great variety of functional groups of interest.[156]

Attending this, 3-mercaptopropionic acid (3-MPA) and 3,3′-thiodipropionic acid (3,3-TDPA), represented in Figure 1.14, have been selected as promising ligands for surface coating of magnetite nanoparticles. Both ligands, contains a carboxyl group, which facilitates the coating with iron oxide due to the high affinity of the carboxyl group towards iron. Then, the –SH or –RSR– remain free to complex the toxic metal ions.

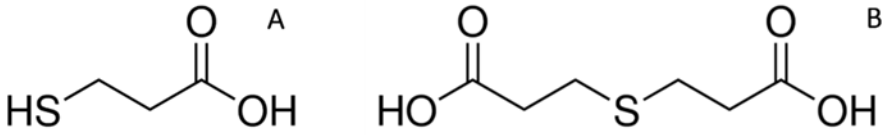

Figure 1.14. Selected ligands for SPION functionalization; 3-MPA (A) and 3,3-TDPA (B).

Following the Pearson's concept, several parameters have been developed with the aim to quantify accurately such model. In 1967, Misono[157] presented a new parameter scale called Misono softness parameter (Y) described in Eq. 1.2,[158] providing a quantitative measure of the tendency of a metal cation to be polarizable and enter into covalent bonding.

$$Y = 10\frac{I_z R}{\sqrt{Z} I_{z+1}} \qquad \text{Eq. 1.2}$$

where R is the ionic radius of a metal cation whose valence is Z and whose ionization potential is I_z.

Therefore, such parameter (Y) may be used to quantify the classification of hard-soft Lewis acids, allowing the prediction of how functional groups should bind metal ions.

1.9. OBJECTIVES

Considering the premises the aim of this thesis is to characterize the interactions between water pollutants with nanostructured systems to provide a basic knowledge of the adsorption processes by characterizing them in terms of loading capacity ant thermodynamic parameters.

- FLUORIDE REMOVAL BY HIERARCHICAL ALUMINA MICROSPHERES

In this concern, one of the main issues of this work is to study fluoride adsorption by high surface hierarchical alumina microspheres HAM and characterize the adsorption process in terms of loading capacity and thermodynamics. The principle points of this section are described below:

- Study and optimization of HAM synthesis by microwave treatment.
- Full characterization of the adsorbent material using a wide range of techniques explained in the methodology chapter.
- Perform potentiometric experiments to describe the kinetics of the F^- adsorption process and to determine the loading capacity of the synthesized materials.
- Determination of the adsorption enthalpy by using a unique, novel experimental approach, which combines potentiometry and ITC, with the aim to provide more accurate and robust thermodynamic parameters.

- METAL IONS REMOVAL WITH SUPERPARAMAGNETIC IRON OXIDE NANOPARTICLES FUNCTIONALIZED WITH SULPHUR CONTAINING LIGANDS

The next fundamental objective of this work is to characterize the adsorption process of HM (Pb(II), Cr(VI), Hg(II) and Cd(II)) and PM (Ag(I) and Pt(IV)) on functionalized magnetic nanoparticles using the novel ITC experimental approach. In addition, ITC can also distinguish the specificity of functionalities eventually added to the surface of nanoparticles towards the HM and PM adsorption.

- Study of the synthesis and functionalization of the coated superparamagnetic iron oxide nanoparticles (SPION).
- Full characterization of the synthesized material by several techniques that are full explained in the methodology chapter.
- Analysis of ITC data to gain information of specificity of functionalities eventually added to the surface of nanoparticles, towards metal ions adsorption.

- Develop adsorption experiments in batch conditions to determine the adsorption efficiency of the modified SPION towards the different metal ions selected.
- Determination of the adsorption enthalpy by using a combination of ITC and ICP-OES, providing accurate thermodynamic values.

1.10. REFERENCES

(1) *Fluorine and the Environment: Agrochemicals, Archeology, Green Chemistry & Water*; Tressaud, A., Ed.; Elsevier, 2006.

(2) WHO; UNICEF. *Progress on Sanitation and Drinking Water – 2015 Update and MDG Assessment*; 2015.

(3) Jadhav, S. V; Bringas, E.; Yadav, G. D.; Rathod, V. K.; Ortiz, I.; Marathe, K. V. Arsenic and Fluoride Contaminated Groundwaters: A Review of Current Technologies for Contaminants Removal. *J. Environ. Manage.* 2015, *162*, 306–325.

(4) Tu agua http://www.aigueshorta.es/ESP/16.asp (accessed Aug 28, 2016).

(5) Fawell, J.; Bailey, K.; Chilton, J.; Dahi, E.; Fewtrell, L.; Magara, Y. *Fluoride in Drinking-Water*; World Health Organization (WHO) and IWA Publishing: London, UK, 2006.

(6) *Fluorine and the Environment : Atmospheric Chemistry, Emissions, & Lithosphere*; Tressaud, A., Ed.; Elsevier, 2006.

(7) Hem, J. D. *Study and Interpretation the Chemical of Natural of Characteristics Water*; United States Geological Survey Water-Supply, 1985.

(8) Marzo (fluorita).jpg (1710×1500) http://www.igme.es/Museo/pieza_mes/2014/imag/marzo (fluorita).jpg (accessed Aug 4, 2016).

(9) Museo Virtual de Mineralogia Universidad de Huelva http://www.uhu.es/museovirtualdemineralogia/galerias/clase3/complejos.html (accessed Aug 4, 2016).

(10) Fluorapatite http://hyperphysics.phy-astr.gsu.edu/hbase/minerals/fluorapatite.html (accessed Aug 4, 2016).

(11) Liteplo, R.; Gomes, R.; Howe, P.; Malcolm, H. *Fluorides (WHO Report)*; Geneva, 2002.

(12) Bhatnagar, A.; Kumar, E.; Sillanpää, M. Fluoride Removal from Water by Adsorption-A Review. *Chem. Eng. J.* 2011, *171* (3), 811–840.

(13) Singh, J.; Singh, P.; Singh, A. Fluoride Ions vs Removal Technologies: A Study. *Arab. J. Chem.* 2014.

(14) Duffus, J. H. "Heavy Metals"— A Meaningless Term? (IUPAC Technical Report). *Pure Appl. Chem.* 2002, *74* (5), 793–807.

(15) *Handbook on the Toxicology of Metals*, Third Edit.; Nordberg, G. F., Fowler, B. A., Nordberg, M., Friberg, L. T., Eds.; Academic Press Inc., 2007.

(16) Foster, W. Inorganic Chemistry (Niels Bjerrum). *J. Chem. Educ.* 1936, *13* (7), 349.

(17) Hashim, M. A.; Mukhopadhyay, S.; Sahu, J. N.; Sengupta, B. Remediation Technologies for Heavy Metal Contaminated Groundwater. *J. Environ. Manage.* 2011, *92* (10), 2355–2388.

(18) Fu, F.; Wang, Q. Removal of Heavy Metal Ions from Wastewaters: A Review. *J. Environ. Manage.* 2011, *92* (3), 407–418.

(19) Lewis, R. J. *Hawley's Condensed Chemical Dictionary*, Fifteenth.; John Wiley & Sons, Inc.: Hoboken, NJ, USA, 2007.

(20) Patterson, J. W.; Passino, R. *Metals Speciation, Separation, and Recovery*; Lewis Publishers, Inc., 1987.

(21) *Environmental Inorganic Chemistry : Properties, Processes, and Estimation Methods*; Bodek, I., Lyman, W. J., Reehl, W. F., Rosenblatt, D. H., Eds.; Pergamon Press Inc., 1988.

(22) Chowdhury, S.; Mazumder, M. A. J.; Al-Attas, O.; Husain, T. Heavy Metals in Drinking Water: Occurrences, Implications, and Future Needs in Developing Countries. *Sci. Total Environ.* 2016, *569–570*, 476–488.

(23) EURL-HM - European Commission https://ec.europa.eu/jrc/en/eurl/heavy-metals (accessed Jul 20, 2016).

(24) Barakat, M. A. New Trends in Removing Heavy Metals from Industrial Wastewater. *Arab. J. Chem.* 2011, *4* (4), 361–377.

(25) Parajuli, D. Development of Some Novel Lignin Derivatives for Adsorptive Removal of Heavy Metals and Recovery of Precious Metals, Saga University, 2006.

(26) WHO. *Lead in Drinking-Water - Background Document for Development of WHO Guidelines for Drinking-Water Quality*, WHO/SDE/WS.; World Health Organization: Geneva, 2011.

(27) Rayner-Canham, G. *Química Inorgánica Descriptiva*, Second Edi.; Prentice Hall, 2013.

(28) WHO. *Exposure to Lead: A Major Public Health Concern*; Geneva, 2010.

(29) WHO. *Air Quality Guidelines for Europe*, Second Edi.; World Health Organization: Copenhagen, 2000.

(30) Sadeghi, S.; Rad, F. A.; Moghaddam, A. Z. A Highly Selective Sorbent for Removal of Cr(VI) from Aqueous Solutions Based on Fe3O4/poly(methyl Methacrylate) Grafted Tragacanth Gum Nanocomposite: Optimization by Experimental Design. *Mater. Sci. Eng. C* 2014, *45*, 136–145.

(31) WHO. *Chromium in Drinking-Water - Background Document for Development of WHO Guidelines for Drinking-Water Quality*, WHO/SDE/WS.; World Health Organization, 2003.

(32) WHO. *Guidelines for Drinking-Water Quality*, Fourth Edi.; World Health Organization: Geneva, 2011.

(33) Fisher, J. F.; WHO; International Programme on Chemical Safety. Elemental Mercury and Inorganic Mercury Compounds: Human Health Aspects. *Concise International Chemical Assessment Document; 50*. World Health Organization: Geneva 2003.

(34) Zhang, S.; Zhang, Y.; Liu, J.; Xu, Q.; Xiao, H.; Wang, X.; Xu, H.; Zhou, J. Thiol Modified Fe3O4@SiO2 as a Robust, High Effective, and Recycling Magnetic Sorbent for Mercury Removal. *Chem. Eng. J.* 2013, *226*, 30–38.

(35) Poulin, J.; Gibb, H. *Mercury: Assessing the Environmental Burden of Disease at National and Local Levels*, Mercury: A.; Prüss-Üstün, A., Ed.; World Health Organization: Geneva, 2008.

(36) Butterman, W. C.; Plachy, J. *Mineral Commodity Profiles: Cadmium*; USGS science for a changing world, 2004.

(37) *Cadmium Review*; Nordic Council of Ministers, 2003; Vol. 1.

(38) WHO. *Exposure to Cadmium: A Major Public Health Concern*; Geneva, 2010.

(39) Tahmasebi, E.; Yamini, Y. Polythiophene-Coated Fe3O4 Nanoparticles as a Selective Adsorbent for Magnetic Solid-Phase Extraction of silver(I), gold(III), copper(II) and palladium(II). *Microchim. Acta* 2014, *181* (5–6), 543–551.

(40) Widmer, R.; Oswald-Krapf, H.; Sinha-Khetriwal, D.; Schnellmann, M.; Böni, H. Global Perspectives on E-Waste. *Environ. Impact Assess. Rev.* 2005, *25*, 436–458.

(41) Lin, T. L.; Lien, H. L. Effective and Selective Recovery of Precious Metals by Thiourea Modified Magnetic Nanoparticles. *Int. J. Mol. Sci.* 2013, *14* (5), 9834–9847.

(42) Lu, Y.; Xu, Z. Precious Metals Recovery from Waste Printed Circuit Boards: A Review for Current Status and Perspective. *Resour. Conserv. Recycl.* 2016, *113* (2016), 28–39.

(43) Peng, X.; Zhang, W.; Gai, L.; Jiang, H.; Wang, Y.; Zhao, L. Dedoped Fe_3O_4/PPy Nanocomposite with High Anti-Interfering Ability for Effective Separation of Ag(I) from Mixed Metal-Ion Solution. *Chem. Eng. J.* 2015, *280*, 197–205.

(44) Cotton, S. A. *Chemistry of Precious Metals*, First Edit.; Blackie Academic and Professional: London, 1997.

(45) Cheremisinoff, N. P. *Handbook of Water and Wastewater Treatment Technologies*; Butterworth-Heinemann, 2002.

(46) Matlock, M. M.; Howerton, B. S.; Atwood, D. A. Irreversible Precipitation of Mercury and Lead. *J. Hazard. Mater.* 2001, *84* (1), 73–82.

(47) Matlock, M. M.; Howerton, B. S.; Atwood, D. A. Chemical Precipitation of Heavy Metals from Acid Mine Drainage. *Water Res.* 2002, *36* (19), 4757–4764.

(48) Hu, C. Y.; Lo, S. L.; Kuan, W. H.; Lee, Y. D. Removal of Fluoride from Semiconductor Wastewater by Electrocoagulation- Flotation. *Water Res.* 2005, *39* (5), 895–901.

(49) Turner, B. D.; Binning, P.; Stipp, S. L. S. Fluoride Removal by Calcite: Evidence for Fluorite Precipitation and Surface Adsorption. *Environ. Sci. Technol.* 2005, *39* (24), 9561–9568.

(50) Huisman, J. L.; Schouten, G.; Schultz, C. Biologically Produced Sulphide for Purification of Process Streams, Effluent Treatment and Recovery of Metals in the Metal and Mining Industry. *Hydrometallurgy* 2006, *83* (1–4), 106–113.

(51) Blue, L. Y.; Van Aelstyn, M. A.; Matlock, M.; Atwood, D. A. Low-Level Mercury Removal from Groundwater Using a Synthetic Chelating Ligand. *Water Res.* 2008, *42* (8–9), 2025–2028.

(52) Blue, L. Y.; Jana, P.; Atwood, D. A. Aqueous Mercury Precipitation with the Synthetic Dithiolate, BDTH2. *Fuel* 2010, *89* (6), 1326–1330.

(53) Li, F. H.; Li, Y. N.; Zhang, C. C.; Fan, Z. G. Recovery of Valuable Elements from Spent YBa2Cu 3O7-x/Ag Composite Superconductor Bulks. *Trans. Nonferrous Met. Soc. China (English Ed.* 2010, *20* (SUPPL.1), s192–s197.

(54) Drouiche, N.; Aoudj, S.; Lounici, H.; Drouiche, M.; Ouslimane, T.; Ghaffour, N. Fluoride Removal from Pretreated Photovoltaic Wastewater by Electrocoagulation: An Investigation of the Effect of Operational Parameters. *Procedia Eng.* 2012, *33* (2009), 385–391.

(55) Mulwanda, J.; Dorfling, C. Recovery of Dissolved Platinum Group Metals from Copper Sulphate Leach Solutions by Precipitation. *Miner. Eng.* 2015, *80*, 50–56.

(56) Korngold, E.; Belfer, S.; Urtizberea, C. Removal of Heavy Metals from Tap Water by a Cation Exchanger. *Desalination* 1996, *104* (3), 197–201.

(57) Feng, D.; Aldrich, C.; Tan, H. Treatment of Acid Mine Water by Use of Heavy Metal Precipitation and Ion Exchange. *Miner. Eng.* 2000, *13* (6), 623–642.

(58) Ruixia, L.; Jinlong, G.; Hongxiao, T. Adsorption of Flouride, Phosphate, and Arsenate Ions on a New Type of Ion Exchange Fiber. *J. Colloid Interface Sci.* 2002, *248*, 268–274.

(59) Zhao, X.; Höll, W. H.; Yun, G. Elimination of Cadmium Trace Contaminations from Drinking Water. *Water Res.* 2002, *36* (4), 851–858.

(60) Oehmen, A.; Viegas, R.; Velizarov, S.; Reis, M. A. M.; Crespo, J. G. Removal of Heavy Metals from Drinking Water Supplies through the Ion Exchange Membrane Bioreactor. *Desalination* 2006, *199* (1–3), 405–407.

(61) Meenakshi, S.; Viswanathan, N. Identification of Selective Ion-Exchange Resin for Fluoride Sorption. *J. Colloid Interface Sci.* 2007, *308* (2), 438–450.

(62) Viswanathan, N.; Meenakshi, S. Role of Metal Ion Incorporation in Ion Exchange Resin on the Selectivity of Fluoride. *J. Hazard. Mater.* 2009, *162* (2–3), 920–930.

(63) Virolainen, S.; Tyster, M.; Haapalainen, M.; Sainio, T. Ion Exchange Recovery of Silver from Concentrated Base Metal-Chloride Solutions. *Hydrometallurgy* 2014, *152*, 100–106.

(64) Nikoloski, A. N.; Ang, K. L.; Li, D. Recovery of Platinum, Palladium and Rhodium from Acidic Chloride Leach Solution Using Ion Exchange Resins. *Hydrometallurgy* 2015, *152*, 20–32.

(65) Zewail, T. M.; Yousef, N. S. Kinetic Study of Heavy Metal Ions Removal by Ion Exchange in Batch Conical Air Spouted Bed. *Alexandria Eng. J.* 2015, *54*, 83–90.

(66) Ayoob, S.; Gupta, A. K.; Bhat, V. T. *A Conceptual Overview on Sustainable Technologies for the Defluoridation of Drinking Water*; 2008; Vol. 38.

(67) Bhandare, A. A.; Argekar, A. P. Separation and Recovery of Platinum and Rhodium by Supported Liquid Membranes Using bis(2-Ethylhexyl)phosphoric Acid (HDEHP) as a Mobile Carrier. *J. Memb. Sci.* 2002, *201*, 233–237.

(68) Qdais, H. A.; Moussa, H. Removal of Heavy Metals from Wastewater by Membrane Processes: A Comparative Study. *Desalination* 2004, *164* (2), 105–110.

(69) Hu, K.; Dickson, J. M. Nanofiltration Membrane Performance on Fluoride Removal from Water. *J. Memb. Sci.* 2006, *279* (1–2), 529–538.

(70) Tahaikt, M.; El Habbani, R.; Ait Haddou, A.; Achary, I.; Amor, Z.; Taky, M.; Alami, A.; Boughriba, A.; Hafsi, M.; Elmidaoui, A. Fluoride Removal from Groundwater by Nanofiltration. *Desalination* 2007, *212*, 46–53.

(71) Kabay, N.; Arar, Ö.; Samatya, S.; Yüksel, Ü.; Yüksel, M. Separation of Fluoride from Aqueous Solution by Electrodialysis: Effect of Process Parameters and Other Ionic Species. *J. Hazard. Mater.* 2008, *153* (1–2), 107–113.

(72) Sehn, P. Fluoride Removal with Extra Low Energy Reverse Osmosis Membranes: Three Years

of Large Scale Field Experience in Finland. *Desalination* 2008, *223*, 73–84.

(73) Algarra, M.; Vázquez, M. I.; Alonso, B.; Casado, C. M.; Casado, J.; Benavente, J. Characterization of an Engineered Cellulose Based Membrane by Thiol Dendrimer for Heavy Metals Removal. *Chem. Eng. J.* 2014, *253*, 472–477.

(74) Cui, Y.; Ge, Q.; Liu, X. Y.; Chung, T. S. Novel Forward Osmosis Process to Effectively Remove Heavy Metal Ions. *J. Memb. Sci.* 2014, *467*, 188–194.

(75) Mehdipour, S.; Vatanpour, V.; Kariminia, H. R. Influence of Ion Interaction on Lead Removal by a Polyamide Nanofiltration Membrane. *Desalination* 2015, *362*, 84–92.

(76) Stajčić, A.; Nastasović, A.; Stajić-Trošić, J.; Marković, J.; Onjia, A.; Radovanović, F. Novel Membrane-Supported Hydrogel for Removal of Heavy Metals. *J. Environ. Chem. Eng.* 2015, *3*, 453–461.

(77) Zhu, W. P.; Gao, J.; Sun, S. P.; Zhang, S.; Chung, T. S. Poly(amidoamine) Dendrimer (PAMAM) Grafted on Thin Film Composite (TFC) Nanofiltration (NF) Hollow Fiber Membranes for Heavy Metal Removal. *J. Memb. Sci.* 2015, *487*, 117–126.

(78) Aftab, B.; Khan, S. J.; Maqbool, T.; Hankins, N. P. Heavy Metals Removal by Osmotic Membrane Bioreactor (OMBR) and Their Effect on Sludge Properties. *Desalination* 2017, *403*, 117–127.

(79) Iben Nasser, I.; Ibn El Haj Amor, F.; Donato, L.; Algieri, C.; Garofalo, A.; Drioli, E.; Ahmed, C. Removal and Recovery of Ag(CN)2- from Synthetic Electroplating Baths by Polymer Inclusion Membrane Containing Aliquat 336 as a Carrier. *Chem. Eng. J.* 2016, *295*, 207–217.

(80) Cobelo-Garcia, A.; Turner, A.; Millward, G. E.; Couceiro, F. Behaviour of palladium(II), platinum(IV), and rhodium(III) in Artificial and Natural Waters: Influence of Reactor Surface and Geochemistry on Metal Recovery. *Anal. Chim. Acta* 2007, *585* (2), 202–210.

(81) Li, W.; Cao, C. Y.; Wu, L. Y.; Ge, M. F.; Song, W. G. Superb Fluoride and Arsenic Removal Performance of Highly Ordered Mesoporous Aluminas. *J. Hazard. Mater.* 2011, *198*, 143–150.

(82) Gong, W. X.; Qu, J. H.; Liu, R. P.; Lan, H. C. Adsorption of Fluoride onto Different Types of Aluminas. *Chem. Eng. J.* 2012, *189–190*, 126–133.

(83) Tomar, V.; Prasad, S.; Kumar, D. Adsorptive Removal of Fluoride from Aqueous Media Using Citrus Limonum (Lemon) Leaf. *Microchem. J.* 2014, *112*, 97–103.

(84) Arce, V. B.; Gargarello, R. M.; Ortega, F.; Romañano, V.; Mizrahi, M.; Ramallo-López, J. M.; Cobos, C. J.; Airoldi, C.; Bernardelli, C.; Donati, E. R.; et al. EXAFS and DFT Study of the Cadmium and Lead Adsorption on Modified Silica Nanoparticles. *Spectrochim. Acta - Part A Mol. Biomol. Spectrosc.* 2015, *151*, 153–163.

(85) Cai, H.; Chen, G.; Peng, C.; Xu, L.; Zhu, X.; Zhang, Z.; Dong, Y.; Shang, G.; Ke, F.; Gao, H.; et al. Enhanced Removal of Fluoride by Tea Waste Supported Hydrous Aluminium Oxide Nanoparticles: Anionic Polyacrylamide Mediated Aluminium Assembly and Adsorption Mechanism. *RSC Adv.* 2015, *5*, 29266–29275.

(86) Madrakian, T.; Afkhami, A.; Zadpour, B.; Ahmadi, M. New Synthetic Mercaptoethylamino Homopolymer-Modified Maghemite Nanoparticles for Effective Removal of Some Heavy Metal Ions from Aqueous Solution. *J. Ind. Eng. Chem.* 2015, *21*, 1160–1166.

(87) Yari, M.; Rajabi, M.; Moradi, O.; Yari, A.; Asif, M.; Agarwal, S.; Gupta, V. K. Kinetics of the Adsorption of Pb(II) Ions from Aqueous Solutions by Graphene Oxide and Thiol Functionalized Graphene Oxide. *J. Mol. Liq.* 2015, *209*, 50–57.

(88) Zhang, H.; Huang, F.; Liu, D.-L.; Shi, P. Highly Efficient Removal of Cr(VI) from Wastewater via Adsorption with Novel Magnetic Fe3O4@C@MgAl-Layered Double-Hydroxide. *Chinese Chem. Lett.* 2015, *26* (9), 1137–1143.

(89) Elwakeel, K. Z.; El-Sayed, G. O.; Darweesh, R. S. Fast and Selective Removal of silver(I) from Aqueous Media by Modified Chitosan Resins. *Int. J. Miner. Process.* 2013, *120*, 26–34.

(90) López-Muñoz, M. J.; Arencibia, A.; Cerro, L.; Pascual, R.; Melgar, Á. Adsorption of Hg(II) from Aqueous Solutions Using TiO2 and Titanate Nanotube Adsorbents. *Appl. Surf. Sci.* 2016, *367*, 91–100.

(91) *Emerging Compounds Removal from Wastewater*; Lofrano, G., Ed.; SpringerBriefs in Molecular Science; Springer Netherlands: Dordrecht, 2012.

(92) Kammerer, J.; Carle, R.; Kammerer, D. R. Adsorption and Ion Exchange: Basic Principles and Their Application in Food Processing. *J. Agric. Food Chem.* 2011, *59* (1), 22–42.

(93) Worch, E. *Adsorption Technology in Water Treatment - Fundamentals, Processes, and Modeling*; De Gruyter: Berlin/Boston, 2012.

(94) *Handbook of Research on Diverse Applications of Nanotechnology in Biomedicine, Chemistry, and Engineering*; Soni, S., Salhotra, A., Suar, M., Eds.; IGI Global: Hershey, PA, 2015.

(95) Mohapatra, M.; Anand, S.; Mishra, B. K.; Giles, D. E.; Singh, P. Review of Fluoride Removal from Drinking Water. *J. Environ. Manage.* 2009, *91* (1), 67–77.

(96) Oller, I.; Malato, S.; Sánchez-Pérez, J. A. Combination of Advanced Oxidation Processes and Biological Treatments for Wastewater Decontamination-A Review. *Sci. Total Environ.* 2011, *409* (20), 4141–4166.

(97) Zhang, L.; Fang, M. Nanomaterials in Pollution Trace Detection and Environmental Improvement. *Nano Today* 2010, *5* (2), 128–142.

(98) Ozin, G. A.; Arsenault, A. C. Nanochemistry: A Chemical Approach to Nanomaterials. *Small* 2006, *2* (5), 678–679.

(99) Guozhong, C. *Nanostructures & Nanomaterials*; Imperial College Press, 2004.

(100) Qu, X.; Alvarez, P. J. J.; Li, Q. Applications of Nanotechnology in Water and Wastewater Treatment. *Water Res.* 2013, *47* (12), 3931–3946.

(101) Cao, G.; Wang, Y. *Nanostructures and Nanomaterials*, Second Edi.; World Scientific, 2011.

(102) Liz-Marzán, L. M. Nanometals: Formation and Color. *Mater. Today* 2004, 26–31.

(103) British Museum - Image gallery: The Lycurgus Cup http://www.britishmuseum.org/research/collection_online/collection_object_details/collection_image_gallery.aspx?assetId=36154001&objectId=61219&partId=1#more-views (accessed Aug 5, 2016).

(104) Roduner, E. Size Matters: Why Nanomaterials Are Different. *Chem. Soc. Rev.* 2006, *35*, 583–

592.

(105) Tiwari, J. N.; Tiwari, R. N.; Kim, K. S. Zero-Dimensional, One-Dimensional, Two-Dimensional and Three-Dimensional Nanostructured Materials for Advanced Electrochemical Energy Devices. *Prog. Mater. Sci.* 2012, *57* (4), 724–803.

(106) Pokropivny, V. V.; Skorokhod, V. V. New Dimensionality Classifications of Nanostructures. *Phys. E Low-Dimensional Syst. Nanostructures* 2008, *40* (7), 2521–2525.

(107) Qu, X.; Brame, J.; Li, Q.; Alvarez, P. J. J. Nanotechnology for a Safe and Sustainable Water Supply: Enabling Integrated Water Treatment and Reuse. *Acc. Chem. Res.* 2012, *46* (3), 834–843.

(108) Ayoob, S.; Gupta, A. K. Performance Evaluation of Alumina Cement Granules in Removing Fluoride from Natural and Synthetic Waters. *Chem. Eng. J.* 2009, *150* (2–3), 485–491.

(109) Dayananda, D.; Sarva, V. R.; Prasad, S. V.; Arunachalam, J.; Ghosh, N. N. A Simple Aqueous Solution Based Chemical Methodology for Preparation of Mesoporous Alumina: Efficient Adsorbent for Defluoridation of Water. *Part. Sci. Technol.* 2015, *33* (1), 8–16.

(110) Yang, C.; Gao, L.; Wang, Y.; Tian, X.; Komarneni, S. Fluoride Removal by Ordered and Disordered Mesoporous Aluminas. *Microporous Mesoporous Mater.* 2014, *197*, 156–163.

(111) Kumar, E.; Bhatnagar, A.; Kumar, U.; Sillanpää, M. Defluoridation from Aqueous Solutions by Nano-Alumina: Characterization and Sorption Studies. *J. Hazard. Mater.* 2011, *186* (2–3), 1042–1049.

(112) Cai, H.; Xu, L.; Chen, G.; Peng, C.; Ke, F.; Liu, Z.; Li, D.; Zhang, Z.; Wan, X. Removal of Fluoride from Drinking Water Using Modified Ultrafine Tea Powder Processed Using a Ball-Mill. *Appl. Surf. Sci.* 2016, *375*, 74–84.

(113) Quintáns-Fondo, A.; Ferreira-Coelho, G.; Paradelo-Núñez, R.; Nóvoa-Muñoz, J. C.; Arias-Estévez, M.; Fernández-Sanjurjo, M. J.; Álvarez-Rodríguez, E.; Núñez-Delgado, A. Promoting Sustainability in the Mussel Industry: Mussel Shell Recycling to Fight Fluoride Pollution. *J. Clean. Prod.* 2016, *131*, 485–490.

(114) Amin, F.; Talpur, F. N.; Balouch, A.; Surhio, M. A.; Bhutto, M. A. Biosorption of Fluoride from Aqueous Solution by White-Rot Fungus Pleurotus Eryngii ATCC 90888. *Environ. Nanotechnology, Monit. Manag.* 2014, *3*, 30–37.

(115) Hamdi, N.; Srasra, E. Removal of Fluoride from Acidic Wastewater by Clay Mineral: Effect of Solid-Liquid Ratios. *Desalination* 2007, *206* (1–3), 238–244.

(116) Vinati, A.; Mahanty, B.; Behera, S. K. Clay and Clay Minerals for Fluoride Removal from Water: A State-of-the-Art Review. *Appl. Clay Sci.* 2015, *114*, 340–348.

(117) Wen, S.; Wang, Y.; Dong, S. Performance and Characteristics of Fluoride Adsorption Using Nanomagnetite graphite–La Adsorbent. *RSC Adv.* 2015, *5* (109), 89594–89602.

(118) Yu, X.; Tong, S.; Ge, M.; Zuo, J. Removal of Fluoride from Drinking Water by Cellulose@hydroxyapatite Nanocomposites. *Carbohydr. Polym.* 2013, *92* (1), 269–275.

(119) Liu, Y.; Fan, Q.; Wang, S.; Liu, Y.; Zhou, A.; Fan, L. Adsorptive Removal of Fluoride from Aqueous Solutions Using Al-Humic Acid-La Aerogel Composites. *Chem. Eng. J.* 2016, *306*, 174–185.

(120) Koilraj, P.; Kannan, S. Aqueous Fluoride Removal Using ZnCr Layered Double Hydroxides and Their Polymeric Composites: Batch and Column Studies. *Chem. Eng. J.* 2013, *234*, 406–415.

(121) Serbezov, A.; Moore, J. D.; Wu, Y. Adsorption Equilibrium of Water Vapor on Selexsorb-CDX Commercial Activated Alumina Adsorbent. *J. Chem. Eng. Data* 2011, *56* (5), 1762–1769.

(122) Kim, Y.; Kim, C.; Rengaraj, S.; Yi, J. Arsenic Removal Using Mesoporous Alumina Prepared via a Templating Method. *Environ. Sci. Technol.* 2004, *38* (3), 924–931.

(123) Sing, K. S. W.; Everett, D. H.; Haul, R. A. W.; Moscou, L.; Pierotti, R. A.; Rouquerol, J.; Siemieniewska, T. Reporting Physisorption Data for gas/Solid Systems with Special Reference to the Determination of Surface Area and Porosity. *Pure Appl. Chem.* 1985, *57* (4), 603–619.

(124) Badoga, S.; Sharma, R.; Dalai, A. K.; Adjaye, J. Synthesis and Characterization of Mesoporous Aluminas with Different Pore Sizes: Application in NiMo Supported Catalyst for Hydrotreating of Heavy Gas Oil. *Appl. Catal. A Gen.* 2015, *489*, 86–97.

(125) Cai, W.; Tan, L.; Yu, J.; Jaroniec, M.; Liu, X.; Cheng, B.; Verpoort, F. Synthesis of Amino-Functionalized Mesoporous Alumina with Enhanced Affinity towards Cr(VI) and CO2. *Chem. Eng. J.* 2014, *239*, 207–215.

(126) Han, C.; Pu, H.; Li, H.; Deng, L.; Huang, S.; He, S.; Luo, Y. The Optimization of As(V) Removal over Mesoporous Alumina by Using Response Surface Methodology and Adsorption Mechanism. *J. Hazard. Mater.* 2013, *254–255* (1), 301–309.

(127) Wang, Y.; Li, W.; Jiao, X. L.; Chen, D. R. Electrospinning Preparation and Adsorption Properties of Mesoporous Alumina Fibers. *J. Mater. Chem. A* 2013, *1* (36), 10720–10726.

(128) Shen, J.; Li, Z.; Wu, Y. nan; Zhang, B.; Li, F. Dendrimer-Based Preparation of Mesoporous Alumina Nanofibers by Electrospinning and Their Application in Dye Adsorption. *Chem. Eng. J.* 2015, *264*, 48–55.

(129) Yahyaei, B.; Azizian, S. Rapid Adsorption of Binary Dye Pollutants onto the Nanostructred Mesoporous Alumina. *J. Mol. Liq.* 2014, *199*, 88–95.

(130) Yu, M. J.; Li, X.; Ahn, W. S. Adsorptive Removal of Arsenate and Orthophosphate Anions by Mesoporous Alumina. *Microporous Mesoporous Mater.* 2008, *113* (1–3), 197–203.

(131) Lee, G.; Chen, C.; Yang, S. T.; Ahn, W. S. Enhanced Adsorptive Removal of Fluoride Using Mesoporous Alumina. *Microporous Mesoporous Mater.* 2010, *127* (1–2), 152–156.

(132) Jagtap, S.; Yenkie, M. K. N.; Labhsetwar, N.; Rayalu, S. Defluoridation of Drinking Water Using Chitosan Based Mesoporous Alumina. *Micropor. Mesopor. Mat.* 2011, *142* (2–3), 454–463.

(133) Sun, Y.; Chen, C.; Tan, X.; Shao, D.; Li, J.; Zhao, G.; Yang, S.; Wang, Q.; Wang, X. Enhanced Adsorption of Eu(III) on Mesoporous Al2O3/expanded Graphite Composites Investigated by Macroscopic and Microscopic Techniques. *Dalton Trans.* 2012, *41* (43), 13388–13394.

(134) Cai, W.; Yu, J.; Gu, S.; Jaroniec, M. Facile Hydrothermal Synthesis of Hierarchical Boehmite: Sulfate-Mediated Transformation from Nanoflakes to Hollow Microspheres. *Cryst. Growth Des.* 2010, *10* (9), 3977–3982.

(135) Bhushan, B. Biomimetics Inspired Surfaces for Drag Reduction and Oleophobicity/philicity. *Beilstein J. Nanotechnol.* 2011, *2*, 66–84.

(136) Kang, D.; Tong, S.; Yu, X.; Ge, M. Template-Free Synthesis of 3D Hierarchical Amorphous Aluminum Oxide Microspheres with Broccoli-like Structure and Their Application in Fluoride Removal. *RSC Adv.* 2015, *5*, 19159–19165.

(137) Wei, W.; Hu, G.; Yu, D.; Mcleish, T.; Su, Z.; Shen, Z. Preparation of Hierarchical Hollow CaCO 3 Particles and the Application as. *J. Am. Chem. Soc.* 2008, *130*, 15808–15810.

(138) Guo, H.; He, Y.; Wang, Y.; Liu, L.; Yang, X.; Wang, S.; Huang, Z.; Wei, Q. Morphology-Controlled Synthesis of Cage-Bell Pd@CeO2 Structured Nanoparticle Aggregates as Catalysts for the Low-Temperature Oxidation of CO. *J. Mater. Chem. A* 2013, *1* (25), 7494–7499.

(139) Peng, C.; Guo, J.; Yang, W.; Shi, C.; Liu, M.; Zheng, Y.; Xu, J.; Chen, P.; Huang, T.; Yang, Y. Synthesis of Three-Dimensional Flower-like Hierarchical ZnO Nanostructure and Its Enhanced Acetone Gas Sensing Properties. *J. Alloys Compd.* 2016, *654*, 371–378.

(140) Yu, P.; Zhang, X.; Wang, D.; Wang, L.; Ma, Y. Shape-Controlled Synthesis of 3D Hierarchical MnO2 Nanostructures for Electrochemical Supercapacitors. *Cryst. Growth Des.* 2009, *2008* (DI), 528–533.

(141) Hua, M.; Zhang, S.; Pan, B.; Zhang, W.; Lv, L.; Zhang, Q. Heavy Metal Removal from Water / Wastewater by Nanosized Metal Oxides : A Review. 2012, *212*, 317–331.

(142) Rossi, L. M.; Quach, A. D.; Rosenzweig, Z. Glucose Oxidase – Magnetite Nanoparticle Bioconjugate for Glucose Sensing. *Anal. Bioanal. Chem.* 2004, *380*, 606–613.

(143) Lu, A. H.; Salabas, E. L.; Schüth, F. Magnetic Nanoparticles: Synthesis, Protection, Functionalization, and Application. *Angew. Chemie - Int. Ed.* 2007, *46* (8), 1222–1244.

(144) Kharisov, B. I.; Dias, H. V. R.; Kharissova, O. V; Jime, M.; Kharisov, B. I. Iron-Containing Nanomaterials : Synthesis, Properties, and Environmental Applications. *RSC Adv.* 2012, *2*, 9325–9358.

(145) Jeong, U.; Teng, X.; Wang, Y.; Yang, H.; Xia, Y. Superparamagnetic Colloids: Controlled Synthesis and Niche Applications. *Adv. Mater.* 2007, *19* (1), 33–60.

(146) Ambashta, R. D.; Sillanpää, M. Water Purification Using Magnetic Assistance: A Review. *J. Hazard. Mater.* 2010, *180* (1–3), 38–49.

(147) Cornell, R. M.; Scwertmann, U. *The Iron Oxides: Struture, Properties, Reactions, Occurences and Uses.*, Second Edi.; Wiley-VCH Verlag GmbH & Co. KGaA,: Weinheim, 2003.

(148) Uheida, A.; Salazar-Alvarez, G.; Björkman, E.; Yu, Z.; Muhammed, M. Fe3O4 and γ-Fe2O3-Fe2O3 Nanoparticles for the Adsorption of Co2+ from Aqueous Solution. *J. Colloid Interface Sci.* 2006, *298* (2), 501–507.

(149) Lin, X.-M.; Samia, A. C. S. Synthesis, Assembly and Physical Properties of Magnetic Nanoparticles. *J. Magn. Magn. Mater.* 2006, *305* (1), 100–109.

(150) Mahmoudi, M.; Sant, S.; Wang, B.; Laurent, S.; Sen, T. Superparamagnetic Iron Oxide Nanoparticles (SPIONs): Development, Surface Modification and Applications in Chemotherapy. *Advanced Drug Delivery Reviews*. Elsevier B.V. 2011, pp 24–46.

(151) Burks, T.; Avila, M.; Akhtar, F.; Göthelid, M.; Lansåker, P. C.; Toprak, M. S.; Muhammed, M.; Uheida, A. Studies on the Adsorption of chromium(VI) onto 3-Mercaptopropionic Acid

Coated Superparamagnetic Iron Oxide Nanoparticles. *J. Colloid Interface Sci.* 2014, *425*, 36–43.

(152) Dupont, D.; Luyten, J.; Bloemen, M.; Verbiest, T.; Binnemans, K. Acid-Stable Magnetic Core – Shell Nanoparticles for the Separation of Rare Earths. *Ind. Eng. Chem. Res.* 2014, *53*, 15222–15229.

(153) Dupont, D.; Brullot, W.; Bloemen, M.; Verbiest, T.; Binnemans, K. Selective Uptake of Rare Earths from Aqueous Solutions by EDTA-Functionalized Magnetic and Nonmagnetic Nanoparticles. *Appl. Mater. Interfaces* 2014, *6*, 4980–4988.

(154) Rutledge, R. D.; Warner, C. L.; Pittman, J. W.; Addleman, R. S.; Engelhard, M.; Chouyyok, W.; Warner, M. G. Thiol-Ene Induced Diphosphonic Acid Functionalization of Superparamagnetic Iron Oxide Nanoparticles. *Langmuir* 2010, *26* (14), 12285–12292.

(155) Pearson, G. Hard and Soft Acids and Bases. *J. Am. Chem. Soc.* 1963, *85* (22), 3533–3539.

(156) Warner, C. L.; Addleman, R. S.; Cinson, A. D.; Droubay, T. C.; Engelhard, M. H.; Nash, M. A.; Yantasee, W.; Warner, M. G. High-Performance, Superparamagnetic, Nanoparticle-Based Heavy Metal Sorbents for Removal of Contaminants from Natural Waters. *ChemSusChem* 2010, *3* (6), 749–757.

(157) Misono, M.; Ochiai, E.; Saito, Y.; Yoneda, Y. A New Dual Parameter Scale for the Strength of Lewis Acids and Bases with the Evaluation of Their Softness. *J. Inorg. Nucl. Chem.* 1967, *29* (11), 2685–2691.

(158) Sposito, G. *Chemical Equilibria and Kinetics in Soils*; Oxford University Press: New York, 1994.

2. METHODOLOGY

2. METHODOLOGY

The aim of this chapter is to present the different techniques used to perform the synthesis and characterization of the materials prepared in this work; hierarchical alumina microspheres and functionalized magnetic nanoparticles, as well as the analytical methods used. The equipment conditions and subsequently, the models used in the interpretation of results are explained.

2.1. SYNTHESIS OF HAM BY AN ANALITYC MICROWAVE

Two types of HAM were synthesized by an **analytic microwave CEM MARS 5** (Figure 2.2), following the procedure described in literature[1–3] with some modifications as described in Figure 2.1.

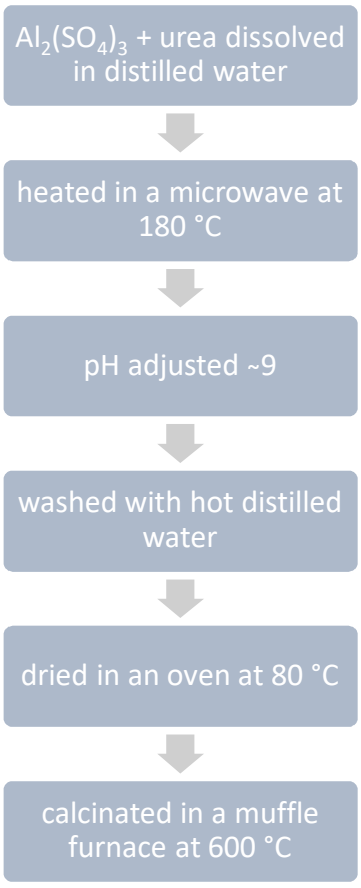

Figure 2.1. Experimental procedure of HAM synthesis.

Microwave radiation has many applications for many laboratory processes. Digestion of samples by microwave systems is one of the most important applications of such instrument in laboratories.

However, in this case the microwave irradiation has been used for the hydrothermal precipitation of HAM.

The microwave system produces radiation by microwave energy, in which the sample, in polar or ionic solutions, rises its temperature rapidly and at elevate pressures. The instrument consists in a microwave power system with user selectable power settings (0-1000W). The interior of the oven is coated with a fluoropolymer, it has a cavity exhaust fan and tubing to vent fumes.[4]

Magnetron Frequency
2455 MHz
Power Output
300 watts ±15%, 600 watts or 12 watts ±15%,
Magnetron Protection
Solid State Isolator (U.S. Patent 4,835.354) to protect magnetron from reflected energy, ensuring constant power output
ESP-1500 Plus Pressure Control System
Inboard pressure control system to monitor and control equilibrium/reaction pressure. Internal pressure control system able to monitor up to 1500psi and control vessel pressures to 800psi
RTP-300 Plus Temperature Control System
PerfectCircle™ provides absolute radial symmetry
Sensors
Pressure and temperature sensing devices to ensure accurate readings and to eliminate arcing (ignition) hazards.

Figure 2.2. The CEM Mars 5 microwave representation and its specifications.

The turntable within the microwave has the capacity to contain 12 microwave vessels, and rotates the samples 355 degrees and reverses 8.5 times per minute to ensure the vessel heating. The reaction vessels are made by PFA (Perfluoroalkoxy), extremely resistant to pressure and temperature and chemically inert. One of the vessels (specialized vessel) is able to monitor temperature and pressure inside itself by a programmable microcomputer.[4] All the reaction vessels possess a security valve escape in order to avoid extremely high pressures. The Mars 5 possess a door safety interlock system which prevents microwave emissions when the door is open.

In a typical synthesis, a solution 0.05M in aluminum sulfate and 0.1M in urea was prepared in 100 mL of distilled water and then stirred thoroughly during 15 minutes. Then 35mL of the prepared solution were added in a Teflon-PFA reaction vessel of 100 mL capacity and then placed on the turntable for uniform heating using a microwave digestion system. The microwave treatment was conducted in a temperature-controlled mode at 180 °C by non-pulse heating time for 3min (type A) or 20min (type B), using 2.45GHz microwave radiation under power range of 0–1000W (using the maximum power). Afterwards the sample was left for cooling until ambient temperature was reached. The pH of the resultant solution was adjusted at ~9 with NaOH. The synthesized material was then collected by centrifugation and washed with hot distilled water and ethanol several times. The precipitate was dried in an oven at 80°C for 12h. In order to convert the resulting ɣ-AlOOH

obtained in this synthesis into Al_2O_3, the powder was calcinated in a muffle furnace at 600 °C for 2h.

Since the formation of the hierarchical architecture and their properties are strongly dependent on the experimental conditions, including reaction time, reaction temperature, concentrations of the reactants and aluminium salt used as a reactant, several variations on the synthesis have been performed with the aim to achieve the hierarchical microspheres with the minimum size. The variations carried out in the synthesis are shown in Figure 2.3.

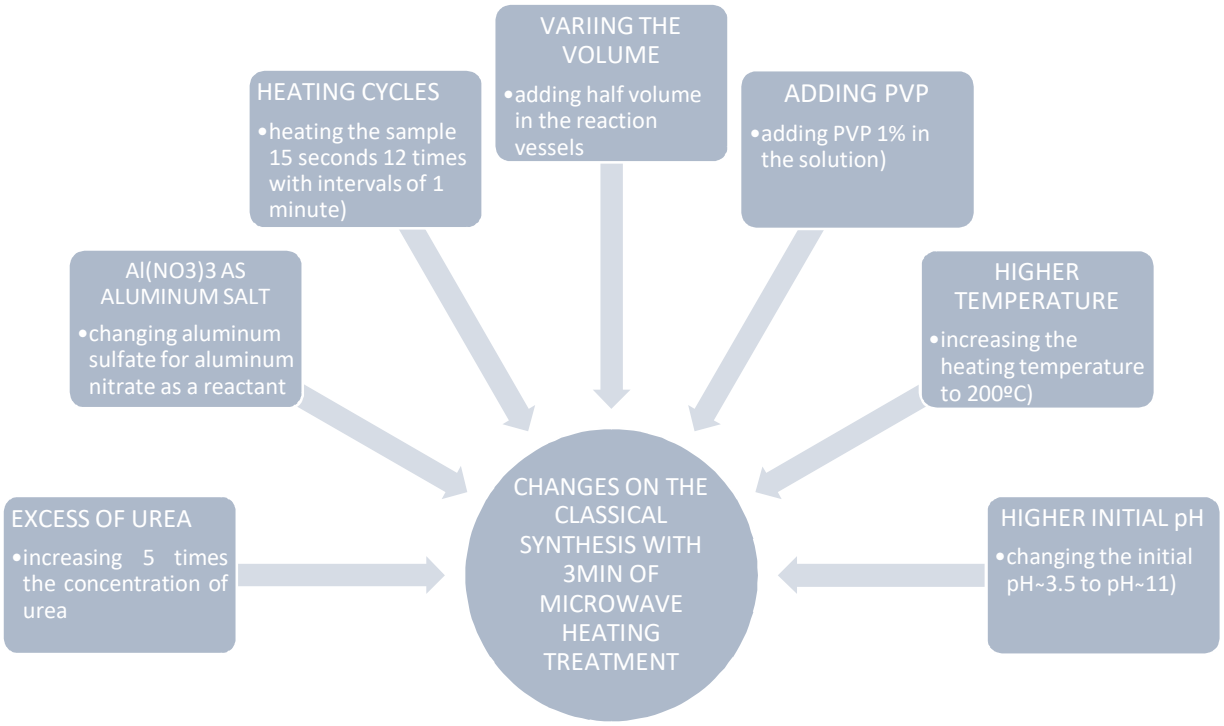

Figure 2.3. Variations carried out on the classical synthesis with 3min of microwave heating.

2.2. SYNTHESIS OF SPION

Iron oxide nanoparticles were synthesized by a co-precipitated method, presented in Figure 2.4, as described elsewhere.[5,6] The formation of the particles follows the equation showed as follows (Eq. 2.1)

$$FeCl_2 + 2FeCl_3 + 8NH_4OH \rightarrow Fe_3O_4(colloid) + 8NH_4Cl + 4H_2O \qquad \text{Eq. 2.1}$$

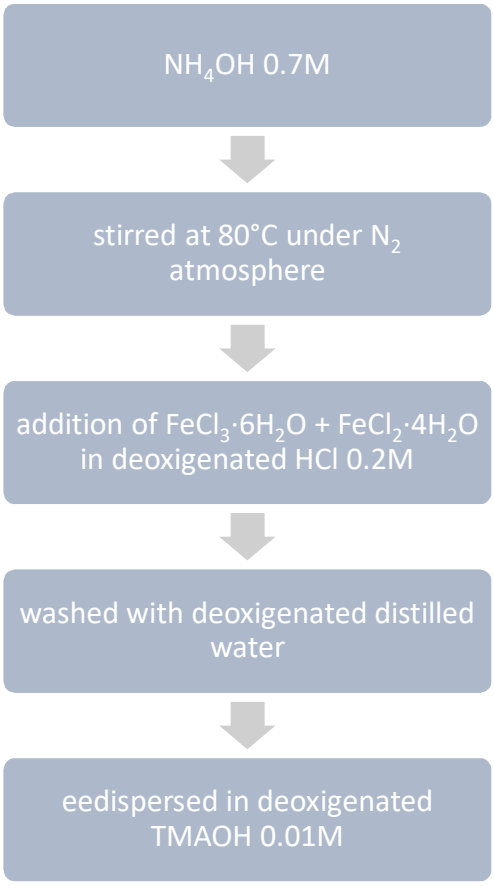

Figure 2.4. Scheme of the procedure of SPION synthesis.

300mL of a stock solution of NH_4OH 0.7M were deoxygenated under nitrogen gas with vigorous magnetically stirring and heated at 70 °C, as it is shown in Figure 2.5-A. The stock solution of Fe(III) and Fe(II) was prepared dissolving the respective chloride salts (Fe(II) : Fe(III) in a molar ratio 1 : 2) in a deoxygenated HCl 0.2M and then added to the NH_4OH. The solution turns in to black immediately, as shown in Figure 2.5-B. The particles were aged during 45 min and then cooled to room temperature with a water bath. The nanoparticles were collected by a magnetic separation and then washed several times with deoxygenated distilled water until neutral pH. The synthesized magnetite was then dispersed in a 0.01M TMAOH (tetramethylammonium hydroxide) aqueous solution previously deoxygenated. The synthesis was carried out in a continuous N_2 bubbling, in order to avoid the oxidation of Fe(II) into Fe(III) and the formation of undesirable iron oxides as maghemite or ferrihydrite.

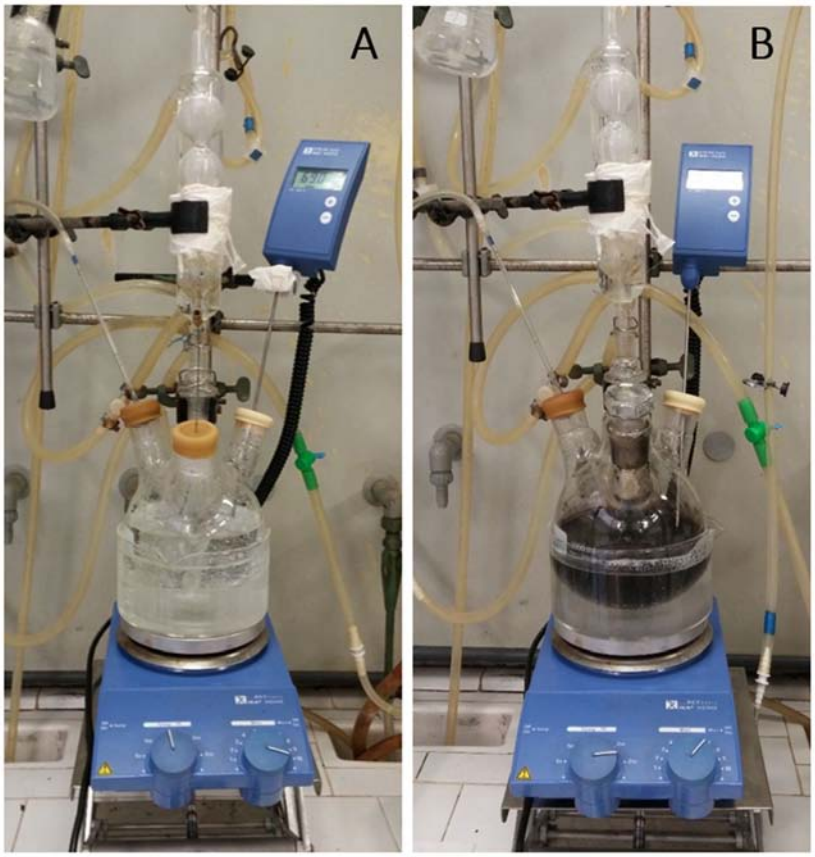

Figure 2.5. Fe_3O_4 synthesis by co-precipitation method. A: NH_4OH deoxygenated and heated, B: magnetite formation after ferric and ferrous solution addition.

2.2.1. SPION FUNCTIONALIZATION

The synthesized SPION have been functionalized following two different procedures; **ligand addition** and **ligand exchange** as explained below:

- **Ligand addition:** A known amount of the synthesized material was suspended in water acidified with HNO_3. The pH_{pzc} of the SPION is 6.8[7], therefore the pH of the SPION containing solution has been adjusted to pH 2.0, in order to have the SPION surface charged positively. In the case of the functionalization with 3-MPA, the published methodology has been followed,[6] where 10mL of SPION suspension, with a known amount of the synthesized material, has been mixed with a solution of the 3-MPA 150 mM in toluene during 24h.

  For 3,3-TDPA coating, it was not possible to use toluene as a solvent, since the ligand is not soluble in that, thus, a mixture of acetone and toluene (1:2) has been used instead of toluene. Then, the 3,3-TDPA solution 150mM in acetone-toluene has been mixed with the SPION suspension during 24h.

After the mixing time, the coated SPION were separated by using a magnetic field and then washed several times with ethanol, in order to remove the remaining ligand deposited on SPION surface. Then, the obtained material has been dried in a vacuum oven.

- Ligand exchange: A known amount of lauric acid (LA) was added to a SPION solution (molar ratio of LA:SPION being 3:2) , before SPION washing and redispersion in TMAOH (last step in Fig. 2.4). After 30min mixing, the SPION coated with LA (SPION@LA) were precipitated in ethanol and then washed several times with toluene and ethanol, to eliminate the LA in excess. [8,9] SPION@LA have been dispersed in 20mL of toluene, then 20mL of ethanol with the desired ligand 150mM were added to the suspension and mixed 24h.[10] Once expired the reaction time, the coated nanoparticles have been washed with ethanol and distilled water several times before drying in an oven under vacuum conditions.

2.3. MATERIALS CHARACTERIZATION

The characterization techniques are essential issues for the development of new materials, allowing to determine their physicochemical proprieties and therefore understood their behaviour in practical applications. Nowadays a wide number of methods exist to describe the properties of such materials.

In order to provide a major knowledge about the potential applications of the NSMs, the synthesized materials have been characterized with the following methodologies:

- Scanning Electron Microscopy

Scanning Electron Microscope (SEM) provides a high-resolution image of the surface morphology of the sample (Figure 2.6). This is one of the most versatile instruments available for the examination and analysis of microstructure morphology as well as the characterization of chemical compositions, thanks to the combination of high magnification, large depth of focus, good resolution, and the ease of observations. SEM images are obtained by the signal produced from the electron beam and specimen interactions, by scanning an electron probe across the surface and monitoring the secondary electrons emitted. Those are produced when an incident electron excites an electron in the sample giving some of its energy in the process, resulting in the emission of these secondary electrons. Then, these are collected by a detector and converted to an image.[11,12]

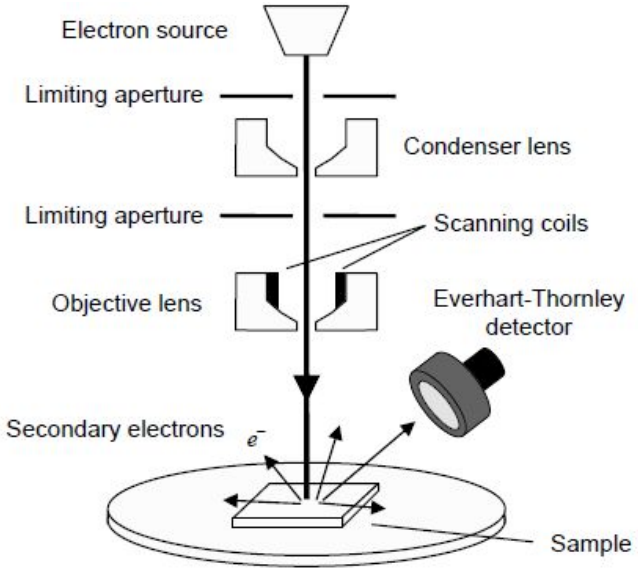

Figure 2.6. Schematic diagram of a SEM set-up.[12]

An ultra-high vacuum system is indispensable for SEMs in order to avoid the scattering on the electron beam and the contamination of the electron guns and other components. [11,12]

SEM technique has been employed in this work to obtain a topography image of the nanostructured adsorbent materials synthesized (HAM and SPION). SEM images were performed in the Servei de Microscopia of the Universitat Autònoma de Barcelona, by a MERLIN FE-SEM (Figure 2.7), ZEISS with the detector EDS Oxford LINCA X-Max and EBSD analysis Oxford Nordlys II (Carl Zeiss Microscopy, LLC., Germany).

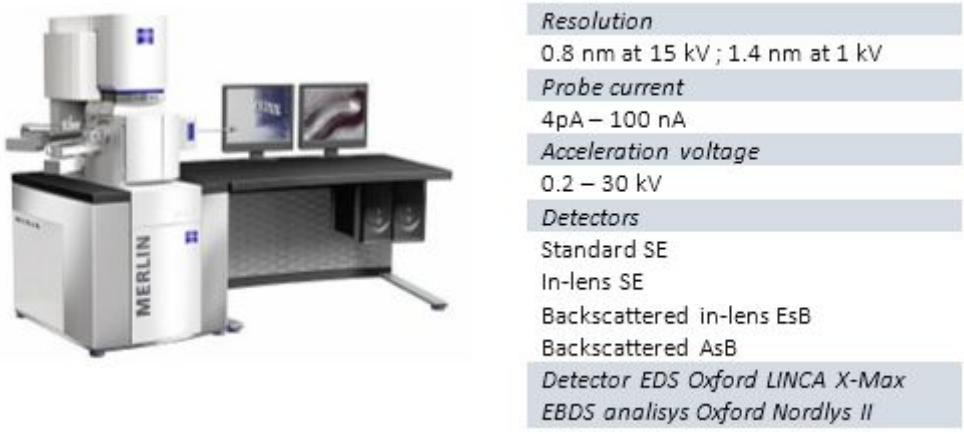

Figure 2.7. Image of the SEM instrument and its main specifications.[13]

The core of MERLIN is the GEMINI II column which, with its double condenser system, achieves an image resolution of 0.8 nanometers at 15kV, or 1.4nm at 1kV. A sample current of up to 100nA is available for analytical purposes such as energy dispersive X-ray spectroscopy (EDS) and diffraction analysis of backscattered electrons (EBSD).[13]

- Transmission Electron Microscopy

Transmission Electron Microscope (TEM) is a powerful tool in material science, providing an image of shape and dimensions of the nanostructured material. It is based on the generation of a high energy electrons beam (100-200keV) which is focused through a very thin sample interacting with it. Certain parts of the irradiated beam are transmitted through the sample creating the TEM image by the elastic and inelastic scattered electrons that traverse the sample. The interactions between the electrons and the atoms of the sample gives the structure features of the material of analysis. TEM operates on the same basic principles as the light microscope but uses electrons instead of light. Because the wavelength of electrons is much smaller than that of light, the optimal resolution attainable for TEM images is many orders of magnitude better than that from a light microscope. Thus, it can reveal the finest details of internal structure.[14]

The instrument requires to work under vacuum conditions, and the sample must be thin enough to transmit sufficient electrons to form an image with minimum energy loss. Therefore, the preparation of the sample is an important aspect of the TEM analysis. Different procedures can be followed to prepare it: for the nanostructures studied in this thesis, a suspension has been prepared in organic solvent (EtOH) and then a small doplet has been deposited and dried on a copper grid special for TEM analysis.

In the present work, TEM was used to characterize the detailed morphology of the synthesized adsorbent materials, both HAM and coated SPION, providing a high-resolution image of them. TEM micrographs were carried out in the Servei de Microscopía of the Universitat Autònoma de Barcelona by a JEM-2011 (Figure 2.8), with a resolution of 0.18nm at 200kV, with an accelerating voltage of 80–200kV and equipped with a camera CCD GATAN 895 USC 4000 and a detector EDS Oxford LINCA with energy resolution of 136eV (Jeol Ltd., Japan).

Resolution
0.18nm at 200 kV
Acceleration voltage
80 – 200 kV
Camera
CCD GATAN 895 USC 4000
Sample holders
Single tilt standard holder
GATAN 677 Single Tilt Multiple Specimen Holder for 5 samples
JEOL Double tilt holder
GATAN single tilt cryo holder
GATAN single tilt tomography cryo holder
Detector EDS Oxford LINCA
Energy resolution: 136 eV

Figure 2.8. TEM equipment image and summary of its specifications.[15]

The high resolution offered by TEM is ideal to analyse the quality, shape, size of NMs. TEM can also be used for a wide range of purposes, including the study of the layers growth, their composition, or the chemical analysis of the sample and allows to visually measure the particle diameter and therefore calculate the average particle size.

- X-ray diffraction

X-ray diffraction (XRD) has become an indispensable tool for identifying nanocrystalline phases as well as crystal size and crystal strain. It is a crystallographic technique used for identifying and quantifying various crystalline phases present in solid materials and powders as well as chemical composition, crystal structure, crystallite size, strain, preferred orientation and layer thickness. XRD monitors the diffraction of X-rays after they interact with the electrons in the atoms of the sample; the X-rays are reflected, and in most cases the waves interfere between them being cancelled. However, when a regular crystalline sample is concerned, a proportion of waves are reinforced forming a constructive interference which is known as diffraction. Such diffraction holds information about the electron distribution in the material producing a characteristic pattern[12,16] of the crystal structure and only occurs when incident angles fulfil the Bragg condition represented in Eq. 2.2:[12]

$$n\lambda = 2d \sin\theta \qquad \text{Eq. 2.2}$$

By varying the angle θ, the Bragg Law condition is satisfied for different *d*-spacing in polycrystalline materials (Figure 2.9). Plotting the angular positions versus intensities produces a diffraction pattern, which is characteristic of the sample. When a mixture of different phases is present, the resultant diffractogram is a superposition of the individual patterns.[12]

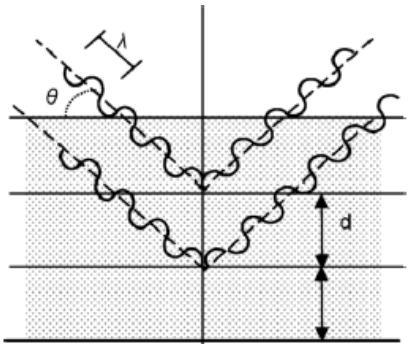

Figure 2.9. Representation of condition for constructive interference.[12]

In a typical XRD pattern, the diffracted intensities are plotted versus the detector angle 2θ. Then, the crystal phases may be identified by comparison of the obtained patterns with those of reference, found in internationally recognized databases (such as *Joint Committee on Powder Diffraction Standards database – JCPDS).*

A useful phenomenon is that as crystallite dimensions enter the nanoscale the peaks broaden with decreasing crystal size. The widths of the diffraction peaks allow the determination of crystalline size, by using variants of the Scherrer equation[12] (Eq. 2.3):

$$t = \frac{K\lambda}{B\cos\theta} \qquad \text{Eq. 2.3}$$

where t is the thickness of the crystal, K is the Scherrer constant which depends on the crystallite shape, λ is the radiation wavelength used to obtain the diffractogram and B is the full width at half maximum of the broadened peak. If a Gaussian function is used to describe the broadened peak, then the Scherrer's constant K is equal to 0.89. The Scherrer equation is derived from Bragg's law and may be used to determine crystallite sizes if the crystals are smaller than 1000Å.[12]

Both synthesized materials have been analized by XRD; HAM were analysed in the Università degli Studi di Udine, while SPION analysis were performed at the Universitat Autònoma de Barcelona. The crystal structure of the alumina based adsorbent (HAM) was determined using a Philips PW 3040/60 X'pert PRO instrument (Figure 2.10) ,equipped with an X'celerator detector and operating at 40 kV and 40 mA, with Ni-filtered Cu K_α radiation. Diffraction profiles were collected in the 2θ range of 5–100° with a step of 0.02 and a counting time of 15 s/step.

Mains Supply
200 – 240 V, single phase, 50 or 60 Hz
Maximum loading current
45 A
Goniometer
Vertical goniometer (theta-theta)
Maximum usable range -40°< 2θ <220°
240 mm radius
X-ray Source
Fully ceramic X-ray tubes
X-rays generated from a Cu anode supplied with 40 kV and a current of 40 mA.

Figure 2.10. Image and specifications of XRD instrument.

Phase identification was carried out by means of the X'Pert accompanying software program PANalytical High Score Plus in conjunction with the JCPDS Database.

The crystallographic phase determination was also undertaken for SPION by analyzing the XRD of the powder, performed by a X-Pert Philips diffractometer (Figure 2.11), using a monochromatized X-ray beam, operating at 45 kV and 40 mA with nickel-filtered Cu K_α radiation. The diffractograms were collected in the the 2θ range of 15–100° with a step of 0.02 and a counting time of 15 s/step.

Mains Supply
200 – 240 V, single phase, 50 or 60 Hz
Maximum loading current
45 A
Goniometer
Goniometer for routine measurements with an automatic sample changer, spinning device, fixed slits and a secondary monochromator. Goniometer provided with two devices for samples and two optics.
X-ray Source
Fully ceramic X-ray tubes X-rays generated from a Cu anode supplied with 45kV and a current of 40 mA.

Figure 2.11. Image and details of XRD instrument available in the UAB.[17]

- **N_2 adsorption isotherms**

The way of adsorption of pure fluids on planar surfaces and porous materials depends on the interplay between the strenght of fluid-wall and fluid-fluid interactions as well as the effects of confined pore space on the state and thermodynamic stability of fluids confined to narrow pores. The IUPAC proposed to classify pores by their internal pore width (defined as the diameter in cas of a cylindrical pore and as the distance between opposite wealls in case of a slit pore):[18]

i) Micropore: pore of internal width less than 2nm

ii) Mesopore: pore of internal width between 2 and 50nm

iii) Macropore: pore of internal width greater than 50nm

The sorption behaviour in macropores (considered as nearly planar surfaces) is completely different from that mesoporous or microporous, as represented in Figure 2.12.

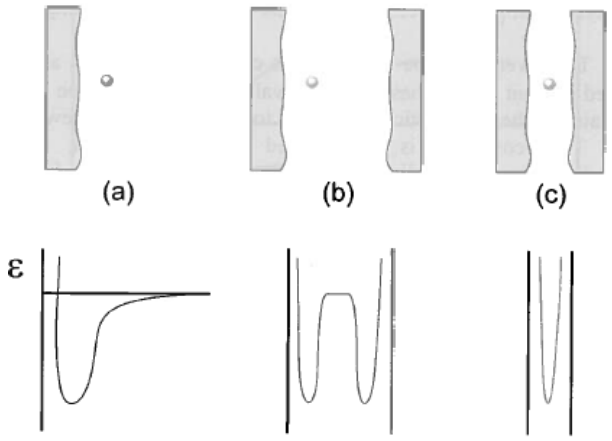

Figure 2.12. Schematic illustration of adsorption potential (ε) on a planar (a); mesoporous (b); and microporous (c).[18]

The representation of the amount adsorbed versus the relative pressure of the gas at constant temperature is called adsorption isotherm. The existence and particular characteristics, has allowed their classification into six different types, published by IUPAC in 1985.[19] However, during the past of the years new characteristic isotherms have been identified and present a relation to particular pore structures.[20] Therefore, the original IUPAC physisoprtion isotherm classifications have been refined, the updated classification isotherms is shown in Figure 2.13.

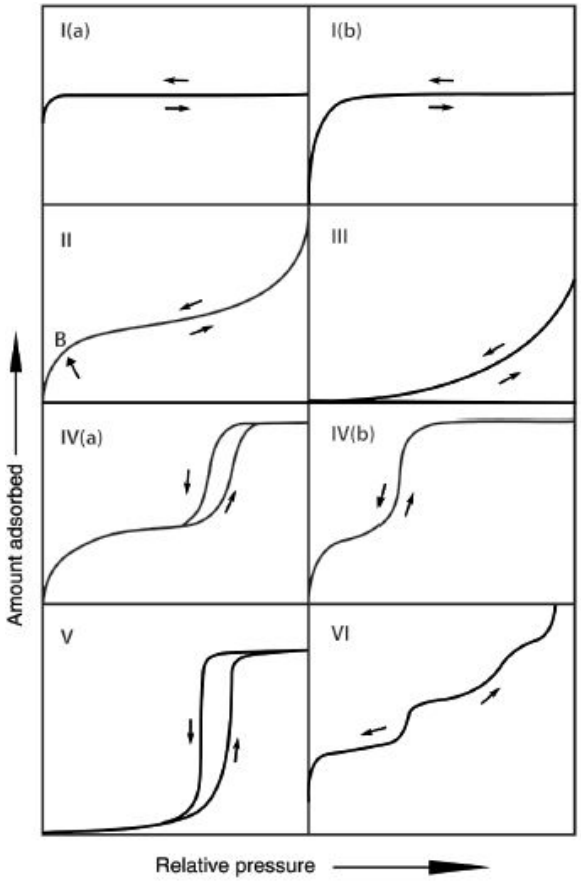

Figure 2.13. Classification of physisoprtion isotherms.[20]

Below are summarized the characteristics of each type of isotherm:[20]

Type I: The reversible Type I isotherm is called Langmuir isotherm, and it is characteristic of microporous solids having small external surfaces. The volume of gas adsorbed is limited by the accessibility of micropores. *Type I(a)* isotherms are given by microporous materials having mainly narrow micropores (of width < ~ 1nm); *Type I(b)* isotherms are found with materials having pore size distributions over a broader range including wider micropores and possibly narrow mesopores (< ~ 2.5nm).

Type II: Reversible Type II isotherms are given by nonporous or macroporous adsorbents. Its characteristic shape is the result of a monolayer-multilayer adsorption without restrictions. A more

gradual curvature (Point B) is an indication of a significant amount of overlap of monolayer coverage and the onset of multilayer adsorption.

Type III: This isotherm has a convex shape and there is no Point B and therefore no identifiable monolayer formation. This type of isotherm is rare and characteristic of systems in which the adsorbent-adsorbate interactions are relatively weak and the adsorbed molecules are clustered around the most favourable sites on the surface of a nonporous or macroporous solid.

Type IV: Isotherms characteristic of mesoporous adsorbents. The adsorption behaviour in mesopores is determined by the adsorbent-adsorptive interactions and also by the interactions between the molecules in the condensed state. The initial monolayer-multilayer adsorption on the mesopore walls is followed by pore condensation. A typical feature of Type IV isotherms is a final saturation plateau, of variable length (sometimes reduced to a mere inflexion point). In *Type IV(a)*, the capillary condensation is accompanied by hysteresis while in *Type IV(b)* completely reversible isotherms are observed.

Type V: The isotherm shape is correlated with Type III. This similitude is attributed to the weak interactions of adsorbent-adsorbate. Type V isotherms are observed for water adsorption on hydrophobic microporous and mesoporous adsorbents.

Type VI: The reversible stepwise isotherm is characteristic of layer-by-layer adsorption on a uniform non-porous surface. The height of each stage represents the capacity for each adsorbed layer, while the sharpness is depends of the system and temperature.

Brunauer–Emmett–Teller theory

N_2 adsorption at -196ºC is a widely used technique to determine the Brunauer–Emmett–Teller (BET) surface area. BET method[21,22] is one of the most widely used methods for evaluating the surface area of porous materials. Indeed, under certain carefully controlled conditions, the BET-area of a nonporous, macroporous or a mesoporous solid can be regarded as the "probe accessible area" (i.e., the effective area available for the adsorption of the specified adsorptive).[20]

The effectiveness of the BET theory is that it enables an experimental determination of the number of molecules required to form a monolayer, despite the fact that exactly one monomolecular layer is never actually formed.[23]

The sample first need to be degassed to remove the surface contamination and adsorbed species. In the analysis performed in this work the samples have been degassed by vacuum and heating. Then, a probe gas (generally N_2) is introduced at cryogenic temperatures; known aliquots are dosed up to saturation pressure, then vacuum is applied and the gas removed, which may result in

hysteresis behaviour. The instrument measures the relative pressure and quantity of gas adsorbed, providing an adsorption isotherm which varies depending on the porosity and characteristic textures of the material. Textural characteristics of all fresh samples were measured according to the BET equation[23] (Eq. 2.4)

$$\frac{1}{W\left[\left(\frac{P_0}{P}\right)-1\right]}=\frac{1}{W_m C}+\frac{C-1}{W_m C}\left(\frac{P}{P_0}\right) \qquad \text{Eq. 2.4}$$

Where P is the pressure, P_0 is the saturation pressure, W is the number of moles adsorbed, W_m is the number of moles adsrobed in the monolayer and C is a parameter related to the heat of adsorption.

The determination of surface areas from BET theory is a straight forward applicaition of the Eq. 2.4. A plot of $1/W[(P_0/P)-1]$ versus P_0/P, will yield a straight line usually in the range $0.05 \leq P_0/P \leq 0.35$.[23]

W_m and C may be found resolving simoltaneously the equations of the slope (s) and the interception (i), Eq. 2.5 and Eq. 2.6 respectively:[23]

$$s=\frac{C-1}{W_m C} \qquad \text{Eq. 2.5}$$

$$i=\frac{1}{W_m C} \qquad \text{Eq. 2.6}$$

From the value W_m, the total surface area can be calculated by the following Eq. 2.7:

$$S = n_m \cdot a_m \cdot N_a \cdot 10^{-21} \qquad \text{Eq. 2.7}$$

where S is the apparent surface area of the material (m^2g^{-1}), a_m is the area occupied by one adsorbate molecule (nm^2 $molecules^{-1}$; in the case of N_2 at -196°C is 0.162nm^2) and N_a is the Avogadro's number ($6.023 \cdot 10^{23}$ molecules mol^{-1}).

Barrett–Joyner–Halenda equation

The Kelvin equation arises from the fact that gas adsorption into pores is a capillary condensation phenomenon involving the formation of a meniscus of liquid inside the pore. The difference of pressure between both sides of the meniscus can be evaluated from the Kelvin equation[24] (Eq. 2.8), which relates the pore size with the amount obtained gas adsorbed at a certain relative pressure. It provides the relationship between the pore radius and the amount of adsorption at a relative pressure.[24]

$$\ln\frac{P}{P_0} = -\frac{2\gamma V_l}{RT}\frac{1}{r_m} \qquad \text{Eq. 2.8}$$

where P_0 = the saturation pressure of the adsorbate (corresponding to an infinite r_m), γ = liquid surface tension, V_l = molar volume of the liquid, T = temperature, r_m = radius of curvature of the meniscus of liquid formed in the pore.

Several methods have been developed for the calculation of the pore size distribution on the basis of the Kelvin equation with a correction term for the thickness of the multilayer adsorbed film.[24] Barrett-Joyner-Halenda (BJH) method has been widely used for such calculations. It is based on the Kelvin equation and corrected for multilayer adsorption, is most widely used for calculations of the porous size distribution over the mesopore and part of the macropore range.[25]

The gas adsorption measurements have been used in this work to determine the surface area of the materials synthesized. These mesurements have been performed in the Università degli Studi di Udine in a Tristar 3000 gas adsorption analyser (Figure 2.14) from Micromeritics. Prior to the adsorption measurements, degasification of the samples was carried out at 150°C during 1h under vacuum conditions.

Pressure
0 – 999 mmHg (resolution0.05 mmHg)
Accuracy manifold temperature
±0.25°C (resolution 0.1°C)
Vacuum pump
20 µmHg (maximum) with antisuckback valve
Environment
Temperature: 10 to 35°C, operating; 0 to 50°C, nonoperating
Humidity: 20 to 80% relative, noncondensing
Electrical
Voltage: 85 to 265 VAC
Frequency: 50/60 Hz
Power: 300 VA, maximum

Figure 2.14. Tristar 3000 (Microcalorimetrics) image and their specifications.[26]

- Dynamic Light Scattering

Dynamic Light Scattering (DLS) is also known as Quasi-Elastic Light Scattering and Photon Correlation Spectroscopy,[12] and is one of the most popular methods used to study the colloidal stability of the particles. The DLS measurements are performed shining a monochromatic light beam, such as a laser, onto a solution containing particles. Such particles are in random motion, called Brownian motion, causing the scattering of the light irradiated. When the scattered lights from two or more particles are added together, there will be a changing destructive or constructive interference. This changes are related to the size of the particle. Therefore, measuring such

fluctuations it is possible to compute the sphere size distribution and give a description of the particle's motion in the medium. [27,28]

The light intensity detected by the detector causes fluctuations over time. These time dependent fluctuations can then be related to particle speed by autocorrelation of the average of the product of the photon count, with a delayed version as a function of the delay time. The autocorrelation function is analyzed by numerically fitting the data with calculations based on assumed particle size distributions.

Analysis of the time dependent fluctuation gives the diffusion coefficient of the particles, *D*. Then, if the viscosity η, of the solution is known, then the radius or a spherical particle, *r*, can be obtained from the *Stokes-Einstein* relation (Eq. 2.9):[12]

$$r = \frac{kT}{6\pi\eta D} \qquad \text{Eq. 2.9}$$

where *k* is Boltzmann's constant (1.3806505×10^{-23} J K^{-1}) and *T* is the absolute temperature.

Range of particle size displayed
1nm to 6 µm
Measurement Time
Approx. 2 minutes
Principles of Thermostatic
Cartridge heater, Peltier element
Rante of Thermostatic Temperaure for Cell Holder
5°C to 70°C
Optical System
Light source: 650 nm Laserdiode, 5 mW Photo-cell detector: Photo-multiplier tube Sample cell: Cuvette cell
Power
100V/120V/230V AC ± 10%, AC input range selection is fully automatic, 50Hz/60 Hz Approx. 150 VA
Operation Temperature
15°C to 35°C

Figure 2.15. DLS representation and its specifications.[29,30]

The DLS measures were performed with a **Horiba LB-550 Particle Size Analyzer** (Figure 2.15). The LB-550's optical design uses a highly sensitive photo multiplier tube to be able to measure the lower concentrations. The optical arrangement which captures only the 180-degree scattered light, allows the light beam to be focused a short distance inside the cell, limiting the maximum amount of scattered light. This allows the measurement of high concentration samples without overloading the detector.

- **Thermogravimetry**

Thermogravimetry (TGA) is a technique based on the variation in a sample mass (gain or loss) when subjected to heat treatment as a function of temperature and/or time. [10,31] Three modes of TGA are commonly used; (1) isothermal TGA (Figure 2.16-A); where the variations in the sample mass are recorded as a function of time at constant temperature, (2) quasi-isothermal TGA (Figure 2.16-B); in which the sample is heated to constant mass at each of a series of increasing temperatures, and (3) dynamic TGA (Figure 2.16-C); the sample is heated with a temperature changing in a predetermined manner, generally at a linear rate. Dynamic TGA, is the most used procedure, therefore it is commonly designated as TGA method.[31]

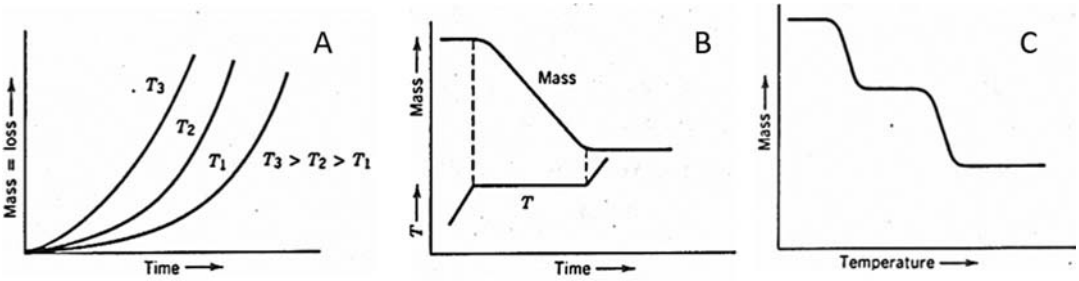

Figure 2.16. Representation of TGA graphics of the three different modes.[31]

Through the mass-change versus temperature curve, it is possible to obtain information about the thermal stability and composition of the sample, the thermal stability of intermediate compounds that may be formed during the heating, and the composition of the residual if any.

In the present work, TGA was used to quantify the quantity of organic ligand (3-MPA) coating the magnetic nanoparticles, being the process represented in Eq. 2.10:

$$A(solid) \rightarrow B(solid) + C(gas) \qquad \text{Eq. 2.10}$$

Weighing Precision
+/- 0.01%
Sensitivity
0.1 µg
Baseline Dynamic Drift
< 50 µg
Isothermal Temp Accuracy
+/- 1°C
Isothermal Temp Precision
+/- 0.1°C
Furnace Cooling (forced air/N2)
1000 to 50°C < 12 min
Temperature Calibration
Curie Point

Figure 2.17. TGA instrument picture along with its specifications.

Such experiments were performed with a **TA Instruments Q500 TGA** (Figure 2.17). The sample (15-20 mg) was placed in a small flat Pt crucible licked by an N_2 flow (60ml min^{-1}) tangent to the sample and then it was heated at a constant rate (10 °C/min) up to 900°C.

- **Fourier Transformation - Infrared spectroscopy**

Infrared spectroscopy (IR spectroscopy) deals with the infrared region of the electromagnetic spectrum, which is light with a longer wavelength and lower frequency than visible light. It covers a range of techniques, mostly based on absorption spectroscopy. The infrared region of the electromagnetic spectrum may be divided into three main sections:[32]

1. *Near-IR*; is the higher energy, approximately 12500–4000 cm^{-1} (0.8–2.5µm wavelength) can excite overtone or harmonic vibrations.
2. *Middle-IR*; 4000–400 cm^{-1} (2.5–25µm) used to study the fundamental vibrations and associated rotational-vibrational structure.
3. *Far-IR*; 400–10 cm^{-1} (25–1000µm), lying adjacent to the microwave region, has low energy and may be used to study rotational spectroscopy.

The main region of interest for analytical purposes is from 4000 to 400 cm^{-1} (middle-IR), which provides useful information about the analized compounds.

The IR absorption spectrum is originated as a result of the absorption of IR radiation by the sample, which results, as shown in Figure 2.18, in transitions between different energy levels of vibrational states when the radiation energy is equal to the energy difference between two of such states.

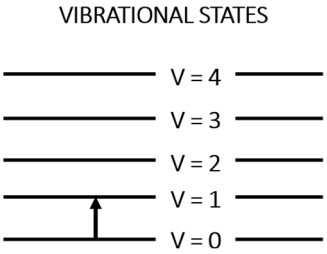

Figure 2.18. The molecule is excited to a higher vibrational state by the adsorption of the infrared radiation (figure adapted from the reference[33]).

The number, position and intensity of the absorption bands of IR spectrum, are mainly determined by the nature of the bond between the atoms involved and therefore its composition and crystal structure.

Then, the infrared spectrum may be represented by Transmittance or Absorbance spectrum. The transmittance at each wavenumber may be calculated by following Eq. 2.11. Then, the transmission spectrum is recovered by plotting the transmittance obtained versus the wavenumbers.

$$T = \frac{I}{I_0} \qquad \text{Eq. 2.11}$$

where T is the transmittance, I_0 is the intensity of the entering radiation (before sample absorption) and I is the transmitted light (after sample absorption).

Likewise, it can be obtained the absorbance spectrum, by the plotting of the absorbance versus the wavenumber. Absorbance at given wavenumber is obtained by using the Lambert-Beer equation (Eq. 2.12)[33]

$$A = \log\left(\frac{I}{I_0}\right) = -\log T \qquad \text{Eq. 2.12}$$

being A the absorbance.

Traditional IR spectrophotometers were constructed with monochromation being carried out using sodium chloride or potassium bromide prisms, but these had the disadvantage that the prisms are hygroscopic and the middle-IR region normally necessitated the use of two different prisms in order to obtain adequate dispersion over the whole range.[32] Thus, in order to overcome the limitations encountered with dispersive instruments, IR spechtrophotometers has evolved in a procedure based on the inteferometry, known as Fourier Transform-Infrared Spectroscopy (FT-IR).

The instruments are commonly based on the Michelson interferometer, where the radiation from an IR source is split into two beams by half-silvered 45° mirror so that the resulting beams are at right angles to each other, producing a unique type of signal which has all of the spectral characteristics of the sample in the beam. Then, the interferogram is converted into an IR spectrum.[32]

Composition
Single reflection diamond crystal, all reflective, gold coated optics, no fragile composite material construction

Spectral range
8000cm^{-1} – 10cm^{-1}

Sample measurement
Ergonomic one-finger clamp mechanism with pressure control
Adjustable and reproducible sample pressure
Rotatable pressure applicator

Working distance
max. sample height: 20 mm

Figure 2.19. Picture of FT-IR instrument and its principle specifications.[34]

Regrding the present research, FT-IR has been used to verify the ligand presence on the SPION surface. The FT-IR spectrum have been recorded in the Università delgi Studi di Udine by the

measurement in the middle-IR region using a **PLATINUM ATR from Bruker integrated into a VECTOR 22 FT-IR spectrometer** (Figure 2.19).

- **Point of Zero Charge**

The point of zero charge (pH_{pzc}) is the pH value at which the sum of positive and negative charges are equals. Whereas it can be assumed that the surface charge has no influence on the adsorption of neutral adsorbates, charged species (acid anions and protonated bases) can be subject to additional attraction or repulsion forces, depending on the signs of the species and surface charges.[35]

Consequently, the pH not only affects the adsorbate (by protonation/deprotonation changing its polarity), but also affect the surface charge of the adsorbent. Adsorbent materials possess functional groups on their surfaces that can be protonated or deprotonated. As a consequence, the surface of such adsorbents is typically positively charged at low pH values and negatively charged at high pH values.[35] Accordingly, the adsorption-adsorbate system is hardly pH-dependent.

Adsorbate character	Relative position of pH_{pzc} and pK_a	pH range	Dominating adsorbate charge	Dominating adsorbent surface charge	Resulting electrostatic interactions
Acidic	$pH_{pzc} < pK_a$	$pH > pK_a$	Negative	Negative	Repulsion
	$pH_{pzc} > pK_a$	$pK_a < pH < pH_{pzc}$	Negative	Positive	Attraction
		$pH > pH_{pzc}$	Negative	Negative	Repulsion
Basic	$pH_{pzc} > pK_a$	$pH > pK_a$	Positive	Positive	Repulsion
	$pH_{pzc} < pK_a$	$pK_a < pH < pH_{pzc}$	Positive	Negative	Attraction
		$pH > pH_{pzc}$	Positive	Positive	Repulsion

Table 2.1. Conditions for electrostatic interactions during adsorption of weak acids and bases charged surfaces.[35]

Table 2.1 summarizes the conditions under which attraction and repulsion forces can be expected. In pH ranges where the adsorbate species have the same charge as the surface, the adsorption is relatively weak, not only as a result of the higher polarity of the charged adsorbate species but also due to additional repulsion forces. Under certain conditions, pH ranges exist where the adsorbate species and the adsorbent surface show opposite charges and, consequently, attraction forces occur. Since these attraction forces act in addition to the van der Waals forces, an adsorption maximum can often be observed in these pH ranges.[35]

In the present work the pH_{pzc} was determined for the alumina based adsorbent as well as modified SPION. The pH_{pzc} for HAM has been determined by solid addition method[36] using 0.1M potassium chloride (KCl) solution with 20 $mg \cdot L^{-1}$ F^-. 20mL of the prepared solution (0.1M KCl with fluoride)

were added into a series of vessels. Then, the initial pH (pH_i) of the solutions was adjusted in the range of 3.0-10.0. After that, 15mL of any solution were added into another vessel with 0.3mg of the adsorbent material. The suspensions were then equilibrated for 48h.

Once the equilibration time was reached, the final pH (pH_f) of the solutions was measured again. The difference between the final and the initial pH ($\Delta pH = pH_i - pH_f$) was plotted versus the pH_i. The pH_{pzc} is given for the point where the curve intersects with abscissa, at this point $\Delta pH = 0$. In order to confirm our results, the experiment was performed at different ionic strength, 0.1M and 0.01M KCl.

The pH_{pzc} of SPION@3-MPA was determined following the methodology published in the literature.[37] Aliquots of 20mL of 0.01M $NaNO_3$ solution have been mixed with 20mg of the adsorbent material. A number of solutions have been prepared, the pH of each solution has been adjusted to a different pH in a range between 3 and 10. After measure the initial pH, 20mL of the prepared solution was mixed with the adsorbent material, then, the suspensions were mixed during 24h. As soon as the reaction time was expired, the final pH of the solutions was measured. As in the previous case, the difference between initial and final pH ($\Delta pH = pH_i - pH_f$) was plotted versus the initial pH, being the pH_{pzc} the point where the curve intersects the abscissa.

2.4. ADSORPTION STUDIES

Adsorption isotherms provide essential information for the understanding of the adsorption mechanism and then for the design of the adsorption systems. The adsorption equilibrium state is defined by a function of three variables: adsorbate concentration, adsorbed amount (loading capacity of the adsorbent), and temperature. However, it is usual to keep the temperature constant during the whole process. Therefore, the adsorption isotherm (Figure 2.20. Adsorption isotherm.Figure 2.20) may be defined in Eq. 2.13:[35]

$$q_{eq} = f(C_{eq}), \quad T = constant \qquad \text{Eq. 2.13}$$

where q_{eq} is the adsorbed amount in the equilibrium state, C_{eq} is the adsorbate concentration in the equilibrium state, and T is the temperature.

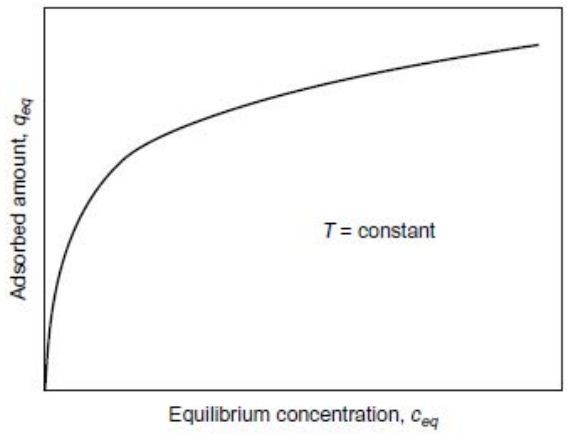

Figure 2.20. Adsorption isotherm.[35]

Up to now there is no an universal isotherm equation to describe all experimental isotherm curves accurately, existing a wide range of models which were developed based on both theoretical and empirical bases[35,38,39] such as Langmuir, Freundlich, Brunauer–Emmett–Teller, Redlich–Peterson, Dubinin–Radushkevich, Temkin, Toth, Koble–Corrigan, Sips, Khan, Hill, Flory–Huggins or Radke–Prausnitz isotherm.

In the present work Freundlich and Langmuir isotherms have been selected as models to describe the adsorption mechanism, since it has been demonstrated that such models better fit the adsorption behaviour of pollutants from wastewaters.[40] In this work, such models have been used to evaluate the adsorption-adsorbate systems of (i) fluoride on HAM and (ii) metal ion on modified SPION. The detailed description of those models are explained below.

- Langmuir model

Langmuir isotherm is one of the best known and most used adsorption model. It is based on the following hypothesis; (1) the adsorbate forms a monolayer on the adsorbent surface, (2) the adsorption takes place at specific homogeneous sites on the adsorbent, (3) once the adsorbate occupies a site; no further adsorption can take place in that site, (4) the solid is supposed to have a limited adsorption capacity, (5) all adsorption sites are identical, retaining a molecule of adsorbate with a sterically energy independent of the adsorbed quantity, (6) the adsorption energy is constant and does not depend on the degree of occupation of an adsorbent's active centers, (7) the strength of the intermolecular attractive forces is believed to fall off rapidly with distance, (8) the adsorbent is structurally homogeneous, and finally (9) there is no interaction between molecules adsorbed on neighbouring sites.[35,38–41]

It has to be taken into account that adsorption process is not manifested alone, since simultaneously the reverse process occurs.[42] Therefore, the dynamic equilibrium of such process is represented by the following reaction (Eq. 2.14):[41,42]

$$\text{free site} + \text{solute} \rightleftharpoons \text{surface complex} \qquad \text{Eq. 2.14}$$

with rate constants of k_a and k_d for the adsorption and desorption processes respectively.

The fraction of occupied sites (θ) corresponds to the degree of the surface coated, and is defined in Eq. 2.15 as follow: [42]

$$\theta = \frac{number\ of\ occupied\ sites}{number\ of\ total\ sites} \qquad \text{Eq. 2.15}$$

The factors involved in the adsorption process are the concentration of adsorbate available for the adsorption (C), and the free sites on the surface to be occupied (1-θ), where the adsorption rate (r_{ads}) is represented by Eq. 2.16. Whereas the desorption depends only on the adsorbed molecules, represented by the occupied sites at the interface θ, where the desorption rate (r_{des}) is defined by Eq. 2.17.

$$r_{ads} = k_{ads} C(1-\theta) \qquad \text{Eq. 2.16}$$

$$r_{des} = k_{des}\theta \qquad \text{Eq. 2.17}$$

At equilibrium, the change in fractional coverage with time is equal to zero so it may be written:

$$0 = k_{ads} C(1-\theta) - k_{des}\theta \qquad \text{Eq. 2.18}$$

Obtaining the following Eq. 2.19

$$\theta = \frac{KC}{KC+1} \qquad \text{Eq. 2.19}$$

where K is the equilibrium constant represented by Eq. 2.20

$$K = \frac{k_{ads}}{k_{des}} \qquad \text{Eq. 2.20}$$

Then, the Langmuir isotherm may be also written as the following Eq. 2.21:[35,38–41]

$$C_{ads} = \frac{Q_{\max} b C_e}{1 + bC_e} \qquad \text{Eq. 2.21}$$

where: C_e= equilibrium concentration (M), C_{ads}= solute adsorbed at equilibrium (mol·g^{-1}), Q_{max} = maximum quantity of solute adsorbed per gram of adsorbent (mol·g^{-1}) and b = Langmuir constant (M^{-1}).

Thus, Langmuir model describes quantitatively an homogeneous adsorption by the formation of a monolayer adsorbate on the adsorbent surface, making possible to obtain the value of the adsorption constant and loading capacity of the adsorption reaction.

- Freundlich model

Freundlich model is also frequently used to describe adsorption-adsorbate systems. In contrast to Langmuir model, the adsorption process is characterized by surfaces with heterogeneous active sites.[35,39] The Freundlich isotherm is an empirical equation used for the description of multilayer adsorption with interaction between adsorbed molecules represented by the Eq. 2.22: [35,38–41]

$$C_{ads} = K_f C_e^{\frac{1}{n}} \qquad \text{Eq. 2.22}$$

where K_f = the Freundlich constant ($(L \cdot mmol^{-1} \cdot g^{-1})^{1/n}$), n = adsorption intensity, C_e = equilibrium concentration of adsorbate (M), C_{ads} = amount of adsorbate adsorbed at equilibrium ($mol \cdot g^{-1}$). The Freundlich constants are empirical constants depends on many environmental factors. The value of 1/n ranges between 0 and 1 indicates the degree of non-linearity between solution concentration and adsorption.[35,40]

The model is applicable to the adsorption on heterogeneous surfaces by a uniform energy distribution and reversible. It can describe neither the linear range at very low concentrations nor the saturation effect at very high concentrations. By contrast, the medium concentration range is often very well represented.[35,40]

It is necessary to know the concentration of the analytes remaining in solution for isotherms development. In this thesis, the selected techniques for this purpose has been; (i) potentiometry, for measuring fluoride concentration in solution, and (ii) Inductively Coupled Plasma, to measure the remaining concentration of metal in aqueous media.

- Potentiometry

Potentiometry allows the fast and direct measurement of the fluoride concentration remaining in aqueous solution after the adsorption on HAM. Potentiometry is one type of electrochemical analysis methods (Figure 2.21 and Figure 2.22) and may be used to measure the potential variation of the indicator electrode, to construct a titration curve or, such in this work, it may be used for measurements in which the interest is in the actual value of the indicator electrode potential in order to find the concentration of an ion. This technique is based on the measurement of the potential of an electrode system in absence of significant current. Such potential depends on the ions present in the solution and their concentration. The dependence of potential between electrodes from concentration of ions is expressed by Nernst equation[43] (Eq. 2.23).

$$E = E_0 \frac{RT}{nF} \ln a \qquad \text{Eq. 2.23}$$

where E = electrode potential, E_0 = standard potential of the electrode, R = universal gas constant (8.314 $J \cdot K^{-1} \cdot mol^{-1}$), F = Faraday constant (96485 $C \cdot mol^{-1}$), T = temperature in K, n = charge of the ion or number of electrons participating in the reaction, a = activity of the electroactive species, which in dilute solutions may be approximated to molar concentration.

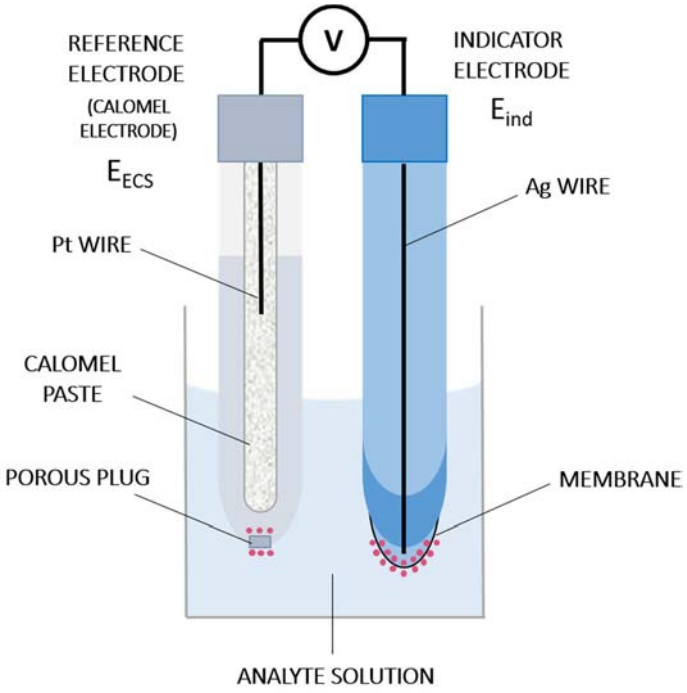

Figure 2.21. Potentiometric measurement system; example for pH measurement (figure adapted from the reference[43]).

Reference electrode is an electrode with known potential which is independent of the analytes concentration or other ions in solution, while the potential of an indicator electrode depends mainly on the concentration of the analytes ions.[43]

Potentiometric measurements enable selective detection of ions in presence of multitude of other substances by using an ion selective electrode.

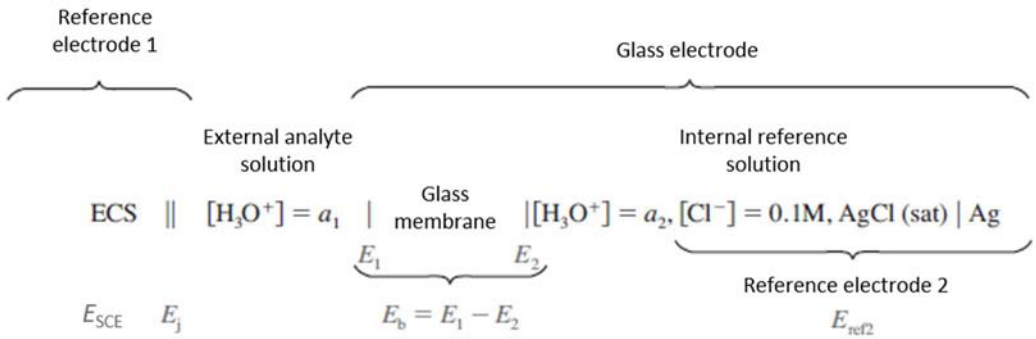

Figure 2.22. Diagram of glass-calomel cell for the measurement of pH. E_{SCE} is the potential of the reference electrode, E_j is the junction potential, a_1 is the activity of hydronium ions in the analyte solution, E_1 and E_2 are the potentials on either side of the glass membrane, E_b is the boundary potential, and a_2 is the activity of hydronium ion in the internal reference solution.[43]

When performing potentiometric measurements, due to the complex nature of overall potential, Nernst equation is often used in form of Eq. 2.24:[32]

$$E_{cell} = K \pm \frac{0.059}{n} \log C \qquad \text{Eq. 2.24}$$

where E_{cell} = overall potential, C = concentration of analyte ions (which can be used instead of activity) and K = constant which includes all remaining potentials in the system (including junction potential and potential of reference electrode). The constant 0.059V includes constant terms from Eq. 2.23 and temperature T = 298.15K. The sign in Eq. 2.24 depends on the ions to be determined: being positive for cations and negative for anions.

In this work, a combined fluoride selective electrode has been used; **Really-Flow™ Solid-State combination fluoride-selective Electrode from Weiss Research** (Figure 2.23), for the measurements of fluoride remaining in solution.

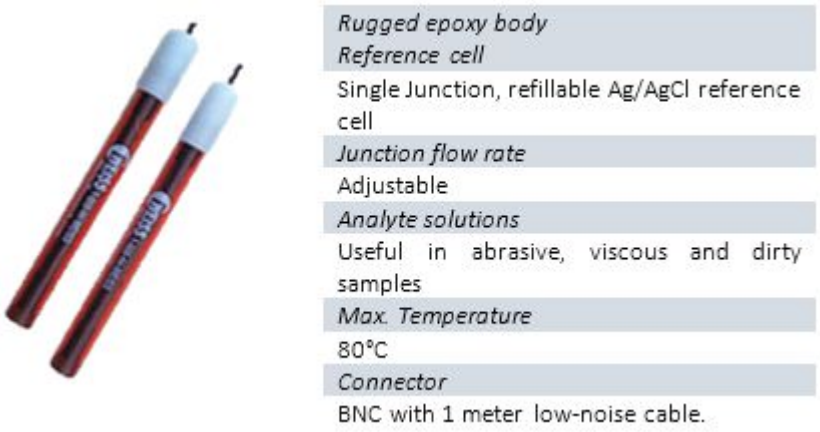

Figure 2.23. The common characteristics and features of combined Ion Selective Electrode.[44]

It is composed by a crystal of LaF_3 sealed into the bottom of a plastic container to produce a fluoride ion electrode. The container is charged with a solution KCl (saturated with AgCl solution) and carries an Ag wire which is coated with AgCl at its lower end: thus, it constitutes an Ag-AgCl reference electrode. The LaF_3 crystal is a conductor for fluoride ions which, being small, can move through the crystal from one lattice defect to another, and equilibrium is established between the crystal face inside the electrode and the internal solution. Likewise, when the electrode is placed in a solution containing fluoride ions, equilibrium is established at the external surface of the crystal. In general, the fluoride concentration at the two faces of the crystal are different and so a potential is established, and since the conditions at the internal face are constant, the resultant potential is proportional to the fluoride ion activity of the tested solution.[32]

To know the free fluoride concentration in solution it is necessary to be related to the potential of the selective electrode (through the Nernst law). In this work, it has been determined by performing

a calibration of the measuring system with solutions of known concentration of the ion (Figure 2.24).

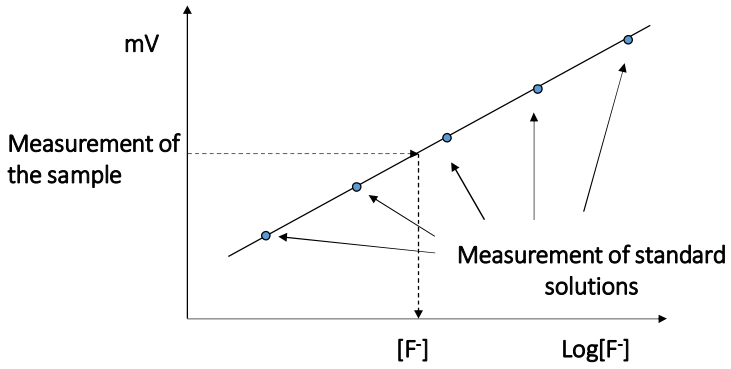

Figure 2.24. Representation of calibration curve used to find the concentration analyte in a sample which a specific potential is measured.

Potentiometric studies for fluoride removal have been done by adding 20mL of 0.5g·L^{-1} HAM suspension into a vessel and then titrating with sodium fluoride (NaF) solution 80mM. 0.5mL of fluoride solution was added to the suspension and once the equilibrium time was expired (1h), the fluoride concentration in solution was measured using the fluoride selective electrode before the consecutive addition. The suspension was kept under stirring during the experiment and in total around 11 additions were made for each experiment.

The experiments were performed in total ionic strength adjustment buffer (TISAB, acetic-acetate buffer solution at pH ~5.5), which was prepared following the procedure described.[45] At the pH fixed by TISAB solution (5.5), the formation of hydrofluoric acid (HF) is negligible and the concentration of hydroxyls (OH^-), the only other anion that the electrode responds to, is insignificant.

Then, potentiometric experiments were fitted both with Langmuir and Freundlich isotherms (see isotherms details in section Langmuir model and Freundlich model).

- Inductively Coupled Plasma Optical Emission Spectrometry

Plasma can be defined as a cloud of highly ionised gas, composed of ions, electrons and neutral particles. In Inductively Coupled Plasma Optical Emission Spectrometry (ICP-OES) the gas, usually argon, is ionised by the influence of a strong electrical field. Plasma sources operate at high temperatures (somewhere between 7000 and 15000K) producing a greater number of excited emitted atoms (especially in the ultraviolet region) than those obtained by the relative low temperatures used in flame emission spectroscopy.[32,43] Further, the plasma source is able to reproduce atomisation conditions with a far greater degree of precision. As a result, spectrum may

be produced for a large number of elements, therefore ICP-OES allows the multi-elemental analysis of a sample in aqueous media. [32,43]

A peristaltic pump carry the sample in the nebulizer, converting such sample into an aerosol in order to be introduced directly inside the plasma flame, as shown in Figure 2.25. There, the sample interacts with electrons and charged ions, dissociating into free atoms which then, losing their electrons, recombines in plasma, emitting radiation at the characteristic wavelengths of the present elements. Such emission is captured by the detector in the UV-Vis region.[43]

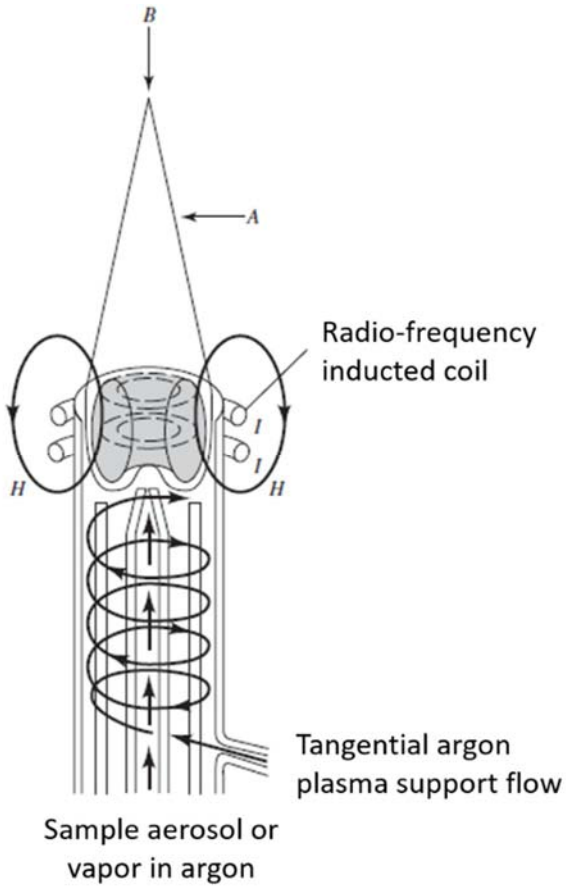

Figure 2.25. Atypical inductively coupled plasma source [43]

In the present work, ICP-OES measurements have been with a **Varian VISTA-MPX CCD Simultaneous ICP-OES** (Figure 2.26) for the measurement of the metal ion concentration (Pb(II), Cr(VI), Cd(II), Hg(II), Ag(I), Pt(IV)) remaining in solution after the adsorption on modified SPION.

Gas flow control
Nebulizer gas 0-1.3 L/min in 0.1 L/min increments (MFC).
Plasma gas 0-22.5 L/min in 1.5 L/min increments.
Auxiliary gas 0-2.25 L/min in 0.75 L/min increments.
Sample introduction
Glass cyclonic-action spraychamber with glass concentric nebulizer and one-piece quartz torch with an extended outer tube that excludes atmospheric gases.
Optic System
Echelle Polychromator
Detector
MPX megapixel CCD detector
Wavelength Range
175-785 nm

Figure 2.26. Image of ICP-OES and its characteristics and features.[46]

The adsorption experiments have been performed at room temperature in batch conditions by mixing 10mL of metal solution, with a concentration within the range of 0.1-1.0mM, with 5mg of functionalized SPION. The suspension was sonicated during 30min and then allowed 30min in contact. After the equilibrium, the magnetic adsorbent was separated from the aqueous phase by decantation with the application of a magnetic field. The remaining solution was then filtered prior the metal ion analysis by ICP-OES. Figure 2.27 shows schematically the procedure of the metal ion adsorption experiments performed.

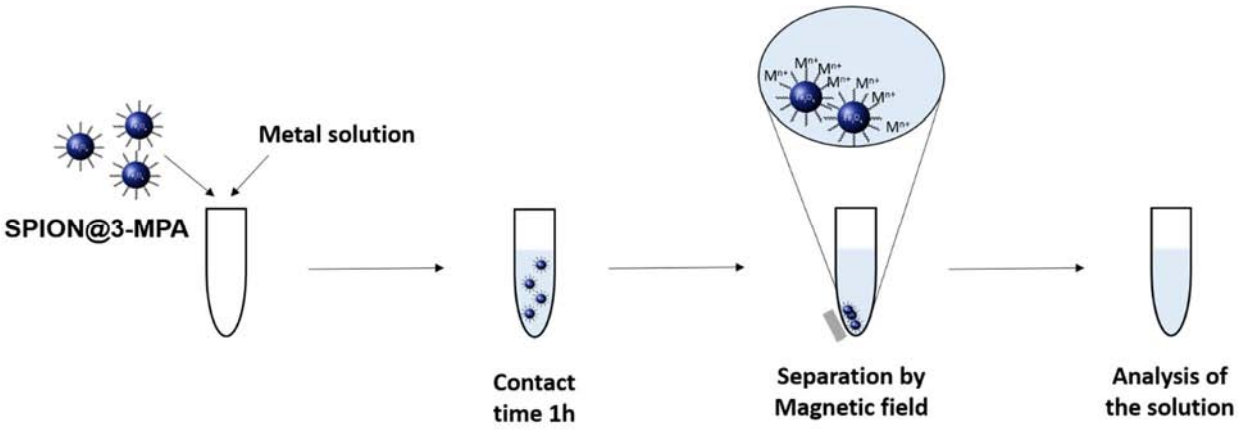

Figure 2.27. Analytical procedure of metal adsorption on functionalized SPION.

The pH selected for the adsorption experiments of Pb(II), Cr(VI), Cd(II), Hg(II) and Ag(I) was 5 (acetic-acetate buffer solution 20mM at pH ~5, prepared in milliQ water). At higher pH (pH > 5) the metals may hydrolyse up to precipitate the corresponding hydroxide ($M(OH)_n$). On the other hand, at pH extremely acidic, the surface of the adsorbent material would be highly protonated inhibiting the adsorption due to electrostatic repulsions. Therefore, pH~ 5 seems to be the best pH for the adsorption experiments. The metal solutions have been obtained by the dissolution of the corresponding metal salts with the prepared buffer solution.

Adsorption experiments for Pt(IV) have been performed in HCl media at pH = 3 (in milliQ water). As it can be appreciated from the speciation of chloroplatinate (Figure 2.28), at pH > 3.5 the chloro-complex of Pt(IV) hydrolyses while at pH < 2 the magnetic particles could dissolve.

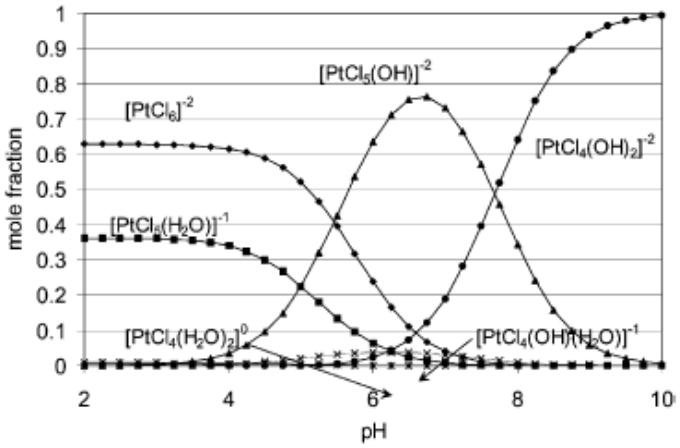

Figure 2.28. Pt speciation from pathway and formation dissociation constants of Stillen and Martell.[47]

Finally, experimental data were fitted both Langmuir and Freundlich isotherms, as specified in section Langmuir model and Freundlich model, to find the adsorption parameters of metal ion adsorption on modified SPION.

- Isothermal Titration Calorimetry

Isothermal Titration Calorimetry (ITC) is a technique which allows measure the heat exchanged in a chemical, physical or biological process.[48] Microcalorimetry does not require that a sample has a particular characteristic (absorption spectrum…) to enable measurement. This technique allows a direct and continuous measurement of the system under study, giving real-time data continuously as the process proceeds.[49] The instrument may operate in two different modes; heat flow mode or power compensation mode.

In the heat flow mode, the heat produced or consumed by the reaction is channelling from the sample through the heat flow sensors comprised of thermoelectric modules. When a temperature gradient is imposed across the thermoelectric module, a voltage is created in accordance with the Seebeck effect.[50] This voltage is proportional to the heat flow through the thermoelectric module and hence, proportional to the rate of heat production or consumption by the sample. One side of the thermoelectric module is in contact with the sample and the other is kept isothermal by a heat sink which is in contact with the TAM III thermostat. All the heat flow calorimeters are of the twin type, consisting of both a sample and a reference side. The measured property is the difference in heat flow between sample and reference. The twin principle reduces baseline noise by eliminating any small fluctuations of the thermostat.[49]

In the power compensation mode, a constant electrical power is applied to the calibration heaters of the sample and reference sides of the calorimeter. If the temperature of the sample increases or decreases due to a reaction or physical event, the heater on the sample side is compensated to keep the sample and reference at the same temperature. The power compensation mode results in a much faster response time making the calorimeters ideal for high resolution while monitoring rapid processes.[49]

ITC experiments have been carried out with a **TAM III thermostat (TA Instruments)** (Figure 2.29) **equipped with a nanocalorimeter** (Figure 2.30) **and an automatic titration syringe**.

Thermostat Specifications	
Thermal media	Oil
Temperature Range	15 to 150°C
Accuracy	< ± 0.1°C
Long Term Stability	< ± 100 µK/24h
Short Terms Stability	< ± 10 µK (p-p)
Scanning Rate	< ± 2°C/h (between 20-150°C)
Calorimeter Specifications	
Short term noise	< ± 10nW
Baseline drift	< ± 40nW/24h
Accuracy	< 2%
Precision	± 100nW

Figure 2.29. TAM III instrument and its specifications.[49]

The TAM III thermostat is a liquid-based system, utilizing a mineral oil to quickly dissipate heat and minimize temperature gradients in the system. In the experiments, the liquid thermostat is maintained at constant temperature for the duration of the experiment. Any heat generated or adsorbed by the sample is continuously measured. Isothermal measurements give quantitative and continuous data reflecting the rate of the system under study.[49]

ITC has been hitherto widely used for the study of chemical equilibria in solution[51–55] and biomolecular interactions,[56] while only a limited number of examples of its application in adsorption studies can be found in the literature.[57–61] In the present work, ICT has been used to measure the exchanged heat reaction of the adsorption of (i) fluoride on HAM and (ii) heavy and precious metals, including Pb(II), Cr(VI), Cd(II), Hg(II), Ag(I) and Pt(IV), on modified SPION.

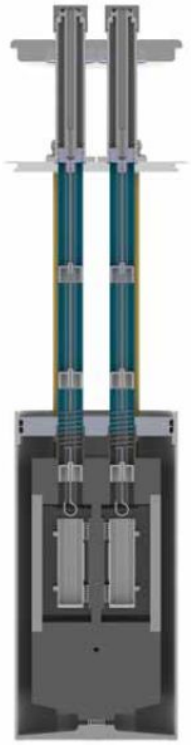

Figure 2.30. Picture of the TAM III nanocalorimeter.[49]

In fluoride adsorption experiments, the samples and the standard solutions have been prepared in TISAB buffer. The sample was stirred continuously at 90rpm and the reference cell was filled with 0.8 mL of distilled water throughout all experiments. About 10 additions of 17.5µL of 80mM fluoride solution were added to 0.7mL of ~0.5g·L^{-1} HAM suspension. The delay time between two consecutive injections was set to 60 min, which was long enough to let the system to reach thermal equilibrium.

In metal ion adsorption experiments, the samples were prepared in acetic-acetate buffer solutions (pH 5). About 14 additions of 14µL of metal ion solution 5mM were added to 0.7mL of ~0.5g·L^{-1} modified SPION suspension stirred continuously at 120rpm. The delay time between the consecutive injections was 1h for all metals except for Pt(IV), which, because of its slow kinetics, needed 2 hours to reach the equilibrium. The reference cell was filled with 0.8 mL of distilled water throughout all experiments.

2.5. ADSORPTION THERMODYNAMICS

The Langmuir constant (*b*) may be used to estimate the thermodynamic parameters Gibbs free energy (ΔG_{ads}), change in enthalpy (ΔH_{ads}), and change in entropy (ΔS_{ads}).

The free energy of adsorption can be related with the Langmuir equilibrium constant, *b*, by the following expression (Eq. 2.25):[62]

$$\Delta G = -RT \ln b \qquad \text{Eq. 2.25}$$

where R is the universal gas constant (8.314 J mol^{-1} K^{-1}).

Enthalpy and entropy changes are also related to the Langmuir constant by the van't Hoff equation (Eq. 2.26):[62]

$$\ln b = \frac{\Delta S_{ads}}{R} - \frac{\Delta H_{ads}}{RT} \qquad \text{Eq. 2.26}$$

Thereby, a plot of ln*b* versus 1/T should be a straight line. ΔH_{ads} and ΔS_{ads} values could be obtained from the slope and intercept of this plot. However, as observed in the Introduction chapter (section General thermodynamic considerations), ΔH_{ads} values calculated by plotting the adsorption constant versus 1/T, provides uncertain and scattered values for the thermodynamic parameter.

In the majority of adsorption studies, the enthalpy associated to de adsorption process has been calculated by van't Hoff equation,[63–65] using the temperature dependence of the Langmuir adsorption constant (Eq. 2.26). However, many studies revealed serious discrepancies between enthalpy values obtained directly from Isothermal Titration Calorimetry (ITC) and from van't Hoff equation and evidenced the large uncertainties associated to the latter method.[59,66–69]

In this work, ITC is applied for the first time to obtain direct determination of ΔH_{ads} for fluoride ion adsorption by HAM and metal ions adsorption on modified SPION, to provide independent and robust thermodynamic parameters.

The values of *b* and Q_{max} obtained by Langmuir isotherm from potentiometric or ICP-OES data have been used to calculate C_e for each titrant addition by numerically solving by Eq. 2.21 in the experimental conditions of the calorimetric titrations. The ΔH_{ads} (kJ mol^{-1}) value has been calculated to best fit the experimental heat for the analytes adsorption according to the modified isotherm[70] (Eq. 2.27) shown below:

$$q_{cum} = \frac{Q_{max} b C_e}{1 + b C_e} \Delta H_{ads} \qquad \text{Eq. 2.27}$$

where: q_{cum} = total heat involved in the reaction per gram of adsorbent (kJ·g^{-1}). Dilution heat (q_{dil}) was also determined to correct the total heat measured (q_{meas}) by the instrument. Thereby $q_{cum} = q_{meas} - q_{dil}$, represents only the heat involved on the adsorption reaction. Statistical analysis of the results has been done with the Solverstat utility for MS-Excel and related tools.[71,72]

2.6. REFERENCES

(1) Cai, W.; Yu, J.; Mann, S. Template-Free Hydrothermal Fabrication of Hierarchically Organized ɣ-AlOOH Hollow Microspheres. *Microporous Mesoporous Mater.* 2009, *122* (1–3), 42–47.

(2) Wu, X.; Zhang, B.; Hu, Z. Microwave Hydrothermal Synthesis of Boehmite Hollow Microspheres. *Mater. Lett.* 2012, *73*, 169–171.

(3) Wu, X.; Zhang, B.; Hu, Z. Microwave Hydrothermal Synthesis of Core-Shell Structured Boehmite. *Mater. Lett.* 2013, *91*, 249–251.

(4) Operation Manual Mars 5. CEM corporation: Mathews, North Carolina 1999.

(5) Uheida, A.; Iglesias, M.; Fontàs, C.; Hidalgo, M.; Salvadó, V.; Zhang, Y.; Muhammed, M. Sorption of Palladium (II), Rhodium (III), and Platinum (IV) on Fe3O4 Nanoparticles. *J. Colloid Interface Sci.* 2006, *301*, 402–408.

(6) Morillo, D.; Uheida, A.; Pérez, G.; Muhammed, M.; Valiente, M. Arsenate Removal with 3-Mercaptopropanoic Acid-Coated Superparamagnetic Iron Oxide Nanoparticles. *J. Colloid Interface Sci.* 2015, *438*, 227–234.

(7) Yean, S.; Cong, L.; Yavuz, C. T.; Mayo, J. T.; Yu, W. W.; Kan, A. T.; Colvin, V. L.; Tomson, M. B. Effect of Magnetite Particle Size on Adsorption and Desorption of Arsenite and Arsenate. *J. Mater. Res.* 2005, *20* (12), 3255–3264.

(8) Mamani, J. B.; Costa-Filho, A. J.; Cornejo, D. R.; Vieira, E. D.; Gamarra, L. F. Synthesis and Characterization of Magnetite Nanoparticles Coated with Lauric Acid. *Mater. Charact.* 2013, *81*, 28–36.

(9) Li, L.; Mak, K. Y.; Leung, C. W.; Chan, K. Y.; Chan, W. K.; Zhong, W.; Pong, P. W. T. Effect of Synthesis Conditions on the Properties of Citric-Acid Coated Iron Oxide Nanoparticles. *Microelectron. Eng. J.* 2013, *110* (11), 329–334.

(10) Warner, C. L.; Addleman, R. S.; Cinson, A. D.; Droubay, T. C.; Engelhard, M. H.; Nash, M. A.; Yantasee, W.; Warner, M. G. High-Performance, Superparamagnetic, Nanoparticle-Based Heavy Metal Sorbents for Removal of Contaminants from Natural Waters. *ChemSusChem* 2010, *3* (6), 749–757.

(11) *Scanning Microscopy for Nanotechnology*; Zhou, W., Wang, Z. L., Eds.; Springer Science+Business Media, LLC, 2006.

(12) Kalantar-zadeh, K.; Fry, B. *Nanotechnology-Enabled Sensors*; Springer Science+Business Media, LLC, 2008.

(13) Merlin | Servei de Microscòpia http://sct.uab.cat/microscopia/content/merlin (accessed May 21, 2016).

(14) Williams, D. B.; Carter, C. B. *The Transmission Electron Microscope*; Springer US: Boston, MA, 2009.

(15) JEM-2011 | Servei de Microscòpia http://sct.uab.cat/microscopia/content/jem-2011 (accessed May 21, 2016).

(16) Rodríguez Gallego, M. *La Difracción de Los Rayos X*; Alhambra: Madrid, 1982.

(17) Difracció de pols | Servei Difracció Raigs X

http://sct.uab.cat/sdrx/content/difracci%25C3%25B3-de-pols (accessed May 21, 2016).

(18) Lowell, S.; Shields, J. E.; Thomas, M. A.; Thommes, M. *Characterization of Porous Solids and Powders: Surface Area, Pore Size and Density*; Particle Technology Series; Springer Science+Business Media: New York, 2004.

(19) Sing, K. S. W.; Everett, D. H.; Haul, R. A. W.; Moscou, L.; Pierotti, R. A.; Rouquerol, J.; Siemieniewska, T. Reporting Physisorption Data for gas/Solid Systems with Special Reference to the Determination of Surface Area and Porosity. *Pure Appl. Chem.* 1985, *57* (4), 603–619.

(20) Thommes, M.; Kaneko, K.; Neimark, A. V.; Olivier, J. P.; Rodriguez-Reinoso, F.; Rouquerol, J.; Sing, K. S. W. Physisorption of Gases, with Special Reference to the Evaluation of Surface Area and Pore Size Distribution (IUPAC Technical Report). *Pure Appl. Chem.* 2015, *87* (9–10), 1051–1069.

(21) Brunauer, S.; Emmett, P. H.; Teller, E. Adsorption of Gases in Multimolecular Layers. *J. Am. Chem. Soc.* 1938, *60* (2), 309–319.

(22) Rouquerol, F.; Rouquerol, J.; Sing, K. *Adsorption by Powders and Porous Solids: Principles, Methodology and Applications.*; Academic Press: London, 1999.

(23) S. Lowell; J. E. Shields. *Powder Surface Area and Porosity*, Third Edit.; Scarlett, B., Ed.; Springer Science+Business Media, B.V., 1991.

(24) Kaneko, K. Determination of Pore Size and Pore Size Distribution 1. Adsorbents and Catalysts. *J. Memb. Sci.* 1994, *96*, 59–89.

(25) Groen, J. C.; Peffer, L. A. A.; Pérez-Ramírez, J. Pore Size Determination in Modified Micro- and Mesoporous Materials. Pitfalls and Limitations in Gas Adsorption Data Analysis. *Microporous Mesoporous Mater.* 2003, *60*, 1–17.

(26) Tristar 3000 Operator's Manual V6.08. Micromeritics Instrument Corporation 2007.

(27) understanding-qels-dynamic-light-scattering | theory | library http://www.wyatt.com/library/theory/dynamic-light-scattering-theory.html (accessed Aug 7, 2016).

(28) Berne, B. J.; Pecora, R. *Dynamic Light Scattering with Applications to Chemsitry, Biology, and Physics*; John Wiley & Sons, Inc., 1976.

(29) Dynamic Light Scattering Particle Size Analyzer LB-550. Insruction Manual. HORIBA Ltd.: Japan 2003.

(30) LB-500/550 - HORIBA http://www.horiba.com/scientific/products/particle-characterization/download-center/instrument-support/lb-500550/ (accessed Aug 16, 2016).

(31) Wendlandt, W. W. *Thermal Analysis*; Wiley, 1986.

(32) Vogel, A. I. *Textbook of Quantitative Chemical Analysis*; Prentice Hall, 1989.

(33) Lin-Vien, D.; Colthup, N. B.; Fateley, W. G.; Grasselli, J. G. *The Handbook of Infrared and Raman Characteristic Frequencies of Organic Molecules*; Academic Press Limited, 1991.

(34) Bruker: Overview https://www.bruker.com/es/products/infrared-near-infrared-and-

raman-spectroscopy/ft-ir/ft-ir-accessories/platinum-atr/overview.html.

(35) Worch, E. *Adsorption Technology in Water Treatment - Fundamentals, Processes, and Modeling*; De Gruyter: Berlin/Boston, 2012.

(36) Kumar, E.; Bhatnagar, A.; Kumar, U.; Sillanpää, M. Defluoridation from Aqueous Solutions by Nano-Alumina: Characterization and Sorption Studies. *J. Hazard. Mater.* 2011, *186* (2–3), 1042–1049.

(37) Madrakian, T.; Afkhami, A.; Zadpour, B.; Ahmadi, M. New Synthetic Mercaptoethylamino Homopolymer-Modified Maghemite Nanoparticles for Effective Removal of Some Heavy Metal Ions from Aqueous Solution. *J. Ind. Eng. Chem.* 2015, *21*, 1160–1166.

(38) Kammerer, J.; Carle, R.; Kammerer, D. R. Adsorption and Ion Exchange: Basic Principles and Their Application in Food Processing. *J. Agric. Food Chem.* 2011, *59* (1), 22–42.

(39) Foo, K. Y.; Hameed, B. H. Insights into the Modeling of Adsorption Isotherm Systems. *Chem. Eng. J.* 2010, *156* (1), 2–10.

(40) Rangabhashiyam, S.; Anu, N.; Giri Nandagopal, M. S.; Selvaraju, N. Relevance of Isotherm Models in Biosorption of Pollutants by Agricultural Byproducts. *J. Environ. Chem. Eng.* 2014, *2* (1), 398–414.

(41) Limousin, G.; Gaudet, J. P.; Charlet, L.; Szenknect, S.; Barthès, V.; Krimissa, M. Sorption Isotherms: A Review on Physical Bases, Modeling and Measurement. *Appl. Geochemistry* 2007, *22*, 249–275.

(42) Sandocal-Ibarra, F. D.; López-Cervantes, J. L.; Garcia-Fadrique, J. Ecuación de Langmuir En Líquidos Simples Y Tensioactivos. *Educ. Química* 2016, *26*, 307–313.

(43) Skoog, D. A.; Holler, F. J.; Crouch, S. R. *Principios de Análisis Instrumental*, Sixth edit.; McGraw-Hill, 2008.

(44) Weiss Electrode Catalog. Weiss Research, Inc.: Houston, Texas 2013.

(45) Tripathy, S. S.; Bersillon, J. L.; Gopal, K. Removal of Fluoride from Drinking Water by Adsorption onto Alum-Impregnated Activated Alumina. *Sep. Purif. Technol.* 2006, *50*, 310–317.

(46) Varian Vista-MPX CCD Simultaneous ICP-OES. Varian Analytical Instruments.

(47) Spieker, W. A.; Liu, J.; Miller, J. T.; Kropf, A. J.; Regalbuto, J. R. An EXAFS Study of the Co-Ordination Chemistry of Hydrogen hexachloroplatinate(IV): 1. Speciation in Aqueous Solution. *Appl. Catal. A Gen.* 2002, *232* (1–2), 219–235.

(48) Wiseman, T.; Williston, S.; Brandts, J. F.; Lin, L. N. Rapid Measurement of Binding Constants and Heats of Binding Using a New Titration Calorimetr. *Anal.Biochem.* 1989, *179* (1), 131–137.

(49) TA Instruments Microcalorimetry. TA Instruments 2012.

(50) J. Di Salvo, F. Thermoelectric Cooling and Power Generation. *Science (80-.).* 1999, *285* (5428), 703–706.

(51) Cavallo, L.; Del Piero, S.; Ducéré, J.; Fedele, R.; Melchior, A.; Morini, G.; Piemontesi, F.; Tolazzi, M. Key Interactions in Heterogeneous Ziegler - Natta Catalytic Systems : Structure

and. *J. Phys. Chem. C* 2007, *111*, 4412–4419.

(52) Endrizzi, F.; Melchior, A.; Tolazzi, M.; Rao, L. Complexation of uranium(VI) with Glutarimidoxioxime: Thermodynamic and Computational Studies. *Dalt. Trans.* 2015, *44* (31), 13835–13844.

(53) Melchior, A.; Peralta, E.; Valiente, M.; Tavagnacco, C.; Endrizzi, F.; Tolazzi, M. Interaction of d(10) Metal Ions with Thioether Ligands: A Thermodynamic and Theoretical Study. *Dalton Trans.* 2013, *42* (17), 6074–6082.

(54) Bernardo, P. Di; Zanonato, P. L.; Melchior, A.; Portanova, R.; Tolazzi, M.; Choppin, G. R.; Wang, Z. Thermodynamic and Spectroscopic Studies of Lanthanides (III) Complexation with Polyamines in Dimethyl Sulfoxide. *Inorg. Chem.* 2008, *47* (3), 1155–1164.

(55) Di Bernardo, P.; Zanonato, P. L.; Benetollo, F.; Melchior, A.; Tolazzi, M.; Rao, L. Energetics and Structure of uranium(VI)-Acetate Complexes in Dimethyl Sulfoxide. *Inorg. Chem.* 2012, *51* (16), 9045–9055.

(56) *Biocalorimetry 2: Applications of Calorimetry in the Biological Sciences*; Ladbury, J. E., Doyle, M. L., Eds.; John Wiley & Sons, Inc., 2004.

(57) Strayer, M. E.; Binz, J. M.; Tanase, M.; Shahri, S. M. K.; Sharma, R.; Rioux, R. M.; Mallouk, T. E. Interfacial Bonding Stabilizes Rhodium and Rhodium Oxide Nanoparticles on Layered Nb Oxide and Ta Oxide Supports. *J. Am. Chem. Soc.* 2014, *136* (15), 5687–5696.

(58) Arakaki, L. N. H.; da Fonseca, M. G.; da Silva Filho, E. C.; de M. Alves, A. P.; de Sousa, K. S.; Silva, A. L. P. Extraction of Pb(II), Cd(II), and Hg(II) from Aqueous Solution by Nitrogen and Thiol Functionality Grafted to Silica Gel Measured by Calorimetry. *Thermochim. Acta* 2006, *450* (1–2), 12–15.

(59) Welsch, N.; Lu, Y.; Dzubiella, J.; Ballauff, M. Adsorption of Proteins to Functional Polymeric Nanoparticles. *Polymer (Guildf).* 2013, *54*, 2835–2849.

(60) Braga, P. R. S.; Costa, A. A.; de Macedo, J. L.; Ghesti, G. F.; de Souza, M. P.; Dias, J. A.; Dias, S. C. L. Liquid Phase Calorimetric-Adsorption Analysis of Si-MCM-41: Evidence of Strong Hydrogen-Bonding Sites. *Microporous Mesoporous Mater.* 2011, *139* (1–3), 74–80.

(61) Drago, R. S.; Dias, S. C.; Torrealba, M.; de Lima, L. Calorimetric and Spectroscopic Investigation of the Acidity of HZSM-5. *J. Am. Chem. Soc.* 1997, *119* (19), 4444–4452.

(62) *Handbook of Research on Diverse Applications of Nanotechnology in Biomedicine, Chemistry, and Engineering*; Soni, S., Salhotra, A., Suar, M., Eds.; IGI Global: Hershey, PA, 2015.

(63) Gong, W. X.; Qu, J. H.; Liu, R. P.; Lan, H. C. Adsorption of Fluoride onto Different Types of Aluminas. *Chem. Eng. J.* 2012, *189–190*, 126–133.

(64) Elwakeel, K. Z.; El-Sayed, G. O.; Darweesh, R. S. Fast and Selective Removal of silver(I) from Aqueous Media by Modified Chitosan Resins. *Int. J. Miner. Process.* 2013, *120*, 26–34.

(65) Liang, X.; Xu, Y.; Sun, G.; Wang, L.; Sun, Y.; Sun, Y.; Qin, X. Preparation and Characterization of Mercapto Functionalized Sepiolite and Their Application for Sorption of Lead and Cadmium. *Chem. Eng. J.* 2011, *174* (1), 436–444.

(66) Liu, Y.; Sturtevant, J. M. Significant Discrepancies between Van't Hoff and Calorimetric

Enthalpies. II. *Protein Sci.* 1995, *4* (12), 2559–2561.

(67) Chaires, J. B. Possible Origin of Differences between Van't Hoff and Calorimetric Enthalpy Estimates. *Biophys. Chem.* 1997, *64* (1–3), 15–23.

(68) Liu, Y.; Sturtevant, J. M. Significant Discrepancies between Van't Hoff and Calorimetric. III. *Biophys. Chem.* 1997, *64*, 121–126.

(69) Mizoue, L. S.; Tellinghuisen, J. Calorimetric vs. Van't Hoff Binding Enthalpies from Isothermal Titration Calorimetry: Ba2+-Crown Ether Complexation. *Biophys. Chem.* 2004, *110* (1–2), 15–24.

(70) Chronister, C. W.; Drago, R. S. Determination of Hydrogen-Bonding Acid Sites on Silica Using the Cal-Ad Method. *J. Am. Chem. Soc.* 1993, *115* (12), 4793–4798.

(71) Comuzzi, C.; Polese, P.; Melchior, A.; Portanova, R.; Tolazzi, M. SOLVERSTAT: A New Utility for Multipurpose Analysis. An Application to the Investigation of Dioxygenated Co(II) Complex Formation in Dimethylsulfoxide Solution. *Talanta* 2003, *59* (1), 67–80.

(72) del Piero, S.; Melchior, A.; Polese, P.; Portanova, R.; Tolazzi, M. A Novel Multipurpose Excel Tool for Equilibrium Speciation Based on Newton-Raphson Method and on a Hybrid Genetic Algorithm. *Ann. Chim.* 2006, *96* (1–2), 29–49.

3. RESULTS AND DISCUSSION

3. RESULTS AND DISCUSSION

In this chapter, the results obtained during the thesis experiments are organized in two main sections, including:

(i) The characterization of HAM and the adsorption studies for fluoride removal

(ii) Functionalized SPION characterization and adsorption studies of metals as Pb(II), Cr(VI), Cd(II), Hg(II), Ag(I) and Pt(IV).

The obtained results are described as follow.

3.2. FLUORIDE REMOVAL BY HIERARCHICAL ALUMINA MICROSPHERES

The current section describes the results obtained in the study performed for the adsorption of fluoride on HAM, from the characterization of the synthesized adsorbent material until the description of the adsorption process in terms of loading capacity and thermodynamic parameters. Figure 3.1 represents a scheme of the content of the current section.

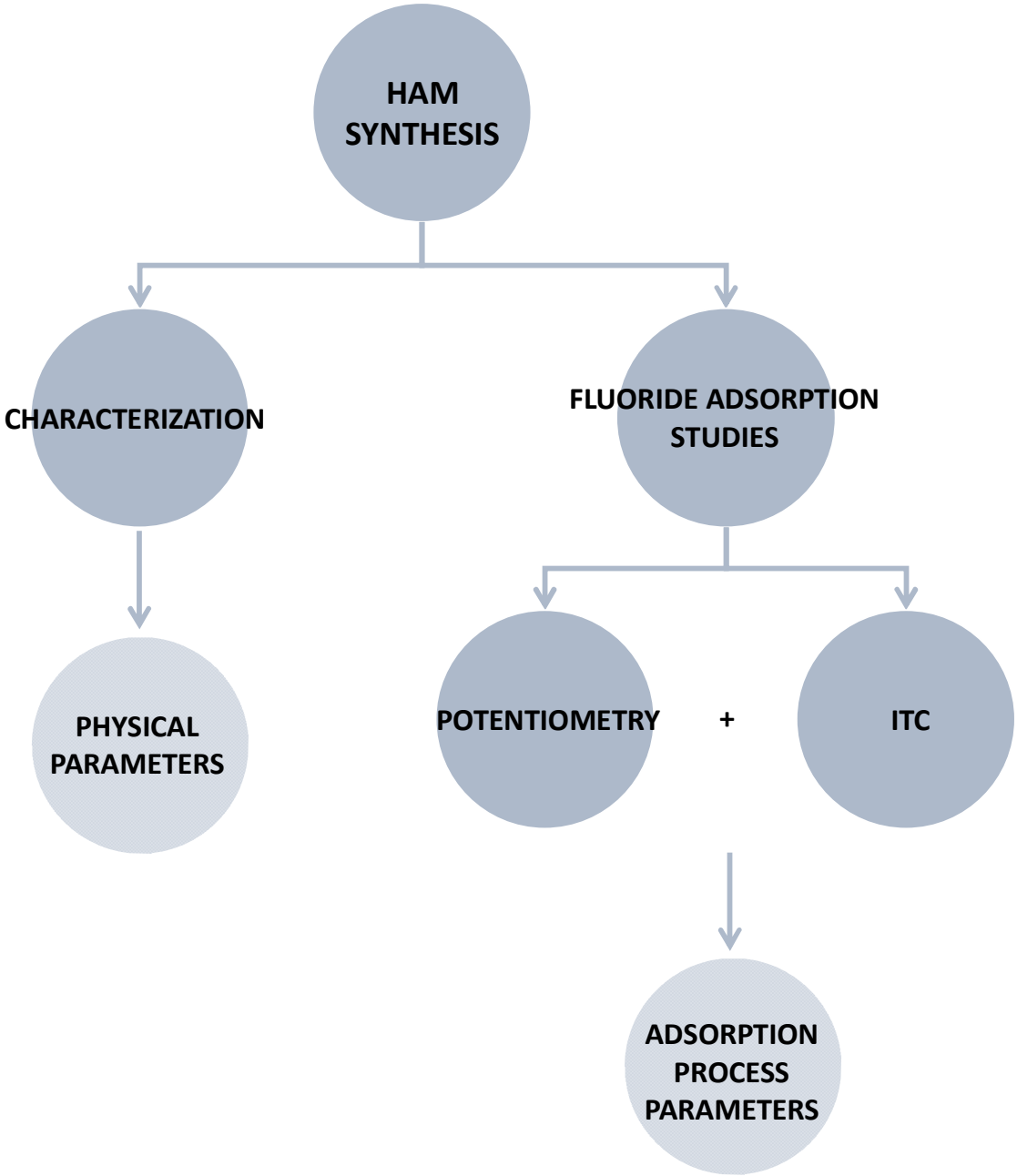

Figure 3.1. Scheme of the performed work for the study of fluoride adsorption on HAM.

3.2.1. Characterization of the Adsorbent Material

The physical features obtained for the synthesized HAM are described below. Such information is of great importance for understanding the behaviour of the adsorbent material for fluoride adsorption. In the present work, the characterization results of the material includes the description of the morphology by SEM and TEM, the distribution of the particles in solution by DLS, the corresponding surface area and porous size by BET and porosimetry, the crystallinity of the material by DRX and the charge of the surface by the study of the pH_{pzc}.

As mentioned in methodology chapter, two different kinds of HAM have been synthesized by varying the time of the microwave treatment, being 3 minutes for HAM type A and 20 min for HAM type B. The description and differences of both materials are described in the following section.

- Scanning Electron and Transmission Electron Microscopy

The characterization of the morphology of the obtained HAM type A and type B have been provided by SEM and TEM, and the corresponding micrographs are shown in **Errore. L'origine riferimento non è stata trovata.**. SEM analysis provides information about the characteristics of the surface along with information about the structure of the synthesized material. TEM allows the evaluation of the shape and size of the material.

Errore. L'origine riferimento non è stata trovata. A-i and B-i show the SEM micrographs obtained for the two kinds of HAM (type A and type B). As revealed in the images, HAM type A and type B present a flower-like hollow microspheres with a highly textured surface and smooth inner wall surface. The microspheres have a diameter of ~0.9µm, which is significantly smaller than those obtained by the published methodology (5µm).[1] The TEM images in **Errore. L'origine riferimento non è stata trovata.** A-ii and B-ii confirmed the texture of the shell wall observed in SEM analysis. They show a magnification of the particles, revealing that the spheres consist in a low cavity with a diameter about 800nm composed by the randomly aggregation of nanoplatelets. The detailed images given in **Errore. L'origine riferimento non è stata trovata.** A-iii and B-iii, evidence that the hierarchical structure of the microspheres is formed by packing of nanoplatelets about 200nm length and thin thickness. In Figure 1 A-iv and B-iv an enlargement of the nanoplatelets evidencing their smooth surface is reported.

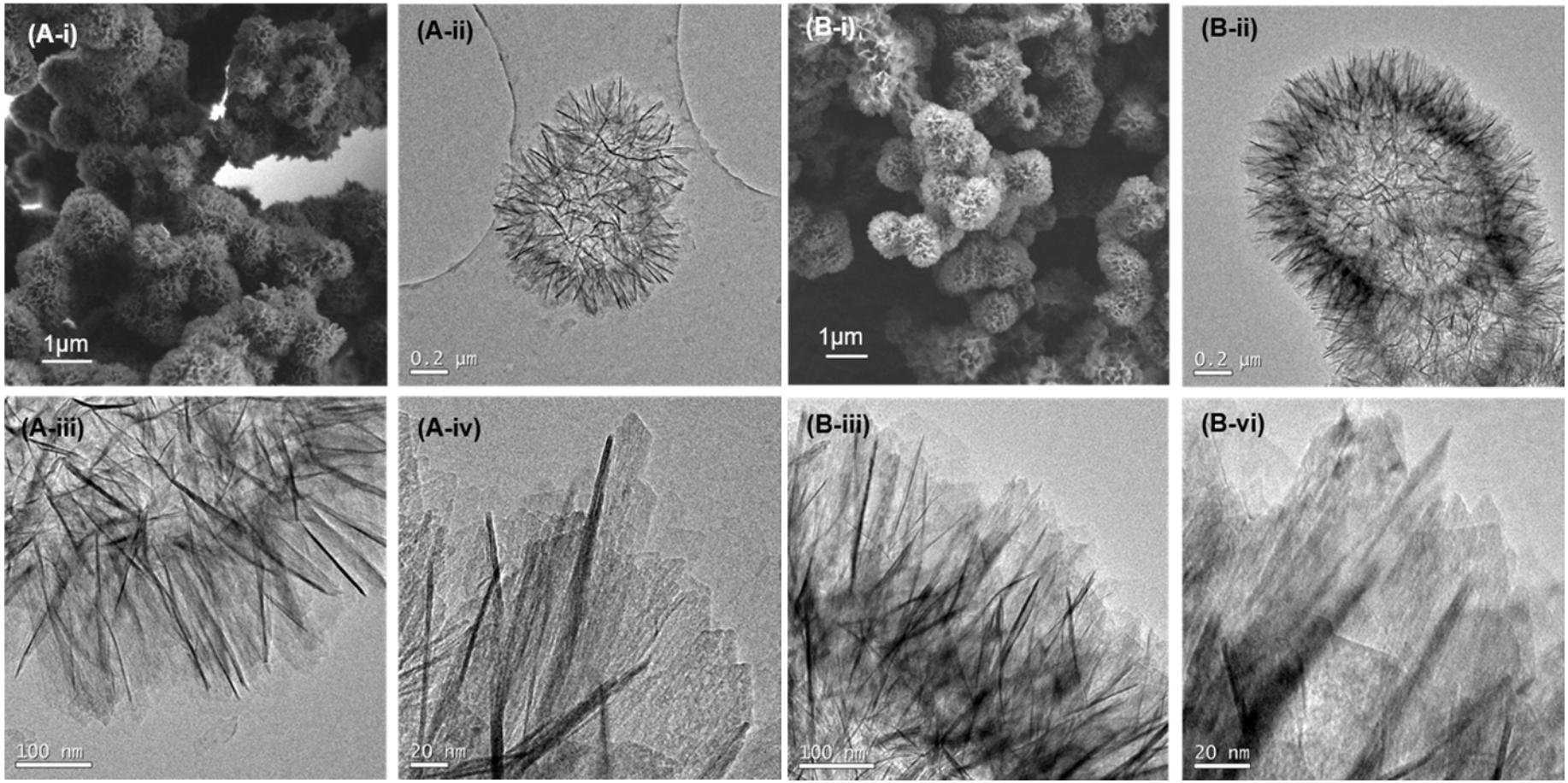

Figure 3.2. Morphological images of HAM type A (Fig. 3.2-A) and type B (Fig. 3.2-B) provided by SEM (A-i and B-i) and TEM (A-ii, A-iii, A-iv, B-ii, B-iii and B-iv) analysis.

To understand if there is any morphological change during the calcination of the nanostructured particles synthesized (see chapter methodology, section Synthesis of hierarchical Al_2O_3 microspheres by an analytic microwave oven), SEM and TEM analysis have been performed of HAM prior calcination. In Figure 3.3, representative SEM (Figure 3.3-i) and TEM (Figure 3.3-ii) images of the un-calcined type B HAM are reported.

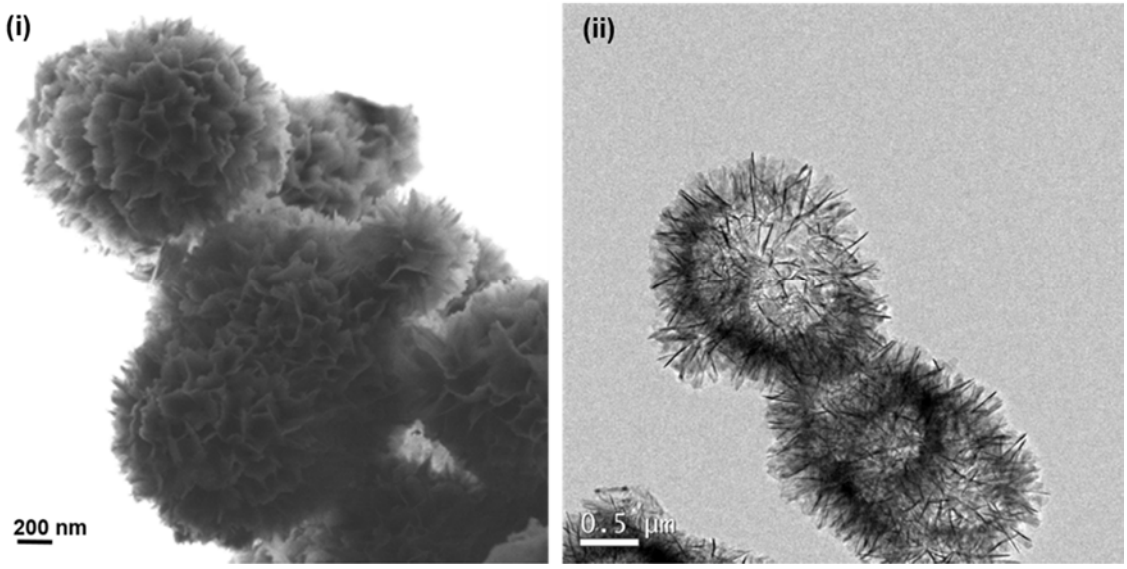

Figure 3.3. SEM (i) and TEM (ii) images of synthesized HAM type B, before calcination process.

It may be observed that uncalcinated HAM have the same characteristic structure of the calcinated material, indicating that hierarchical morphology is stable, even after high temperature treatment, therefore, the characteristic hierarchical structure is formed during the hydrothermal precipitation of the HAM.

As reported in the introduction chapter (section 1.7.2. Nanostructured materials), the small size seems to be an advantage for the effectiveness of the adsorbent materials. Therefore, several additional syntheses have been carried out with the aim to achieve HAM smaller than type A and type B. Table 3.1 summarizes the particle sizes obtained in each synthesis.

Description	Particle size (µm)
Exces of urea	1.0
$Al(NO_3)_3$ as aluminum salt	0.5
Heating cycles	1.7
Varying the volume	1.5
Adding PVP	1.5
Higher temperature	1.5
Higher initial pH	3.7

Table 3.1. Size comparison of the synthesized HAM with some modifications.

As it may be observed, equal or higher sizes have been obtained excepted with the exception of the synthesis with the different aluminium salt as a reactant. However, as appreciated in Figure 3.4, the morphology of the material is completely different. In this case the, nanoplatelets have been obtained without hierarchically assembling, as observed in previous works.[1,2]

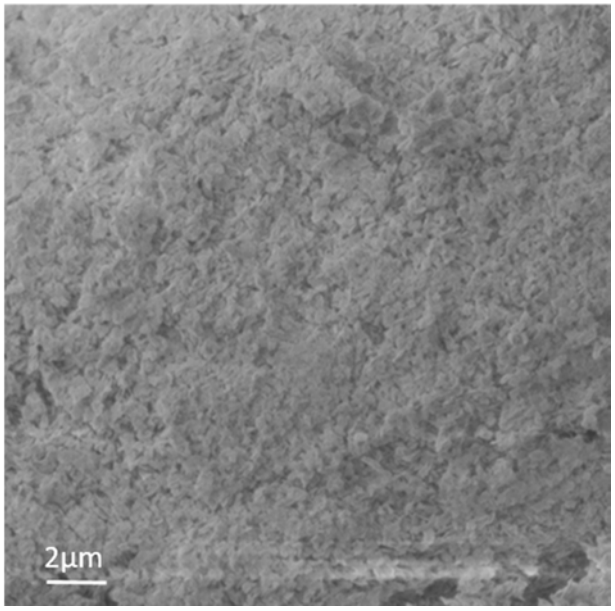

Figure 3.4. SEM images of HAM synthesized with a different aluminium salt.

The controlled synthesis of hierarchical structures is a key challenge in materials chemistry : in the particular case of hierarchical alumina microspheres, it is demonstrated in the literature that the presence of sulfate ions (SO_4^{2-}) is required for the formation of the hierarchical hollow microspheres, where the sulfate-mediated process involves the formation of nanoplatelets followed by cooperative assembly and localized ripening.[1,2] The objective to decrease the spheres size maintaining a proper morphology is not reached in our synthesis, consequently the work has been focused on the initial HAM type A and type B.

- Surface characterization

The N_2 adsorption and porosimetry studies are of great importance giving specific information about the surface of the adsorbent material, the specific surface area and the pore size distribution.

Figure 3.5 presents the adsorption-desorption isotherms. Such isotherm may be classified as Type IV (a),[3] which is characteristic of mesoporous materials[4] (methodology chapter, section N_2 adsorption isotherms at -196 ºC). Therefore, the H3 type-hysteresis loop[5] at high relative pressures; over pressure P/P_o of 0.7 in both types A and B, indicates the presence of mesoporous formed between the assembly of nanoplatelets.[2]

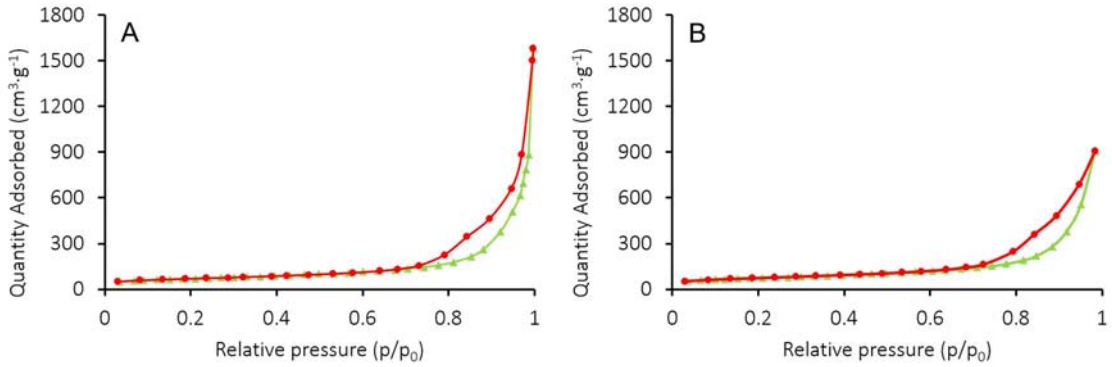

Figure 3.5. N_2 adsorption (green triangles) and desorption (red circles) isotherms of HAM for type A (Figure 2A) and sample B (Figure 2B).

The BET surface areas of HAM type A and type B, as well as the pore size are summarized in Table 3.2.

Adsorbent	Surface area ($m^2\ g^{-1}$)	Pore size (nm)	Pore volume ($cm^3\ g^{-1}$)
HAM type A	254	12.96	1.07
HAM type B	241	25.55	2.32

Table 3.2. Surface characteristics of HAM of type A and B.

A high surface area is obtained, quite similar for both materials, being 254 and 241 $m^2\ g^{-1}$ for type A and B respectively, which will favour the adsorption capacity of fluoride on the synthesized material. As explained in methodology chapter, (section N_2 adsorption isotherms at -196 ºC) a mesoporous material normally contains pores with diameters between 2-50 nm,[4] the pore size was determined to be 12.96 nm with a pore volume of 1.07$cm^3 \cdot g^{-1}$ for sample A and 25.55 nm and 2.32 $cm^3 \cdot g^{-1}$ for sample B, confirming the mesoporosity of our material. Because of the characteristic downy surface of the particles, the synthesized alumina has excellent porous properties and seems to exhibit a great potential for fluoride adsorption.

- Dynamic Light Scattering

The particle size distribution of the two HAM analyzed by DLS is represented in Figure 3.6.
In Figure 3.6-A the HAM suspension of type A show an average diameter between 0.6 and 1µm. This value corresponds approximately with the diameter of the particles, which means that the particles aggregation is almost absent in the working conditions. The distribution of type B is shown in Figure 3.6-B, which indicates an average size larger than type A.

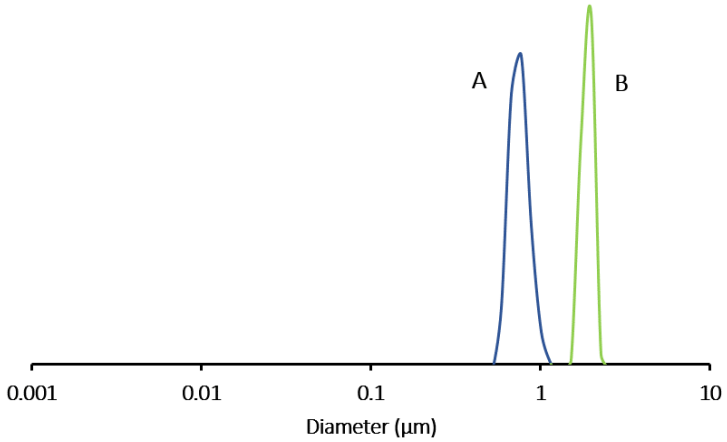

Figure 3.6. Particle size distribution of HAM for type A (blue) and B (green) determined by DLS (suspension in TISAB solution).

- Point of Zero Charge

The pH_{pzc} obtained for both type A and B was 9.0 at different ionic strength (0.1M and 0.01M). Consequently, at working pH = 5.5, the surface of the adsorbent is positively charged which means that the fluoride will be attracted by electrostatic forces, the interaction between alumina surface and the fluoride containing solution may be represented by the following reactions:[6–8]

$$\equiv AlOH + H^{+} \rightarrow AlOH_2^{+} \qquad \text{Eq. 3.1}$$

$$AlOH_2^{+} + F^{-} \rightarrow AlF + H_2O \qquad \text{Eq. 3.2}$$

- X-ray diffraction

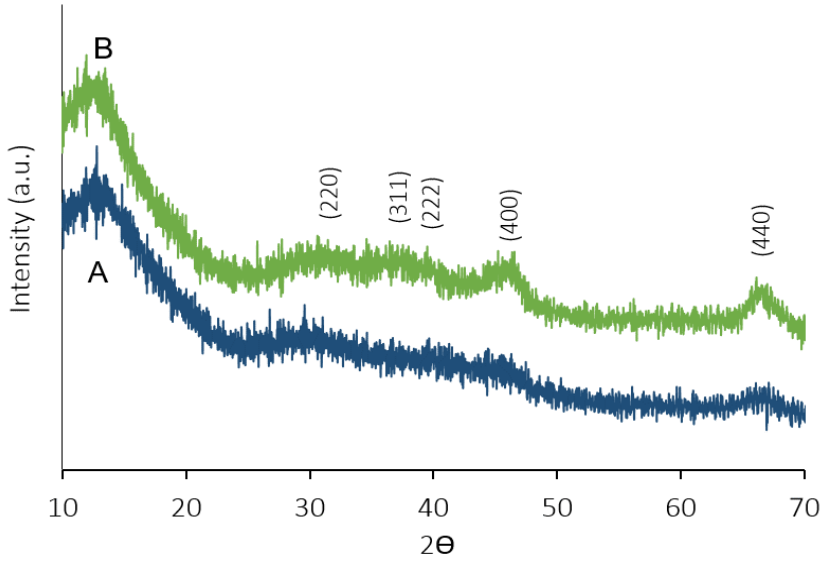

Figure 3.7. X-Ray diffraction (XRD) patterns of HAM for type A (blue) and B (green) samples.

The XRD diffractogram of HAM type A in the Figure 3.7 reveals no clear peaks, indicating that the adsorbent is amorphous. On the contrary, the diffractogram of the analysed microspheres of HAM

type B showed some characteristic peaks for aluminum oxide in accordance with Al_2O_3 reference standard diffractogram (JCDPS card No. 10-0425). However, the low intensity of such peaks evidenced that the material is a poorly crystalline solid.

The DRX study is a crucial factor for the material efficiency analysis, since it has been demonstrated in the literature that the crystallinity of adsorbents has a significant influence on the adsorption capacity of the materials.[9–11]

Adsorbent	Particle size distribution (DLS) (µm)	Surface area ($m^2\ g^{-1}$)	Pore size (nm)	Pore volume ($cm^3\ g^{-1}$)	pH_{zpc}
HAM type A	0.6 – 1.0	254.09	12.96	1.07	9.0
HAM type B	1.5 – 2.6	241.62	25.55	2.32	9.0

Table 3.3. Summary of the characteristics of HAM type A and B.

- In both syntheses (HAM type A and type B), hollow alumina microspheres have been obtained composed by three levels of hierarchical organization: (i) amorphous alumina at the nanoscale, (ii) mesoscale packing of the nanoplatelets in the shell wall, and (iii) assembly of a sphere enclosing an internal cavity of 800nm.
- Both materials have a high surface area, which is an advantage for the adsorption process.
- A higher degree of crystallinity for type B than type A may be observed. As low crystallinity of the alumina base materials seems to be an advantage for their absorption capacity, HAM type A seems to be a more promising material than type B.

3.2.2. Fluoride adsorption studies on hierarchical alumina microspheres

In the following section, the results of the study of fluoride adsorption process on HAM are presented. The adsorption reaction has been characterized in terms of kinetics and thermodynamics.

3.2.2.1. Fluoride adsorption kinetics on HAM (type A)

The kinetics of the adsorption reaction has been measured for an adsorbent dose of 0.5g L^{-1} (type A) and initial concentration of 16mM of fluoride. The fluoride concentration remaining in solution was constantly measured with short intervals of time, at the beginning of the reaction, and between larger intervals, when the reaction was closer to equilibrium state. The obtained experimental data are plotted in Figure 3.8, where the $[F^-]_e/[F^-]_0$ ratio *vs.* time (h) is represented, as well as the fitting with both mono and bi-exponential Eq. 3.3 and Eq. 3.4 respectively. The fitted results are summarized in Table 3.4.

$$[F^-]_e = a_1 e^{-k_1 t} \quad \text{Eq. 3.3}$$

$$[F^-]_e = a_1 e^{-k_1 t} + a_2 e^{-k_2 t} \quad \text{Eq. 3.4}$$

where a_i = initial concentration for each exponential (M), k_i = constant rates (h^{-1}), t = time (h).

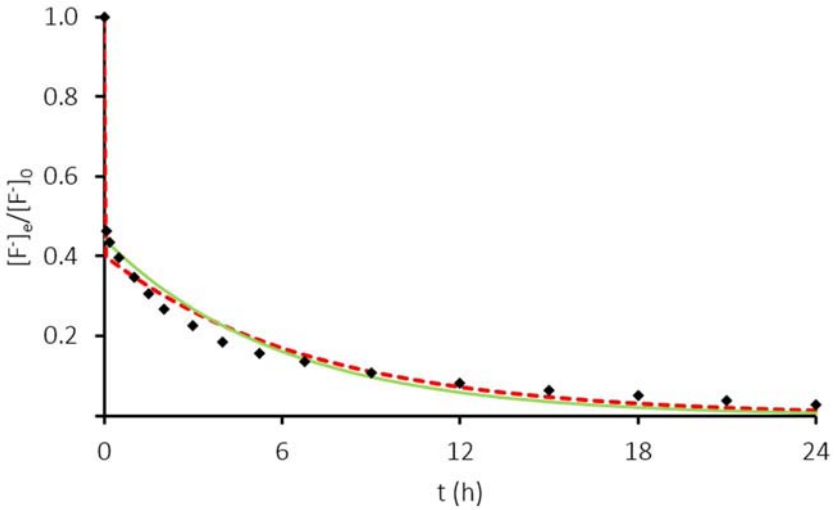

Figure 3.8. Fluoride adsorption kinetics on HAM (type A, 0.5 g·L^{-1}, pH = 5.5, T = 298.15K, $[F^-]_0$ = 16mM) fitted with mono- (green line) and bi- (dashed red line) exponential functions.

As can be observed by the correlation coefficient (R^2), experimental data fits better by bi-exponential model with respect the mono-exponential model, suggesting the presence of a first reaction followed by a much slower adsorption process (k_2 is 3 orders of magnitude lower than k_1, Table 3.4). This phenomenon was also observed by fluoride adsorption on MgAl-CO_3 layered double hydroxides.[12] As it can be appreciated, the first and fast adsorption occurs during the first hour then the rate decreases and after 3 hours only the 25% of the initial fluoride concentration is still present, reaching the equilibrium state in 24h.

Mono-exponential model			Bi-exponential model				
a_1 (M)	k_1 (h^{-1})	R^2	a_1 (M)	k_1 (h^{-1})	a_2 (M)	k_2 (h^{-1})	R^2
7.0	0.17	0.905	9.5	129.99	6.4	0.15	0.982

Table 3.4. Mono and bi-exponential parameters for the first-order kinetic model.

However, as shown in Figure 3.9, the signal measured by ITC, which represents the heat evolved for each addition of fluoride on HAM suspension (for both type A and B), reaches the baseline in 60 minutes. That fact means that the heat exchanged related to the fluoride adsorption on the alumina microspheres expires within one hour.

Although the equilibrium is not yet reached according to the overall reaction model (Figure 3.8), in ITC experiments it seems that only the first process produces a detectable thermal effect. Therefore, calorimetric experiments were analysed by using $[F^-]_e$ values calculated from potentiometric data with the same delay time between additions (60 min.) as in calorimetry.

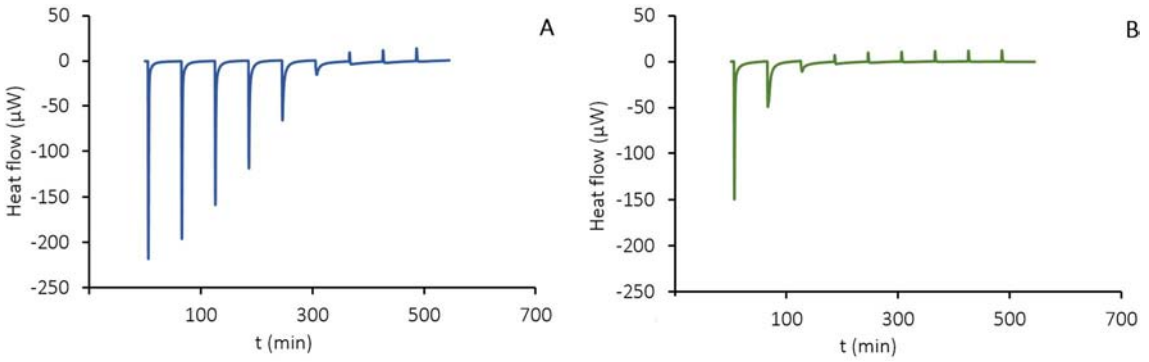

Figure 3.9. ITC for fluoride adsorption into HAM of type A (blue) and type B (green). Each peak corresponds to an injection of 17.5µl of 80mM fluoride solution to 0.7mL of 0.5g L^{-1} HAM suspension.

3.2.2.2. Fluoride adsorption isotherms

Potentiometric studies have been performed by the titration of fluoride solution (NaF solution 80mM) on 20mL of HAM suspension 0.5g L^{-1}. The fluoride concentration remaining in solution was measured once the equilibrium time was reached (1h), by using a fluoride selective electrode at constant temperature of 298.15K (see Methodology).

Experimental data for fluoride adsorption by both HAM type A and type B have been fitted with Langmuir and Freundlich isotherms (Figure 3.10), the obtained parameters are summarized in Table 3.5.

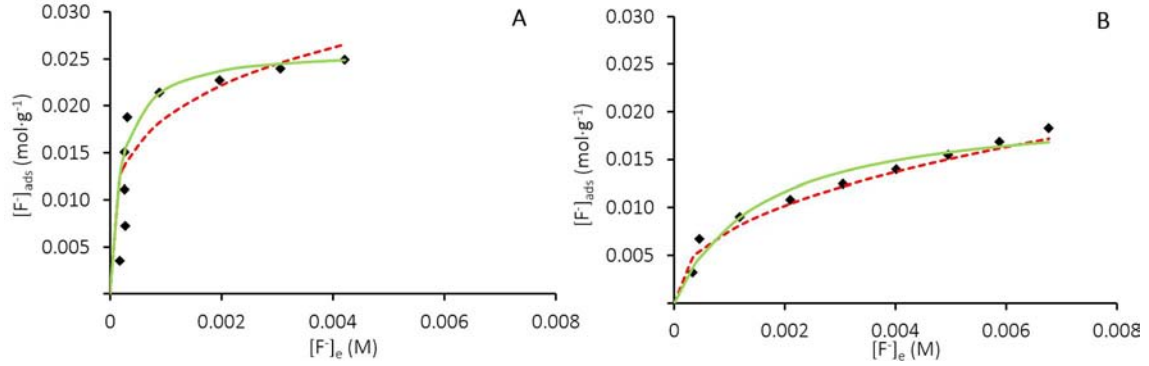

Figure 3.10. Experimental fluoride adsorption isotherms presenting the experimental data fitted with Langmuir (green line) and Freundlich (dashed red line) models with 1h between injections for type A and B.

As it can be seen by the correlation coefficient (Table 3.5), experimental data are better represented by Langmuir model than Freundlich model, suggesting the presence of homogeneous adsorption, where all the fluoride ions a microspheres form a monolayer on the surface.

HAM	Langmuir equation				Freundlich equation		
	Q_{max} (mol g^{-1})	b (M^{-1})	log b	R^2	n	K_f (L $mmol^{-1}$ g^{-1})	R^2
A	0.026 ±0.001	4563 ±486	3.66 ±0.11	0.979	5.9 ±0.5	20.2 ±0.3	0.871
B	0.020 ±0.001	598 ±100	2.78 ±0.17	0.967	2.3 ±0.1	7.6 ±0.3	0.895

Table 3.5. Langmuir and Freundlich isotherm parameters for fluoride adsorption by HAM of type A and B with different experimental conditions.

Comparing the adsorption constant of HAM type A and type B, Langmuir constant obtained for type A is significantly higher than that obtained for type B (∼1 order of magnitude, Table 3.5), indicating that the synthetic protocol has an important effect on this parameter. While the difference in the BET surface areas of both samples is not remarkable, DLS experiments evidenced higher particle aggregation in type B (Figure 3.6 and Table 3.3). Attending the premises mentioned in section 2.3 (X-ray diffraction), it seems that the higher efficiency in fluoride removal for type A than type B is mainly due to the different crystallinity of the two samples, as previously found in the literature.[13–15]

Crystalline materials used as adsorbent often suffer from disadvantages related to low adsorption capacity and high cost because of the high crystallinity and less porous structure, while amorphous adsorbents may present higher adsorption capacity because of their porous and highly hydrated structure, allowing the ions diffusion into the structure rather than the restricted external surface sites.[9–11] Hence, the low crystallinity of alumina-based materials seems to be an advantage for their adsorption capacity.[11,13,15] According to the aforementioned observations, HAM type A seems the most efficient material for fluoride adsorption.

The Q_{max} of the material results higher for sample A than sample B, being 0.026 and 0.020 moles of fluoride per gram of material, respectively (Table 3.5).

Additional potentiometric experiments have been performed in order to complete the adsorption studies; (i) potentiometric titrations for uncalcinated HAM, to verify that the synthesized material is higher effective after the thermal process (ii) potentiometric batch titrations (type A), to corroborate that the results are the same in batch and continuous titrations, (iii) potentiometric titrations with 12h delay between additions (type A), in order to study the adsorption of fluoride at long times. The obtained results regarding these additional experiments (ii) and (iii) are summarized in Table 3.6.

Concerning the experiment performed with uncalcinated HAM, it has been observed that the fluoride adsorption was significantly lower, with a maximum loading observed ∼ 0.08 millimoles of

fluoride per gram of adsorbent. This confirms the importance of the calcination process during synthesis of the adsorbent material.

In Figure 3.11 the experimental data obtained in the potentiometric batch experiments carried out for type A are represented. As can be seen, the obtained results (Figure 3.11 and Table 3.6) confirmed the values obtained previously in continuous titration experiments.

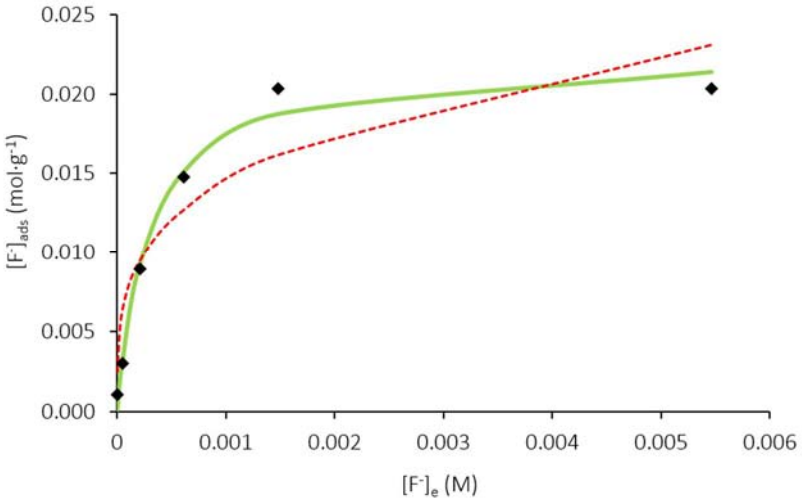

Figure 3.11. Experimental fluoride adsorption data (batch method) fitted with Langmuir (green line) and Freundlich (dashed red line) models with 1h of contact time (type A sample).

The potentiometric experiments with 12h delay between additions (Figure 3.12) show an adsorption constant quite similar to that obtained with a 1h delay, while the loading capacity is ~50% larger (Table 3.6). However, long time should be needed to reach such adsorption levels, which would not be practical and effective for a real application of the material.

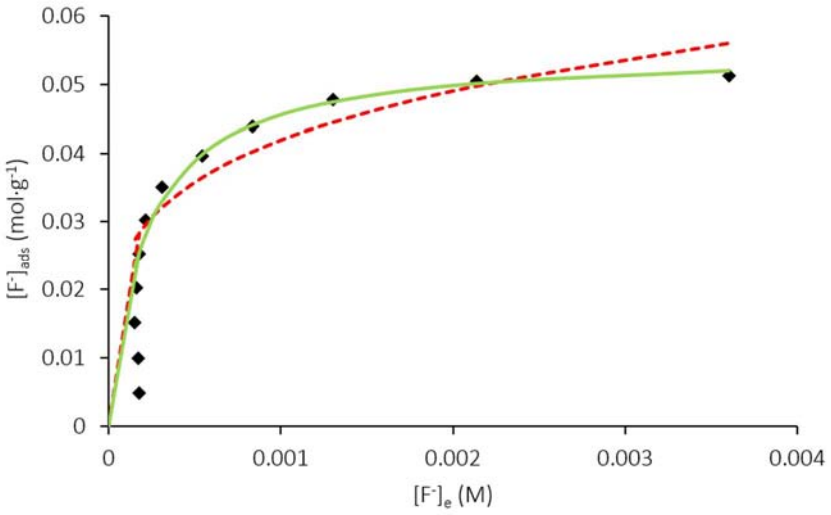

Figure 3.12. Fluoride adsorption data presenting fitted with Langmuir (green line) and Freundlich (dashed red line) models with 12h delay between injections (type A sample).

Exp.	Langmuir equation					Freundlich equation		
	Q_{max} (mol·g^{-1})	b(M^{-1})	log b	R^2	n	K_f (L·mmol^{-1} g^{-1})	log K_f	R^2
Batch	0.022 ±0.001	3308 ±646	3.52 ±0.02	0.997	4 ±1	15 ±2	1.18 ±0.13	0.883
12h delay	0.055 ±0.001	4820 ±393	368 ±0.08	0.999	4.4 ±0.6	42 ±1	1.62 ±0.02	0.847

Table 3.6. Langmuir and Freundlich isotherm parameters for fluoride adsorption by HAM of type A with batch method with 1h as contact time, with 12h as a delay time.

3.2.2.3. Thermodynamic parameters

ITC provided the heat evolved following adsorption process of fluoride on HAM type A and type B. Then, with the loading capacity and adsorption constant obtained by potentiometry, the ΔH_{ads} (kJ mol^{-1}) value has been calculated as the best fit of the experimental heat for the F^- adsorption, according to the modified Langmuir isotherm (Eq. 2.14, methodology chapter). In Figure 3.13 experimental and calculated q_{cum} values for type A and B are represented. It may be appreciated that, for type B, after the third injection the heat flow measured for the remaining injections corresponds to the dilution heat indicating that the adsorption process is finished, while for type A 6 injections are needed. It is also evidenced that the total heat evolved in fluoride adsorption in type A is higher than in type B, which confirms that type A is a more efficient adsorbent for fluoride removal than type B.

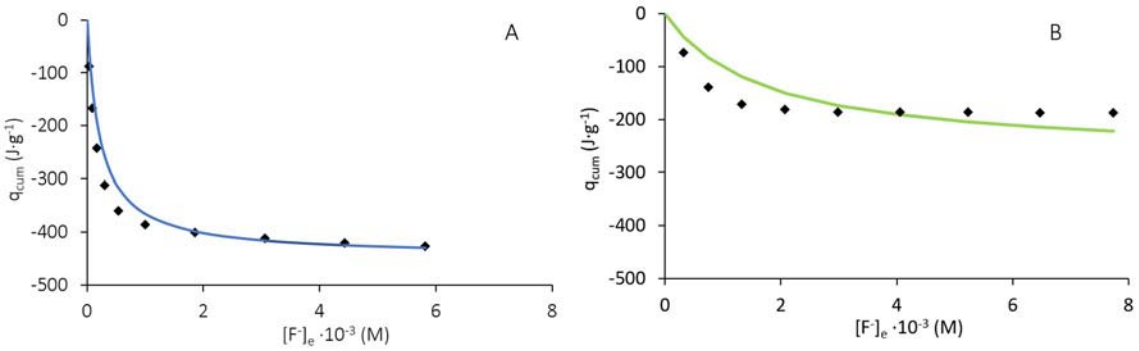

Figure 3.13. Experimental calorimetric data fitted with calorimetric Langmuir isotherm (line) for type A (blue) and B (green) HAM.

The thermodynamic parameters obtained for the adsorption process of fluoride on HAM (type A and B) are summarized in Table 3.7.

Type	ΔG_{ads} (kJ mol^{-1})	ΔH_{ads} (kJ mol^{-1})	$T\Delta S_{ads}$ (kJ mol^{-1})
HAM A	-20.9 ±0.2 kJ mol^{-1}	-17.7 ±0.6 kJ mol^{-1}	3.2 ±0.8 kJ mol^{-1}
HAM B	-15.8 ±0.4 kJ mol^{-1}	-13.3 ±0.9 kJ mol^{-1}	2.5 ±1.3 kJ mol^{-1}

Table 3.7. Thermodynamics of fluoride adsorption process onto HAM.

It may be observed that the adsorption process is spontaneous and clearly exothermic for both type A and B samples (Table 3.7). Exothermic enthalpies generally are related to physical adsorption processes,[16] and typically ΔH_{ads} for physical adsorption assume values from −4 to −40 kJ mol^{-1}.[16] Therefore, the obtained results claim a physical process of the adsorption of fluoride on both HAM.

The adsorption enthalpy obtained for type B (ΔH_{ads} = -13.3 ±0.9 kJ mol^{-1}) is less negative than the value obtained for type A (ΔH_{ads} = -17.7 ±0.6 kJ mol^{-1}). The difference in the ΔH_{ads} values obtained for the two types of HAM is 4.4 kJ mol^{-1}, which is not large, but not even negligible. It is interesting to note that the $T\Delta S_{ads}$ values (Table 3.7) are quite similar for the two materials (+3.2 and +2.5 kJ mol^{-1} for type A and B respectively), indicating that the adsorption process takes place with a slightly positive entropy change, related to the desolvation process of fluoride when adsorbing on the microspheres surface. When F^- ions are adsorbed, the molecules that solvate the anion are free, increasing the entropy of the system. This positive entropy change is in agreement with previous results adsorption of metal cations[17,18] and reflects the increase disorder due to charge neutralization and desolvation of the fluoride anion.

To compare our method for the determination of ΔH_{ads} with the standard van't Hoff interpolation (Eq. 1.3, Introduction chapter) normally used in previous works,[7,19–27] the adsorption parameters were calculated for HAM (type A) also at 318 K (Table 3.8).

Temp. (K)	Langmuir equation					Freundlich equation		
	Q_{max} (mol g^{-1})	b(M^{-1})	log b	R^2	n	K_f (L mmol^{-1} g^{-1})	log K_f	R^2
318.15	0.039 ±0.002	4165 ±794	3.62 ±0.19	0.961	3.1 ±0.5	31 ±1	1.49 ±0.03	0.721
298.15	0.026 ±0.001	4563 ±486	3.66 ±0.11	0.979	5.9 ±0.5	20.2 ±0.3	1.31 ±0.01	0.871

Table 3.8. Fluoride adsorption parameters found at different temperatures.

The obtained ΔH_{ads} calculated by van't Hoff equation; ΔH_{ads} ~-4 kJ mol^{-1}, is less negative than the same value obtained by ITC experiments. However, it should be considered that when ΔH_{ads} is determined using van't Hoff equation the propagated uncertainty on the ΔH_{ads} values can be large. Thus, an ideal ΔH_{ads} determined by van't Hoff equation should be calculated using very precise values of equilibrium constants and in a large range of temperature where, on the other hand, the heat capacity is not rigorously constant. Therefore, the direct determination of the heat exchanged by ITC seems to be the sole way to obtain reliable heats of adsorption and calculate ΔH_{ads} values.

3.2.2.4. Comparison with literature data

A wide range of adsorbent materials for water defluoridation have been tested, from biosorbents to engineered materials. Some of the most representative alumina-based materials are summarized in **Errore. L'origine riferimento non è stata trovata.**,[7,15,19–24,28–33] to compare our material with the most similar adsorbents reported. In **Errore. L'origine riferimento non è stata trovata.** some selected non-alumina-based materials features are reported,[25–27,34–38] for comparison with other available materials.

It may be observed that the maximum loading capacities of the studied materials (Q_{max}) results higher than those found for other alumina-based adsorbents (**Errore. L'origine riferimento non è stata trovata.**) and for other adsorbent materials (**Errore. L'origine riferimento non è stata trovata.**). Most of the works studied the fluoride removal with F^- concentrations lower than in the present work: taking into account that the effluents of industries that contribute in the release of fluoride on the environment reach concentrations of thousands of mg F^- L^{-1},[39] it is important to investigate the behavior of the adsorbent materials also at high fluoride concentrations.

Moreover, several studies on fluoride adsorption at high concentrations[26,28,33,37,38] can be found in the literature. The adsorption capacity is comparable with our adsorbent material just in one case.[28] The high efficiency of the HAM could be associated to the structure of the hierarchical material. As mentioned before,[35] the mesoporosity and the high surface area gives to the material a high number of active sites. In addition, hierarchical materials avoid the aggregation of the nanoplatelets, thus favouring the exposure of their entire surface to adsorb F^-.

A remarkable parameter obtained in this work is the ΔH_{ads}; the enthalpy associated to the adsorption process is quite significant since it allows the design of the best conditions both for the uptake and for the eventual successive release of a given chemical species. In previous works,[7,19–27,38] the enthalpy related to de fluoride adsorption process has been always calculated by the van't Hoff equation, and the values were quite scattered and either positive or negative (**Errore. L'origine riferimento non è stata trovata.** and **Errore. L'origine riferimento non è stata trovata.**).

The determination of reproducible ΔH_{ads} for the synthesized materials HAM type A and B should be of great help for the best design of the adsorption/desorption system. In this work, ΔH_{ads} has been determined by ITC with the aim to provide more accurate and robust thermodynamic parameters for fluoride adsorption on HAM.

Adsorbent	Particle size	Initial F^- (mM)	Adsorbent dosage (g L^{-1})	pH	Temp. (K)	Contact time (h)	Adsorption capacity (mmol g^{-1})	*b* (M^{-1})	ΔH_{ads} (kJ mol^{-1})	Ref.
Nano alumina	-	0.05 – 5.3 (1 - 100mg L^{-1})	1.0	6.15	298	24	0.8 (15.43mg g^{-1})	3240	14.8	21
Aluminum hydroxide	-	-	0.5	4	303	2	3.4 (63.5mg g^{-1})	623.7 (0.033L mg^{-1})	-18.45	7
Fe_3O_4@$Al(OH)_3$	240-340nm	0 – 8.5 (0 - 160mg L^{-1})	1.0	6.5	298	1	4.7 (88.48mg g^{-1})	5557 (0.2L mg^{-1})	6.8	19
Mesoporous calcium-doped alumina	-	0.1 – 52.9 (2 - 1000mg L^{-1})	0.1	6.5	298	12	23.8 (450mg g^{-1})	-	-	28
Al_2O_3	12-15µm	0.5 – 7.9 (10 - 150mg L^{-1})	1.0	6	298	48	4.4 (83.33mg g^{-1})	37800 (2.000L mg^{-1})	36.66	22
Ordered mesoporous alumina	300-800nm	0.3 – 10.6 (5 - 200mg L^{-1})	0.5	6	298	12	7.1 (135mg g^{-1})	13854 (0.733L mg^{-1})	-	30
Heated nano-gibbsite	-	0.263 - 3.947	2.0	6.0	4	4	1.6 (30.55mg g^{-1})	0.272	-	29
Natroalunite microtubes	-	0.3 – 10.6 (5 - 200mg L^{-1})	1.0	7.0	298	24	4.5 (85.84mg g^{-1})	3.750	-30.80	23
Amorphous aluminum oxide microspheres	-	0.3 – 7.9 (5 - 150mg L^{-1})	0.5	7.0	298	-	6.7 (126.90mg g^{-1})	7938 (0.42L mg^{-1})	-	15
Chitosan based mesoporous alumina	-	-	2.0	6.8	303	24	0.4 (8.264mg g^{-1})	2319 (0.1227L mg^{-1})	-0.8	20
Tea-APAM-Al	-	0.3 – 10.6 (5 - 200mg L^{-1})	1.0	5.0	308	3	2.2 (42.14mg g^{-1})	1767.1 (0.09350L mg^{-1})	-	31
Tea-Al-Fe	-	0.5 – 10.5 (10 - 200mg L^{-1})	2.0	7.0	298	2	1.0 (18.52mg g^{-1})	1051.9 (0.05537L mg^{-1})	-	32
Al_2O_3–ZrO_2	-	2.6 – 7.9 (50 - 150mg L^{-1})	1.0	2.0	318	4	6.0 (114.54mg g^{-1})	228.0 (0.012L mg^{-1})	-2.414	24
CaO-Activated Alumina	-	0.05 – 52.9 (1 - 1000mg L^{-1})	6.6	5.5	298	48	5.3 (101.01mg g^{-1})	930.9 (0.049L mg^{-1})		33
HAM type A	900nm	2.0 - 16.0	0.5	5.5	298.15	12[a]	55.0	4820	-	Present work
HAM type A	900nm	2.0 - 16.0	0.5	5.5	298.15	1[a]	26.0	4563	-17.7 ±0.6	Present work
HAM type B	900nm	2.0 - 16.0	0.5	5.5	298.15	1[a]	20.4	598	-13.3 ±0.9	Present work

Table 3.9. Fluoride removal parameters for several alumina-based adsorbents. In parentheses, the original values in the cited references are reported. [a]Delay time between fluoride solution additions.

Adsorbent	Particle size	Initial F^- (mM)	Adsorbent dosage (g L^{-1})	pH	Temp. (K)	Contact time (h)	Adsorption capacity (mmol g^{-1})	b (M^{-1})	ΔH_{ads} (kJ mol^{-1})	Ref.
Clay	-	1.2 – 124.2 (23.6 - 2360mg L^{-1})	33.3	2-3	298	48-96	4.9 (93.45mg g^{-1})	93.28 (4.91E-3L mg^{-1})	-	[37]
Waste mud	-	0.3 – 50.0 (5 - 950 mgL^{-1})	1.0	5.0	293	1	2.5 (46.7mg g^{-1})	1489.5 (0.0784L mg^{-1})	11.18	[38]
Nanomagnetite graphite –La	-	0.1 – 12.9 (1.97 - 244.6mg L^{-1})	0.2	7.0	298	24	4.1 (77.12 mg g^{-1})	718.2 (0.038L mg^{-1})	21.13	[26]
Mixed-phase nano iron oxides	50-200nm	0.5 – 5.3 (10 - 100mg L^{-1})	1.2	7.0	298	8	2.8 (53.19mg g^{-1})	1.1 (0.06L g^{-1})	-94.67	[25]
Bone char	-	0.1 – 1.1 (1 - 20mg L^{-1})	1.0	5.0	298	120-168	0.4 (7.74mg g^{-1})	29447.4 (1.55L mg^{-1})	-	[34]
MgO microspheres	-	-	1.0	7.0	298	12	6.1 (115.5mg g^{-1})	1481.9 (0.078L mg^{-1})	-	[35]
Magnetic cationic hydrogel - La	-	0 – 4.2 (0 - 80mg L^{-1})	0.3	7.0	298	0.17	7.9 (149.99mg g^{-1})	7219.4 (0.38L mg^{-1})	-	[36]
UiO-66-NH_2	100nm	0.5 – 3.7 (10 - 70mg L^{-1})	0.5	-	293	2	3.1 (58.82mg g^{-1})	6725.4 (0.354L mg^{-1})	-28.21	[27]
HAM type A	900nm	2.0 - 16.0	0.5	5.5	298.15	12[a]	55.0 (1.0g g^{-1})	4820	-	Present work
HAM type A	900nm	2.0 - 16.0	0.5	5.5	298.15	1[a]	26.0 (491.4mg g^{-1})	4563	-17.7 ±0.6	Present work
HAM type B	900nm	2.0 - 16.0	0.5	5.5	298.15	1[a]	20.4 (385.6mg g^{-1})	598	-13.3 ±0.9	Present work

Table 3.10. Fluoride removal parameters for several adsorbing materials (data relative to the HAM prepared in this work are also recalled for comparison). In parentheses, the original values in the cited references are reported. [a] Delay time between fluoride solution additions.

3.2.3. Conclusions

New HAM adsorbents have been synthesized and used for fluoride removal. SEM, TEM, BET and XRD diffraction studies reveal a high porous structure of amorphous alumina. The two types show similar physical characteristics with small differences in pore size and specific surface area. The main difference between the two samples is the presence of crystalline phase, smaller pore size and higher surface area in the one prepared with a shorter microwave treatment (type A). The kinetic study reveals a bi-exponential model indicating a two-step process for fluoride adsorption.

Fluoride adsorption experiments evidenced that the amorphous HAM (type A) have a superior affinity for F^- ion than type B, being the Langmuir constant about 1 order of magnitude higher. Adsorption experiments have shown that synthesized materials have a high efficiency towards defluoridation, with a maximum loading capacity of 0.026 moles of fluoride per gram of material after 1h contact time, which is significantly better than most other materials reported in the literature. Therefore, the high defluoridation capacity shown by the reported results on HAM, makes these materials potential candidates for wastewater treatment.

The combined potentiometric-ITC method has been used to calculate the adsorption parameters and, for the first time, to obtain the ΔH_{ads} value by direct measurement of the heat associated to the process. Contrarily to the data presented in most previous works, clearly negative enthalpy values for fluoride adsorption are obtained. However, also exothermic processes have found in the literature. Several investigations revealed serious discrepancies between the enthalpy calculated by van't Hoff equation or by ITC, related to the propagated uncertainties of the equilibrium constant and the variations in the heat capacity at different temperatures. Therefore, ITC is a good tool to measure the ΔH_{ads} with excellent accuracy.

3.3. METAL IONS REMOVAL WITH SUPERPARAMAGNETIC IRON OXIDE NANOPARTICLES FUNCTIONALIZED WITH SULPHUR CONTAINING LIGANDS

In the next section, the study of HM and PM adsorption on modified SPION is described, including the characterization of the coated SPION and the adsorption study of Hg(II), Pb(II), Cr(VI), Cd(II), Ag(I) and Pt(IV) on the obtained material. A brief scheme of the work is presented in Figure 3.14

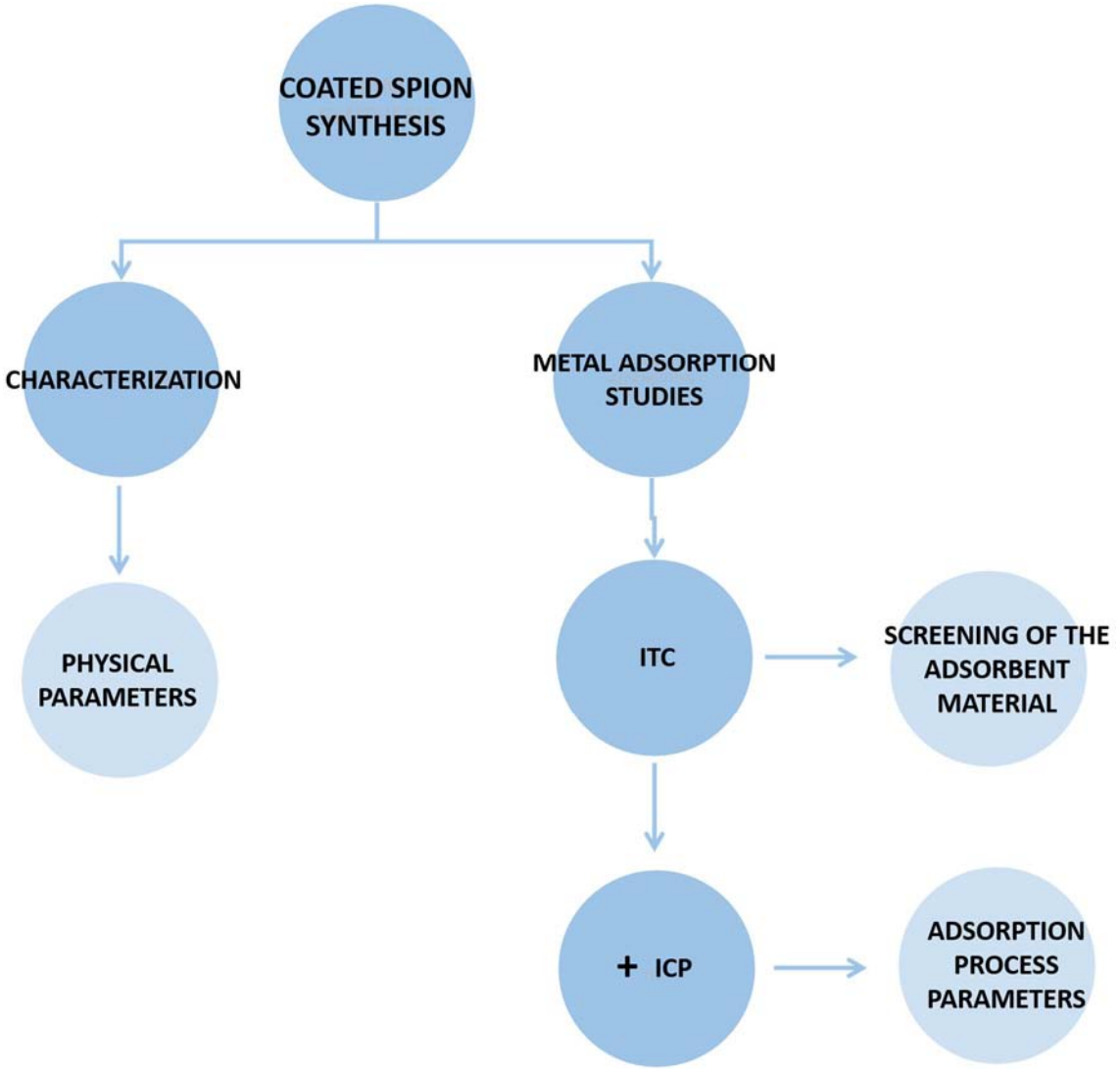

Figure 3.14. Schematic representation of the developed study of metal adsorption on functionalized SPION.

3.3.1. Characterization of the adsorbent material

In the present section, the characterization consisted in the determination of the presence of ligand on the surface of the SPION, which was verified by FT-IR and EDX performed by SEM and quantified by TGA, the morphology of the adsorbent, which was analysed by SEM and TEM, the determination of the specific surface area, determined by the study of N_2 adsorption at -196ºC. Finally, DRX was used to define crystallinity of the material and DLS for determining the particles aggregation. The obtained results are summarized in the following section.

3.3.1.1. Determination of SPION surface coating

LIGAND ADDITION

- FT-IR Spectra

FT-IR analysis have been carried out in order to identify the functional groups coating the modified SPION surface and thus, verify the surface coating with 3-MPA and 3,3-TDPA.

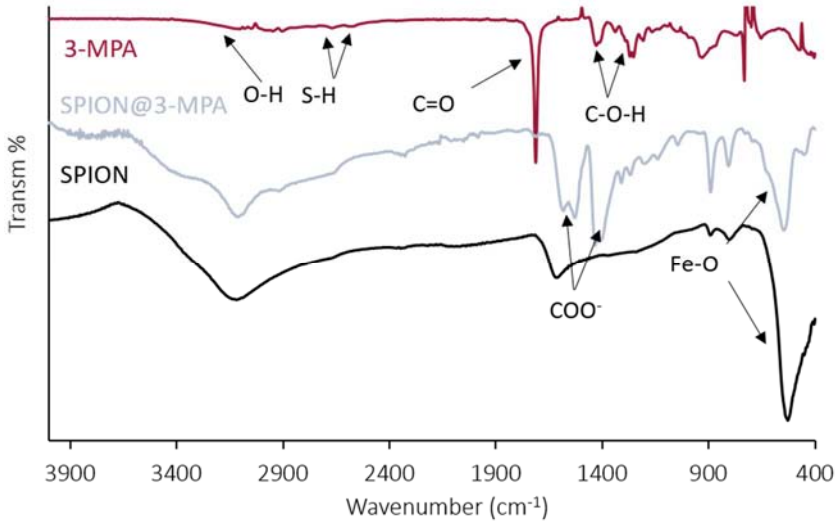

Figure 3.15. Spectrum of bare SPION, 3-MPA, and SPION coated 3-MPA.

In Figure 3.15, the FT-IR spectra of SPION shows a band at 524cm^{-1}, characteristic of Fe-O vibrations.[40] The spectrum of the free ligand 3-MPA reveals a peak in 3100cm^{-1}, which corresponds to the O-H vibrations, while the presence of the functional group S-H is evidenced by the two weak bands at 2669 cm^{-1} and 2573 cm^{-1}. The strong band at 1710cm^{-1} identifies the C=O vibrations, and the two peaks at 1433cm^{-1} and 1251cm^{-1} are attributed to C-O-H stretching.

The spectra of SPION@3-MPA is also represented in Figure 3.15. Since the 3-MPA ligand present two characteristic functional groups: -SH and –COOH, it would be expected that the thiol coated nanoparticles showed a stretching band near 2573cm^{-1}, related to S-H stretching. However,

because of its weak intensity it is typically not observed in thin films.[40] On the other hand, also the strong band characteristic of C=O vibration is expected. Although this peak is not observed, when comparing with SPION spectra, two new bands at 1540cm^{-1} and 1400cm^{-1} are shown, corresponding to the COO^- stretching. This indicates that the –COOH group became $–COO^-$ evidencing that the binding of the ligand to the SPION surface occurs through the carboxylate anion.[40]

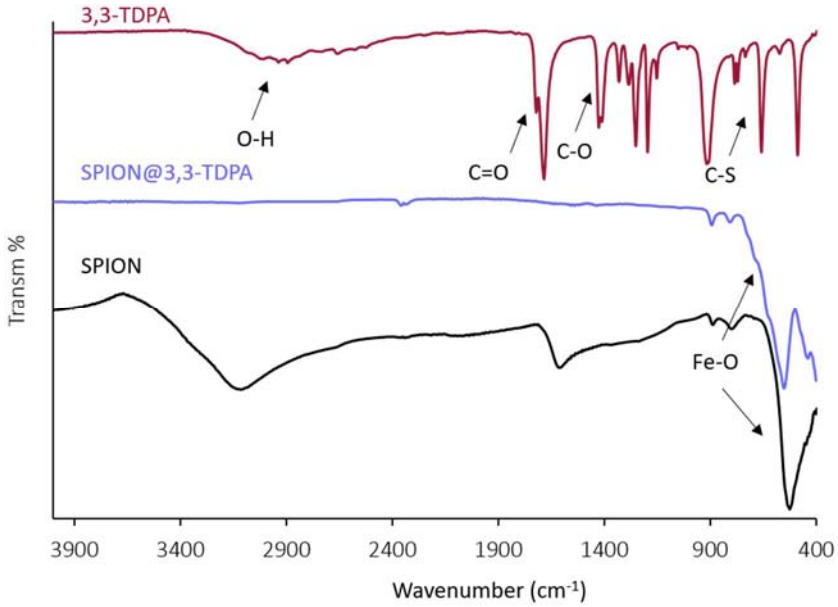

Figure 3.16. Spectrum of naked SPION, 3,3-TDPA, and SPION coated 3,3-TDPA.

The spectra of the ligand 3,3-TDPA, present in Figure 3.16, show three characteristic peaks which correspond to the O-H band around 2950cm^{-1}, the C=O stretching at 1685cm^{-1} and the C-S vibration, characteristic of that ligand, observed at 660cm^{-1}.[41]

In the SPION@3,3-TDPA spectra, it would be expected to detect the two bands corresponding to the COO^- vibrations evidencing the binding of the ligand to the SPION surface, as well as the band assigned to C-S vibration characteristic of 3,3-TDPA ligand: none of these bands is observed, it is only appreciated the Fe-O band around 524cm^{-1} as in bare-SPION spectra.

Therefore, one can conclude that 3,3-TDPA functionalization was not successful.

- Thermogravimetry

TGA allowed the quantification of 3-MPA coating the SPION particles, by measuring the percentage of mass loss. In Figure 3.17 is observed an initial weight loss about 1% for both SPION and SPION@3-MPA until 200°C, which is related to the loss of hydroxyl groups and/or adsorbed water.[42] The 0.8% of weight loss for naked SPION above 200°C is related to the decomposition of amorphous iron

hydroxides followed by iron oxide formation,[43] while the 12.9% of mass loss of the coated SPION is associated to the decomposition of the 3-MPA attached on the particles surface.[43] Thus, TGA analysis confirm the functionalization of the NP with an amount of 1.4mmol g^{-1} of 3-MPA coating the SPION surface.

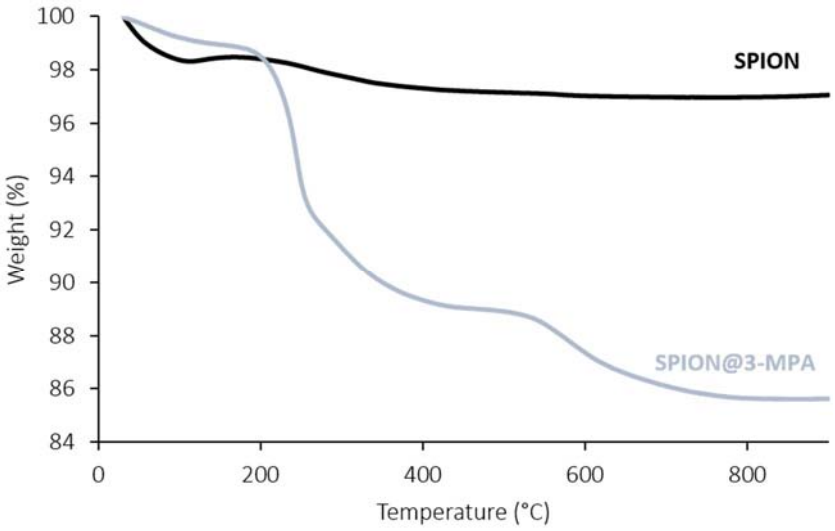

Figure 3.17. TGA curves for SPION and SPION coated 3-MPA by ligand addition method.

- Scanning Electron and Transmission Electron Microscopy

SEM and TEM pictures of SPION@3-MPA are shown in Figure 3.18. In the SEM images (Figure 3.18-A and B), a general view of the synthesized material is exhibit, where is observed that the particles are spherical with some aggregation, which could be related to the coating of the NP.

TEM micrographs (Figure 3.18-C and D), illustrate the original size of the particles, with a mean diameter of 10-30nm. However, TEM analysis also confirms the existence of some aggregation. Although, EDX analysis confirmed the presence of sulphur on the adsorbent material, the coating layer on the magnetic particles was sufficiently thin that TEM was almost unable to detect its presence around the SPION core.

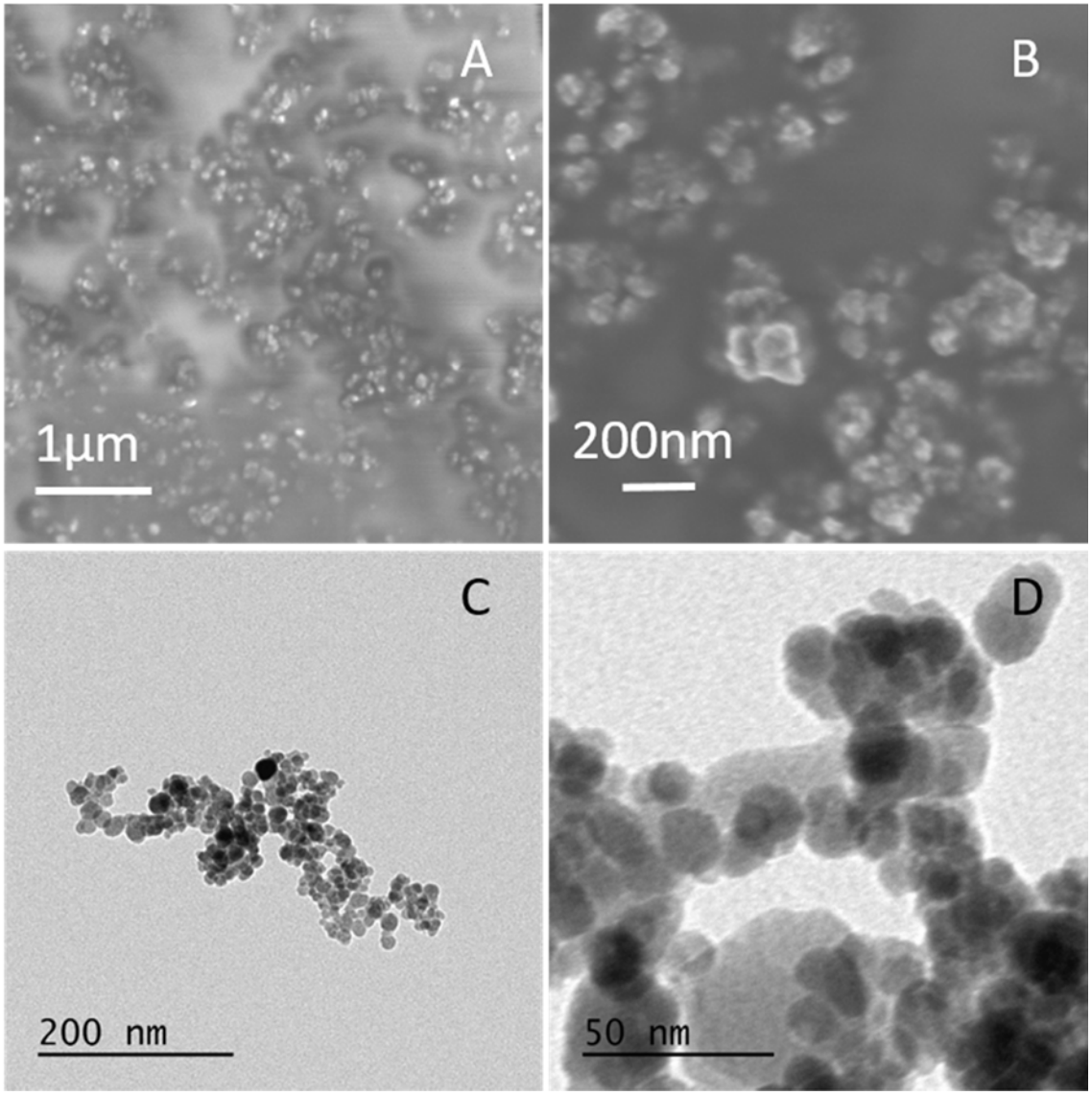

Figure 3.18. SEM and TEM micrographs of SPION@3-MPA.

LIGAND EXCHANGE

- **FT-IR Spectra**

Each FT-IR spectrum of bare and coated SPION (Figure 3.19) shows a characteristic Fe-O band around 520cm^{-1}.[40] While the uncoated SPION does not show any other significant peak, the particular bands of COO^- at 1500cm^{-1} and 1400cm^{-1} are observed for SPION@LA, SPION@3-MPA and SPION@3,3-TDPA spectrum, evidencing that the ligand binding to the surface by the carboxylate anion[40] for LA, 3-MPA and 3,3-TDPA respectively. It is difficult to identify the functionalization of the modified SPION by ligand exchange method, thus, to assess the ligand exchange of LA with 3-MPA or 3,3-TDPA, changes in the spectra before and after such process were analysed. The SPION@LA spectrum, as well as the free ligand (LA), show distinctive C-H vibrations

at 2850cm^{-1} and 2915cm^{-1}. The decreased or complete disappearance of such bands, as observed in SPION@3-MPA and SPION@3,3-TDPA spectra, indicate the surface ligand exchange.[40]

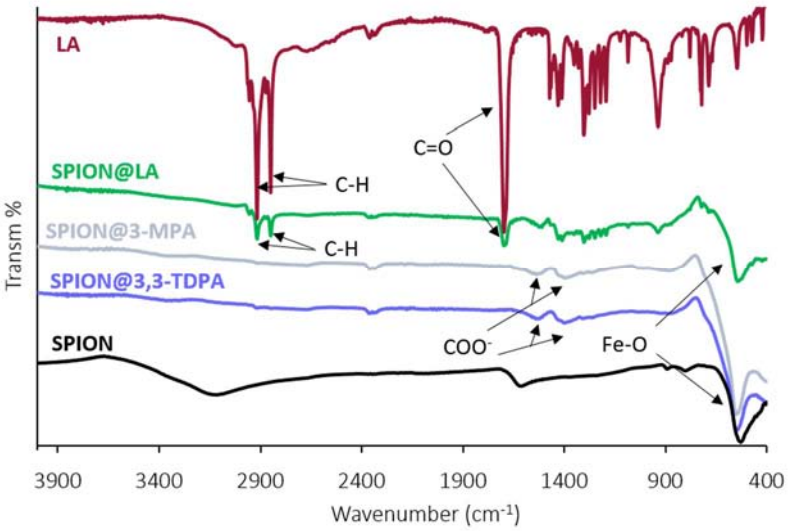

Figure 3.19. FT-IR of the precursor and the exchanged ligands bonded to SPION surface.

The above results of the preliminary analysis confirm the 3-MPA and 3,3-TDPA SPION coating by ligand exchange method.

- Thermogravimetry

The thermograms obtained for SPION@LA, SPION@3-MPA and SPION@3,3-TDPA as well as for uncoated SPION are presented in Figure 3.20. The weight loss observed until 200°C for bare and coated SPION is indicative to the removal of hydroxyl groups and/or adsorbed water.[42] Above this temperature, the weight loss for uncoated SPION is related to the decomposition of amorphous iron hydroxides followed by iron oxide formation.[43] The mass loss observed for coated SPION above 200°C, arises from the decomposition of the organic ligand added to the SPION surface.[43] TGA curve of SPION@LA shows a mass loss with two distinct steps; the first between 200°C and 400°C followed by a second decrease between 400°C and 700°C. This phenomena is related to the existence of two distinct populations of LA coated on the iron oxide surface, where the nanoparticles are coated with a well-organized surfactant bilayer of primary and secondary surfactants.[44] The TGA analysis confirm the functionalization of SPION, in which the ligand amount coating SPION was 0.8mmol g^{-1}, 0.3mmol g^{-1} and 0.4mmol g^{-1} for LA, 3-MPA and 3,3-TDPA respectively. Notice that the amount of 3-MPA added to the SPION surface with ligand exchange method (0.3mmol g^{-1}), is significantly lower than with ligand addition method (1.4mmol g^{-1}).

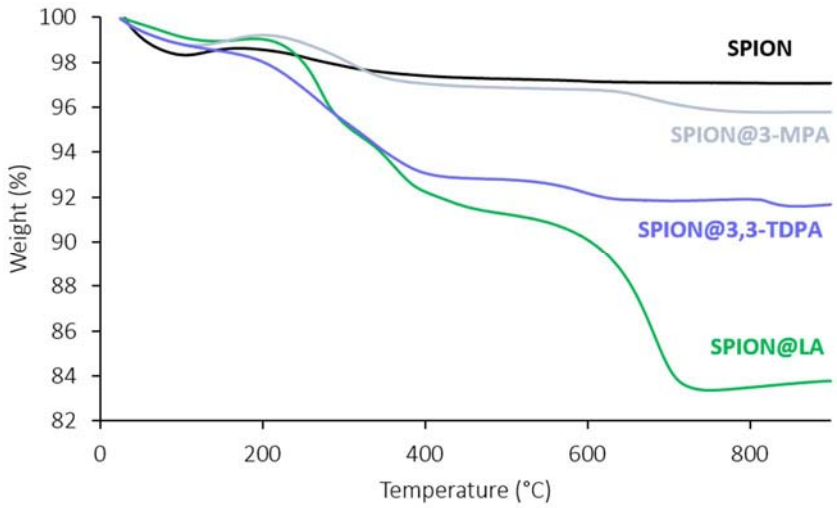

Figure 3.20. TGA curves for SPION and SPION coated by ligand exchange method.

- Scanning Electron Microscopy

SEM analyses have been performed for SPION@3-MPA and SPION@3,3-TDPA, nevertheless the presence of sulphur atoms on the particle surface was not detected by the EDX analysis. It could be attributed to the low quantity of ligand coating the SPION surface, as observed by TGA analysis. Thus, there was no certainty that the ligand exchange method had worked; consequently, the ligand exchange methodology was discarded.

The successive characterization of the material, as well as the adsorption experiments have been performed for SPION@3-MPA obtained by the functionalization by ligand addition method.

3.3.1.2. Characterization of SPION@3-MPA

- X-ray diffraction

The crystalline properties of functionalized SPION have been analysed by XRD and are shown in Figure 3.21. The SPION@3-MPA difractograms exhibits a single phase analogous to the characteristic reflections of magnetite (Fe_3O_4), corresponding to the (111), (220), (311), (400), (422), (511) and (400) planes as confirmed by JCPDS database (JCPDS, Card N°19). This reveals that the 3-MPA coating does not result in the oxidation of the bare SPION.

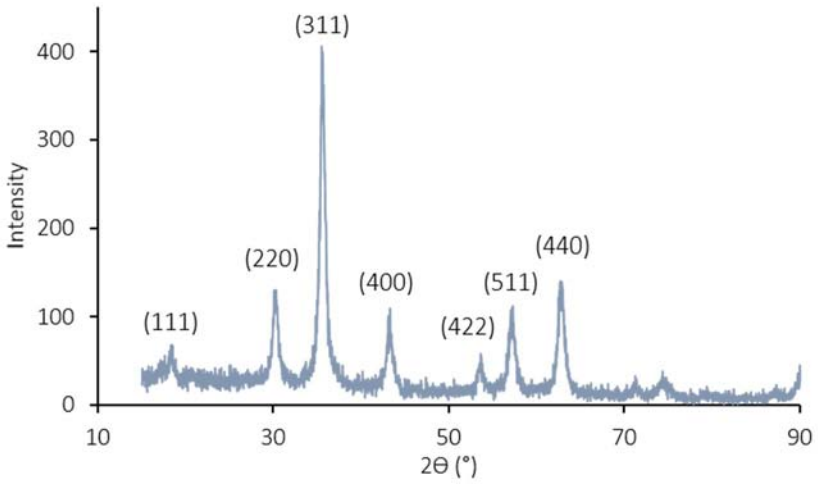

Figure 3.21. XRD spectra for SPION@3-MPA and its crystallographic plans.

- Surface area

The BET surface area data for the bare and the coated SPION have been calculated from N_2 adsorption analysis at -196 °C. The BET surface area for bare SPION has been found to be 92.3 m^2 g^{-1}, while resulted in 63.4m^2 g^{-1} for SPION@3-MPA. Therefore, the BET analysis indicate that the BET surface area decreases when the particles are coated by the organic ligand.

- Dynamic Light Scattering

DLS measurement is shown in Figure 3.22, and presents a particle size distribution of ~800nm. Such value is much higher than the particle size viewed by TEM (between 10-30nm). This observation could result from the aggregation of the NP induced for the ligand coating, as detected in previous SEM and TEM analyses.

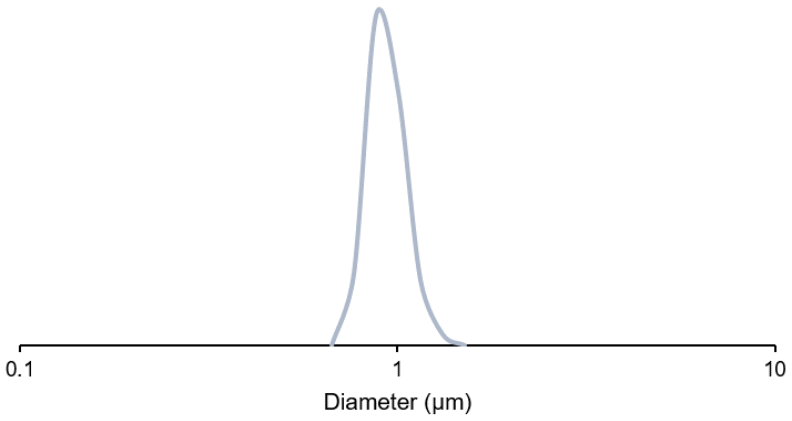

Figure 3.22. DLS analysis for SPION@3-MPA.

- Point of zero charge

The pH_{pzc} obtained for SPION@3-MPA was pH_{pzc} = 4.0. Hence, pH_{pzc} of the coated SPION shifted from 6.8[45] for uncoated SPION to 4.0 for the functionalized material. Therefore, as the working pH

(5.0) is higher than pH_{pzc} (4.0), the SPION@3-MPA surface is negatively charged, meaning that the metals cations would be attracted by electrostatic forces.

Adsorbent	Particle size (TEM) (nm)	Particle size distribution (DLS) (nm)	Surface area ($m^2\ g^{-1}$)	3-MPA layer (mmol g^{-1})	pH_{zpc}
SPION@3MPA	10-30	800	63.4	1.2	4

Table 3.11. Summary of the SPION@3MPA characteristics obtained.

In view of the results obtained, it may be claimed that 3-MPA is bounded to particles surface through the carboxylate anion following the mechanism[46] shown below:

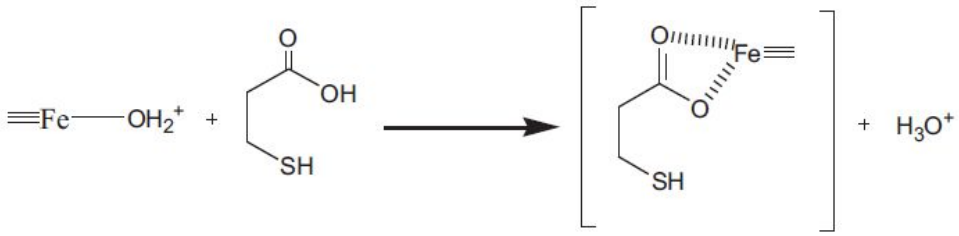

where ≡Fe represents SPION surface.

Figure 3.23. Functionalization mechanism of 3-MPA on SPION surface.[46]

Such functionalization is promoted by the leaving group OH_2 allowing the carboxylate binding to the SPION surface, increasing the amount of functionalized Fe atoms on the SPION surface.[46]

3.3.2. Metal adsorption studies on SPION@3-MPA

The next section describe the results obtained in the research of HM (Pb(II), Cr(VI), Cd(II), and Hg(II)) and PM (Ag(I) and Pt(IV)) adsorption on functionalized magnetic nanoparticles, characterizing the adsorption processes in terms of loading capacity and thermodynamic parameters. The scope of the presented research was not only the determination of thermodynamic parameters by a new experimental method, that combines ICP-OES and ITC, but the use of ITC as a screening of the adsorbent material. Thus, ITC provides information about the exchanged reaction heat, but also allows the comparison of the effectiveness of SPION@3-MPA as adsorbent towards the different studied metal ions. The details of the obtained results are described below.

3.3.2.1. ITC for material screening

Figure 3.24 displays ITC results of metal ions adsorption on SPION@3-MPA, where a higher thermal effect for Ag(I) and Hg(II) adsorption on coated SPION, followed by Pt (IV) > Cr(VI) ~ Pb(II) > Cd(II) may be observed.

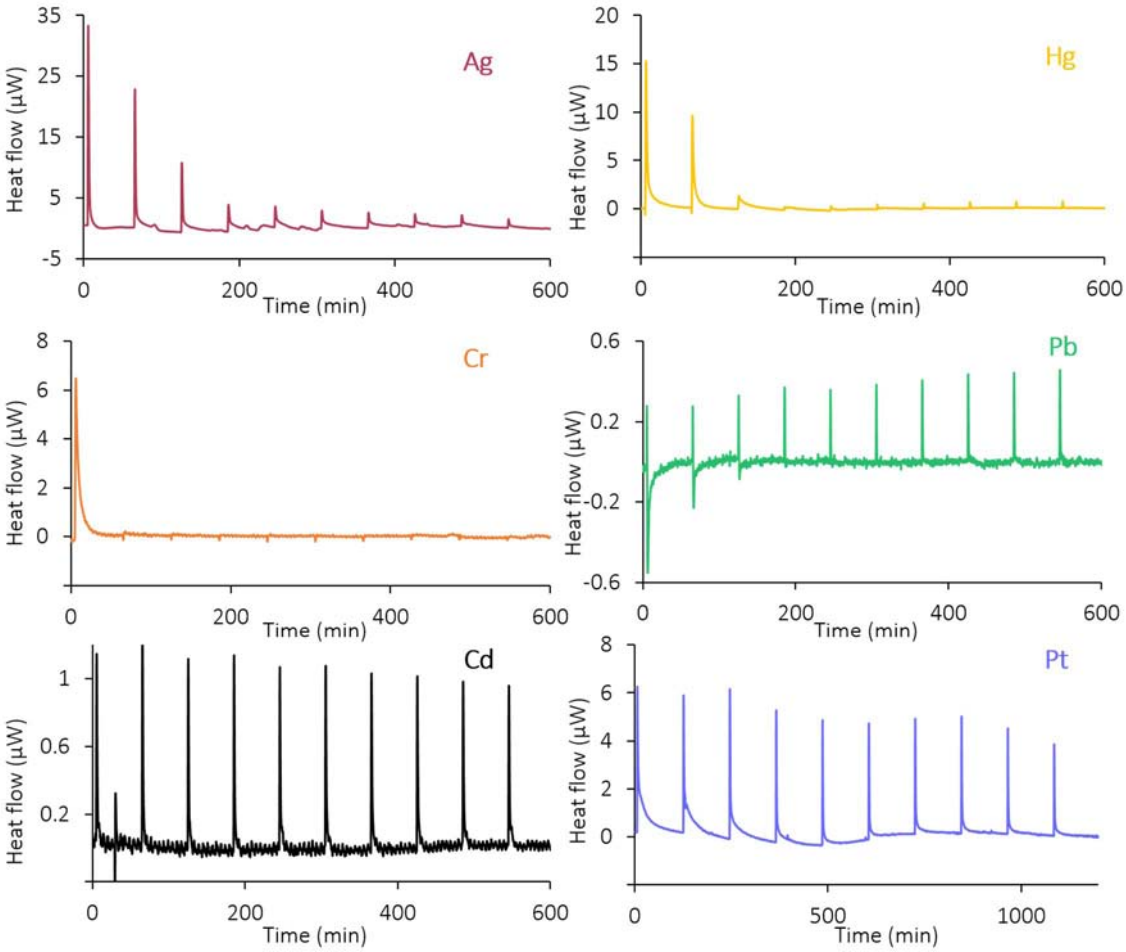

Figure 3.24. Titration thermograms formed by the heats per unit of time released after the injection of 14µL of Ag(I), Hg(II), Cr(VI), Cd(II), Pb(II) or Pt(IV) solution into 0.7mL of 0.5g L^{-1} SPION@3-MPA suspension.

In ITC measurements for Ag (I), Hg(II) and Pt(IV) adsorption, significant peaks are initially observed. Those are due to the heat exchange for the adsorption of the metal cations in SPION@3-MPA, while the other peaks show the dilution heat of the metal solution on the SPION@3-MPA suspension.

Regarding the Cd(II) thermogram, the same small heat is released during the whole experiment, meaning that only dilution of Cd(II) solution on the SPION@3-MPA suspension is observed. Thus, that there is not detectable adsorption by ITC of such metal on SPION@3-MPA.

In the titration of Cr(VI) on SPION@3-MPA suspension, a first intense peak is observed followed by minor peaks (related to dilution heat), indicating that most of the Cr(VI) ions are adsorbed in the first injection. It has to be considered that Cr(VI) in solution is found in different ionic forms depending on the pH conditions. At the working pH (pH=5), hydrochromate ion ($HCrO_4^-$) is the predominating form.[43] Therefore, as the pH_{pzc} (pH_{pzc}=4) of SPION@3-MPA is lower than the working pH (pH=5), the dominating charge on the adsorbent surface would be negative, resulting in a repulsion of the electrostatic interactions.

Finally, in the Pb(II) titration, change in the sign of the heat exchanged is observed. The first peaks shown a negative heat exchanged, indicating an endothermic adsorption process. However the intensity of such peaks is very low compared with those of Ag(I), Hg(II) or Pt(IV), showing a small adsorption of Pb(II) on SPION@3-MPA. Successive peaks show a positive heat exchange, and as in the other experiments, those peaks mean the dilution heat of the metal solution on the suspension.

Therefore, a first and relatively simple screening of the SPION@3-MPA for the adsorption of different metals may be performed by ITC, in which the SPION@3-MPA displays the following selectivity order Ag(I) ~ Hg(II) > Pt(IV) > Cr(VI) ~ Pb(II) >> Cd(II).

3.3.2.2. Metal adsorption isotherms

Adsorption experiments for metal ions adsorption on SPION@3-MPA have been performed in batch conditions, where 10mL of metal concentration between 0.1-1mM have been mixed with 5mg of SPION@3-MPA. Once the equilibrium time was expired, the magnetic adsorbent has been removed from the solution by the application of a magnetic field. The metal concentration remaining in solution was then analysed by ICP-OES, and the experimental data obtained have been fitted with Langmuir and Freundlich models in order to found the best description of the adsorption mechanism. The fitted isotherms are not shown with the aim of brevity; the obtained parameters are summarized in Table 3.12.

As observed in ITC experiments, Cd(II) adsorption shows dilution heat for each injection of metal solution, indicating that there is no adsorption of such metal on SPION@3-MPA. Therefore, ICP experiments were not performed for Cd(II) adsorption.

Metal	pH	Langmuir equation				Freundlich equation		
		Q_{max} (mol g^{-1})	b (M^{-1})	log b	R^2	n	K_f (L $mmol^{-1}$ g^{-1})	R^2
Pb(II)	5	0.00014 ±0.00001	20799 ±7207	4.3 ±0.3	0.986	4.4 ±0.9	0.16 ±0.01	0.943
Cr(VI)	5	0.000127 ±0.000004	50702 ±14115	4.7 ±0.3	0.996	10 ±3	0.133 ±0.009	0.735
Hg(II)	5	0.0017 ±0.0001	137727 ±32392	5.1 ±0.2	0.998	3.5 ±0.9	3.1 ±0.8	0.837
Ag(I)	5	0.0015 ±0.0001	92481 ±21320	4.9 ±0.2	0.997	4 ±1	2.3 ±0.6	0.879
Pt(IV)	3	0.00031 ±0.00001	368483 ±129319	5.6 ±0.3	0.997	12 ±2	0.342 ±0.008	0.951

Table 3.12. Langmuir and Freundlich isotherm parameters for metal adsorption by SPION@3-MPA.

The correlation coefficient (R^2) reported in Table 3.12, which is a measure of the goodness-of-fit, indicates that experimental data complies with Langmuir model better than Freundlich model for every metal, pointing out the homogeneity of the active sites of the thiolated SPION surface.

In Figure 3.25 the Q_{max} obtained for each metal is represented, showing that Q_{max} is higher for Hg(II) ~ Ag(I) than for the other metal ions, followed by Pt(IV), Pb(II) ~ Cr(VI) respectively. These results are in agreement with those observed by ITC, where the higher thermal effect was observed for Ag(I) and Hg(II).

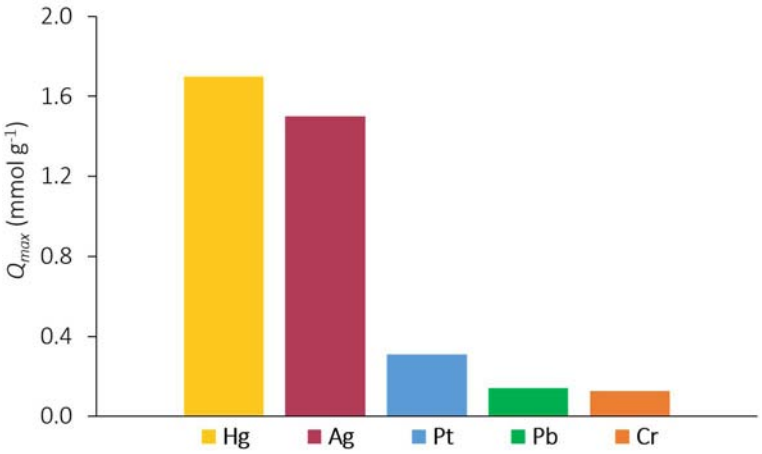

Figure 3.25. Comparison of Q_{max} of Ag(I), Hg(II), Pb(II), Cr(VI) and Pt(IV) on SPION@3-MPA.

For the better understanding of the Q_{max} of SPION@3-MPA towards the different metal ions, is necessary to study the nature of the binding chemistry of the immobilized ligand with the different metal ions. As mentioned in the Introduction chapter (section 1.8.2.3), by considering the Pearson's HSAB theory,[47] a first approximation of the efficiency of the adsorbent towards the different metals adsorption may be performed. Where the Q_{max} of the material functionalized with a soft ligand (thiol) would be higher for soft metals, such as Hg(II) or Ag(I), and limited by ligand:metal stoichiometry.[48] This approximation could be useful for "very soft" metals; however, for harder metal cations this prediction is not accurate. Misono softness parameter[49] (see Introduction chapter, Eq. 1.4 in section 1.8.2.3), is a useful tool to quantify the "softness" of the metals (Table 3.13).

	Misono softness parameter	Q_{max} (meq g^{-1})
Hg(II)	4.42	1.7
Ag(I)	4.05	1.5
Pb(II)	3.58	0.3
Cd(II)	3.03	0
Cr(VI)	-	-
Pt(IV)	-	-

Table 3.13. Loading capacity found for each metal cation along with the Misono softness parameter.

When plotting the calculated parameter against the Q_{max} of the adsorbent for each metal, a correlation may be found as presented in Figure 3.26, where is exhibited that a higher Misono parameter means a higher loading capacity.

Notice that the correlation between Misono parameter and the Q_{max} of the adsorbent is expressed in terms of milliequivalents per gram rather than millimoles per gram, indicating that charge accumulation at the interface is a significant consideration to determine the equilibrium.[48] The accumulation of metal cations on the interface decreases the effective basicity of the thiol ligand field by shifting the equilibrium to alleviate the repulsive electropositive interactions between the cations. Such effect is higher for those metals with weaker binding affinities (lower Misono parameter), occurring the saturation at lower Q_{max},[48] as in the case of Pb(II) and Cd(II). This is why adsorption has been observed for Pb(II) but not for Cd(II), even though Pb(II) and Cd(II) show a small difference between their Misono parameters. On the contrary, Hg(II) and Ag(I) (higher Misono parameter) are less influenced for this effect, in consequence, a significant higher Q_{max} for such metals has been obtained.

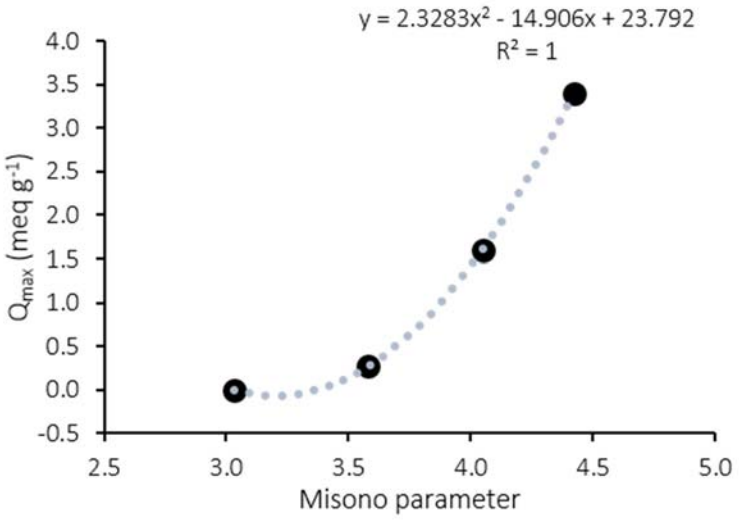

Figure 3.26. Correlation between Misono softness parameter and loading capacity of the SPION@3-MPA.

Comparing the "softer" metals, meaning those with higher Misono parameter (Hg(II) and Ag(I)), is observed a higher Q_{max} for Hg(II), in terms of milliequivalents per gram of adsorbent, as well as in terms of millimoles per gram of adsorbent. While the lower end of the binding curve is dominated by equilibrium effects, the upper end of the curve is limited by stoichiometry,[48] meaning that Ag(I) is bound with a 1:1 stoichiometry, while Hg(II) should interact with two S atoms. However, considering that the adsorbent material contains 1.4mmol of ligand per gram of SPION, Hg(II) (Q_{max} =1.7mmol g^{-1}) could be interacting with 1 thiol instead of two in agreement with other reported studies.[50,51]

On the other hand, Cr(VI) and Pt(IV) have not been compared with the Misono parameter because they are found in solution as hydrochromate and chloroplatinate respectively, thus, the binding chemistry of such complexes with SPION@3-MPA would be conditioned by other factors.

At pH = 5 Cr(VI) is found in solution as $HCrO_4^-$, therefore, there is a repulsion electrostatic interaction between the ion and the surface charged negatively, avoiding the adsorption of that metal. On the contrary, at pH = 3, the complex formed by Pt(IV) and Cl^- is charged negatively, thus, it would be attracted by the positively charged surface favouring the recovery of Pt(IV) by SPION@3-MPA.

3.3.2.3. Thermodynamic parameters

ITC has measured the time-dependent evolution of the heat exchanged upon injections of an aliquot of metal ion solution into the SPION@3-MPA suspension. After the correction with the dilution heat of the metal solution on the SPION@3-MPA suspension, the heat change measured along with the Langmuir parameters provided by ICP-OES, have been fitted with the modified Langmuir isotherm (Eq.2.14, section 2.4) in order to determine the ΔH_{ads} (kJ mol^{-1}) for each metal.

Figure 3.27 exhibits the experimental and calculated q_{cum} values for each metal studied. It may be observed that the total heat evolved in Ag(I) and Hg(II) adsorption is significantly higher than for the other metals, confirming that the synthesized adsorbent is more efficient for Ag(I) and Hg(II) followed by Pt(IV), and Cr(VI) ≅ Pb(II) respectively.

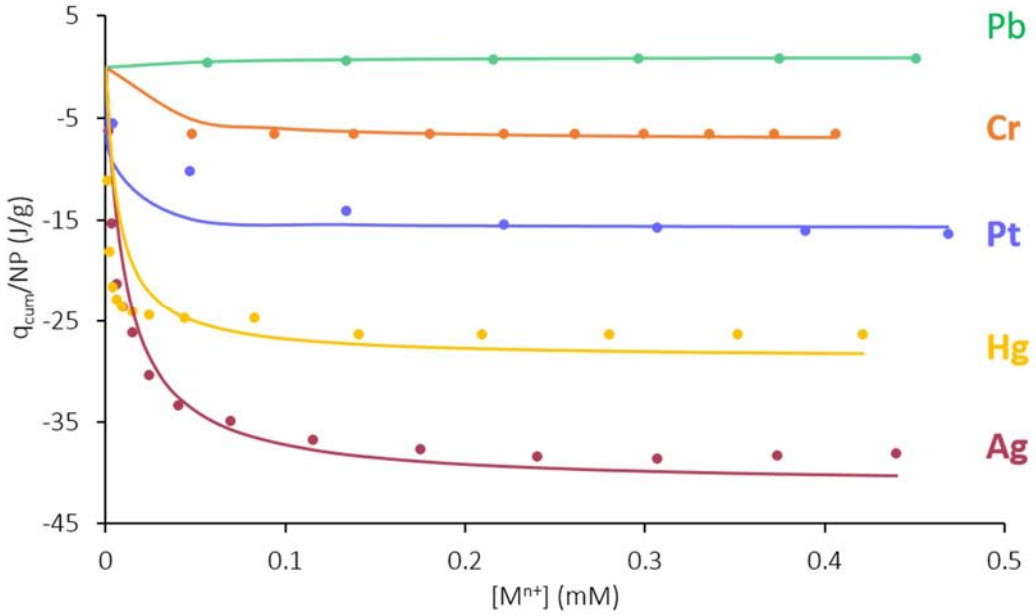

Figure 3.27. Experimental calorimetric data (points) fitted with calorimetric Langmuir isotherm (line) for Ag(I), Hg(II), Cr(VI), Pb(II) and Pt(IV).

The thermodynamic parameters obtained for metal adsorption process on SPION@3-MPA are summarized in Table 3.14

Metal	ΔG_{ads} (kJ·mol^{-1})	ΔH_{ads} (kJ·mol^{-1})	ΔS_{ads} (J mol^{-1}K^{-1})
Ag(I)	-28.3 ±0.5	-27.2 ±0.7	4 ± 4
Hg(II)	-29.3 ±0.5	-16.0 ±0.6	44 ± 4
Pb(II)	-24.6 ±0.8	6.5 ±0.1	104.5 ±0.9
Cr(VI)	-26.9 ±0.7	-57.1 ±0.7	-101 ±1
Pt(IV)	-31.8 ±0.9	-50 ±2	-81 ±2

Table 3.14. Thermodynamic parameters obtained for metal adsorption on SPION@3-MPA.

This reveals that the adsorption process is spontaneous for every metal and exothermic except for Pb(II). As mentioned in section 3.2.2.3, exothermic ΔH_{ads} generally are related to physical adsorption processes.[16] Nevertheless, other studies reported in the literature[52,53] reveals several cases where an endothermic ΔH_{ads} has been obtained for Pb(II) adsorption process.

The results of this study show that the adsorption reaction takes place with a positive entropy change (ΔS_{ads}) for Ag(I), Hg(II) and Pb(II), indicating an increase of the randomness of solid-solution interface related to the desolvation process of the metal ions when adsorbing on the SPION@3-MPA surface. Notice that the obtained ΔS_{ads} for the Ag(I) adsorption process is close to zero, indicating that the contribution of the entropy on the reaction is almost null. On the other hand, negative ΔS_{ads} values have been obtained for Cr(VI) and Pt(IV) adsorption.

The ΔS_{ads} value may be used to indicate if the adsorption process is an associative or dissociative mechanism. When ΔS_{ads} becomes greater than -10 J mol^{-1} K^{-1}, the dissociative mechanism becomes dominant, while for lower values agree with associative processes.[53] Considering these premises, ΔS_{ads} greater than -10 J mol^{-1} K^{-1} have been obtained for Ag(I), Hg(II) and Pb(II), implying a dissociative mechanism. On the contrary, lower ΔS_{ads} values resulted for Cr(VI) and Pt(IV), indicating that an associative mechanism is involved in their adsorption process.

The ΔH_{ads} related to the metal adsorption have been calculated by van't Hoff equation in most of the studies.[52,54] Considering the large uncertainties that such method present on the obtained result, the direct determination of the heat exchanged by ITC seems to be the sole way to obtain reliable heats of adsorption and calculate more accurate and robust ΔH_{ads} values.

3.3.2.4. Comparison with the literature

Nowadays, the utilization of several adsorbent materials for the sequestration of HM (due to their risk for human beings) and PM (because of the increasing demand of such metals combined with

their limited resources available) has been studied. The Table 3.15, [50,52,54–60] gives a comparison between the affinity of SPION@3-MPA prepared in this thesis and some thiol-functionalized adsorbents reported in the literature for the adsorption of HM and PM.

The synthesized SPION@3-MPA shows better affinity for Ag(I) (1.5mmol g^{-1}) than the azole modified chitosan[54] (1.40 mmol g^{-1}) or the thiol-functionalized silica[55] (0.70mmol g^{-1}). While exhibit a lower adsorption capacity regarding Pt(IV) adsorption compared with other adsorbents.

The Q_{max} obtained for Hg(II) adsorption is higher than other materials reported in the literature, showing a higher affinity, when comparing SPION@3-MPA with thiol functionalized silica[56] or respect Fe_3O_4@SiO_2–SH[50]. Therefore, the difference between the Q_{max} of synthesized material compared with those available in the literature, means that the SPION@3-MPA is a competitive material for Hg(II) adsorption.

Regarding Cr(VI) and Pb(II), the adsorption efficiency of prepared SPION@3-MPA is comparable with those materials found in the literature.[52,56–58] SPION@3-MPA present a high efficiency towards Cr(VI) (0.127mmol g^{-1}) compared with mercapto functionalized silica[58] (0.10mmol g^{-1}) but it is lower when compared to mercapto functionalized sepiolite[57] (0.16mmol g^{-1}). The same situation is observed when comparing the loading capacity for Pb(II) adsorption. SPION@3-MPA shows a higher value (0.14mmol g^{-1}) contrasted with thiol functionalized silica[56] (0.08mmol g^{-1}), however, other materials such as mercapto functionalized sepiolite[52] exhibit a higher efficiency (0.461mmol g^{-1}) than the synthesized material.

Notice that most of the materials that has reported a better efficiency than SPION@3-MPA, also show significantly higher amount of sulphur present in the adsorbent than for the synthesized material of this work. The amount of ligand on the adsorbent surface is a decisive factor for the chelate ability of the material. Hence, the capacity of an adsorbent to remove metallic ions from water will be limited by the amount of functional groups available to trap them.

It should be also highlighted that most of the materials reported in Table 3.15 present higher contact times than those applied in this study. Since the time taken for metal ions adsorption is of considerable importance for possible applications, the SPION@3-MPA presented in this work, seems to be the most effective with the minor time.

Metal	Adsorbent	S % (mmol g^{-1})	Initial M^{n+} (mM)	Adsorbent dosage (g L^{-1})	pH	Temp. (K)	Contact time (h)	Adsorption capacity (mmol g^{-1})	*b* (M^{-1})	ΔH_{ads} (kJ mol^{-1})	Ref.
Ag(I)	Chitosan/azole	2.7	-	100.0	6.7	298	6	1.40	601	-15.5	54
Ag(I)	Thiol functionalized silica	1.2 (3.79%)	0.9 - 13.3 (96-1436mg L^{-1})	6.7	6.0	298	48	0.703 (75.8 mg g^{-1})	-	-	55
Ag(I)	SPION@3-MPA	1.4	0.1 - 1.0	0.5	5.0	298	1[a]	1.5 ±0.1	92481 ±21320	-27.2 ±0.7	This work
Pb(II)	Mercapto functionalized sepiolite	1.6	0 - 0.9 (0 180mg L^{-1})	1.0	-	299	24	0.46 (95.50mg g^{-1})	(0.12mg $^{-1}$)	33.6	52
Pb(II)	Thiol functionalized silica	-	-	10.0	-	298	24	0.08 (17.1541mg g^{-1})	14110 (0.0681L mg^{-1})	-	56
Pb(II)	SPION@3-MPA	1.4	0.1 - 1.0	0.5	5.0	298	1[a]	0.14 ±0.01	20799 ±7168	-24.6 ±0.8	This work
Cr (VI)	Mercapto functionalized sepiolite	-	0.1 - 2.0 (5-100mg L^{-1})	4.0	4.5	298	-	0.16 (8.253mg g^{-1})	1924 (0.037 L mg^{-1})	-	57
Cr (VI)	Mercapto functionalized silica	2.1	0.1 - 3.0	10.0	6.0	room	24	0.10	-	-	58
Cr (VI)	SPION@3-MPA	1.4	0.1 - 1.0	0.5	5.0	298	1[a]	0.127 ±0.004	50702 ±14115	-57.1 ±0.7	This work
Hg (II)	Fe_3O_4@SiO_2–SH	0.8 (2.64%)	0.02 - 0.50 (5-100mg L^{-1})	0.2	6.5	303	4	0.74 (148.8mg g^{-1})	155 (1.290 g L^{-1})	-	50
Hg (II)	Thiol functionalized silica	-	-	10.0	-	298	24	0.93 (186.4019mg g^{-1})	14322 (0.0714 L mg^{-1})	-	56
Hg (II)	SPION@3-MPA	1.4	0.1 - 1.0	0.5	5.0	298	1[a]	1.7	137727 ±32392	-16.0 ±0.6	This work
Pt(IV)	Thiolated mesoporous silicas	2.4 (7.59%)	-	1.0	2.0	298	48	1.19 (232.6mg g^{-1})	2898948 (14.86L mg^{-1})	-	59
Pt(IV)	Straw-SH	2.71 (8.70%)	-	-	1.0	room	24	1.95 (380mg g^{-1})	-	Exothermic	60
Pt(IV)	SPION@3-MPA	1.4	0.1 - 1.0	0.5	3.0	298	2[a]	0.31 ±0.01	368483 ±129319	-50 ±2	This work

Table 3.15. Parameters of metal adsorption for several thiol-functionalized adsorbents. In parentheses, the original values in the cited references are reported. [a]Delay time between metal solution additions.

3.3.3. Conclusions

The ligand employed in this work (3-MPA) has been selected for its possible capabilities as chelator of HM and PM. In addition, the proposed synthesis does not need to use a great quantity of reactants and the ligand can be purchased in their usable form. Finally, the prepared nanoparticles functionalized with the thiol containing ligand, are easily dispersed in water for their use and also easily recovered from the aqueous media with the application of a magnetic field.

Both Langmuir and Freundlich models have been used to describe the metal adsorption process, characterizing the relationship between the metal adsorbed and the concentration remaining in solution. Langmuir model represents better experimental data for each studied metal, meaning a homogeneous adsorption.

The trend of adsorption observed by ITC for SPION@3-MPA was higher for Ag(I) and Hg(II) followed by Pt(IV) > Cr(VI) ~ Pb(II) >> Cd(II). Such results have been confirmed by ICP-OES, evidencing that ITC is a good tool for adsorbent screening. They also are in agreement with the relation of the binding of metal cations to the thiolated surface determined by the Misono softness parameter.

SPION@3-MPA is a competitive adsorbent for Ag(I), Hg(II) and Pb(II) comparable to several adsorbents found in the literature, with a maximum loading capacity of 1.7mmol of Hg(II) per gram of adsorbent. Cr(VI) anionic species are poorly adsorbed due to the repulsive electrostatic interactions between the anion and the surface negatively charged of the particles. While the recovery of Pt(IV) occurs dominantly by electrostatic attraction of the anionic chloroplatinate and the protonated thiol groups of the SPION@3-MPA.

This study proposed not only a method for metal removal, but also a new methodology for metal adsorption study by a novel combination of ITC and ICP-OES, which provides accurate thermodynamic parameters.

3.4. REFERENCES

(1) Cai, W.; Yu, J.; Mann, S. Template-Free Hydrothermal Fabrication of Hierarchically Organized ɣ-AlOOH Hollow Microspheres. *Microporous Mesoporous Mater.* 2009, *122* (1–3), 42–47.

(2) Cai, W.; Yu, J.; Gu, S.; Jaroniec, M. Facile Hydrothermal Synthesis of Hierarchical Boehmite: Sulfate-Mediated Transformation from Nanoflakes to Hollow Microspheres. *Cryst. Growth Des.* 2010, *10* (9), 3977–3982.

(3) Thommes, M.; Kaneko, K.; Neimark, A. V.; Olivier, J. P.; Rodriguez-Reinoso, F.; Rouquerol, J.; Sing, K. S. W. Physisorption of Gases, with Special Reference to the Evaluation of Surface Area and Pore Size Distribution (IUPAC Technical Report). *Pure Appl. Chem.* 2015, *87* (9–10), 1051–1069.

(4) Lowell, S.; Shields, J. E.; Thomas, M. A.; Thommes, M. *Characterization of Porous Solids and Powders: Surface Area, Pore Size and Density*; Particle Technology Series; Springer Science+Business Media: New York, 2004.

(5) Sing, K.; Williams, R. Physisorption Hysteresis Loops and the Characterization of Nanoporous Materials. *Adsorpt. Sci. Technol.* 2004, *22* (10), 773–782.

(6) Tripathy, S. S.; Bersillon, J. L.; Gopal, K. Removal of Fluoride from Drinking Water by Adsorption onto Alum-Impregnated Activated Alumina. *Sep. Purif. Technol.* 2006, *50*, 310–317.

(7) Sujana, M. G.; Soma, G.; Vasumathi, N.; Anand, S. Studies on Fluoride Adsorption Capacities of Amorphous Fe/Al Mixed Hydroxides from Aqueous Solutions. *J. Fluor. Chem.* 2009, *130* (8), 749–754.

(8) Chai, L.; Wang, Y.; Zhao, N.; Yang, W.; You, X. Sulfate-Doped Fe3O4/Al2O3 Nanoparticles as a Novel Adsorbent for Fluoride Removal from Drinking Water. *Water Res.* 2013, *47* (12), 4040–4049.

(9) Cui, H.; Li, Q.; Gao, S.; Shang, J. K. Strong Adsorption of Arsenic Species by Amorphous Zirconium Oxide Nanoparticles. *J. Ind. Eng. Chem.* 2012, *18* (4), 1418–1427.

(10) Su, Y.; Cui, H.; Li, Q.; Gao, S.; Shang, J. K. Strong Adsorption of Phosphate by Amorphous Zirconium Oxide Nanoparticles. *Water Res.* 2013, *47* (14), 5018–5026.

(11) Du, J.; Sabatini, D. A.; Butler, E. C. Synthesis, Characterization, and Evaluation of Simple Aluminum-Based Adsorbents for Fluoride Removal from Drinking Water. *Chemosphere* 2014, *101*, 21–27.

(12) Lv, L.; He, J.; Wei, M.; Evans, D.; Zhou, Z. Treatment of High Fluoride Concentration Water by MgAl-CO3 Layered Double Hydroxides: Kinetic and Equilibrium Studies. *Water Res.* 2007, *41* (7), 1534–1542.

(13) Mcbride, M. B.; Wessellnk, L. G. Chemisorpton of Catechol on Gibbsite, Boehmite, and Noncrystalline Alumina Surfaces. *Environ. Sci. Technol.* 1988, *22* (6), 703–708.

(14) Li, Y. H.; Wang, S. G.; Cao, a Y.; Zhao, D.; Zhang, X. F.; Xu, C. L.; Luan, Z. K.; Ruan, D. B.; Liang, J.; Wu, D. H.; et al. Adsorption of Fluoride from Water by Amorphous Alumina Supported on Carbon Nanotubes, Chem. *Phys. Lett.* 2001, *350* (December), 412–416.

(15) Kang, D.; Tong, S.; Yu, X.; Ge, M. Template-Free Synthesis of 3D Hierarchical Amorphous Aluminum Oxide Microspheres with Broccoli-like Structure and Their Application in Fluoride Removal. *RSC Adv.* 2015, *5* (25), 19159–19165.

(16) Bhatnagar, A.; Minocha, A. K.; Sillanpää, M. Adsorptive Removal of Cobalt from Aqueous Solution by Utilizing Lemon Peel as Biosorbent. *Biochem. Eng. J.* 2010, *48* (2), 181–186.

(17) Drago, R. S.; Dias, S. C.; Torrealba, M.; de Lima, L. Calorimetric and Spectroscopic Investigation of the Acidity of HZSM-5. *J. Am. Chem. Soc.* 1997, *119* (19), 4444–4452.

(18) Arakaki, L. N. H.; Filha, V. L. S. A.; Germano, A. F. S.; Santos, S. S. G.; Fonseca, M. G.; Sousa, K. S.; Espínola, J. G. P.; Arakaki, T. Silica Gel Modified with Ethylenediamine and Succinic Acid-Adsorption and Calorimetry of Cations in Aqueous Solution. *Thermochim. Acta* 2013, *556*, 34–40.

(19) Zhao, X.; Wang, J.; Wu, F.; Wang, T.; Cai, Y.; Shi, Y.; Jiang, G. Removal of Fluoride from Aqueous Media by Fe3O4@Al(OH)3 Magnetic Nanoparticles. *J. Hazard. Mater.* 2010, *173*, 102–109.

(20) Jagtap, S.; Yenkie, M. K. N.; Labhsetwar, N.; Rayalu, S. Defluoridation of Drinking Water Using Chitosan Based Mesoporous Alumina. *Micropor. Mesopor. Mat.* 2011, *142* (2–3), 454–463.

(21) Kumar, E.; Bhatnagar, A.; Kumar, U.; Sillanpää, M. Defluoridation from Aqueous Solutions by Nano-Alumina: Characterization and Sorption Studies. *J. Hazard. Mater.* 2011, *186* (2–3), 1042–1049.

(22) Gong, W. X.; Qu, J. H.; Liu, R. P.; Lan, H. C. Adsorption of Fluoride onto Different Types of Aluminas. *Chem. Eng. J.* 2012, *189–190*, 126–133.

(23) Zhu, B.-S. S.; Jia, Y.; Jin, Z.; Sun, B.; Luo, T.; Yu, X.-Y. Y.; Kong, L.-T. T.; Huang, X.-J. J.; Liu, J.-H. H. Controlled Synthesis of Natroalunite Microtubes and Spheres with Excellent Fluoride Removal Performance. *Chem. Eng. J.* 2015, *271*, 240–251.

(24) Zhu, J.; Lin, X.; Wu, P.; Zhou, Q.; Luo, X. Applied Surface Science Fluoride Removal from Aqueous Solution by Al(III)– Zr (IV) Binary Oxide Adsorbent. *Appl. Surf. Sci.* 2015, *357*, 91–100.

(25) Mohapatra, M.; Rout, K.; Singh, P.; Anand, S.; Layek, S.; Verma, H. C.; Mishra, B. K. Fluoride Adsorption Studies on Mixed-Phase Nano Iron Oxides Prepared by Surfactant Mediation-Precipitation Technique. *J. Hazard. Mater.* 2011, *186* (2–3), 1751–1757.

(26) Wen, S.; Wang, Y.; Dong, S. Performance and Characteristics of Fluoride Adsorption Using Nanomagnetite graphite–La Adsorbent. *RSC Adv.* 2015, *5* (109), 89594–89602.

(27) Lin, K. Y. A.; Liu, Y. T.; Chen, S. Y. Adsorption of Fluoride to UiO-66-NH2 in Water: Stability, Kinetic, Isotherm and Thermodynamic Studies. *J. Colloid Interface Sci.* 2016, *461*, 79–87.

(28) Li, W.; Cao, C. Y.; Wu, L. Y.; Ge, M. F.; Song, W. G. Superb Fluoride and Arsenic Removal Performance of Highly Ordered Mesoporous Aluminas. *J. Hazard. Mater.* 2011, *198*, 143–150.

(29) Vithanage, M.; Rajapaksha, A. U.; Bootharaju, M. S.; Pradeep, T. Surface Complexation of Fluoride at the Activated Nano-Gibbsite Water Interface. *Colloids Surfaces A Physicochem. Eng. Asp.* 2014, *462*, 124–130.

(30) Yang, C.; Gao, L.; Wang, Y.; Tian, X.; Komarneni, S. Fluoride Removal by Ordered and Disordered Mesoporous Aluminas. *Micropor. Mesopor. Mat.* 2014, *197*, 156–163.

(31) Cai, H.; Chen, G.; Peng, C.; Xu, L.; Zhu, X.; Zhang, Z.; Dong, Y.; Shang, G.; Ke, F.; Gao, H.; et al. Enhanced Removal of Fluoride by Tea Waste Supported Hydrous Aluminium Oxide Nanoparticles: Anionic Polyacrylamide Mediated Aluminium Assembly and Adsorption Mechanism. *RSC Adv.* 2015, *5*, 29266–29275.

(32) Cai, H.-M.; Chen, G.-J.; Peng, C.-Y.; Zhang, Z.-Z.; Dong, Y.-Y.; Shang, G.-Z.; Zhu, X.-H.; Gao, H.-J.; Wan, X.-C. Removal of Fluoride from Drinking Water Using Tea Waste Loaded with Al/Fe Oxides: A Novel, Safe and Efficient Biosorbent. *Appl. Surf. Sci.* 2015, *328*, 34–44.

(33) Camacho, L. M.; Torres, A.; Saha, D.; Deng, S. Adsorption Equilibrium and Kinetics of Fluoride on Sol-Gel-Derived Activated Alumina Adsorbents. *J. Colloid Interface Sci.* 2010, *349* (1), 307–313.

(34) Medellin-Castillo, N. A.; Leyva-Ramos, R.; Padilla-Ortega, E.; Perez, R. O.; Flores-Cano, J. V.; Berber-Mendoza, M. S. Adsorption Capacity of Bone Char for Removing Fluoride from Water Solution. Role of Hydroxyapatite Content, Adsorption Mechanism and Competing Anions. *J. Ind. Eng. Chem.* 2014, *20* (6), 4014–4021.

(35) Jin, Z.; Jia, Y.; Luo, T.; Kong, L. T.; Sun, B.; Shen, W.; Meng, F. L.; Liu, J. H. Efficient Removal of Fluoride by Hierarchical MgO Microspheres: Performance and Mechanism Study. *Appl. Surf. Sci.* 2015, *357*, 1080–1088.

(36) Dong, S.; Wang, Y. Characterization and Adsorption Properties of a Lanthanum-Loaded Magnetic Cationic Hydrogel Composite for Fluoride Removal. *Water Res.* 2016, *88*, 852–860.

(37) Hamdi, N.; Srasra, E. Removal of Fluoride from Acidic Wastewater by Clay Mineral: Effect of Solid-Liquid Ratios. *Desalination* 2007, *206* (1–3), 238–244.

(38) Kemer, B.; Ozdes, D.; Gundogdu, A.; Bulut, V. N.; Duran, C.; Soylak, M. Removal of Fluoride Ions from Aqueous Solution by Waste Mud. *J. Hazard. Mater.* 2009, *168* (2–3), 888–894.

(39) Bhatnagar, A.; Kumar, E.; Sillanpää, M. Fluoride Removal from Water by Adsorption-A Review. *Chem. Eng. J.* 2011, *171* (3), 811–840.

(40) Warner, C. L.; Addleman, R. S.; Cinson, A. D.; Droubay, T. C.; Engelhard, M. H.; Nash, M. A.; Yantasee, W.; Warner, M. G. High-Performance, Superparamagnetic, Nanoparticle-Based Heavy Metal Sorbents for Removal of Contaminants from Natural Waters. *ChemSusChem* 2010, *3* (6), 749–757.

(41) Pournara, A.; Kovala-Demertzi, D.; Kourkoumelis, N.; Georgakopoulos, S.; Kostas, I. D. Platinum/3,3'-thiodipropionic Acid Nanoparticles as Recyclable Catalysts for the Selective Hydrogenation of Trans-Cinnamaldehyde. *Catal. Commun.* 2014, *43*, 57–60.

(42) Kumar, R.; Inbaraj, B. S.; Chen, B. H. Surface Modification of Superparamagnetic Iron Nanoparticles with Calcium Salt of Poly(ɣ-Glutamic Acid) as Coating Material. *Mater. Res. Bull.* 2010, *45*, 1603–1607.

(43) Burks, T.; Avila, M.; Akhtar, F.; Göthelid, M.; Lansåker, P. C.; Toprak, M. S.; Muhammed, M.; Uheida, A. Studies on the Adsorption of chromium(VI) onto 3-Mercaptopropionic Acid Coated Superparamagnetic Iron Oxide Nanoparticles. *J. Colloid Interface Sci.* 2014, *425*, 36–43.

(44) Shen, L.; Laibinis, P. E.; Hatton, T. A. Bilayer Surfactant Stabilized Magnetic Fluids: Synthesis and Interactions at Interfaces. *Langmuir* 1999, *15* (2), 447–453.

(45) Yean, S.; Cong, L.; Yavuz, C. T.; Mayo, J. T.; Yu, W. W.; Kan, A. T.; Colvin, V. L.; Tomson, M. B. Effect of Magnetite Particle Size on Adsorption and Desorption of Arsenite and Arsenate. *J. Mater. Res.* 2005, *20* (12), 3255–3264.

(46) Morillo, D.; Uheida, A.; Pérez, G.; Muhammed, M.; Valiente, M. Arsenate Removal with 3-Mercaptopropanoic Acid-Coated Superparamagnetic Iron Oxide Nanoparticles. *J. Colloid Interface Sci.* 2015, *438*, 227–234.

(47) Pearson, G. Hard and Soft Acids and Bases. *J. Am. Chem. Soc.* 1963, *85* (22), 3533–3539.

(48) Mattigod, S. V.; Parker, K.; Fryxell, G. E. Correlation of Heavy Metal Binding Capacity of Thiol-SAMMS Using the Misono Softness Parameter. *Inorg. Chem. Commun.* 2006, *9* (1), 96–98.

(49) Misono, M.; Ochiai, E.; Saito, Y.; Yoneda, Y. A New Dual Parameter Scale for the Strength of Lewis Acids and Bases with the Evaluation of Their Softness. *J. Inorg. Nucl. Chem.* 1967, *29* (11), 2685–2691.

(50) Zhang, S.; Zhang, Y.; Liu, J.; Xu, Q.; Xiao, H.; Wang, X.; Xu, H.; Zhou, J. Thiol Modified Fe3O4@SiO2 as a Robust, High Effective, and Recycling Magnetic Sorbent for Mercury Removal. *Chem. Eng. J.* 2013, *226*, 30–38.

(51) Pan, S.; Shen, H.; Xu, Q.; Luo, J.; Hu, M. Surface Mercapto Engineered Magnetic Fe3O4 Nanoadsorbent for the Removal of Mercury from Aqueous Solutions. *J. Colloid Interface Sci.* 2012, *365* (1), 204–212.

(52) Liang, X.; Xu, Y.; Wang, L.; Sun, Y.; Lin, D.; Sun, Y.; Qin, X.; Wan, Q. Sorption of Pb2+ on Mercapto Functionalized Sepiolite. *Chemosphere* 2013, *90* (2), 548–555.

(53) Yari, S.; Abbasizadeh, S.; Mousavi, S. E.; Moghaddam, M. S.; Moghaddam, A. Z. Adsorption of Pb(II) and Cu(II) Ions from Aqueous Solution by an Electrospun CeO_2 Nanofiber Adsorbent Functionalized with Mercapto Groups. *Process Saf. Environ. Prot.* 2015, *94* (C), 159–171.

(54) Elwakeel, K. Z.; El-Sayed, G. O.; Darweesh, R. S. Fast and Selective Removal of silver(I) from Aqueous Media by Modified Chitosan Resins. *Int. J. Miner. Process.* 2013, *120*, 26–34.

(55) Quang, D. V.; Lee, J. E.; Kim, J. K.; Kim, Y. N.; Shao, G. N.; Kim, H. T. A Gentle Method to Graft Thiol-Functional Groups onto Silica Gel for Adsorption of Silver Ions and Immobilization of Silver Nanoparticles. *Powder Technol.* 2013, *235*, 221–227.

(56) Rostamian, R.; Najafi, M.; Rafati, A. A. Synthesis and Characterization of Thiol-Functionalized Silica Nano Hollow Sphere as a Novel Adsorbent for Removal of Poisonous Heavy Metal Ions from Water: Kinetics, Isotherms and Error Analysis. *Chem. Eng. J.* 2011, *171* (3), 1004–1011.

(57) Marjanović, V.; Lazarević, S.; Janković-Častvan, I.; Potkonjak, B.; Janaćković, D.; Petrović, R. Chromium (VI) Removal from Aqueous Solutions Using Mercaptosilane Functionalized Sepiolites. *Chem. Eng. J.* 2011, *166* (1), 198–206.

(58) Bois, L.; Bonhommé, A.; Ribes, A.; Pais, B.; Raffin, G.; Tessier, F. Functionalized Silica for Heavy Metal Ions Adsorption. *Colloids Surfaces A Physicochem. Eng. Asp.* 2003, *221* (1–3), 221–230.

(59) Barczak, M.; Dobrzyńska, J.; Oszust, M.; Skwarek, E.; Ostrowski, J.; Zięba, E.; Borowski, P.;

Dobrowolski, R. Synthesis and Application of Thiolated Mesoporous Silicas for Sorption, Preconcentration and Determination of Platinum. *Mater. Chem. Phys.* 2016, *181*, 126–135.

(60) Wang, J.; Li, J.; Wei, J. Adsorption Characteristics of Noble Metal Ions onto Modified Straw Bearing Amine and Thiol Groups. *J. Mater. Chem. A* 2015, *3* (35), 18163–18170.

4. GENERAL CONCLUSIONS

In this PhD thesis, synthesized nanostructured materials have been applied for the adsorption of pollutants such as fluoride, HM and PM from aqueous media. These materials have been chosen because of the high surface area that they offer in a very small volume. Therefore, they present ideal characteristics as adsorbent materials for the treatment of wastewater. This thesis work has been divided in two main sections, the first one regards the fluoride adsorption on HAM, while the second one focuses on the removal of heavy and precious metals by using functionalized SPION as adsorbent material.

In both cases the adsorption process has been described in terms of loading capacity and thermodynamic parameters. The loading capacity has been determined by standard methods, while the adsorption enthalpy has been determined directly by Isothermal Titration Calorimetry. In previous works reported in the literature, the enthalpy related to the pollutant adsorption process has been always calculated by van't Hoff equation. However, several studies evidenced the large uncertainties of such method. Therefore, ITC is a good tool for the determination of the adsorption enthalpy, providing more accurate and robust thermodynamic parameters.

The main conclusions for the study of the adsorption of fluoride on HAM are:

- Two new HAM adsorbents have been synthesized and used for fluoride removal.
- The characterization of the materials reveal a high porous structure of amorphous alumina for both HAM, differing mostly in crystallinity (being type A less crystalline).
- The kinetic study reveals a bi-exponential model indicating a two-step process for fluoride adsorption.
- The adsorption experiments evidenced that the amorphous HAM (type A) have a superior affinity for F^- ion than type B, being the Langmuir constant about 1 order of magnitude higher.
- A high efficiency towards defluoridation has been obtained, with a maximum loading capacity of 0.026 moles of fluoride per gram of material, which is significantly better than other materials reported in the literature.
- The combined potentiometric-ITC method has been used to calculate the adsorption parameters and, for the first time, to obtain the ΔH_{ads} value by direct measurement of the heat associated to the process.
- Clearly negative enthalpy values for fluoride adsorption are obtained.
- Several investigations revealed serious discrepancies between the enthalpy calculated by van't Hoff equation or by ITC, related to the propagated uncertainties of the equilibrium constant

and the variations in the heat capacity at different temperatures. Therefore, ITC is a good tool to measure the ΔH_{ads} with excellent accuracy.

Regarding the study of HM and PM on functionalized SPION, it may be concluded:

- The ligand employed in this work (3-MPA) has been selected for its possible capabilities as chelator of HM and PM.
- The prepared modified nanoparticles, are easily dispersed in water for their use and also easily recovered from the aqueous media with the application of a magnetic field.
- Both Langmuir and Freundlich models have been used to describe the metal adsorption process, being the Langmuir isotherm the better representation of experimental data for each studied metal (meaning a homogeneous adsorption).
- The trend of adsorption observed by ITC for SPION@3-MPA was a higher thermal effect for Ag(I) and Hg(II), followed by Pt(IV) > Cr(VI) ~ Pb(II) >> Cd(II).
- Calorimetric results have been confirmed by ICP-OES, evidencing that ITC is a good tool for adsorbent screening.
- SPION@3-MPA is a competitive adsorbent for Ag(I), Hg(II) and Pb(II) comparable to several adsorbents found in the literature, with a maximum loading capacity of 1.7mmol of Hg(II) per gram of adsorbent.
- Cr(VI) anionic species are poorly adsorbed due to the repulsive electrostatic interactions between the anion and the surface negatively charged of the particles.
- The recovery of Pt(IV) occurs dominantly by electrostatic attraction of the anionic chloroplatinate and the protonated thiol groups of the SPION@3-MPA.
- This study proposed not only a method for metal removal, but also a new methodology for metal adsorption study by a novel combination of ITC and ICP-OES, which provides accurate thermodynamic parameters.

ANNEX

National and international congress contributions

- Poster presentation: Marilena Tolazzi, Sara Gràcia, Manuel Valiente, Andrea Melchior "Heavy and precious metal adsorption from water by spion functionalized with 3-mercaptopropionic acid" AICAT 2016 – XXXVIII Convegno Nazionale, 21-23 September 2016, Lecce (Italy).
- Poster presentation: Sara Gràcia, Andrea Melchior, Manuel Valiente, Marilena Tolazzi "SPION functionalized with 3-MPA for metal adsorption" AICIng 2016 – X Convegno Nazionale, 11-14 September 2016, Udine (Italy).
- Oral presentation: Sara Gràcia, Andrea Melchior, Manuel Valiente, Marilena Tolazzi: "Efficient Fluoride Adsorption by mesoporous Hierarchical Alumina Microspheres" International Symposia on Metal Complexes – ISMEC, Volume 6 - ISMEC 2016, 7-10 June 2016, Barcelona (Spain).
- Invited communication (Andrea Melchior): Andrea Melchior, Clotilde Gaillard, Sara Gràcia, Marilena Tolazzi, Isabelle Billard: *"Speciation and structure of the Ni(II)/nitrate system in BumimTf2N Ionic Liquid"* International Symposium on Metal Complexes – ISMEC – Volume 5 -ISMEC 2015, 24-28 June 2015, Wrocław (Poland).
- Oral presentation: Andrea Melchior, Sara Gràcia, Manuel Valiente, Marilena Tolazzi: *"Caratterizzazione di farmaci e nanocarriers mediante metodi termodinamici, spettroscopici e teorici*" PRIN Meeting: Nanomed (Workshop on Nanomaterials for biomedical applications), 23-24 April 2015, Bologna (Italy).
- Poster presentation: Andrea Melchior, Sara Gràcia, Manuel Valiente, Marilena Tolazzi "*Thermodynamics of fluoride adsorption onto mesoporous alumina nanoparticles*" AICIng 2014 – IX Convegno Nazionale, 14-17 September 2014, Lecce (Italy).
- Poster presentation: Sara Gràcia, Andrea Melchior, Manuel Valiente, Marilena Tolazzi: "*Potentiometric and calorimetric study of fluoride adsorption onto mesoporous alumina nanoparticles*" International Symposia on Metal Complexes – ISMEC, Volume 4 - ISMEC 2014, 8-12 June 2014, Pavia (Italy).

Publications

- Sara Gràcia Lanas, Manuel Valiente, Eleonora Aneggi, Alessandro Trovarelli, Marilena Tolazzi and Andrea Melchior. *Efficient fluoride adsorption by mesoporous hierarchical alumina microspheres.* RSC Adv., 2016. Accepted - DOI: 10.1039/c5ra27371d

The next publication concerns a different topic of the thesis work. However, it is relevant since the contribution in this paper has been performed applying the knowledge about the ITC acquired during the PhD thesis:

- Andrea Melchior, Clotilde Gaillard, Sara Gràcia Lanas, Marilena Tolazzi, Isabelle Billard, Sylvia Georg, Lola Sarrasin, and Maria Boltoeva. *Nickel(II) Complexation with Nitrate in Dry [C4mim][Tf2N] Ionic Liquid: A Spectroscopic, Microcalorimetric, and Molecular Dynamics Study*. I*norg. Chem.,* 2016, *55* (7), pp 3498–3507.

RSC Advances

PAPER

Cite this: *RSC Adv.*, 2016, **6**, 42288

Efficient fluoride adsorption by mesoporous hierarchical alumina microspheres†

Sara Gràcia Lanas,[a] Manuel Valiente,[b] Eleonora Aneggi,[a] Alessandro Trovarelli,[a] Marilena Tolazzi[a] and Andrea Melchior*[a]

Received 21st December 2015
Accepted 18th April 2016

DOI: 10.1039/c5ra27371d

www.rsc.org/advances

Mesoporous Hierarchical Alumina Microspheres (HAM) with high efficiency for fluoride removal have been synthesized and characterized. Two types of HAM, differing mostly in crystallinity, surface area and pore size have been obtained. Fluoride adsorption studies have been carried out by means of potentiometry and Isothermal Titration Calorimetry (ITC). The latter method has been applied for the first time to obtain direct determination of the adsorption enthalpy (ΔH_{ads}) of F^- ion on HAM. The kinetics of the reaction revealed a two-step process for fluoride adsorption on the adsorbent material. The ΔH_{ads} values obtained are clearly negative for the different samples investigated. Experimental adsorption data are well fitted by a Langmuir isotherm. The adsorption constant obtained for type A is 1 order of magnitude higher than for type B, showing that the synthetic protocol has a remarkable effect on this parameter. The highest defluoridation capacity reaches 26 mmol g^{-1} after 1 hour of equilibration for the amorphous HAM, which is higher than for other adsorbents reported in the literature.

Introduction

Groundwater contamination by fluoride is recognized as a serious problem worldwide, as fluoride can be toxic to humans in the case of chronic exposure to elevated concentrations.[1] Minerals containing fluoride are used by industries for several purposes such as glass and ceramic production, semiconductor manufacturing, brick and iron works, aluminum smelters and phosphate fertilizers.[1,2] Aside from natural geological fluoride enrichment of groundwater, anthropogenic contamination can elevate fluoride concentrations from ten to thousands of mg L^{-1}, much higher than the standard level recommended by the World Health Organization (1.5 mg L^{-1}).[1]

Fluoride absorbed by consumption of contaminated water is rapidly distributed through the body and integrated into the teeth and bones. The prolonged assumption of fluoride can cause several diseases, such as skeletal fluorosis.[1] Many health issues caused by fluoride consumption are irreversible,[3] thus it is necessary to control the fluoride concentration in drinking water.

The available water defluoridation methods include: adsorption,[3–12] precipitation,[13] electro-coagulation[14] or ion-exchange.[15] Among these technologies, adsorption seems to be most powerful method for fluoride removal from contaminated water, since it offers simplicity of plant design and lower energy and operative costs.[16]

Several materials have been tested for water defluoridation, for example alumina (Al_2O_3),[7,17] biosorbents,[18] clays[19] and composite materials.[20] However, most of fluoride sorption methods are unable to reach the concentration limit requested by international regulations (1.5 mg L^{-1})[1] thus, the optimization of materials for water defluoridation is still an actual challenge.

Alumina is recognized as one of the most effective materials for fluoride removal because of the high surface area and porosity, thermal stability and low solubility in a wide pH range.[21] For this application, several mesoporous alumina-based materials have been developed by modifying the original substrate and showed interesting defluoridation capacity.[6,9,22–24]

Hierarchically structured metal oxides have been recently employed in a wide range of applications from adsorption,[12,25,26] drug delivery,[27] catalysis,[28] to sensors[29] and electronic conversion and storage.[30] Among them, alumina-based hierarchical structures received a special attention due to its low cost and eco-friendly properties.[12]

The scope of this work is to study fluoride adsorption by high surface hierarchical alumina microspheres (HAM) and characterize the adsorption process in terms of loading capacity and thermodynamics.

HAM have been prepared and characterized by modification of standard methods, while adsorption studies have been carried out using a unique experimental approach, which combines potentiometry and Isothermal Titration Calorimetry (ITC).

[a]*Dipartimento Politecnico, Laboratori di Tecnologie Chimiche, Università di Udine, via del Cotonificio 108, 33100 Udine, Italy. E-mail: andrea.melchior@uniud.it*

[b]*Departamento de Quimica, Centre GTS, Universitat Autònoma de Barcelona, Campus Bellaterra Edificio CN, Barcelona, Spain*

† Electronic supplementary information (ESI) available. See DOI: 10.1039/c5ra27371d

In particular, ITC is an extremely powerful and high sensitive technique able to directly provide the heat evolved in a chemical process and then obtain useful information, such as stability constants and reaction enthalpy values. This technique has been hitherto widely used for the study of chemical equilibria in solution[31–35] and biomolecular interactions,[36] while only a limited number of examples of its application in adsorption studies can be found in the literature.[37–44]

Accurate data on the enthalpy associated to the adsorption process allow the design of the best conditions both for the uptake and for the eventual successive release of a given chemical species. In previous works, fluoride adsorption has been often modeled with Langmuir isotherm[5,7] and the associated enthalpy (ΔH_{ads}) has been calculated by the van't Hoff equation (using the temperature dependence of the Langmuir adsorption constant). However, many studies considered the discrepancies between enthalpy values obtained directly (ITC) and from van't Hoff equation and evidenced the large uncertainties associated to the latter method.[45–47] In this work, ITC is applied for the first time to obtain direct determination of ΔH_{ads} for fluoride ion adsorption by HAM to provide independent and more robust thermodynamic parameters.

Materials and methods

Synthesis of adsorbent material

Two types of HAM were synthesized using the methodology reported previously[48–50] with some modifications. All the reagents were of the analytical grade and used without any further purification. In a typical synthesis, a solution 0.05 M in aluminum sulfate and 0.1 M in urea was prepared in 100 mL of distilled water and then stirred thoroughly during 15 minutes. Then 35 mL of the prepared solution were added in a Teflon-lined digestion vessel of 100 mL capacity and then placed on a turntable for uniform heating using a microwave digestion system. The microwave treatment was conducted in a temperature-controlled mode at 180 °C by non-pulse heating time for 3 min (type A) or 20 min (type B), using 2.45 GHz microwave radiation under power range of 0–1000 W (using maximum power). Afterwards the sample was left for cooling until ambient temperature was reached. The pH of the resultant solution was adjusted at ~9 with NaOH. The synthesized material was then collected by centrifugation and washed with hot distilled water and ethanol several times. The precipitate was dried in an oven at 80 °C for 12 h. In order to convert the resulting γ-AlOOH obtained in this synthesis into Al_2O_3, the powder was calcinated in a muffle furnace at 600 °C for 2 hours.

Material characterization

The particles were analyzed by transmission electron microscopy (TEM) using a Transmission Electronic Microscope JEM-2011, resolution: 0.18 nm at 200 kV, accelerating voltage: 80–200 kV, equipped with camera: CCD GATAN 895 USC 4000, detector EDS Oxford LINCA with energy resolution: 136 eV. Scanning electron microscopy (SEM) analyses were performed by MERLIN FE-SEM, ZEISS with the detector EDS Oxford LINCA X-Max and EBSD analysis Oxford Nordlys II.

Textural characteristics of all fresh samples were measured according to the Brunauer–Emmett–Teller (BET) equation by nitrogen adsorption isotherms at −196 °C. Pore size distributions were calculated by applying the Barrett–Joyner–Halenda (BJH) method to the isotherms desorption branch. These measurements were carried out in a Tristar 3000 gas adsorption analyzer (Micromeritics). Prior to the adsorption measurements, the samples were degassed at 150 °C during 1 h.

The particle size distribution was determined by dynamic light scattering (DLS) on a Horiba LB-550 Particle Size Analyzer. Around 5 mg of HAM A and B respectively were suspended in 10 mL of TISAB solution. The suspensions were sonicated during 15 min previously to the DLS measurement.

X-ray powder diffraction (XRD) patterns were determined using a Philips PW3040/60 PRO instrument (equipped with an x'celerator detector) operating at 40 kV and 40 mA with Ni-filtered Cu K_α radiation. Diffraction profiles were collected in the 2θ range of 5–100 °C with a step of 0.02 and counting time of 15 s per step.

The pH value of zero point charge (pH_{zpc}) was determined by solid addition method[2] using 0.1 M potassium chloride (KCl) solution with 20 mg L^{-1} F^-. 20 mL of the prepared solution (0.1 M KCl with fluoride) were added into a series of vessels. Then, the initial pH (pH_i) of the solutions was adjusted in the range of 3.0–10.0. After that, 15 mL of any solution were added into another vessel with 0.3 mg of the adsorbent material. The suspensions were then equilibrated for 48 h.

Once the equilibration time was reached, the final pH (pH_f) of the solutions was measured again. The difference between the final and the initial pH ($\Delta pH = pH_i - pH_f$) was plotted *versus* the pH_i. The point of zero charge is given for the point where the curve intersect with abscissa, at this point $\Delta pH = 0$. In order to confirm our results, the experiment was performed at different ionic strength, 0.1 M and 0.01 M KCl.

Potentiometry

Potentiometric studies for fluoride removal were performed adding 20 mL of 0.5 g L^{-1} HAM suspension into a vessel and then titrating with sodium fluoride (NaF) solution 80 mM. 0.5 mL of fluoride solution was added to the suspension and once the equilibrium time was expired (1 h), the fluoride concentration in solution was measured using a fluoride selective electrode (Really-Flow™ Solid-State combination fluoride-selective Electrode, Weiss Research) before the consecutive addition. The suspension was kept under stirring during the experiment and in total around 9–13 equal-volume additions were made for each experiment.

The experiments were performed in total ionic strength adjustment buffer (TISAB), which was prepared following the procedure described.[51] At the pH fixed by TISAB solution, the formation of hydrofluoric acid (HF) is negligible and the concentration of hydroxyls (OH^-), the only other anion that the electrode responds to, is insignificant.

Potentiometric data have been fitted both with Langmuir and Freundlich isotherms at different temperatures (298.15 and 318.15 K).[5–8,52] The Langmuir isotherm describes an

homogeneous sorption, where all active sites have equal affinity for the adsorbate, and makes possible to obtain the value of the adsorption constant (b) and loading capacity (Q_{max}) of the HAM[53,54] according to the equation:

$$[F^-]_{ads} = \frac{Q_{max} b [F^-]_e}{1 + b[F^-]_e} \quad (1)$$

where: $[F^-]_e$ = equilibrium fluoride concentration (M), $[F^-]_{ads}$ = fluoride adsorbed at equilibrium (mol g^{-1}), Q_{max} = maximum quantity of adsorbed F^- per gram of HAM (mol g^{-1}) and b = Langmuir constant (M^{-1}).

Freundlich isotherm specifies the adsorption for heterogeneous surfaces characterized by the heterogeneity factor $1/n$ represented by equation:

$$[F^-]_{ads} = K_f [F^-]_e^{\frac{1}{n}} \quad (2)$$

K_f is the Freundlich constant ((L $mmol^{-1}$ $g^{-1})^{1/n}$).

Additional batch titrations were performed for sample A only. In a typical experiment, 20 mL of fluoride solutions with different initial concentrations (0.5–16 mM) were mixed with 10 mg of HAM for a specified contact time (1 h) at 298.15 K. After the equilibrium, fluoride concentration was then measured using the fluoride selective electrode.

Isothermal titration calorimetry

Fluoride samples and the standard solutions for calorimetric studies were also prepared in TISAB buffer. ITC experiments have been carried out at 298.15 K using a TAMIII thermostat (TA Instruments) equipped with a nanocalorimeter (1 mL cell volume) and an automatic titration syringe. The sample was stirred continuously at 90 rpm and the reference cell was filled with 0.8 mL of distilled water throughout all experiments.

In a typical experiment, about 10 additions of 17.5 μl of 80 mM fluoride solution were added to 0.7 mL of ~0.5 g L^{-1} HAM suspension. The delay time between two consecutive injections was set to 60 min, which was long enough to let the system to reach thermal equilibrium.

The values of b and Q_{max} calculated with Langmuir isotherm from potentiometric data have been used to calculate $[F^-]_e$ for each titrant addition by numerically solving eqn (1) in the experimental conditions of the calorimetric titrations. The ΔH_{ads} (kJ mol^{-1}) value has been calculated to best fit the experimental heat for the fluoride adsorption according to the modified isotherm[42] shown below:

$$q_{cum} = \frac{Q_{max} b [F^-]_e}{1 + b[F^-]_e} \Delta H_{ads} \quad (3)$$

where: q_{cum} = total heat involved in the reaction per gram of adsorbent (kJ g^{-1}). Dilution heat (q_{dil}) was also determined to correct the total heat measured (q_{meas}) by the instrument. Thereby $q_{cum} = q_{meas} - q_{dil}$, represents only the heat involved on the adsorption reaction. Data analysis has been done within the MS-Excel using Solverstat and EST utilities.[55,56]

Results and discussion

Characterization of the adsorbent material

The SEM and TEM micrographs obtained for the two samples (type A and B) do not reveal significative difference. The SEM images in Fig. 1A-i and B-i reveal flower-like hollow microspheres with a highly textured surface and smooth inner wall surface. The microspheres have a diameter of ~0.9 μm, which is significantly smaller than those obtained by the published methodology (5 μm).[48] In Fig. 1A-ii and B-ii TEM images show a magnification of the particles, where the detailed morphology of the flower-like microspheres (consisting in a randomly assembly of nanoplatelets) can be seen. The detailed TEM images given in Fig. 1A-iii and B-iii, evidence the hierarchical structure of the particles formed by the packing of nanoplatelets about 200 nm length and thin thickness. In Fig. 1A-iv and B-iv an enlargement of the nanoplatelets evidencing the smooth surface is also shown.

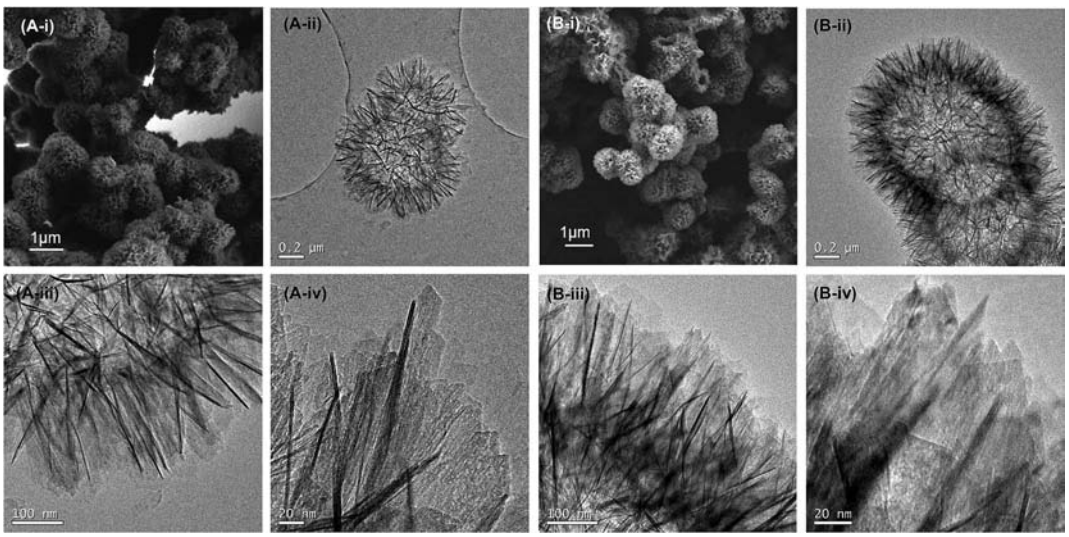

Fig. 1 SEM (A-i and B-i) and TEM (A-ii, A-iii, A-iv, B-ii, B-iii and B-iv) images of synthesized HAM of type A and B.

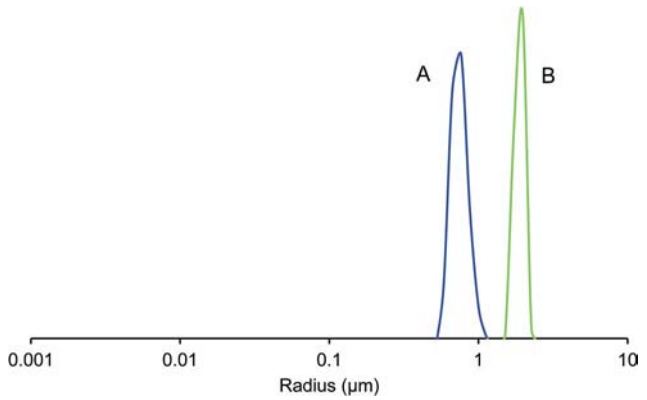

Fig. 2 Particle size distribution of HAM for type A (blue) and B (green) determined by DLS (suspension in TISAB).

In Fig. S1 (ESI†) representative SEM and TEM images of the uncalcined type B HAM are reported. It can be seen that the microspheres have the same characteristic structure of the calcined HAM, indicating that the hierarchical morphology is stable, even after high temperature treatment.

The particle size distribution of the two samples analyzed by DLS is represented in Fig. 2. In Fig. 2A it can be seen that the HAM suspension of type A was obtained with an average diameter between 0.6 and 1 μm. This value corresponds approximately with the diameter of the particles, which means that the particles aggregation is almost absent in our working conditions. The distribution of type B is shown in Fig. 2B, which indicates an average size larger than type A.

The adsorption–desorption isotherms (Fig. 3) can be classified as Type IV,[57] characteristic of mesoporous materials.[57] The H3 type-hysteresis loop[58] at high relative pressures (over pressure P/P_o of 0.7 in both types A and B) indicates the presence of mesoporous formed between the assembly of the nanoplatelets.[59] The BET surface area of the synthesized material was found to be 254.1 $m^2\ g^{-1}$ and 241.6 $m^2\ g^{-1}$ for type A and B respectively. A mesoporous material normally contains pores with diameters between 2 and 50 nm. The BJH pore size was determined to be 12.96 nm with a pore volume of 1.07 $cm^3\ g^{-1}$ for sample A and 25.55 nm and 2.32 $cm^3\ g^{-1}$ for sample B, which confirms the mesoporosity of our material. Because of the characteristic downy surface of the particles, the synthesized alumina has excellent porous properties and seems to exhibit a great potential for fluoride adsorption.

No clear peaks were observed in the diffractogram of type A (Fig. 4), indicating that the HAM are amorphous while the microspheres of type B showed some characteristic peaks for aluminum oxide in accordance with Al_2O_3 reference standard diffractogram (JCDPS card no. 10-0425). However, the low intensity of the signals evidenced that the material is a poorly crystalline solid.

It has been previously suggested that the crystallinity of alumina based adsorbents to have an influence on the fluoride adsorption capacity[60] and that low crystallinity of alumina-based materials seems to be an advantage for their adsorption capacity.[12,60–62] According to these observations, type A, in principle, would be the most efficient material for a fluoride adsorption.

The point of zero charge for both type A and B is $pH_{zpc} = 9.0$ at different ionic strength (0.1 M and 0.01 M KCl). At the working pH = 5.5, the surface of the alumina is positively charged, therefore the interaction of alumina surface with the solution containing F^- could be represented by the following reactions:[3,8,51]

$$\equiv AlOH + H^+ \leftrightarrow \equiv AlOH_2^+ \quad (4)$$

$$\equiv AlOH_2^+ + F^- \leftrightarrow \equiv AlF + H_2O \quad (5)$$

The physical features of samples A and B are summarized in Table S1.†

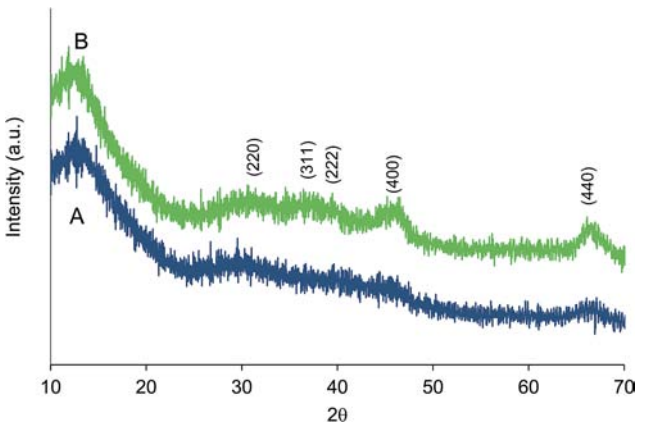

Fig. 4 X-ray diffraction (XRD) patterns of HAM for type A (blue) and B (green) samples.

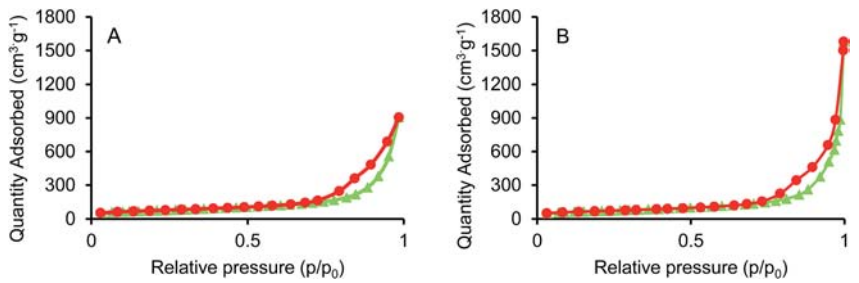

Fig. 3 N_2 adsorption (green triangles) and desorption (red circles) isotherms of HAM for type A (Fig. 2A) and sample B (Fig. 2B).

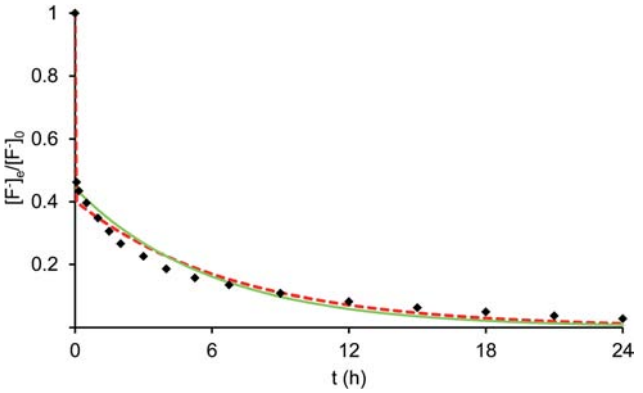

Fig. 5 Fluoride adsorption kinetics on HAM (type A, 0.5 g L^{-1}, pH = 5.5, T = 298.15 K, $[F^-]_0$ = 16 mM) fitted with mono- (green line) and bi- (dashed red line) exponential functions.

Fluoride adsorption

In Fig. 5 the $[F^-]_e/[F^-]_0$ ratio *vs.* time (h) plot for an adsorbent dose of 0.5 g L^{-1} and initial concentration of 16 mM of fluoride is shown (type A). Experimental data were fitted with both mono and bi-exponential eqn (6) and (7):

$$[F^-]_e = a_1 e^{-k_1 t} \quad (6)$$

$$[F^-]_e = a_1 e^{-k_1 t} + a_2 e^{-k_2 t} \quad (7)$$

The fitting results obtained are summarized in Table S3† in the ESI.† The bi-exponential model better fits the experimental data with respect to the mono-exponential and suggests the presence of a fast first reaction followed by a much slower process (k_2 is 3 orders of magnitude lower than k_1, Table S3†). This has also been observed for fluoride absorption by MgAl–CO_3 layered double hydroxides.[63] The fast adsorption step occurs during the first hour, then the rate decreases and, after 3 h, 75% of the initial fluoride is removed.‡

In Fig. 6, the heat evolved for each addition of fluoride to HAM suspension (for type A and B) is shown. The heat signal reaches the baseline in 60 minutes that is, the heat exchanged related to the F^- adsorption on the HAM expires in 1 hour. Although the equilibrium is not yet reached according to the overall reaction model (Fig. 5), in ITC experiments it seems that only the first process produces a detectable thermal effect. Therefore, calorimetric experiments were analyzed by using $[F^-]_e$ values calculated from potentiometric data with the same delay time between additions (60 min) as in calorimetry (Table 1).

Potentiometric data for fluoride adsorption by HAM (type A and B) were fitted both with the Langmuir and Freundlich isotherms (Fig. 7) and the resulting parameters are reported in Table 1. Potentiometric batch titrations carried out for type A sample confirmed the values obtained (Fig. S2 and Table S2 in the ESI†).

‡ a_i = initial concentration for each exponential (M), k_i = constant rates (h^{-1}), t = time (h).

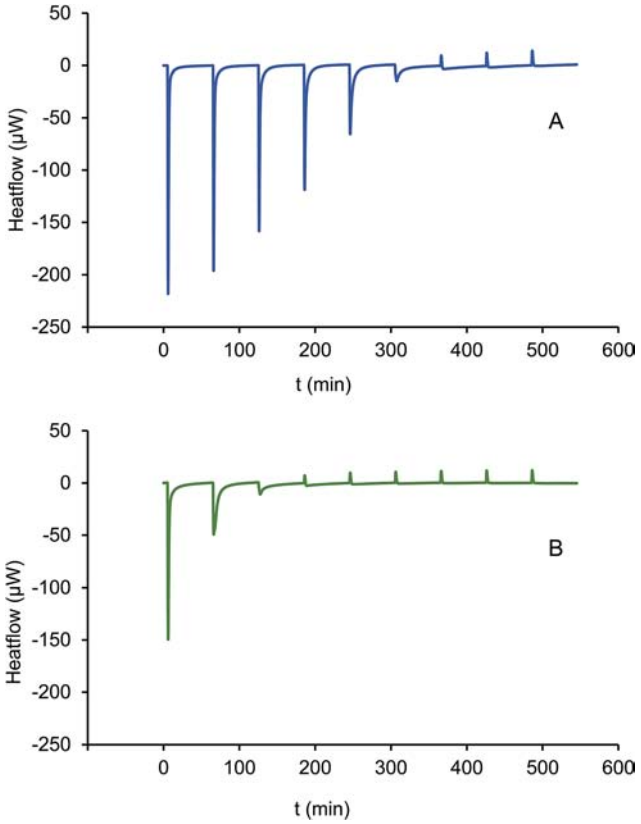

Fig. 6 ITC for fluoride adsorption into HAM of type A (blue) and type B (green). Each peak corresponds to an injection of 17.5 μl of 80 mM fluoride solution to 0.7 mL of 0.5 g L^{-1} HAM suspension.

Experimental points are better represented by the Langmuir than the Freundlich model suggesting the presence of a homogeneous anion adsorption, forming a monolayer on the positively charged surface of the microspheres. The Langmuir constant obtained for type A is significantly higher than for type B (~1 order of magnitude, Table 1) showing that the synthetic protocol has a remarkable effect on this parameter. While the difference in the BET surface areas of both samples is not remarkable, DLS experiments evidenced higher particle aggregation in type B (Fig. 2 and Table S1†). However, the higher efficiency in fluoride removal for type A than type B seems also to be related to the different crystallinity of the two samples, as previously found.[12,60–62]

The maximum loading capacity of the material (Q_{max}) results higher for sample A than sample B, being 0.026 and 0.020 moles of fluoride per gram of material, respectively. These values are higher than those found for other alumina-based adsorbents which are reported in Table 2[2,3,5–7,9–12,64–67] and for other adsorbent materials reported in Table S4 in the ESI.†[20,68–72]

The high efficiency of the HAM could be associated to the structure of the hierarchical material. As suggested,[70] the mesoporosity and the elevated surface area gives to the material a high number of active sites exposed to the surface. In addition, the particularity of the hierarchical materials avoids the aggregation of the nanoplatelets, exposing their entire surface to adsorb F^-.[70]

Table 1 Langmuir and Freundlich isotherm parameters for fluoride adsorption by HAM of type A and B with different experimental conditions

Type	Temperature (K)	Delay time (h)	Langmuir equation					Freundlich equation		
			Q_{max} (mol g^{-1})	b (M^{-1})	log b	R^2	n	K_f (L mmol^{-1} g^{-1})	log K_f	R^2
A	318.15	1	0.039 ± 0.002	4165 ± 794	3.62 ± 0.19	0.961	3.1 ± 0.5	31 ± 1	1.49 ± 0.03	0.721
A	298.15	1	0.026 ± 0.001	4563 ± 486	3.66 ± 0.11	0.979	5.9 ± 0.5	20.2 ± 0.3	1.31 ± 0.01	0.871
A	298.15	12	0.055 ± 0.001	4820 ± 394	3.68 ± 0.08	0.999	4.4 ± 0.6	42 ± 1	1.62 ± 0.02	0.847
B	298.15	1	0.020 ± 0.001	598 ± 100	2.78 ± 0.17	0.967	2.3 ± 0.1	7.6 ± 0.3	0.88 ± 0.04	0.895

Similar potentiometric experiments with 12 h delay between additions have been also performed (type A) to study the adsorption of fluoride at long times (Fig. S3†). The resulting adsorption constant is quite similar to that obtained with a 1 h delay, while the loading capacity is ~50% larger.

The experimental and calculated q_{cum} values for type A and B are shown in Fig. 8. In type B, after the third injection the heat flow measured for the remaining injections corresponds to the dilution heat indicating that the adsorption process is finished, while for type A 6 injections are needed. It is also evidenced that the total heat evolved in fluoride adsorption in type A is significantly higher than in type B, which confirms that type A is a more efficient adsorbent for fluoride removal than type B.

The process is clearly exothermic for both type A and B samples (Table 2) and, as can be observed, the adsorption enthalpy obtained for type B ($\Delta H_{ads} = -13.3 \pm 0.9$ kJ mol^{-1}) is less negative than the value obtained for type A ($\Delta H_{ads=} -17.7 \pm 0.6$ kJ mol^{-1}). The ΔH_{ads} values obtained previously by van't Hoff equation are in most cases positive[2,5,7] and spread over a wide range (6.8–36.6 kJ mol^{-1}). Nevertheless, also negative ΔH_{ads} have been reported for other alumina-based adsorbents,[3,64] natroalunite microtubes,[11] nanosized iron oxides[68] or UiO-66-NH$_2$ [72] (values ranging from −0.8 to −94.7 kJ mol^{-1}, Table 2 and S4†).

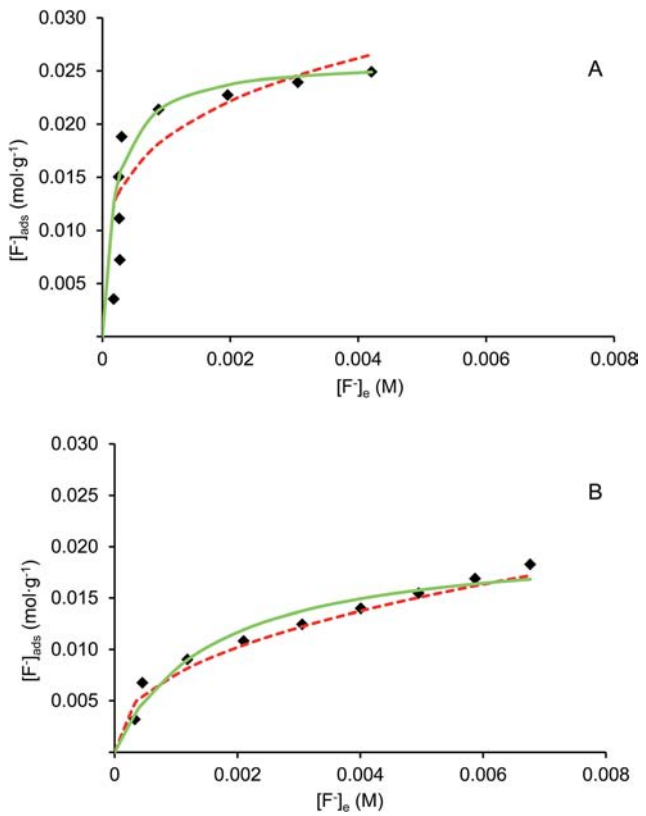

Fig. 7 Experimental fluoride adsorption isotherms presenting the experimental data fitted with Langmuir (green line) and Freundlich (dashed red line) models with 1 h between injections for type A and B.

To compare our method for the determination of ΔH_{ads} with the standard van't Hoff interpolation, normally used in previous works,[2,3,5,7,11,20,64,68,72] the adsorption parameters were determined for HAM (type A) also at 318 K (Table 1).

The ΔH_{ads} value calculated by the van't Hoff equation ($\Delta H_{ads} \sim -4$ kJ mol^{-1}), is less negative than that obtained by ITC measurements. However, when ΔH_{ads} is calculated with the van't Hoff equation, the propagated uncertainty on the ΔH_{ads} values can be large. Thus, an ideal ΔH_{ads} determined by van't Hoff equation should be calculated using very precise values of equilibrium constants and in a large range of temperature where, on the other hand, the heat capacity is not rigorously constant. Therefore, the direct determination of the heat exchanged by ITC seems to be the sole way to obtain reliable heats of adsorption and calculate ΔH_{ads} values.

It can be noticed that the $T\Delta S_{ads}$ terms (obtained from the ΔG_{ads} calculated with the b values at 298.15 K in Table 1 and the ΔH_{ads} values in Table 2) are nearly the same for the two materials (+3.2 and +2.6 kJ mol^{-1} for HAM A and B respectively). This positive entropy change is in agreement with previous results adsorption of metal cations[39,43] and reflects the increase disorder due to charge neutralization and desolvation of the fluoride anion.

Conclusions

In this work, two new HAM adsorbents have been synthesized and used for fluoride removal. SEM, TEM, BET and XRD diffraction studies reveal a high porous structure of amorphous alumina. The two types show similar physical characteristics with small differences in pore size and specific surface area. The main difference between the two samples is the presence of crystalline phase, smaller pore size and higher surface area in the one prepared with a shorter microwave treatment (type A). The kinetic study reveals a bi-exponential model indicating a two-step process for fluoride adsorption.

Fluoride adsorption experiments evidenced that the amorphous HAM (type A) have a superior affinity for F$^-$ ion than type

Table 2 Fluoride removal parameters for several alumina-based adsorbents. In parentheses the original values reported in the references

Adsorbent	Particle size	Initial F^- (mM)	Adsorbent dosage (g L^{-1})	pH	T (K)	Contact time (h)	Adsorption capacity (mmol g^{-1})	b (M^{-1})	ΔH (kJ mol^{-1})	Ref.
Nano alumina	—	0.05–5.3 (1–100 mg L^{-1})	1.0	6.15	298	24	0.8 (15.43 mg g^{-1})	3240	14.8	2
Aluminum hydroxide	—	—	0.5	4	303	2	3.4 (63.5 mg g^{-1})	623.7 (0.033 L mg^{-1})	−18.45	3
Fe_3O_4@$Al(OH)_3$	240–340 nm	0–8.5 (0–160 mg L^{-1})	1.0	6.5	298	1	4.7 (88.48 mg g^{-1})	5557 (0.2 L mg^{-1})	6.8	5
Mesoporous calcium-doped alumina	—	0.1–52.9 (2–1000 mg L−1)	0.1	6.5	298	12	23.8 (450 mg g^{-1})	—	—	6
Al_2O_3	12–15 μm	0.5–7.9 (10–150 mg L^{-1})	1.0	6	298	48	4.4 (83.33 mg g^{-1})	37 800 (2.000 L mg^{-1})	36.66	7
Ordered mesoporous alumina	300–800 nm	0.3–10.6 (5–200 mg L^{-1})	0.5	6	298	12	7.1 (135 mg g^{-1})	13 854 (0.733 L mg^{-1})	—	9
Heated nano-gibbsite	—	0.263–3.947	2.0	6.0	4	4	1.6 (30.55 mg g^{-1})	0.272	—	10
Natroalunite microtubes	—	0.3–10.6 (5–200 mg L^{-1})	1.0	7.0	298	24	4.5 (85.84 mg g^{-1})	3.750	−30.80	11
Amorphous aluminum oxide microspheres	—	0.3–7.9 (5–150 mg L^{-1})	0.5	7.0	298	—	6.7 (126.90 mg g^{-1})	7938 (0.42 L mg^{-1})	—	12
Chitosan based mesoporous alumina	—	—	2.0	6.8	303	24	0.4 (8.264 mg g^{-1})	2319 (0.1227 L mg^{-1})	−0.8	64
Tea-APAM-Al	—	0.3–10.6 (5–200 mg L^{-1})	1.0	5.0	308	3	2.2 (42.14 mg g^{-1})	1767.1 (0.09350 L mg^{-1})	—	65
Tea-Al-Fe	—	0.5–10.5 (10–200 mg L^{-1})	2.0	7.0	298	2	1.0 (18.52 mg g^{-1})	1051.9 (0.05537 L mg^{-1})	—	66
Al_2O_3–ZrO_2	—	2.6–7.9 (50–150 mg L^{-1})	1.0	2.0	318	4	6.0 (114.54 mg g^{-1})	228.0 (0.012 L mg^{-1})	−2.414	67
HAM type A	900 nm	2.0–16.0	0.5	5.5	298.15	12[a]	55.0 (1.0 g g^{-1})	4820	—	Present work
HAM type A	900 nm	2.0–16.0	0.5	5.5	298.15	1[a]	26.0 (491.4 mg g^{-1})	4563	−17.7 ± 0.6	Present work
HAM type B	900 nm	2.0–16.0	0.5	5.5	298.15	1[a]	20.4 (385.6 mg g^{-1})	598	−13.3 ± 0.9	Present work

[a] Delay time between fluoride solution additions.

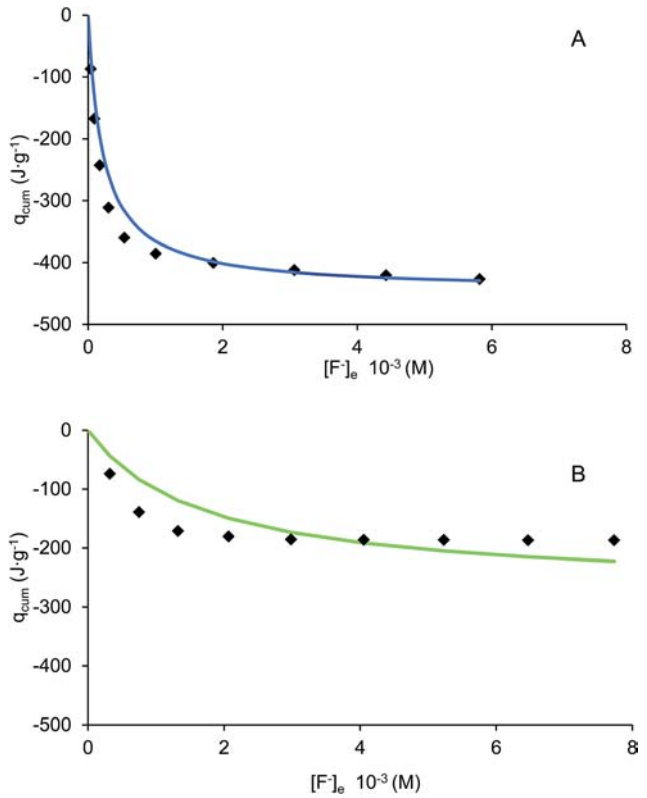

Fig. 8 Experimental calorimetric data fitted with calorimetric Langmuir isotherm (line) for type A (blue) and B (green) HAM.

B, being the Langmuir constant about 1 order of magnitude higher. Adsorption experiments have shown that synthesized materials have a high efficiency towards defluoridation, with a maximum loading capacity of 0.026 moles of fluoride per gram of material after 1 h contact time, which is significantly better than most other materials reported in the literature. Therefore our results show that the synthesized HAM have high defluoridation capacity, which makes them a potential candidate for water treatment.

The combined potentiometric-ITC method has been used to calculate the adsorption parameters and, for the first time, to obtain the ΔH_{ads} value by direct measurement of the heat associated to the process. Contrarily to the data presented in most previous works, clearly negative enthalpy values for fluoride adsorption are obtained here. Therefore, ITC can be a useful tool for an accurate and relatively fast screening of sorbent materials.

Acknowledgements

The present work has been partially supported by the Spanish MINECO grant CTM2012-30970.

References

1 Environmental Health Criteria, Fluorides, World Health Organization (WHO), Geneva, 2002.
2 E. Kumar, A. Bhatnagar, U. Kumar and M. Sillanpää, *J. Hazard. Mater.*, 2011, **186**, 1042–1049.
3 M. G. Sujana, G. Soma, N. Vasumathi and S. Anand, *J. Fluorine Chem.*, 2009, **130**, 749–754.
4 B. D. Turner, P. Binning and S. L. S. Stipp, *Environ. Sci. Technol.*, 2005, **39**, 9561–9568.
5 X. Zhao, J. Wang, F. Wu, T. Wang, Y. Cai, Y. Shi and G. Jiang, *J. Hazard. Mater.*, 2010, **173**, 102–109.
6 W. Li, C. Y. Cao, L. Y. Wu, M. F. Ge and W. G. Song, *J. Hazard. Mater.*, 2011, **198**, 143–150.
7 W. X. Gong, J. H. Qu, R. P. Liu and H. C. Lan, *Chem. Eng. J.*, 2012, **189–190**, 126–133.
8 L. Chai, Y. Wang, N. Zhao, W. Yang and X. You, *Water Res.*, 2013, **47**, 4040–4049.
9 C. Yang, L. Gao, Y. Wang, X. Tian and S. Komarneni, *Microporous Mesoporous Mater.*, 2014, **197**, 156–163.
10 M. Vithanage, A. U. Rajapaksha, M. S. Bootharaju and T. Pradeep, *Colloids Surf., A*, 2014, **462**, 124–130.
11 B.-S. Zhu, Y. Jia, Z. Jin, B. Sun, T. Luo, X.-Y. Yu, L.-T. Kong, X.-J. Huang and J.-H. Liu, *Chem. Eng. J.*, 2015, **271**, 240–251.
12 D. Kang, S. Tong, X. Yu and M. Ge, *RSC Adv.*, 2015, **5**, 19159–19165.
13 D. Thakre, S. Jagtap, A. Bansiwal, N. Labhsetwar and S. Rayalu, *J. Fluorine Chem.*, 2010, **131**, 373–377.
14 M. Bennajah, B. Gourich, A. H. Essadki, C. Vial and H. Delmas, *Chem. Eng. J.*, 2009, **148**, 122–131.
15 N. Chubar, *J. Colloid Interface Sci.*, 2011, **357**, 198–209.
16 L. H. Velazquez-Jimenez, E. Vences-Alvarez, J. L. Flores-Arciniega, H. Flores-Zuñiga and J. R. Rangel-Mendez, *Sep. Purif. Technol.*, 2015, **150**, 292–307.
17 J. Chilton, E. Dahi, M. Lennon and P. Jackson, *Fluoride in Drinking-water*, World Health Organization (WHO), Geneva, 2006.
18 V. Tomar, S. Prasad and D. Kumar, *Microchem. J.*, 2014, **112**, 97–103.
19 N. Hamdi and E. Srasra, *Desalination*, 2007, **206**, 238–244.
20 S. Wen, Y. Wang and S. Dong, *RSC Adv.*, 2015, **5**, 89594–89602.
21 Y. Kim, C. Kim, I. Choi, S. Rengaraj and J. Yi, *Environ. Sci. Technol.*, 2004, **38**, 924–931.
22 Y. Q. He, N. N. Zhang and X. D. Wang, *Chin. Chem. Lett.*, 2011, **22**, 859–862.
23 J. Han, Z. Du, W. Zou, H. Li and C. Zhang, *Chem. Eng. J.*, 2015, **262**, 571–578.
24 M. Nazari and R. Halladj, *J. Taiwan Inst. Chem. Eng.*, 2014, **45**, 2518–2525.
25 J. Zhang, S. Liu, J. Lin, H. Song, J. Luo, E. M. Elssfah, E. Ammar, Y. Huang, X. Ding, J. Gao, S. Qi and C. Tang, *J. Phys. Chem. B*, 2006, **110**, 14249–14252.
26 W. Cai, J. Yu and M. Jaroniec, *J. Mater. Chem.*, 2010, **20**, 4587.
27 W. Wei, G. Hu, D. Yu, T. Mcleish, Z. Su and Z. Shen, *J. Am. Chem. Soc.*, 2008, **130**, 15808–15810.
28 H. Guo, Y. He, Y. Wang, L. Liu, X. Yang, S. Wang, Z. Huang and Q. Wei, *J. Mater. Chem. A*, 2013, **1**, 7494–7499.
29 C. Peng, J. Guo, W. Yang, C. Shi, M. Liu, Y. Zheng, J. Xu, P. Chen, T. Huang and Y. Yang, *J. Alloys Compd.*, 2016, **654**, 371–378.

30 P. Yu, X. Zhang, D. Wang, L. Wang and Y. Ma, *Cryst. Growth Des.*, 2009, **2008**, 528–533.
31 L. Cavallo, S. Del Piero, J.-M. Ducéré, R. Fedele, A. Melchior, G. Morini, F. Piemontesi and M. Tolazzi, *J. Phys. Chem. C*, 2007, **111**, 4412–4419.
32 F. Endrizzi, A. Melchior, M. Tolazzi and L. Rao, *Dalton Trans.*, 2015, **44**, 13835–13844.
33 A. Melchior, E. Peralta, M. Valiente, C. Tavagnacco, F. Endrizzi and M. Tolazzi, *Dalton Trans.*, 2013, **42**, 6074–6082.
34 P. Di Bernardo, P. L. Zanonato, A. Melchior, R. Portanova, M. Tolazzi, G. R. Choppin and Z. Wang, *Inorg. Chem.*, 2008, **47**, 1155–1164.
35 P. Di Bernardo, P. L. Zanonato, F. Benetollo, A. Melchior, M. Tolazzi and L. Rao, *Inorg. Chem.*, 2012, **51**, 9045–9055.
36 J. E. Ladbury and M. L. Doyle, *Biocalorimetry 2: Applications of Calorimetry in the Biological Sciences*, Wiley, Chichester, 2004.
37 M. E. Strayer, J. M. Binz, M. Tanase, S. M. Kamali Shahri, R. Sharma, R. M. Rioux and T. E. Mallouk, *J. Am. Chem. Soc.*, 2014, **136**, 5687–5696.
38 L. N. H. Arakaki, M. G. da Fonseca, E. C. da Silva Filho, A. P. D. M. Alves, K. S. de Sousa and A. L. P. Silva, *Thermochim. Acta*, 2006, **450**, 12–15.
39 L. N. H. Arakaki, V. L. S. A. Filha, A. F. S. Germano, S. S. G. Santos, M. G. Fonseca, K. S. Sousa, J. G. P. Espínola and T. Arakaki, *Thermochim. Acta*, 2013, **556**, 34–40.
40 N. Welsch, Y. Lu, J. Dzubiella and M. Ballauff, *Polymer*, 2013, **54**, 2835–2849.
41 P. R. S. Braga, A. A. Costa, J. L. de Macedo, G. F. Ghesti, M. P. de Souza, J. A. Dias and S. C. L. Dias, *Microporous Mesoporous Mater.*, 2011, **139**, 74–80.
42 C. W. Chronister and R. S. Drago, *J. Am. Chem. Soc.*, 1993, **115**, 4793–4798.
43 R. S. Drago, S. C. Dias, M. Torrealba and L. de Lima, *J. Am. Chem. Soc.*, 1997, **119**, 4444–4452.
44 W. Lin, J. Walter, A. Burger, H. Maid, A. Hirsch, W. Peukert and D. Segets, *Chem. Mater.*, 2015, **27**, 358–369.
45 Y. Liu and J. M. Sturtevant, *Protein Sci.*, 1995, **4**, 2559–2561.
46 Y. Liu and J. M. Sturtevant, *Biophys. Chem.*, 1997, **64**, 121–126.
47 L. S. Mizoue and J. Tellinghuisen, *Biophys. Chem.*, 2004, **110**, 15–24.
48 W. Cai, J. Yu and S. Mann, *Microporous Mesoporous Mater.*, 2009, **122**, 42–47.
49 X. Wu, B. Zhang and Z. Hu, *Mater. Lett.*, 2012, **73**, 169–171.
50 X. Wu, B. Zhang and Z. Hu, *Mater. Lett.*, 2013, **91**, 249–251.
51 S. S. Tripathy, J. L. Bersillon and K. Gopal, *Sep. Purif. Technol.*, 2006, **50**, 310–317.
52 S. G. Wang, Y. Ma, Y. J. Shi and W. X. Gong, *J. Chem. Technol. Biotechnol.*, 2009, **84**, 1043–1050.
53 G. Limousin, J. P. Gaudet, L. Charlet, S. Szenknect, V. Barthès and M. Krimissa, *Appl. Geochem.*, 2007, **22**, 249–275.
54 K. Y. Foo and B. H. Hameed, *Chem. Eng. J.*, 2010, **156**, 2–10.
55 C. Comuzzi, P. Polese, A. Melchior, R. Portanova and M. Tolazzi, *Talanta*, 2003, **59**, 67–80.
56 S. del Piero, A. Melchior, P. Polese, R. Portanova and M. Tolazzi, *Ann. Chim.*, 2006, **96**, 29–49.
57 S. Lowell, J. E. Shields, M. A. Thomas and M. Thommes, *Characterization of Porous Solids and Powders: Surface Area, Pore Size and Density*, Kluwer Academic Publishers, Dordrecht, 2004.
58 K. S. W. Sing and R. T. Williams, *Adsorpt. Sci. Technol.*, 2004, **22**, 773–782.
59 W. Cai, J. Yu, S. Gu and M. Jaroniec, *Cryst. Growth Des.*, 2010, **10**, 3977–3982.
60 J. Du, D. A. Sabatini and E. C. Butler, *Chemosphere*, 2014, **101**, 21–27.
61 M. B. McBride and L. G. Wessellnk, *Environ. Sci. Technol.*, 1988, **22**, 703–708.
62 Y. H. Li, S. Wang, A. Cao, D. Zhao, X. Zhang, C. Xu, Z. Luan, D. Ruan, J. Liang, D. Wu and B. Wei, *Chem. Phys. Lett.*, 2001, **350**, 412–416.
63 L. Lv, J. He, M. Wei, D. Evans and Z. Zhou, *Water Res.*, 2007, **41**, 1534–1542.
64 S. Jagtap, M. K. N. Yenkie, N. Labhsetwar and S. Rayalu, *Microporous Mesoporous Mater.*, 2011, **142**, 454–463.
65 H. Cai, G. Chen, C. Peng, L. Xu, X. Zhu, Z. Zhang, Y. Dong, G. Shang, F. Ke, H. Gao and X. Wan, *RSC Adv.*, 2015, **5**, 29266–29275.
66 H. M. Cai, G. J. Chen, C. Y. Peng, Z. Z. Zhang, Y. Y. Dong, G. Z. Shang, X. H. Zhu, H. J. Gao and X. C. Wan, *Appl. Surf. Sci.*, 2015, **328**, 34–44.
67 J. Zhu, X. Lin, P. Wu, Q. Zhou and X. Luo, *Appl. Surf. Sci.*, 2015, **357**, 91–100.
68 M. Mohapatra, K. Rout, P. Singh, S. Anand, S. Layek, H. C. Verma and B. K. Mishra, *J. Hazard. Mater.*, 2011, **186**, 1751–1757.
69 N. A. Medellin-Castillo, R. Leyva-Ramos, E. Padilla-Ortega, R. O. Perez, J. V. Flores-Cano and M. S. Berber-Mendoza, *J. Ind. Eng. Chem.*, 2014, **20**, 4014–4021.
70 Z. Jin, Y. Jia, T. Luo, L. T. Kong, B. Sun, W. Shen, F. L. Meng and J. H. Liu, *Appl. Surf. Sci.*, 2015, **357**, 1080–1088.
71 S. Dong and Y. Wang, *Water Res.*, 2016, **88**, 852–860.
72 K. Y. A. Lin, Y. T. Liu and S. Y. Chen, *J. Colloid Interface Sci.*, 2016, **461**, 79–87.

Inorganic Chemistry

Article

pubs.acs.org/IC

Nickel(II) Complexation with Nitrate in Dry $[C_4mim][Tf_2N]$ Ionic Liquid: A Spectroscopic, Microcalorimetric, and Molecular Dynamics Study

Andrea Melchior,*[,†] Clotilde Gaillard,[‡] Sara Gràcia Lanas,[†] Marilena Tolazzi,[†] Isabelle Billard,*[,§,∥] Sylvia Georg,[⊥] Lola Sarrasin,[‡] and Maria Boltoeva*[,⊥,#]

[†]Dipartimento di Chimica, Fisica e Ambiente, Università di Udine, Via Cotonificio 108, I-33100 Udine, Italy

[‡]Institut de Physique Nucléaire de Lyon, Université de Lyon, CNRS-IN2P3, 69622 Villeurbanne cedex, France

[§]Université Grenoble Alpes, LEPMI, CNRS, F-38000 Grenoble, France

[∥]CNRS, LEPMI, F-38000, Grenoble, France

[⊥]Université de Strasbourg, IPHC, 23 rue du Lœss 67037 Strasbourg, France

[#]CNRS, UMR7178, 67037 Strasbourg, France

Supporting Information

ABSTRACT: The complex formation of nitrate ions with nickel(II) in dry $[C_4mim][Tf_2N]$ ionic liquid (IL) was investigated by means of UV−visible spectrophotometry, isothermal titration calorimetry (ITC), extended X-ray absorption fine structure spectroscopy (EXAFS), and molecular dynamics (MD) simulations. EXAFS spectroscopy and MD simulations show that the solvated Ni(II) cation is initially coordinated by the oxygens of the $[Tf_2N]^-$ anion of IL, which can behave either as mono- or bidentate. Spectroscopic and thermodynamic data show that Ni(II) is able to form up to three stable mononuclear complexes with nitrate in this solvent. The stability constants for $Ni(NO_3)_j$ complexes (j = 1−3) calculated from spectrophotometry and ITC experiments decrease in the order $\log K_1 > \log K_2 > \log K_3$. The formation of the first two species is enthalpy-driven, while the third species is entropy-stabilized. The UV−vis spectra of solutions containing different nitrate/Ni(II) ratios show that the metal ion retains the six-coordinate geometry. Furthermore, the EXAFS evidences that nitrate is always bidentate. Molecular dynamics simulations show that the $[Tf_2N]^-$ anions bind Ni(II) through the sulfonyl oxygen atoms and can coordinate either as monodentate or chelate. The analysis of the MD data shows that introduction of nitrates in the first coordination sphere of the metal ion results in remarkable structural rearrangement of the ionic liquid.

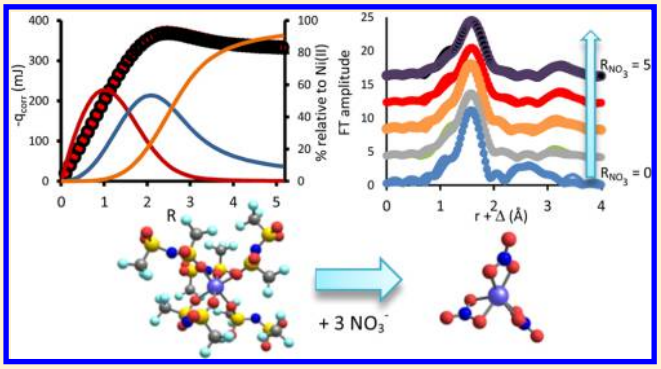

INTRODUCTION

Nickel and its compounds have many industrial and commercial uses. Particularly, nickel alloys and steels are used for some demanding applications, such as fabrication of nuclear reactor components. However, the intense neutron flux in power reactors yields nickel-63 (half-life 100.1 years), which is of great importance in radioactive waste treatment and long-term storage because of its high radiotoxicity. It is necessary, therefore, to control the nickel quantity to comply with the low-level radioactive waste classification requirements. Currently, the method of the measurement of ^{63}Ni activity is based on solvent extraction with chloroform.[1] However, the use of chlorinated solvents will be limited by the REACH regulation due to their adverse effects toward the environment and human health. One possible alternative is the use of room-temperature ionic liquids (RTILs). These solvents have attracted much attention as "environmentally friendly", owing to their practically negligible vapor pressure, stability, and (supposed) low toxicity.[2−5] Moreover, RTILs exhibit properties that render their handling much more easy, as they are stable to air and water, nonvolatile, and nonflammable. They also display very good solvation properties for neutral and for charged species. For those reasons, RTILs are interesting media for a wide variety of applications, such as separations, extractions, chemical analysis, electrochemistry, and catalysis.[2,3,6,7]

A better understanding of the coordination chemistry of transition metals with a range of complexing agents in RTILs is fundamental to define the molecular interactions that can influence extraction processes. In particular, the thermodynamic parameters of complex formation along with structural information on the species formed by a metal ion in a given

Received: December 23, 2015
Published: March 21, 2016

DOI: 10.1021/acs.inorgchem.5b02937
Inorg. Chem. 2016, 55, 3498−3507

Table 1. Overall ($\log \beta_j$) and Stepwise ($\log K_j$) Stability Constants and Thermodynamic Parameters (kJ mol^{-1}) Relative to the Reaction $Ni^{2+} + jNO_3^- \leftrightarrows [Ni(NO_3)_j]^{2-j}$ in $[C_4mim][Tf_2N]$ (T = 298.15 K) Determined by Microcalorimetry

j	$\log \beta_j$	$\Delta G_{\beta j}$	$\Delta H_{\beta j}$	$T\Delta S_{\beta j}$	$\log K_j$	ΔG_{Kj}	ΔH_{Kj}	$T\Delta S_{Kj}$
1	4.2(2)	−23.9(1)	−18.61(1)	5.3	4.2	−23.9	−18.6	5.3
2	7.5(3)	−42.8(1)	−42.64(1)	0.2	3.3	−18.9	−24.0	−5.1
3	10.1(4)	−57.6(5)	−30.62(1)	27.0	2.6	−14.8	12.0	26.8

solution are fundamental quantities that need to be known for the design of an efficient Ni(II) extraction procedure.

The thermodynamics of metal complex formation has been widely explored in nonaqueous solutions,[8−15] while in RTILs very few examples of stability constants determinations are present in the literature for transition metals[16] and f-block elements.[17−20] It is also noticeable that no complexation enthalpy (with the exception of Nd^{3+} and Eu^{3+} ions with nitrate and a calixarene ligand, respectively)[18,19] has been previously determined in RTILs, despite the key-role of this parameter for the understanding of the strength of the metal−ligand interaction and the role of the processes occurring in solution upon complexation. From a structural point of view, X-ray absorption spectroscopy (EXAFS), molecular dynamics (MD) simulations, and density functional theory (DFT) calculations have been applied previously to study lanthanides,[18,21−26] actinides,[20,27−29] alkaline earths,[30,31] and transition metals[32−34] in RTILs.

In this article, we report the results of the experimental and theoretical study of Ni(II) solvation and complex formation with nitrate ions in dry 1-methyl-3-butyl-imidazolium bis(trifluoromethanesulfonyl)imide ($[C_4mim][Tf_2N]$). The interest of nitrate ligand as complexant is due to the fact that liquid−liquid extraction experiments are often performed with aqueous solutions containing high nitrate concentration, and thus the metal ion can be distributed among several species. To this end, we used a combination of experimental spectrophotometric, EXAFS, and microcalorimetric studies with theoretical methods (MD simulations). Used in conjunction, these can provide fundamental and insightful data, offering the possibility to explore the solvation and complexation phenomena of Ni(II) ion in RTILs.

EXPERIMENTAL SECTION

Reagents. 1-Butyl-3-methylimidazolium bis(trifluoromethanesulfonyl)imide ionic liquid (IL, high-purity grade 99.5%), hereinafter indicated as $[C_4mim][Tf_2N]$, and nickel(II) bis(trifluoromethanesulfonyl)imide salt ($Ni(Tf_2N)_2$, 99.5% purity) from Solvionic (Toulouse, France) were used without further purification. $[C_4mim][NO_3]$ IL was synthesized following the procedure reported in the literature.[20] Acetonitrile of analytical grade was dried with molecular sieves just before use. Deionized water from a Milli-Q purification system (Millipore) of resistivity 18.2 MΩ·cm was used for the preparation of aqueous solutions. The highly hygroscopic ILs $[C_4mim][Tf_2N]$ and $[C_4mim][NO_3]$ were dried as described in ref 20. The salt $Ni(Tf_2N)_2$ was dried under vacuum without heating.

Thermodynamics of Ni-Nitrate Complexation. All measurements in this work were performed at 298.15 K. The stability constants of Ni(II)/nitrate complexes were obtained both from UV−vis spectrophotometric titrations and isothermal titration calorimetry (ITC).

The spectrophotometric titration was performed in batch system where each sample was prepared by using $Ni(Tf_2N)_2$ and $[C_4mim][NO_3]$ stock solutions in $[C_4mim][Tf_2N]$. The concentration of nickel(II) in the solutions was kept constant to 0.030 M, while the nitrate concentration was varied from 0 to 0.156 M ($R_{NO_3^-} = C_{NO_3^-}/C_{Ni(II)}$ ranging from 0 to 5.2). Samples were dried just before measurements to remove any residual water, and their final water content, checked by coulometric technique (Karl Fischer titration, Mettler Toledo DL 32), was found below 100 ppm (i.e., 0.008 M). A total of 14 samples at different mole ratio was analyzed. The absorbance spectra were recorded on a Cary 100 UV−vis spectrophotometer in a rectangular quartz cell with Teflon stopper of 10 mm path length (Hellma Analytics) in the region of 350−900 nm. The wavelength resolution was fixed at 1.0 nm. The data were collected in double-beam mode. The reference solution was a neat $[C_4mim][Tf_2N]$. Data treatment was performed using the HypSpec program.[35] The UV−vis spectrum of the 1:0 species was defined as the one of nickel(II) dissolved in dry IL ($R_{NO_3^-}$ = 0). The UV−vis spectrum of pure $[C_4mim][NO_3]$ was also used as an input data, although this species displays a negligible absorbance in the 350−900 nm range.

ITC experiments were performed to obtain the reaction enthalpy (and the stability constants) values for the formation of Ni(II)-nitrate complexes in $[C_4mim][Tf_2N]$. Titrations were performed using a TAMIII thermostat (TA Instruments) equipped with a nanocalorimeter and an automated titration syringe (Hamilton, 250 μL). To avoid the presence of moisture, the sample and reference cells were loaded in a drybox with N_2 atmosphere and then inserted in the calorimeter. For the preparation of Ni(II) solution, 0.5 mL of a Ni(II) 0.03 M solution was diluted in a total volume of 1 mL with IL to obtain a 0.015 M Ni(II) solution. The NO_3^- solution was prepared by weighing the required amount of the pure solution of $[C_4mim][NO_3]$ and then diluting with IL.

In the ITC experiments the reaction cup contained 750 μL of Ni(II) solution in $[C_4mim][Tf_2N]$ stirred by a gold propeller maintained at 80 rpm. The system was allowed to equilibrate before starting the titration experiments until a very stable baseline signal was obtained. Normally, ∼50 additions of 4 μL were done with a delay of 20 min between each other. The raw data were treated by Nano Analyzer Software to obtain the measured heat for each addition (q_{meas}). The dilution heat (q_{dil}) was then measured by titrating 0.75 mL of pure IL with the $[C_4mim][NO_3]$ solution in absence of Ni(II). Therefore, the heat involved in complex formation of NO_3^- with Ni(II) (q_{corr}) was: $q_{corr} = q_{meas} - q_{dil}$.

ITC data were used to calculate the $\log \beta_j$ and ΔH_{β_j} values by means of the computer program HypDeltaH,[36] which minimizes the objective function U described by the equation[37] $U = \sum_{(i=1)}^{N} (q_{corr} - q_{calc})^2$, where q_{calc} is the heat calculated on the basis of β_j, ΔH_{β_j}, and the total concentrations of the reagents. Additional statistical analysis was done using the Solverstat tool.[38,39]

The values of the stability constants $\log \beta_1$ and $\log \beta_2$ obtained by ITC (Table 1) showed a better standard deviation than those obtained by spectrophotometric titrations.

X-ray Absorption Spectroscopy. Five solutions were analyzed, containing various molar ratios between Ni(II) and nitrate ($0 < R_{NO_3^-} < 5.5$) in dry IL, the Ni(II) concentration being 0.03 M. Measurements were performed on the XAFS beamline at the ELETTRA synchrotron (Trieste, Italy) and on the SAMBA beamline at SOLEIL synchrotron (Saint-Aubin, France) using a double crystal Si(111) monochromator. Analyses were made at the nickel K-edge (8.33 keV) in transmission and fluorescence mode. The monochromator energy was calibrated by a nickel foil for the Ni K-edge. The X-ray absorption of the samples was measured in sealed Eppendorf tubes (2 mL) or in an in-house cell. EXAFS data reduction was made using ATHENA software.[40] Data analysis was performed with the

DOI: 10.1021/acs.inorgchem.5b02937
Inorg. Chem. 2016, 55, 3498−3507

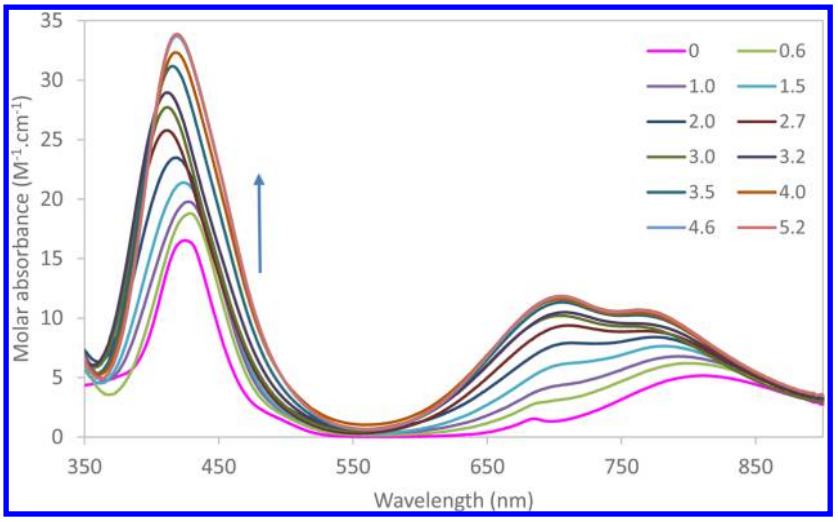

Figure 1. Absorption spectra of nickel(II) solutions in dry $[C_4mim][Tf_2N]$ at various nitrate/Ni(II) molar ratio ($R_{NO_3^-}$). The molar absorbance reported corresponds to the experimental absorbance divided by the total Ni(II) concentration in each sample (0.03M) and the optical path length (1 cm).

FEFFIT code, using phase and backscattering amplitude functions generated with the FEFF 8.1 code[41,42] from crystallographic structures. Fits of the Fourier transform (FT) k^3-weighted EXAFS data to the EXAFS equation were performed in R-space between 0.8 and 4.0 Å. The k-range used was 2.0−12.0 $Å^{-1}$. The amplitude reduction factor (S_0^2) was held constant to 1 for all fits. The shift in the threshold energy (E_0) was allowed to vary as a global parameter for all atoms. In all fits, the coordination number of nickel(II) was fixed to 6, as it is known that this ion is hexacoordinated. For the sample corresponding to $R_{NO_3^-}$ = 0.0 (nickel in dry IL), the number of sulfur atoms from Tf_2N ligands was linked to the number of oxygen atoms present in the first coordination sphere. In the case of nitrate ligands, the number of distal oxygen atoms is linked to the fitted number of nitrogen atoms. Also, strong multiple scattering contributions due either to nitrate ions or to Tf_2N anions complexed to nickel were taken into account without adding any fitted parameters (N, σ^2, and R were linked to single scattering paths).

Molecular Dynamics Simulations. Several RTIL solutions (Table S1) were simulated by classical molecular dynamics (MD). In our approach the $[Ni(NO_3)_j]^{2-j}$ species were considered as unique entities, as the nitrate anions are not allowed to dissociate. DFT calculations were done on the $[Ni(NO_3)_j]^{2-j}$ complexes to calculate the point charges to be used in MD simulations. The complexes were optimized at DFT level using the LANL2DZ ECP[43] for Ni(II) and the Gaussian-type 6-31+G(d,p) basis set for O and N atoms. The point charges were calculated using the electrostatic potential (ESP) ChelpG scheme[44] for the various $[Ni(NO_3)_j]^{2-j}$ species in the presence of a solvent simulated by the SMD polarizable solvation model[45] with the parameters given for $[C_4mim][Tf_2N]$ IL.[46] In Table S2 the ESP charges employed for the various atom types are reported. All quantum chemical calculations were performed with Gaussian09.[47]

In MD simulations, nitrate anions were considered to behave as bidentate on the basis of EXAFS evidence of this work, even if several Ni(II) complexes with monodentate nitrate have been obtained in the solid state.[48,49] Following a procedure previously applied,[50] for nitrate complexes in RTIL, nitrate anions were constrained to maintain this coordination mode during the simulation by assigning a force constant of 500 kcal mol^{-1} $Å^{-2}$ to the Ni−O_{NO_3} bonds (with equilibrium Ni−O distances taken from the DFT-optimized structures). Additionally, an O−Ni−O bending term was added in the $[Ni(NO_3)_3]^-$ species to keep it six-coordinated as in the DFT-optimized structure during the MD simulation, in agreement with the coordination number obtained from EXAFS fitting.

The Lennard-Jones parameters for nitrate and nickel ion were taken from refs 51 and 52, respectively. Cross terms in van der Waals interactions were constructed using the Lorentz−Berthelot rules. The force field for $[C_4mim][Tf_2N]$ IL was taken from refs 52 and 53. Nonbonded interactions were calculated using a 12 Å cutoff, while electrostatic interactions were calculated with the Particle Mesh Ewald (PME) method.[54]

The LINCS algorithm to integrate the equations of motion (2 fs time step) was applied.

MD simulations were run at 300 K in the NVT ensemble with box size adjusted to obtain the density of the pure IL. After an equilibration period of 1 ns, a 5 ns production run was done, and trajectory data for analysis were collected every 100 steps. All MD simulations were done using the Gromacs 4.6.5 program.[55]

RESULTS AND DISCUSSION

Thermodynamics of Complex Formation. In the $[C_4mim][Tf_2N]$ IL, the starting nickel solvate is a negatively charged species of general formula $[Ni(Tf_2N)_n]^{2-n}$ rather than the six-coordinated solvate with a net +2 charge as usually found in water or other organic solvents.[12,56,57] When nitrate is added to the nickel solution in $[C_4mim][Tf_2N]$, the weakly coordinating anions are displaced from the cation as in reaction 1:

$$Ni(Tf_2N)_n^{2-n} + jNO_3^- \rightleftarrows [Ni(Tf_2N)_{n-m}(NO_3)_j]^{2-j-(n-m)} + mTf_2N^- \quad (1)$$

The definition of the reference state for the reacting species is essential for the calculation of the thermodynamic parameters. In a recent work,[34] on the basis of DFT calculations, UV−vis spectroscopy, and electrospray ionization mass spectrometry, it has been proposed that Ni(II) ion is solvated by three chelated $[Tf_2N]^-$ anions to form the $[Ni(Tf_2N)_3]^-$ species only in liquid state. However, the $[Tf_2N]^-$ anion has a significant steric hindrance, which disfavors the chelate arrangement; thus, it should not be excluded that the $[Tf_2N]^-$ anion can act either as monodentate or chelating in the starting $[Ni(Tf_2N)_n]^{2-n}$ solvate, for example, as found in the structure of the $[Co(Tf_2N)_4]^{2-}$ complex.[58] Therefore, the possibility that solvated nickel can be distributed among several $[Ni(Tf_2N)_n]^{2-n}$ species in equilibrium should be taken into account. The nature of the Ni(II) reacting species becomes even more undefined if it is considered that the

DOI: 10.1021/acs.inorgchem.5b02937
Inorg. Chem. 2016, 55, 3498−3507

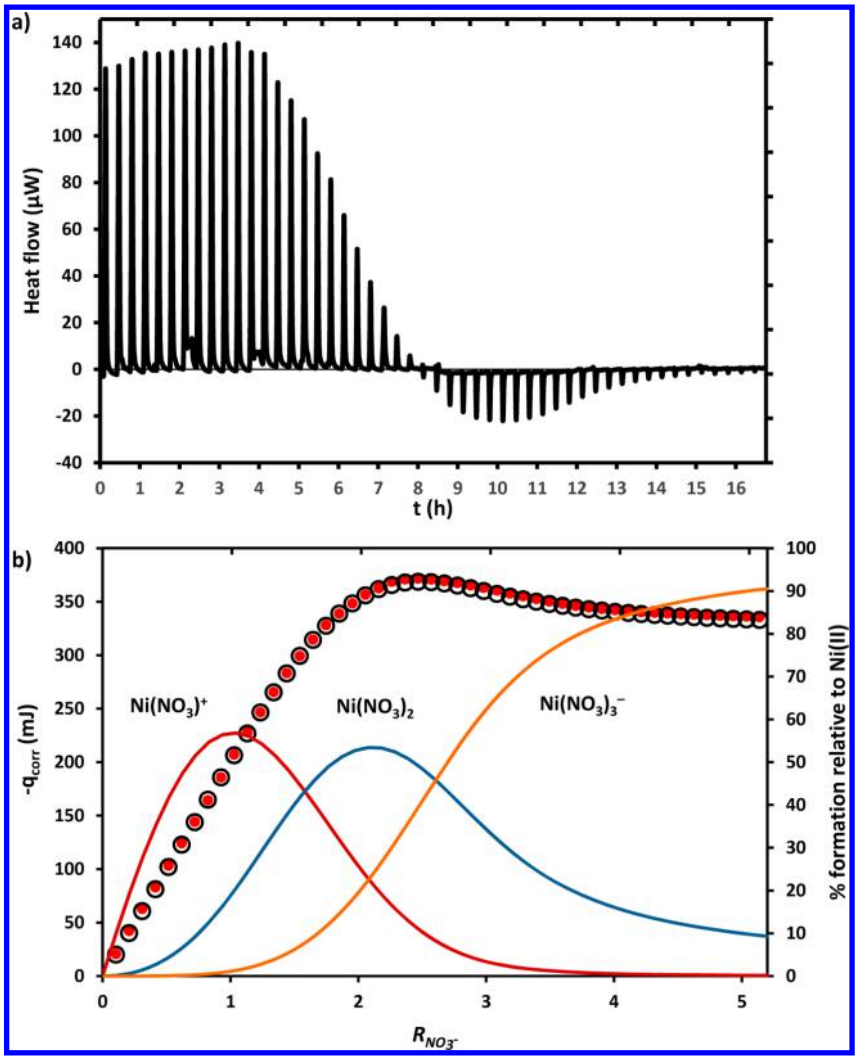

Figure 2. (a) ITC profile for the complex reaction of NO_3^-–Ni(II) at 298.15 K. Each peak corresponds to an addition of 4 μL of NO_3^- 0.26 M to 0.75 mL of Ni(II) 0.015 M solution. Positive sign of the heat flux corresponds to an exothermic reaction in our calorimeter output. (b) Cumulative heat (q_{corr}) observed (red dots) and calculated (empty dots) on the basis of the log β_j and ΔH_{β_j} values reported in Table 1 vs the nickel/nitrate molar ratio ($R_{NO_3^-}$). The corresponding $Ni(NO_3)_j^{2-j}$ speciation as a function of the NO_3^- added is reported.

negatively charged solvated metal cation is strongly interacting with a second sphere composed mainly by cations of the IL;[28] thus, the charge and nature of the reactive species depends on how many spheres are considered.[20] It should be also underlined that in complex formation studies, it is fundamental to control the ionic strength of the solution, which is generally achieved by the addition of an inert salt in large quantities as compared to the reagents. As previously discussed,[17,20] if one assumes that the ILs are fully dissociated in the medium, the ionic strength in this solution is high enough (~3.4 mol L^{-1}) that the complex formation should have a negligible impact at the Ni(II) concentrations employed in our experiments (in the range of 1×10^{-2} M).

Following all these considerations, the overall stability constants (β_j) obtained in this work should be considered as "conditional constants" for the complexation equilibrium reported in eq 2, where the charges on the Ni(II) species are purely formal:

$$Ni^{2+} + jNO_3^- \rightleftarrows [Ni(NO_3)_j]^{2-j}\beta_j = \frac{[Ni(NO_3)_j]^{2-j}}{[Ni^{2+}][NO_3^-]^j} \quad (2)$$

In Figure 1 the experimental UV–vis spectra of $Ni(Tf_2N)_2$ in dry $[C_4mim][Tf_2N]$ are displayed as a function of the nitrate content (for ratio $0 < R_{NO_3^-} < 5.2$). In the absence of nitrate, the spectrum at $R_{NO_3^-} = 0$ exhibits 3 maxima at 430, 691, and 815 nm. This spectrum is in agreement with the one obtained by Katase et al. for Ni(II) solution in the dry [trimethyl-*n*-hexylammonium][Tf_2N] IL.[59] Addition of nitrate ions in $Ni(Tf_2N)_2$-$[C_4mim][Tf_2N]$ solutions leads to both an increase of the peak intensity and to a band shift. A red shift and a blue shift are observed, respectively, for the bands at 691 and 815 nm as the nitrate concentration increases. The 430 nm band position remains identical for $R_{NO_3^-} < 1$, then it shifts to shorter wavelengths for $1 < R_{NO_3^-} < 3$, and finally it shifts to longer wavelengths for $R_{NO_3^-} > 3$. Thus, the maximum of absorbance observed is located at 412 nm for $R_{NO_3^-} = 3$, while it is at 419 nm for $R_{NO_3^-} \geq 4$. Then, all spectra are identical for $R_{NO_3^-} \geq 4.6$, which indicates that the nickel speciation remains stable in solution above this ratio.

DOI: 10.1021/acs.inorgchem.5b02937
Inorg. Chem. 2016, 55, 3498–3507

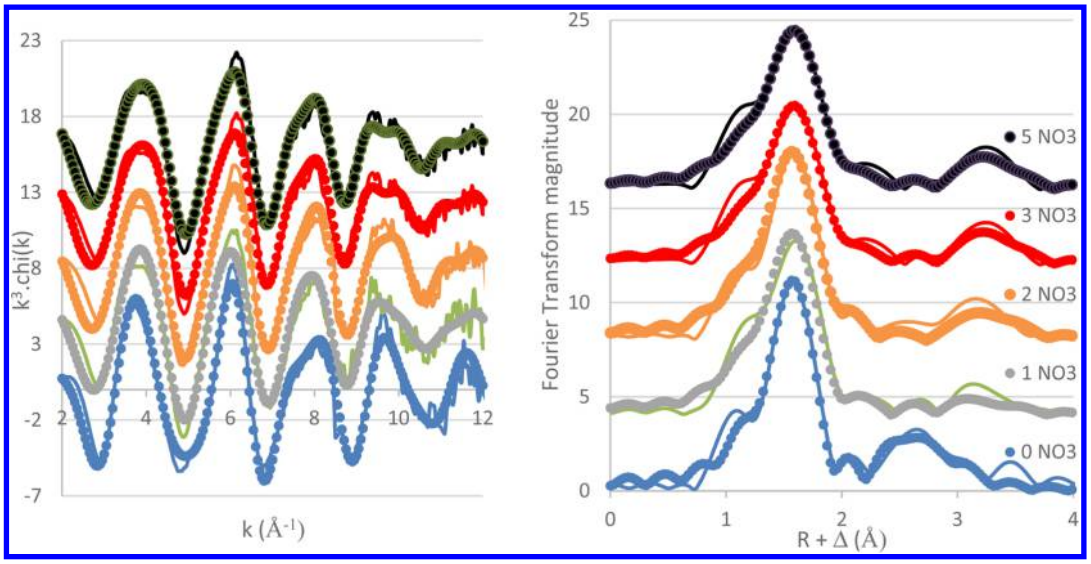

Figure 3. EXAFS data (left) and their corresponding FT (right) of Ni(II) in the IL $[C_4mim][Tf_2N]$, as a function of the nitrate concentration. [Ni(II)] = 0.03 M. For sake of clarity, spectra are shifted along the *y*-axis.

The set of 14 spectra was used to obtain the stability constants (β_j) of the different complexes formed in solution. Four different species $[Ni(NO_3)_j]^{2-j}$ (j = 0−3), involved in the equilibria written in eq 2, were considered. The presence of the 1:4 complex was discarded on the basis of EXAFS results (see below). The best fit was obtained with a model including the formation of the 1:1 and 1:3 species ($\log \beta_1 = 3.7(8)$ and $\log \beta_3 = 7.6(8)$) with the calculated molar absorbance of each species as displayed in Figure S2 and the resulting speciation given in Figure S1. The introduction in the fit of the 1:2 complex, even if considered as a nonabsorbing species, could not lead to any stable fitting. To check the presence of the 1:2 species, ITC experiments were performed. Calorimetric data (Figure 2a) show that when the $R_{NO_3^-}$ is low an exothermic process is present, while an endothermic process is operating after the addition of a significant amount of $[C_4mim][NO_3]$ ($R_{NO_3^-} \approx 2.5$). The fit of ITC data (Figure 2b) is compatible with the formation of three successive mononuclear species ($[Ni(NO_3)_j]^{2-j}$, with j = 1−3). In this case, the exclusion of the $[Ni(NO_3)_2]$ species leads to a poor data fit. The stability constants of the nickel complexes obtained by ITC data are reported in Table 1 together with related enthalpy and entropy values. The stabilities of the complexes decrease with the number of coordinated nitrates and result to be similar to those obtained in dry acetonitrile by kinetic methods.[60] The overall formation enthalpy values are always negative, while the corresponding entropy terms are positive or close to zero. However, the ΔH_{Kj} values (stepwise) are negative for the formation of the 1:1 and 1:2 species and negative for the 1:3 species, which is formed in an entropy-driven process ($T\Delta S_{K3}$= +26.8 kJ mol^{-1}). This trend is different from the values obtained for the Nd^{3+}/nitrate complexes in dry $[C_4mim][Tf_2N]$, where highly stable species are formed with both negative enthalpy and entropy terms.[18] According to the model proposed in reaction 1, the entropic terms can be explained by the release of $[Tf_2N]^-$ anions from the first coordination sphere of the Ni(II) ion, which is not compensated by desolvation of nitrate. The coordination of one nitrate should promote the release of up to two $[Tf_2N]^-$ anions from the first solvation sphere of Ni(II) ion with a consequent large entropy gain. However, this does not agree with our results, where $T\Delta S_{K1}$ and $T\Delta S_{K3}$ are positive (+ 5.3 and +26.8 kJ mol^{-1}), while $T\Delta S_{K2}$ is small and negative (−5.1 kJ mol^{-1}). This result suggests that outer sphere effects, such as different solvation of the Ni(II) complexes and reorganization of the IL around the Ni(II) complex, play an important role in determining the thermodynamics parameters.

X-ray Absorption Spectroscopy. EXAFS spectra and their corresponding FT are displayed in Figure 3. Distances (R + Δ) on the FT are not real interatomic distances, as they are not corrected by the phase shift (Δ). The strong peak observed on the FT at R + Δ ≈ 1.6 Å corresponds to the first Ni coordination sphere composed of six oxygen atoms.

Note that the obtained EXAFS spectra are the result of an average of the Ni coordination sphere in each sample, and thus, may correspond to a mixture of different species. In Figure S3 the speciation of the five analyzed samples calculated on the basis of the stability constants in Table 1 is reported. The fitting results for the five analyzed samples are given in Table 2. The first sample ($R_{NO_3^-}$ = 0) corresponds to nickel dissolved in a dry IL. As expected, Ni(II) ions are coordinated only by $[Tf_2N]^-$ ions. The coordination occurs through six oxygen atoms of SO_2 groups, at a distance of 2.03 Å, which is typical for Ni(II) in octahedral coordination.[61−63] A sulfur shell is also present at an average distance of 3.23 Å. The SO_2 groups can bind nickel either in monodentate or in bidentate fashion, which should lead to significant differences on the Ni−S interatomic distance. We could not find in the literature any structural study of nickel/Tf_2N complexes, in the solid or liquid state. However, one cobalt(II)/Tf_2N compound that we may use for comparison purposes has been characterized.[58] Indeed, cobalt and nickel have similar chemical properties, and at their divalent state they exhibit close ionic radii (83 pm for Ni(II) and 79 pm for Co(II)). This species is composed of $[Co(Tf_2N)_4]^{2-}$ clusters, where Co(II) is complexed by two monodentate $[Tf_2N]^-$ and two bidentate $[Tf_2N]^-$, with the following distances: Co−S(monodentate) = 3.19 Å versus Co−S(bidentate) = 3.27 and 3.31 Å. The Ni−S bond length obtained in this work (3.23 Å, Table 2) is intermediate, which could suggest that the Ni(II) coordination sphere is composed

DOI: 10.1021/acs.inorgchem.5b02937
Inorg. Chem. 2016, 55, 3498−3507

Table 2. X-ray Absorption Spectroscopy Fit Results[a]

$R_{NO_3^-}$	paths	N	R (Å)	σ^2 (Å^2)	E_0 (eV)	R_{factor}
0	O	6[b]	2.03	0.006	6.3	0.04
	S	6	3.23	0.012		
1	O	6[b]	2.05	0.007	−3.8	0.05
	N	1.0	2.50	0.002		
	(O(NO_3)	1.0	3.72	0.005		
2	O	6[b]	2.04	0.006	−4.1	0.04
	N	2.0	2.46	0.007		
	O(NO_3)	2.0	3.74	0.004		
3	O	6[b]	2.05	0.008	−2.4	0.04
	N	3.2	2.51	0.009		
	O(NO_3)	3.2	3.75	0.005		
5.5	O	6[b]	2.06	0.008	−2.4	0.04
	N	3.2	2.51	0.009		
	O(NO_3)	3.2	3.75	0.005		

[a]N is the coordination number (±20%), R the interatomic distance (±0.02 Å), σ^2 is the Debye−Waller factor (±0.001 Å^2), E_0 is the shift in threshold energy, and the R_{factor} indicates the goodness of the fit as defined in ref 42. The path O(NO_3) corresponds to the distal oxygen of nitrate groups. [b]Fixed parameters.

of a mixture of monodentate and bidentate Tf_2N anions as depicted in Scheme 1.

Scheme 1. Possible Coordination Modes of the $[Tf_2N]^-$ Anion

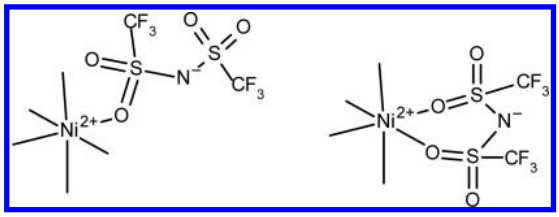

This kind of mixed coordination for Tf_2N anions to metallic ions was also evidenced for Ti(IV),[64] Eu(III),[26] or U(VI)[28] complexes.

As a consequence of the complexation of nitrate ions to nickel ($R_{NO_3^-} > 0$), specific features appear on the FT, in particular, a strong peak at $R + \Delta \approx 3.2$ Å (Figure 3). The coordination of nitrates entails the presence of a nitrogen shell and of a distal oxygen shell, but also of strong multiple scattering contributions. According to the coordination mode of nitrate ions to nickel, these features occur at different distances. In particular, the distal oxygen lies at a distance of ∼4 Å for a monodentate NO_3^- group, while it is located at ∼3.7 Å from nickel for a bidentate NO_3^- group. Also, the nitrogen atom is closer to nickel in a bidentate fashion than in a monodentate fashion (2.5 vs 2.9 Å).[65,66] Looking at our fit results, it is clear that nitrate ions are coordinated in a bidentate fashion to nickel in the IL. The analysis of the spectra shows also that there are no significant changes at $R \geq 3$; thus, the maximum stoichiometry of the Ni(II)/nitrate species is 1:3. This result is in agreement with the speciation obtained by ITC data (Figure S3) and is indicative that nitrate ions are very strong ligands for nickel in the dry IL. Spectroscopic data show that $[Tf_2N]^-$ anions are progressively removed from the Ni(II) coordination sphere and that the cation is completely desolvated in the 1:3 species.

Molecular Dynamics Simulations. Molecular dynamics simulations on the solvated Ni(II) cation reveal that it is coordinated by the oxygen of the SO_2 moiety of the $[Tf_2N]^-$ anions during all simulation time. The radial distribution functions (RDFs) of the Ni−O(Tf_2N) pairs (Figure 4a) present an intense peak centered at 2.15 Å corresponding to six oxygen atoms (Table 3). It is interesting to note that two peaks are obtained for the Ni−N(Tf_2N) integrating for 5.0 nitrogen atoms at 3.75 and 4.45 Å (Table 3). This is indicative that five $[Tf_2N]^-$ anions can coordinate the Ni(II) cation as monodentate (only one sulfonyl group binds the metal) or chelate with two oxygens of the two different sulfonyl groups coordinated (Scheme 1 and Figure 5a). This result is not unexpected, since both coordination modes of the $[Tf_2N]^-$ anions have been already observed in previous MD simulations on solvated UO_2^{2+} cation.[67] The $[C_4mim]^+$ cations surround the solvated Ni(II) and form a large shell, as it can be seen from the maximum of the Ni−N(C_4mim) RDF at 7.65 Å, which corresponds to approximately seven molecules (Table 3 and Figure 4a). In the snapshot in Figure 5a it is clearly visible that the $[Ni(Tf_2N)_5]^{3-}$ unit is surrounded by $[C_4mim]^+$ cations, which constitute a complete second shell. A shell of $[Tf_2N]^-$ anions alternates to the cations as seen from the weak maximum of the Ni−N(Tf_2N) RDF at 10.75 Å (Figure 4a, Table S3).

When the solvated $Ni(NO_3)^+$ species is considered, the main peak of the Ni−O(Tf_2N) RDF decreases in intensity with 4.0 coordinated oxygen atoms (Figure 4b and Table 3). The Ni−N(Tf_2N) RDF in this case presents a single peak centered at 4.53 Å and integrating for 4 N atoms. This result shows that in the 1:1 Ni/nitrate complex the coordinated $[Tf_2N]^-$ anions are monodentate only and that one $[Tf_2N]^-$ was released. In this case the Ni−N(C_4mim) RDF has a maximum at 7.53 Å and corresponds to approximately eight cations (Table 3). However, given the low intensity of the Ni−N(C_4mim) RDF, it is difficult to define a clear-cutoff radius to calculate the integral. It appears that cations solvating the $[Ni(Tf_2N)_4(NO_3)]^{3-}$ unit are arranged in a shell similar to that of the solvated Ni(II) ion. This is also evident in the snapshot in Figure 5b where the cations completely surround the Ni(II) species. A possible origin of this similarity between the cation distribution found for the Ni(II) solvate and for the 1:1 complex is that the total charge of the Ni(II) complex (−3) does not change and that the average volume occupied by the $[Ni(Tf_2N)_4(NO_3)]^{3-}$ complex is not very different with respect to that occupied by $[Ni(Tf_2N)_5]^{3-}$. Again, a second shell of $[Tf_2N]^-$ anions alternates to the cations as seen from the weak maximum at 10.33 Å (Figure 4b and Table S3).

In the case of the solvated 1:2 species the highest peak of Ni−O(Tf_2N) and Ni−N(Tf_2N) RDFs correspond to 2.0 O and N atoms indicating that only two anions remain coordinated to Ni(II) in a monodentate fashion. According to this model, in the second complexation step two $[Tf_2N]^-$ anions are released, and the $[Ni(Tf_2N)_2(NO_3)_2]^{2-}$ complex is formed. The maximum of the Ni−N(C_4mim) RDF is now shifted to 5.03 Å from Ni(II) and roughly corresponds to ∼4.4 IL cations. The snapshot of the MD trajectory in Figure 5c well depicts this change of distribution in the ions around $[Ni(Tf_2N)_2(NO_3)_2]^{2-}$ with respect to the previous systems (Figure 5a,b).

In the case of $Ni(NO_3)_3^-$, the Ni−O(Tf_2N) and Ni−N(Tf_2N) RDFs do not show sharp peaks, as no anions are coordinated. Only a residual peak at 2.68 Å (n = 0.4) indicates that the $[Tf_2N]^-$ anion can weakly interact with Ni(II) cation.

DOI: 10.1021/acs.inorgchem.5b02937
Inorg. Chem. 2016, 55, 3498−3507

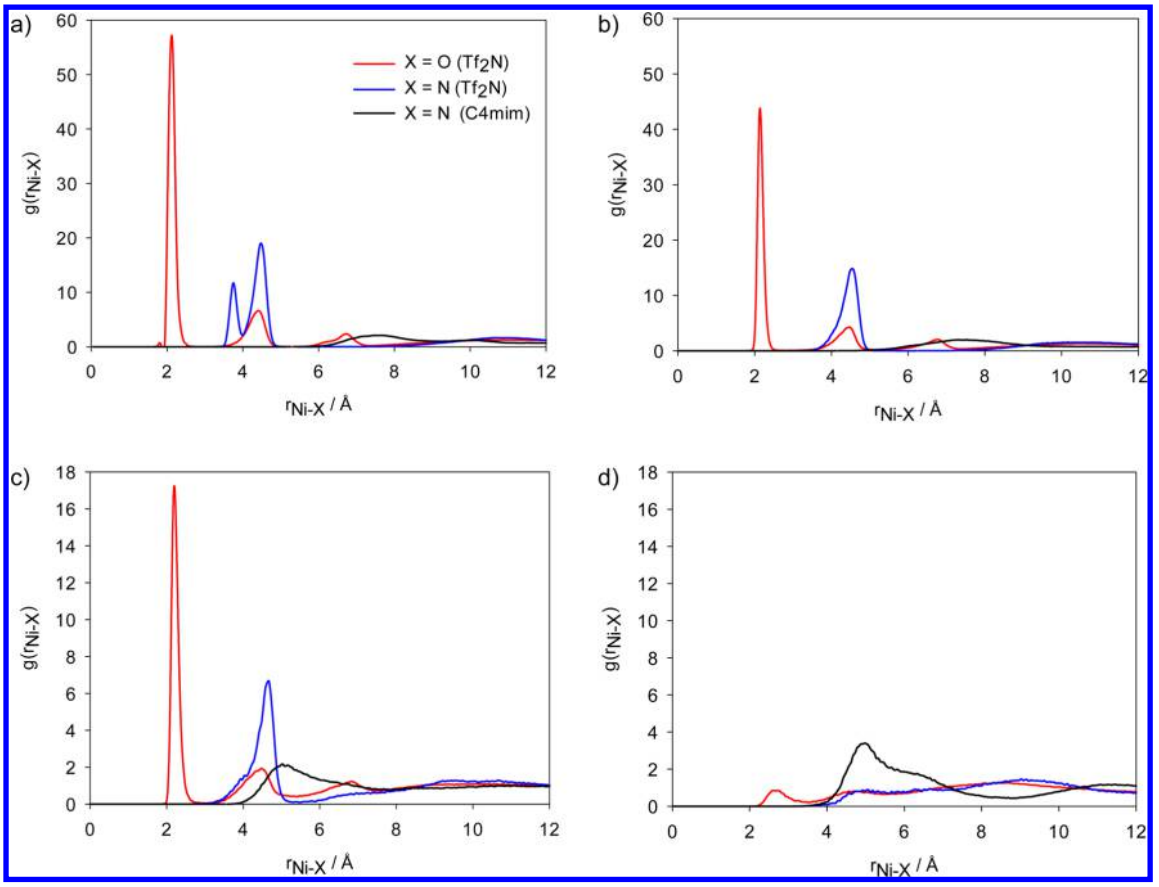

Figure 4. RDFs relative to nickel center of the O and N atoms of the $[Tf_2N]^-$ anions and of the aromatic N atoms of the $[C_4mim]^+$ cations.

Table 3. Position and the Integration Numbers (n) for the Main Maxima of the Radial Distribution Functions in Figure 4a–d

	Ni^{2+}		$Ni(NO_3)^+$		$Ni(NO_3)_2$		$Ni(NO_3)_3^-$	
	$g(r)_{max}$, Å	n	$g(r)_{max}$, Å	n	$g(r)_{max}$, Å	n	$g(r)_{max}$, Å	n
Ni–O (Tf_2N^-)	2.15	6.0	2.12	4.0	2.18	2.0	2.68	0.4
Ni–N (Tf_2N^-)	3.75/4.45	5.0	4.53	4.0	4.68	2.0	4.93	0.6
Ni–NA (C_4mim^+)	7.65	~13.7	7.30	~16.5	5.03	~8.8	4.98	~11.7

The maximum of the Ni–N(C_4mim) RDF is now only slightly shifted to 4.98 Å and corresponds to ~6 cations (Table 3).

According to EXAFS and MD results, one bidentate $[Tf_2N]^-$ anion is replaced by a bidentate nitrate in the first complexation step, while in the second and third steps, two monodentate $[Tf_2N]^-$ anions are replaced by one bidentate nitrate. On this basis, one would expect more positive ΔS_{Kj} values for the formation of the 1:2 and 1:3 complexes with respect to the 1:1, which is not in agreement with what was experimentally found. Therefore, it seems that outer-sphere effects (such as the rearrangement of the solvent structure around the solute) give an important contribution in determining the observed trend of the thermodynamics parameters. From the RDFs obtained in this work (Figure 4a–d), it emerges that the complexation reactions induce a marked change in the distribution of the $[C_4mim]^+$ and $[Tf_2N]^-$ ions in the second sphere of the Ni(II) solute (Tables 3 and S3). In particular, it is interesting to note that the first maximum of the Ni-NA($[C_4mim]^+$) RDF is located at 7.65 Å for the Ni(II) solvate, and its position has a small change when the 1:1 complex is considered (7.3 Å, Figure 4a,b, Table 3). The Ni-NA($[C_4mim]^+$ maximum position has a pronounced shift to 5.03 Å (1:2 complex) to form a more compact shell and finally remains nearly unchanged (4.98 Å) for the 1:3 complex. This rearrangement is also observed for the outer-sphere anions, as the second maximum of the Ni–N(Tf_2N) RDFs shifts from 10.65 to 9.03 Å in the four simulations (Figure 4a–d and Table S3). In conclusion, MD simulations show that the outer-sphere environment around the Ni(II) center changes in the various complexations steps, and this could also have an influence on the overall observed thermodynamics parameters.

■ CONCLUSIONS

This combined experimental and theoretical study of the complexation of Ni(II) in the $[C_4mim][Tf_2N]$ IL shows that three stable mononuclear species of the type $Ni(NO_3)_j$ (j = 1–3) are formed. Therefore, contrarily to what is observed in water, nitrate is a strong ligand for this cation in this medium, in agreement with previous studies in this IL for other ions.[17,18,28] This can be mainly related to the poor coordination ability of the Tf_2N^- anions toward Ni(II). However, also the weak solvation of the nitrate anion in the dry IL may contribute to the high stability of the Ni(II) complexes. On this basis, in the presence of a significant amount of water in the IL (like in real liquid–liquid extraction conditions), a decrease of the stability

DOI: 10.1021/acs.inorgchem.5b02937
Inorg. Chem. 2016, 55, 3498–3507

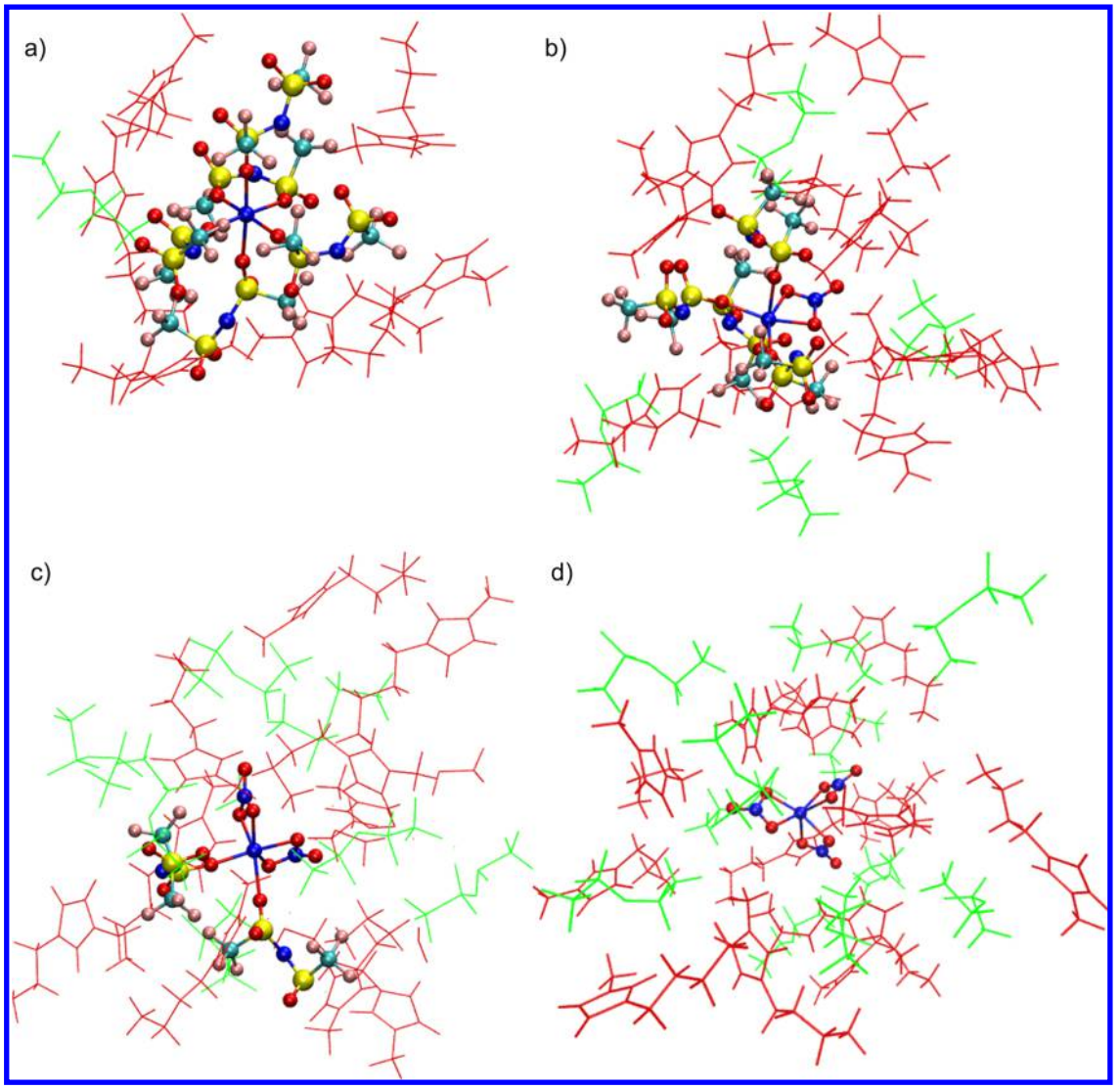

Figure 5. Random snapshots taken from the MD simulations: solvated Ni(II) species (balls and sticks) and outer shell ions (wireframe) located within a radius of 6.5 Å of the Ni(II) solvate ($[C_4mim]^+$ = red, $[Tf_2N]^-$ = green).

and number of species formed is expected, as already observed for Nd(III).[17,18]

Thermodynamic parameters show that the first two complexes are enthalpy-stabilized, while the third one is formed in an entropy-driven process. In particular, the trend of the entropy terms ($T\Delta S_{Kj}$ = +5.3, −5.1, and +26.8 kJ mol^{-1} for j = 1−3) is unexpected on the basis of the change of number of species in the complexation reaction and suggests that outer-sphere effects play an important role.

Spectroscopic data confirm that the Ni(II) cation retains a six-coordinated octahedral geometry in all species and that the nitrate, as also previously found for other cations, coordinates in a bidentate mode in all species. Furthermore, EXAFS spectra confirm that the $[Tf_2N]^-$ anions are completely released in the formation of the final 1:3 species.

Molecular dynamics simulations show that the starting Ni(II) solvate is the $[Ni(Tf_2N)_5]^{3-}$ complex, with the $[Tf_2N]^-$ anions coordinating either as mono or bidentate through the oxygen atoms of two different sulfonyl groups. The species with one nitrate results to be $[Ni(NO_3)(Tf_2N)_4]^{3-}$ with the anions coordinating as monodentate only. When a further nitrate is inserted in the first coordination sphere of nickel, two Tf_2N^- anions are released to form the $[Ni(NO_3)_2(Tf_2N)_2]^{2-}$ species where, again, the anions are coordinating the cation as monodentate. The RDFs obtained from MD simulations show a marked reorganization of the outer-sphere liquid structure in the successive complexation steps, especially evident when passing from the 1:1 to 1:2 species. This result indicates that the most remarkable outer-sphere solvent rearrangement is occurring in the second complexation step, for which the experimental ΔS_{K2} term is small and negative. This finding also supports the hypothesis that outer-sphere effects can have a remarkable weight in determining the trend in the entropy values obtained in this IL.

■ ASSOCIATED CONTENT

Supporting Information

The Supporting Information is available free of charge on the ACS Publications website at DOI: 10.1021/acs.inorgchem.5b02937.

Speciation calculated from UV−vis data fitting, calculated molar absorbances, composition of simulated systems, gas-phase optimized $[Ni(NO_3)_i]^{2-j}$ species and their corresponding ESP charges, speciation calculated on

DOI: 10.1021/acs.inorgchem.5b02937
Inorg. Chem. 2016, 55, 3498−3507

basis of stability constants, position for RDF maxima beyond the first, full citation of Gaussian09. (PDF)

AUTHOR INFORMATION

Corresponding Authors

*E-mail: andrea.melchior@uniud.it. (A.M.)
*E-mail: maria.boltoeva@iphc.cnrs.fr. (M.B.)

Notes

The authors declare no competing financial interest.

ACKNOWLEDGMENTS

We acknowledge the ELETTRA synchrotron (Trieste, Italy) and the SOLEIL synchrotron (Saint-Aubin, France) for providing the synchrotron radiation facilities, and we would like to thank the XAFS/ELETTRA and SAMBA/SOLEIL staffs for their assistance during EXAFS measurements. A.M. acknowledges CINECA (Italy) for computing time (Project No. IscrC-HM2015-1).

REFERENCES

(1) *Radiochemistry in Nuclear Power Reactors;* Lin, C. C., Ed.; The National Academies Press: Washington, DC, 1996.
(2) Koel, M. *Crit. Rev. Anal. Chem.* **2005**, *35* (3), 177−192.
(3) Plechkova, N. V.; Seddon, K. R. *Chem. Soc. Rev.* **2008**, *37* (1), 123−150.
(4) Podgoršek, A.; Pensado, A. S.; Santini, C. C.; Costa Gomes, M. F.; Pádua, A. a H. *J. Phys. Chem. C* **2013**, *117* (7), 3537−3547.
(5) Docherty, K. M.; Kulpa, C. F., Jr. *Green Chem.* **2005**, *7* (4), 185.
(6) Armand, M.; Endres, F.; MacFarlane, D. R.; Ohno, H.; Scrosati, B. *Nat. Mater.* **2009**, *8* (8), 621−629.
(7) Olivier-Bourbigou, H.; Magna, L.; Morvan, D. *Appl. Catal., A* **2010**, *373*, 1−56.
(8) Di Bernardo, P.; Melchior, A.; Portanova, R.; Tolazzi, M.; Zanonato, P. L. *Coord. Chem. Rev.* **2008**, *252*, 1270−1285.
(9) Di Bernardo, P.; Zanonato, P. L.; Benetollo, F.; Melchior, A.; Tolazzi, M.; Rao, L. *Inorg. Chem.* **2012**, *51* (16), 9045−9055.
(10) Comuzzi, C.; Melchior, A.; Polese, P.; Portanova, R.; Tolazzi, M. *Eur. J. Inorg. Chem.* **2003**, *10*, 1948−1955.
(11) Melchior, A.; Peralta, E.; Valiente, M.; Tavagnacco, C.; Endrizzi, F.; Tolazzi, M. *Dalton Trans.* **2013**, *42* (17), 6074−6082.
(12) Di Bernardo, P.; Melchior, A.; Tolazzi, M.; Zanonato, P. L. *Coord. Chem. Rev.* **2012**, *256* (1−2), 328−351.
(13) Del Piero, S.; Di Bernardo, P.; Fedele, R.; Melchior, A.; Polese, P.; Tolazzi, M. *Eur. J. Inorg. Chem.* **2006**, No. 18, 3738−3745.
(14) Cavallo, L.; Del Piero, S.; Ducéré, J.-M.; Fedele, R.; Melchior, A.; Morini, G.; Piemontesi, F.; Tolazzi, M. *J. Phys. Chem. C* **2007**, *111* (11), 4412−4419.
(15) Piccinelli, F.; Bettinelli, M.; Melchior, A.; Grazioli, C.; Tolazzi, M. *Dalt. Trans.* **2015**, *44* (1), 182−192.
(16) Popov, K.; Vendilo, A.; Pletnev, I.; Rönkkömäki, H.; Lajiunen, L. H. J. In *Ionic Liquids: Theory, Properties, New Approaches;* Kokorin, A., Ed.; InTech, 2011.
(17) Ansari, S. A.; Liu, L.; Dau, P. D.; Gibson, J. K.; Rao, L. *RSC Adv.* **2014**, *4* (72), 37988.
(18) Liu, L.; Tian, G.; Rao, L. *Solvent Extr. Ion Exch.* **2013**, *31* (4), 384−400.
(19) Ansari, S. A.; Liu, L.; Rao, L. *Dalton Trans.* **2015**, *44* (6), 2907−2914.
(20) Georg, S.; Billard, I.; Ouadi, A.; Gaillard, C.; Petitjean, L.; Picquet, M.; Solov'ev, V. *J. Phys. Chem. B* **2010**, *114* (12), 4276−4282.
(21) Binnemans, K. In *Comprehensive Inorganic Chemistry II: From Elements to Applications;* Reedijk, J., Poeppelmeier, K., Eds.; Elsevier, **2013**; Vol. 2, pp 641−673.10.1016/B978-0-08-097774-4.00228-X
(22) Stumpf, S.; Billard, I.; Gaillard, C.; Panak, P. J.; Dardenne, K. *Radiochim. Acta* **2008**, *96* (1), 1−10.
(23) Billard, I.; Gaillard, C. *Radiochim. Acta* **2009**, *97* (7), 355−359.
(24) Chaumont, A.; Wipff, G. *Inorg. Chem.* **2009**, *48* (10), 4277−4289.
(25) Chaumont, A.; Wipff, G. *Chem. - Eur. J.* **2004**, *10* (16), 3919−3930.
(26) Gaillard, C.; Billard, I.; Chaumont, A.; Mekki, S.; Ouadi, A.; Denecke, M. A.; Moutiers, G.; Wipff, G. *Inorg. Chem.* **2005**, *44* (23), 8355−8367.
(27) Gaillard, C.; Boltoeva, M.; Billard, I.; Georg, S.; Mazan, V.; Ouadi, A.; Ternova, D.; Hennig, C. *ChemPhysChem* **2015**, *16* (12), 2653−2662.
(28) Gaillard, C.; Chaumont, A.; Billard, I.; Hennig, C.; Ouadi, A.; Wipff, G. *Inorg. Chem.* **2007**, *46* (12), 4815−4826.
(29) Chaumont, A.; Klimchuk, O.; Gaillard, C.; Billard, I.; Ouadi, A.; Hennig, C.; Wipff, G. *J. Phys. Chem. B* **2012**, *116* (10), 3205−3219.
(30) Fujii, K.; Hamano, H.; Doi, H.; Song, X.; Tsuzuki, S.; Hayamizu, K.; Seki, S.; Kameda, Y.; Dokko, K.; Watanabe, M.; Umebayashi, Y. *J. Phys. Chem. C* **2013**, *117* (38), 19314−19324.
(31) Tsuzuki, S.; Shinoda, W.; Matsugami, M.; Umebayashi, Y.; Ueno, K.; Mandai, T.; Seki, S.; Dokko, K.; Watanabe, M. *Phys. Chem. Chem. Phys.* **2015**, *17* (1), 126−129.
(32) Takemura, S.; Kawakami, S.; Harada, M.; Iida, M. *Inorg. Chem.* **2014**, *53* (18), 9667−9678.
(33) De Vreese, P.; Brooks, N. R.; Van Hecke, K.; Van Meervelt, L.; Matthijs, E.; Binnemans, K.; Van Deun, R. *Inorg. Chem.* **2012**, *51* (9), 4972−4981.
(34) Bortolini, O.; Chiappe, C.; Ghilardi, T.; Massi, A.; Pomelli, C. S. *J. Phys. Chem. A* **2015**, *119* (21), 5078−5087.
(35) Gans, P.; Sabatini, A.; Vacca, A. *Talanta* **1996**, *43* (10), 1739−1753.
(36) Gans, P.; Sabatini, A.; Vacca, A. *J. Solution Chem.* **2008**, *37* (4), 467−476.
(37) Izatt, R. M.; Christensen, J. J.; Snow, R. L.; Eatough, D. *J. Phys. Chem.* **1968**, *72* (4), 1208−1213.
(38) Comuzzi, C.; Polese, P.; Melchior, A.; Portanova, R.; Tolazzi, M. *Talanta* **2003**, *59* (1), 67−80.
(39) Del Piero, S.; Melchior, A.; Polese, P.; Portanova, R.; Tolazzi, M. *Ann. Chim.* **2006**, *96* (1−2), 29−49.
(40) Ravel, B.; Newville, M. *J. Synchrotron Radiat.* **2005**, *12* (4), 537−541.
(41) Ankudinov, A. L.; Rehr, J. J. *Phys. Rev. B: Condens. Matter Mater. Phys.* **2000**, *62* (4), 2437−2445.
(42) Newville, M.; Ravel, B.; Haskel, D.; Rehr, J. J.; Stern, E. A.; Yacoby, Y. *Phys. B* **1995**, *208*−*209*, 154−156.
(43) Hay, P. J.; Wadt, W. R. *J. Chem. Phys.* **1985**, *82* (1), 270.
(44) Breneman, C. M.; Wiberg, K. B. *J. Comput. Chem.* **1990**, *11* (3), 361−373.
(45) Marenich, A. V.; Cramer, C. J.; Truhlar, D. G. *J. Phys. Chem. B* **2009**, *113* (18), 6378−6396.
(46) Bernales, V. S.; Marenich, A. V.; Contreras, R.; Cramer, C. J.; Truhlar, D. G. *J. Phys. Chem. B* **2012**, *116* (30), 9122−9129.
(47) Frisch, M. J. et al. *Gaussian09,* Revision D.01; Gaussian, Inc: Wallingford, CT, 2009.
(48) Schoonhoven, J. W. F. M.; Driessen, W. L.; Reedijk, J.; Verschoor, G. C. *J. Chem. Soc., Dalton Trans.* **1984**, *6*, 1053.
(49) Michaud, A.; Fontaine, F.-G.; Zargarian, D. *Inorg. Chim. Acta* **2006**, *359* (9), 2592−2598.
(50) Gaillard, C.; Chaumont, A.; Billard, I.; Hennig, C.; Ouadi, A.; Georg, S.; Wipff, G. *Inorg. Chem.* **2010**, *49* (14), 6484−6494.
(51) Hoffmann, M. M.; Darab, J. G.; Palmer, B. J.; Fulton, J. L. *J. Phys. Chem. A* **1999**, *103* (42), 8471−8482.
(52) Canongia Lopes, J. N.; Deschamps, J.; Pádua, A. A. H. *J. Phys. Chem. B* **2004**, *108* (6), 2038−2047.
(53) Köddermann, T.; Paschek, D.; Ludwig, R. *ChemPhysChem* **2007**, *8* (17), 2464−2470.
(54) Frenkel, D.; Smit, B. *Understanding molecular simulation: from algorithms to applications,* 2nd ed.; Academic Press: Harcourt, FL, 2002.
(55) Van Der Spoel, D.; Lindahl, E.; Hess, B.; Groenhof, G.; Mark, A. E.; Berendsen, H. J. C. *J. Comput. Chem.* **2005**, *26*, 1701−1718.

DOI: 10.1021/acs.inorgchem.5b02937
Inorg. Chem. 2016, 55, 3498−3507

(56) Comuzzi, C.; Melchior, A.; Polese, P.; Portanova, R.; Tolazzi, M. *Eur. J. Inorg. Chem.* **2002**, *8*, 2194−2201.
(57) Di Bernardo, P.; Zanonato, P. L.; Melchior, A.; Portanova, R.; Tolazzi, M.; Choppin, G. R.; Wang, Z. *Inorg. Chem.* **2008**, *47* (3), 1155−1164.
(58) Nockemann, P.; Pellens, M.; Van Hecke, K.; Van Meervelt, L.; Wouters, J.; Thijs, B.; Vanecht, E.; Parac-Vogt, T. N.; Mehdi, H.; Schaltin, S.; Fransaer, J.; Zahn, S.; Kirchner, B.; Binnemans, K. *Chem. - Eur. J.* **2010**, *16* (6), 1849−1858.
(59) Katase, T.; Imashuku, S.; Murase, K.; Hirato, T.; Awakura, Y. *Sci. Technol. Adv. Mater.* **2006**, *7* (6), 502−510.
(60) Hoffmann, H.; Janjic, T.; Sperati, R. *Ber. Bunsen Phys. Chem.* **1974**, *78* (3), 223−230.
(61) Inada, Y.; Sugimoto, K.; Ozutsumi, K.; Funahashi, S. *Inorg. Chem.* **1994**, *33* (9), 1875−1880.
(62) Carriat, J. Y.; Che, M.; Kermarec, M.; Verdaguer, M.; Michalowicz, A. *J. Am. Chem. Soc.* **1998**, *120* (9), 2059−2070.
(63) Ansell, S.; Neilson, G. W. *Biophys. Chem.* **2004**, *107* (3), 229−241.
(64) Johnson, A. L.; Davidson, M. G.; Jones, M. D.; Lunn, M. D. *Inorg. Chim. Acta* **2010**, *363* (10), 2209−2214.
(65) Siegler, M. A.; Parkin, S.; Selegue, J. P.; Brock, C. P. *Acta Crystallogr., Sect. B: Struct. Sci.* **2008**, *64* (6), 725−737.
(66) Siegler, M. A.; Parkin, S.; Brock, C. P. *Acta Crystallogr., Sect. B: Struct. Sci.* **2012**, *68* (4), 389−400.
(67) Gaillard, C.; Chaumont, A.; Billard, I.; Hennig, C.; Ouadi, A.; Wipff, G. *Inorg. Chem.* **2007**, *46* (12), 4815−4826.

DOI: 10.1021/acs.inorgchem.5b02937
Inorg. Chem. 2016, 55, 3498−3507

Nowadays the environmental pollution is a great global enemy, being one of the problems that most affect the whole world. This PhD thesis focuses on the elimination of certain aqueous contaminants, such as fluoride or different metal ions. Nanostructured materials have been applied as innovative adsorption method to remove the aforementioned water pollutants. These materials present a high surface area in a very small volume, being ideal characteristics as materials for the treatment of wastewater.

The first chapter of the thesis focuses on the removal of fluoride from contaminated water by using hierarchical alumina microspheres (HAM), while the second part of the thesis focuses on the removal of heavy metals and precious metals from contaminated water. In this case, functionalized magnetic nanoparticles (SPION, Super Paramagentic Iron Oxide Nanoparticles) have been chosen as adsorbent.

The adsorption processes have been described in terms of loading capacity and thermodynamic parameters, by using a new experimental approach with Isothermal Titration Calorimetry (ITC). ITC is applied for the first time in this work to obtain direct determination of ΔH_{ads} for fluoride ion adsorption by HAM and metal ions in functionalized SPION to provide independent and more robust thermodynamic parameters